

**Nanoscale thermal, acoustic, and magnetic  
dynamics probed with soft x-ray light**

by

**Mark E. Siemens**

B.S., Engineering Physics, Colorado School of Mines, 2003

A thesis submitted to the  
Faculty of the Graduate School of the  
University of Colorado in partial fulfillment  
of the requirements for the degree of  
Doctor of Philosophy  
Department of Physics

2010

This thesis entitled:  
Nanoscale thermal, acoustic, and magnetic dynamics probed with soft x-ray light  
written by Mark E. Siemens  
has been approved for the Department of Physics

---

Prof. Henry C. Kapteyn

---

Prof. Margaret M. Murnane

Date \_\_\_\_\_

The final copy of this thesis has been examined by the signatories, and we find that both the content and the form meet acceptable presentation standards of scholarly work in the above mentioned discipline.

Siemens, Mark E. (Ph.D., Physics)

Nanoscale thermal, acoustic, and magnetic dynamics probed with soft x-ray light

Thesis directed by Prof. Margaret M. Murnane and Prof. Henry C. Kapteyn

This thesis discusses the application of coherent, ultrafast beams of soft x-ray light from high-order harmonic generation (HHG) to study thermal, acoustic, and magnetic processes in nanostructures. This short-wavelength light is a uniquely powerful probe of surface dynamics since it has both a very short wavelength and duration.

First, this thesis reports the first observation and quantitative measurements of the transition from diffusive to ballistic thermal transport for the case of heat flow away from a heated nanostructure into a bulk substrate. This measurement provides insight into the fundamentals of thermal energy transport away from nanoscale hot spots, and demonstrates a fundamental limit to the energy dissipation capability of nanostructures. Further, we propose a straightforward correction to the Fourier law for heat diffusion, necessary for thermal management in nanoelectronics, nano-enabled energy systems, nanomanufacturing, and nanomedicine.

Second, this work discusses dynamic measurements of ultra-high frequency surface acoustic waves (SAW) and the first SAW dispersion measurement in a nanostructured system. These results are directly applicable to adhesion and thickness diagnostics of very thin films.

Finally, this thesis reports the first use of light from HHG to study magnetic orientation. Using the transverse magneto-optic Kerr effect and soft x-ray light near the M-absorption edges of Fe, Co, and Ni, magnetic asymmetries up to 8% are observed from thin Permalloy (Ni<sub>80</sub>Fe<sub>20</sub>) films. This signal is 1-2 orders of magnitude higher than that observed using optical methods, showing great promise for dynamic imaging of domain flipping at the 100 nm level.

## Acknowledgements

My experience as a graduate student at CU/JILA was awesome- mostly because of the people around me. Margaret and Henry were fantastic advisors, giving me great resources and freedom to accomplish this work. Ronggui Yang was as an extra advisor, giving up many afternoons to patiently explain heat transfer to me. In the KM group, I worked with many people who often gave up their time to help me fix my laser or figure out my experiment, including (in order of Margaret's email list): David Gaudiosi, Tim Lei, Ariel Paul, Erez Gershgoren, Nick Wagner, Etienne Gagnon, Amy Lytle, Xiaoshi Zhang, Isabell Thomann, Daisy Raymondson, Tenio Popmintchev, Xibin Zhou, Andrea Wuest, Arvinder Sandhu, Guido Saathoff, Robynne Hooper, Wen Li, Richard Sandberg, Ming-Chang Chen, Alon Bahabad, Michael Gerrity, Craig Hogle, Matt Seaberg, Ethan Townsend, and Adrienne Pon. I worked more closely with a few others: Jing Yin made me laugh a lot, Oren Cohen inspired me to think big scientifically and always got the same thing for lunch as me at the Thai place, and Luis Miaja-Avila was a great friend from the time we took classes together until we both finally graduated. Finally, a special thanks to those I worked with daily: Ra'anana Tobey for "teaching me all he knows", Qing Li for pushing me to understand more with her questions, and Chan La-O-Vorakiat for his enthusiasm for life and fun-to-say last name. It was a pleasure working with all of you, and I will miss you greatly.

Of course, the person I have been most encouraged, challenged, and loved by is my beautiful wife Katie. I can't imagine the last four years without her (or Abbie!).

# Contents

## Chapter

<b>1</b>	Introduction	1
1.1	Pump-probe measurement technique . . . . .	2
1.2	Outline . . . . .	3
<b>2</b>	Ultrafast laser-initiated transport: photons, electrons, and phonons	6
2.1	Photons . . . . .	6
2.2	Electrons . . . . .	9
2.3	Phonons . . . . .	12
2.4	Modeling thermal transport in real systems: circuit analogy . . . . .	16
2.4.1	Energy transport across an interface . . . . .	16
2.4.2	Energy transport in the bulk . . . . .	18
2.4.3	Putting the pieces together . . . . .	19
2.5	Conclusion . . . . .	20
<b>3</b>	High-order harmonic generation	21
3.1	Introduction . . . . .	21
3.2	Advantages of EUV light . . . . .	21
3.2.1	Shorter wavelength . . . . .	22
3.2.2	Elemental selectivity . . . . .	23
3.3	High-order harmonic generation . . . . .	24

3.3.1	Step 1: Tunneling ionization . . . . .	26
3.3.2	Step 2: Free electron propagation in a laser field . . . . .	28
3.3.3	Step 3: Recombination and radiation . . . . .	30
3.3.4	HHG in hollow waveguides . . . . .	32
3.3.5	Characteristics of HHG . . . . .	33
3.4	Conclusion: Unique advantages of HHG . . . . .	35
<b>4</b>	<b>Time-resolved EUV holography</b>	<b>37</b>
4.1	Holography with EUV light from HHG . . . . .	38
4.2	Fresnel propagation model . . . . .	42
4.3	Longitudinal acoustic propagation measurement . . . . .	46
4.4	Advantages of probing surface displacement with EUV light . . . . .	48
4.5	Conclusion . . . . .	51
<b>5</b>	<b>Experimental setup for EUV probing of dynamics in nanostructures</b>	<b>54</b>
5.1	EUV detection and noise management . . . . .	54
5.1.1	Laser system and beampath stability . . . . .	55
5.1.2	Acquisition technique: chopping faster . . . . .	56
5.1.3	The danger of normalization . . . . .	58
5.2	Sample design and fabrication . . . . .	59
5.3	Experimental setup . . . . .	61
5.3.1	Pump beam setup . . . . .	61
5.3.2	Glancing-incidence toroidal focusing mirror for EUV light . . . . .	63
5.3.3	Aluminum filter holder and CCD adapter . . . . .	65
5.3.4	Mechanical setup . . . . .	69
5.4	Data acquisition and analysis . . . . .	70
5.4.1	Data acquisition and time-dependent signal extraction . . . . .	71
5.4.2	Signal linearity . . . . .	71

5.5	Time-resolved EUV acquisition outlook . . . . .	74
<b>6</b>	<b>High-Frequency Surface Acoustic Wave Propagation in Nanostructures</b>	<b>77</b>
6.1	Surface acoustic wave propagation for thin film measurements . . . . .	78
6.2	EUV measurements of SAW dynamics . . . . .	81
6.2.1	Are we really seeing surface acoustic wave propagation? . . . . .	81
6.2.2	Surface acoustic wave dispersion measurements . . . . .	84
6.3	SAW dispersion calculation: Modified thin film theory . . . . .	86
6.3.1	SAW dispersion due to a thin film: Perturbative Auld model . . . . .	87
6.3.2	SAW dispersion due to a thin film: Nelson model . . . . .	90
6.3.3	Comparing models to the data . . . . .	93
6.4	Conclusion . . . . .	94
<b>7</b>	<b>Quasi-ballistic heat transport from nanoscale interfaces</b>	<b>96</b>
7.1	Ballistic thermal transfer in and through a nanostructure . . . . .	97
7.1.1	The Boltzmann transport equation for transport in a nanostructure . . . . .	98
7.1.2	Basic theory of quasi-ballistic thermal transfer in a nanostructure . . . . .	99
7.1.3	Experimental observations of ballistic transport in nanostructures . . . . .	101
7.2	Quasi-ballistic thermal transport at an interface . . . . .	103
7.2.1	Thermal boundary resistance across a bulk-constricted interface . . . . .	104
7.2.2	Simple analytical prediction: ballistic-diffusive model . . . . .	106
7.2.3	Propagating vs reservoir phonons . . . . .	110
7.2.4	Previous experiment and open questions . . . . .	114
7.3	Measurement of ballistic heat transport at a nanoscale interface . . . . .	114
7.4	Multiphysics model for data analysis . . . . .	116
7.4.1	Thermal transport across the interface and diffusion . . . . .	116
7.4.2	Thermal expansion . . . . .	122
7.4.3	Fresnel optical propagation . . . . .	128

7.4.4	Discussion of model results . . . . .	128
7.4.5	Fitting the model to our experimental data . . . . .	130
7.5	Implications of the measurement . . . . .	133
7.6	Discussion of the time-resolved measurement . . . . .	136
7.7	EUV probing of nanoscale thermal transport outlook . . . . .	137
7.8	Conclusion . . . . .	139
<b>8</b>	<b>Magneto-optics with EUV light</b>	<b>140</b>
8.1	Historical development of the magneto-optic Kerr effect (MOKE) . . . .	141
8.2	Derivation of the transverse magneto-optic Kerr effect . . . . .	142
8.2.1	Macroscopic (phenomenological) description . . . . .	142
8.2.2	Microscopic (fundamental) description . . . . .	145
8.3	Experimental Magneto-Optic Kerr effect using EUV from HHG . . . . .	148
8.3.1	Experimental setup . . . . .	148
8.3.2	Magnetic contrast measured with EUV light from HHG . . . . .	152
8.3.3	Hysteresis measurement . . . . .	153
8.3.4	Surface sensitivity measurement . . . . .	154
8.4	Outlook: EUV measurement of demagnetization dynamics . . . . .	155
8.5	Conclusion . . . . .	157
<b>9</b>	<b>Conclusion</b>	<b>158</b>
	<b>Bibliography</b>	<b>161</b>
	<b>Appendix</b>	
<b>A</b>	<b>Fresnel propagation code</b>	<b>178</b>
<b>B</b>	<b>Multiphysics thermal and optical model</b>	<b>180</b>

## Chapter 1

### Introduction

The remarkable advances in nanofabrication technology in the past few decades have opened up unprecedented opportunities in the engineering of optical, electronic, magnetic, and thermal properties of materials. These advances have been in large part by the relentless microelectronics industry (which is, of course, driven by a desire to take your money), so it is natural that electronic properties at the nanoscale have received a tremendous amount of attention. Similarly, there are many scientifically interesting and useful applications of optical phenomena at the nanoscale, including field enhancement. Advances in magnetism have been driven in part by the information storage industry, and individual bits stored on a hard disk, spintronic devices and magnetic random access memory are already exploiting sub-micron magnetic structures. Finally, thermal management in nanostructures is becoming increasingly “hot”, with applications requiring both optimized transport (e.g. heat-sinking a transistor) and minimized transport (e.g. thermoelectric energy conversion).

Nanostructures not only provide extremely fine engineering control useful for applications, but also offer opportunities to observe the fundamental length scales of physical phenomena. The confined walls of a nanostructure can be smaller than optical wavelengths, magnetic domains in the bulk, or phonon scattering distances (or even phonon wavelengths). By looking at the system properties as a function of nanostructure size and temperature, insight into physical fundamentals and the interaction of energy

carriers is possible.

This thesis focuses on the study of physical phenomena in nanostructures on with length scales near the fundamental limits of acoustic, thermal, and magnetic effects.

## 1.1 Pump-probe measurement technique

Most of the experiments discussed in this thesis make use of the pump-probe technique, in which a laser pulse is split into a stronger pulse that excites a system and a weaker, time-delayed pulse probing the change caused by the pump. Using ultrafast lasers at optical wavelengths ( $\lambda \sim 400 \text{ nm} - 800 \text{ nm}$ ), it has been possible to measure optical excitation of electrons in metals [1] and semiconductors, phonon transport in the bulk and in thin films, ultrafast phase transformations and fundamental electron and phonon transport in exotic systems such as carbon nanotubes and gold nanorods.

However, optical light is not always useful for exciting or observing the phenomena we want to see. Observing acoustic, thermal, and magnetic effects in materials is particularly difficult because the reflection of optical light couples very weakly to these processes. Another problem is that imaging resolution is limited by the wavelength of the probe light by the diffraction limit, so optical light is limited to images with  $\sim 500 \text{ nm}$  resolution. Very sensitive detection of surface displacement can be obtained using an optical interferometer, but there is potential for even better interferometric sensitivity if shorter-wavelength light is used. Finally, direct excitation of inner-shell electrons also requires higher energy (shorter wavelength) light. Direct excitation is useful for studies such as element-specific imaging [2], Auger decay [3], or x-ray absorption fine structure measurements [4].

There is clearly a strong case to use shorter wavelength (ultraviolet to x-ray) light in pump-probe experiments. High-order harmonic generation (HHG) is an ideal source for such experiments because it produces light that is

- coherent, allowing for interferometric measurement and detection,
- tunable and short-wavelength, with light generated in the Extreme Ultraviolet (or soft x-ray) region of the spectrum from 10 - 1 keV (120 - 1 nm),
- ultrafast, with pulses less than 10 fs in duration,
- bright – A pulse energy of greater than 10 nJ is possible when phase-matched.

We will describe experiments implementing HHG light as a highly-sensitive probe of nanoscale surface dynamics in thermal, acoustic, and magnetic systems.

## 1.2 Outline

We will begin with an introduction to the physics of ultrafast laser-solid interactions in Chapter 2. The chapter describes the physical processes that occur when an ultrafast laser pulse hits a material: photon absorption by an electron, electron-electron and then electron-phonon coupling. A discussion of phonon diffusion follows, including a derivation of the Fourier law for thermal transport. The chapter concludes with a simple method for accounting for competing transport mechanisms in a system, both in the bulk and at an interface.

In Chapter 3, the high-order harmonic generation process is introduced. The semiclassical three step model is reviewed, along with the benefits of performing high harmonic generation in a hollow waveguide. The unique advantages of light from HHG over alternative sources of EUV and soft x-ray light are considered.

Chapter 4 presents a proof-of-principle experiment showing thermal and acoustic effects measured in a thin film system. This experiment demonstrates that EUV light from HHG is a sensitive tool for measuring very small thermal and acoustic dynamics that can be determined from surface deformations. Furthermore, because the index of refraction of most materials at EUV wavelengths is very insensitive to density changes,

we make a pure surface phase measurement, unpolluted by a change in surface reflectivity. This is in contrast to experiments at optical wavelengths, where thermal density changes lead to a large change in reflectivity and complicates a determination of the dynamic surface profile.

The experimental setup for measuring very small thermal, acoustic, and magnetic signals is explained in detail in Chapter 5. Techniques for enhancing the stability of the light from HHG and filtering other sources of noise are discussed. The basic optical pump, EUV probe experimental geometry is introduced, along with design and fabrication details for a typical nanostructured sample. Representative data is shown along with an explanation of the process of extracting useful information from raw data.

In Chapter 6, experiments studying surface acoustic wave (SAW) propagation in nanostructures are discussed. As described in Chapter 5, an ultrafast optical laser pulse hits a nanostructured sample, impulsively stressing the surface with a periodicity set by the nanostructure. This periodic and impulsive stress launches SAWs that propagate along the surface with a penetration depth depending on their wavelength: deep penetration from long wavelengths, and shallow penetration for short wavelengths. SAW wavelengths as short as 125 nm are considered, with a frequency of nearly 50 GHz and a penetration depth of  $\sim 20$  nm, almost an order of magnitude better than what is possible using optical excitation methods to generate the SAW. This technique therefore has applications in studying the properties of and interfaces beneath very thin films.

At the same time as the SAW propagation is occurring, the heated nanostructures are also cooling, as energy is transported into the substrate. Chapter 7 discusses this thermal transport, emphasizing the effect of reducing the size of a nanoscale heated region below the phonon mean free path of the heat sink. In this domain, heat transport near the interface can no longer be considered diffusive, as there are not enough scattering events to establish local thermal equilibrium. However, the Fourier law for thermal transport assumes that diffusion is valid over any length scale. This assumes

additional scattering events, which causes a significant over-prediction of the heat flux away from nanoscale heat sources and may have catastrophic effects in thermal engineering of nanoscale devices. This chapter discusses the first experimental observation and quantitative measurement of this effect, as well as a proposed method for correcting the Fourier law at small length scales: addition of a size-dependent interfacial resistivity that accounts for the over-prediction caused by assumed diffusion. Excellent agreement between this model and the experimental data are observed.

Chapter 8 introduces the first measurements of static magnetic flipping asymmetry with soft x-ray light from HHG. These experiments make use of the transverse magneto-optic Kerr effect (T-MOKE). The signal observed is commensurate with that obtained from synchrotron radiation. Near the absorption edges of the magnetic elements under study (nickel and iron in a thin film Permalloy  $\text{Ni}_{80}\text{Fe}_{20}$  sample), the signal is more than two orders of magnitude higher than that measured optically. This strong contrast is very promising for future experiments exploring ultrafast demagnetization and dynamic microscopy of domain flipping.

The thesis is concluded in Chapter 9 with a summary of the thermal, acoustic, and magnetic phenomena observed with soft x-ray light. It closes with a few remarks about the future outlook of HHG light as a source for studying surface processes. The appendices provide two MATLAB programs. The program in Appendix A performs Fresnel propagation, and is useful for determining how light diffracts from a surface with nanoscale features (either static nanstructure or laser thermal deformation). Appendix B provides a multiphysics model for laser heating, heat diffusion, thermal expansion, and optical diffraction from a thermally-deformed surface and subsequent propagation. The model was used in the data analysis for Chapter 7.

## Chapter 2

### Ultrafast laser-initiated transport: photons, electrons, and phonons

The interaction of photons, electrons, and phonons has been studied extensively and is covered in a number of textbooks [5, 6]. In this introduction, I will focus on the issue of energy transport driven by short-pulse laser excitation, and heat transfer mediated by interfaces at short length scales. Characteristic time scales for the processes discussed in this chapter are given in Table 2.1.

#### 2.1 Photons

When considering the energy-carrying ability of electromagnetic radiation (photons), it is usually easiest to think in terms of the particle nature, where each photon has an energy given by

$$E = h\nu, \tag{2.1}$$

where  $h$  is Planck's constant ( $h = 6.626 \times 10^{-34}$  m<sup>2</sup>kg/s) and  $\nu = c/\lambda$  is the frequency of the photon inversely proportional to the wavelength. 800 nm (red- on the edge of infrared) light has a frequency of  $3.74 \times 10^{14}$  Hz, so each photon has an energy of  $E = 2.48 \times 10^{-19}$  J. The unwieldiness of such numbers can be alleviated by a change of units to electron volts ( $1 \text{ eV} = 1.6 \times 10^{-19}$  J, the energy gained by a free electron after accelerating through a 1 V electrostatic potential), where a 600 nm photon has an energy of 1.55 eV.

Fundamental physical processes	Interaction	Time scale (s)
Optical electronic excitation	photon-e	$10^{-14}$
Electron thermalization	e-e	$10^{-13}$
Electron cooling	e-phonon	$10^{-13} - 10^{-12}$
Phonon relaxation	phonon-phonon	$10^{-12}$
Thermal diffusion	phonon-bulk	$10^{-12} - 10^{-11}$
Thermal melting	bulk-bulk	$10^{-11}$
Thermal ablation	bulk-free	$10^{-10}$

Table 2.1: Time scale of ultrafast interactions (Adapted from D. von der Linde, et. al. [7]). The line separates thermal (below) from nonthermal (above) processes. Melting and ablation will occur only for sufficiently high incident intensities.

A typical natural light source emits its radiation over  $4\pi$  steradians and is incoherent, that is, light is emitted in all directions and there is no relation between one photon and another in direction or phase. The transport of energy by photons has taken a tremendous step forward with the invention and development of the laser, which allowed for the creation of coherent beams of photons that have

- (1) directionality, useful for the efficient transport of energy or information, and
- (2) both spatial coherence (photons move “in step” across the laser beam) and temporal coherence (photons move “in step” over time past a single point), allowing for high-precision interference measurements and holography.

\*\*\*\* The primary fundamental laser-matter interaction is the absorption of photons by electrons, which drives electrons from their equilibrium states to excited states. In the case of CW (continuous wave, i.e. unpulsed) laser illumination, the time between excitation events is longer than the relaxation of the energized electrons by electron-electron and electron-phonon collisions [8]. This means that there is equilibrium between the electrons and phonons in the system during the laser-heating process.

In contrast to the CW case, ultrafast lasers have pulses  $\sim 20$  fs (1 femtosecond =  $1 \times 10^{-15}$  s), a time almost inconceivably short: a pulse traveling at the speed of light in air is only  $3 \mu\text{m}$  long, about 1/30th the diameter of a human hair. Modern ultrafast

lasers are based on Kerr lens modelocking, in which thermal lensing in the laser crystal creates a condition of stable operation for pulsed, rather than CW, operation [9, 10]. Titanium-doped sapphire is an excellent lasing medium for these ultrafast lasers because it has very good thermal conductivity (making it easier to remove excess heat) and very broadband absorption and emission. That this is important can be seen from the Heisenberg uncertainty relations for energy time:

$$\Delta E \Delta t \geq \hbar/2. \quad (2.2)$$

From this expression, it is clear that to get a pulse that is very short in time, a broad range of energies is required. Ti:Sapphire has an emission bandwidth of  $\sim 250$  nm, centered at approximately 800 nm [11], so this is where most ultrafast lasers operate. Of course, just having a broadband source does not guarantee ultrafast pulses, so dispersion compensation (correcting small phase drift between wavelengths as the bluer wavelengths travel slightly slower than the red in air) is also critical, and can be accomplished in an oscillator by the use of a prism pair. Laser oscillators give fairly weak pulses,  $< 20$  nJ/pulse [10], but these can be amplified using a stretcher-compressor chirped pulse amplifier also based on lasing in a Ti:Sapphire crystal [12].

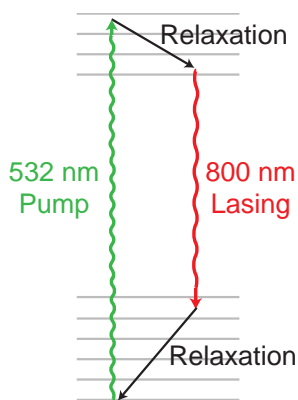


Figure 2.1: Laser energy level diagram for Ti:Sapphire. Note the wide bands for absorption and emission, providing a broad frequency base for ultrafast pulse generation.

The applications of ultrafast laser pulses are numerous: they can measure dy-

dynamic processes with unprecedented temporal resolution, and initiate nonlinear and nonequilibrium energy transfer. Femtosecond-level resolution is important because the fundamental time scales of many carrier interactions and transport processes are on this level. For example, molecules vibrate on a time scale of 10-100 fs and electrons are ionized (ripped off of atoms) and excited between levels in less than 1 fs. Another key feature of ultrafast lasers is their high peak power. For example, given the same total energy, a 100 fs pulse has a peak energy density 13 orders of magnitude higher than a CW laser. Because the peak intensity of ultrafast lasers is so high, a single pulse can initiate highly-nonlinear physical processes, such as the high-order harmonic generation process discussed in Chapter 3.

## 2.2 Electrons

The concentrated energy delivered by an ultrashort laser pulse can generate highly excited, nonequilibrium electron distributions. The electrons are excited by direct photon absorption (see Figure 2.2) on a timescale limited only by the duration of the laser pulse (therefore the electron response time is less than 10 fs and is negligible). The spatial depth profile is determined by the optical penetration depth in the metal ( $\zeta_o \sim 10$  nm at an optical wavelength of 800 nm- see Table 2.2), as shown in the top row in Figure 2.3.

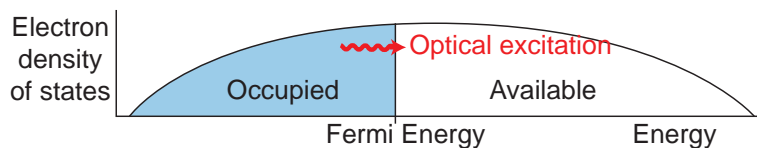


Figure 2.2: Electron density of states near the Fermi energy for a typical metal. If an optical pulse is incident on the material, a photon of energy  $E = h\nu$  can be absorbed by an electron, creating the nonequilibrium electron distribution shown in the first step of Figure 2.3. In the case of very short pulses with high peak intensities, multiphoton ionization can excite electrons from deeper in the valence band or from lower-energy bands, but it is still less likely than direct photon-electron absorption.

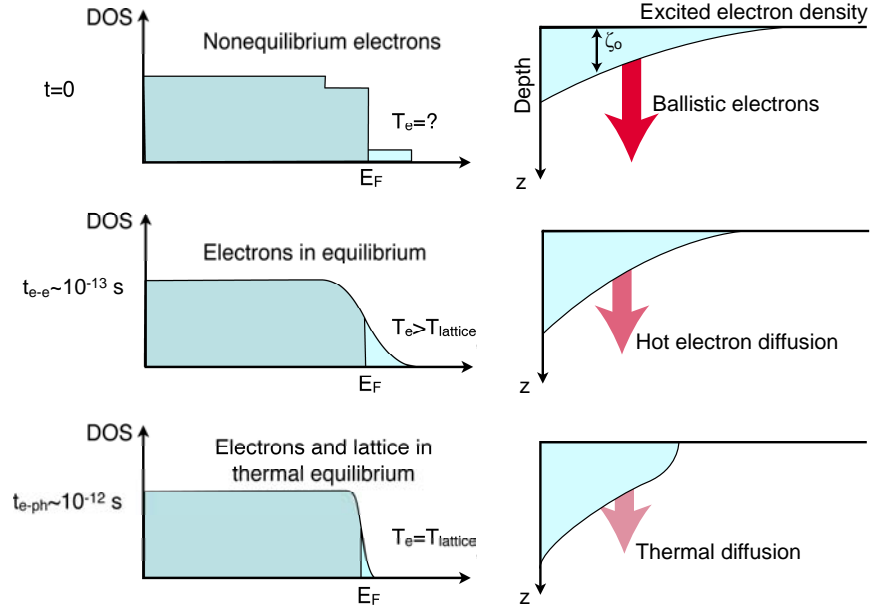


Figure 2.3: Non-equilibrium relaxation dynamics of electrons in a bulk metal excited by an ultrafast laser pulse. Time since the arrival of the pulse increases from top to bottom (labeled on the far left). The left column shows the electron density of states as a function of energy ( $E_F$  is the Fermi energy), while the right column shows the depth distribution of the electrons excited above the Fermi energy by the pulse. At times earlier than  $t_{e-e}$ , the excited electrons are out of equilibrium with the rest of the electrons, and only at times later than  $t_{e-ph}$  are phonons in equilibrium with the electrons. Figure modified from [13].

Immediately following excitation, the excited electrons travel ballistically deeper into the material at velocities close to the Fermi velocity (determined by the electron energy at the Fermi level,  $v_F \sim 10^6$  m/s). The average distance of travel (penetration depth  $\zeta_e$ ) of these ballistic electrons is also called the mean free path  $\Lambda_e$ , and is dependent on the strength of electron-electron scattering in the metal (proportional to the electrical conductivity). Values range from over 100 nm for noble metals to 10-20 nm for d-band metals; ballistic electron penetration depths are shown for a few common metals in Table 2.2. As the excited ballistic electrons travel out among unheated electrons and scatter with them, eventually (50-100 fs after initial laser excitation) an electron equilibrium is reached (sometime around 50-100 fs after initial laser excitation), as shown in the second row in Figure 2.3. At this point, electron transport is no longer ballistic, and

diffusive electron transport carries energy still deeper, though much more slowly than in the ballistic case. However, these thermalized electrons are still out of equilibrium with the lattice phonons.

Metal	$\zeta_o$ (nm)	$\zeta_e$ (nm)
Gold	13	105
Silver	12	142
Aluminum	7.5	46
Nickel	14	11
Chromium	18	14

Table 2.2: Optical penetration ( $\zeta_o = \lambda/4\pi n_i$ , where  $n_i$  is the imaginary component of the index of refraction) at 800 nm [14] and hot electron transport ( $\zeta_e$ ) depths in selected metals.  $\zeta_{e,Ni}$  is an estimate, but others are from experiment [13].

Electrons will finally interact with the lattice on an even longer time scale given by the electron-phonon coupling time ( $t_{e-ph} \sim 10^{-12}$  s). This can be described by a two temperature model (the caption of Figure 2.4 refers to a “Three temperature model”, with the only difference being that it includes an additional temperature for the spins in the system) proposed by Anisimov [15,16], in which the electrons and lattice (phonons) have separate temperatures ( $T_e$  and  $T_l$ ) and heat capacities ( $C_e$  and  $C_l$ ). The system can then be modeled as two coupled differential equations

$$C_e \frac{\partial T_e}{\partial t} = k \nabla^2 T_e - \alpha(T_e - T_l) + A(r, t), \quad (2.3)$$

$$C_l \frac{\partial T_l}{\partial t} = G(T_e - T_l), \quad (2.4)$$

where  $k$  is the thermal conductivity,  $A(r, t)$  is the pulsed heating of the driving laser, and  $G$  is the electron-phonon coupling constant [17]. As the electron and phonon temperatures equilibrate, the electron temperature typically drops by one to two orders of magnitude because the heat capacity of the electrons is so much smaller than that of the phonons (e.g. in Ni,  $C_e = 3.74 \times 10^5$  and  $C_l = 39.52 \times 10^5$  J/m<sup>3</sup>K), as shown in Figure 2.4.

Further transport of heat is by thermal diffusion, with the phonons and electrons

in equilibrium, as shown in the bottom row of Figure 2.3. It should be noted that this picture of electron transport through diffusion and before eventual coupling to the lattice is valid only for metals. For semiconductors and insulators, the electron mobility is much lower and the transport will be dominated by phonons.

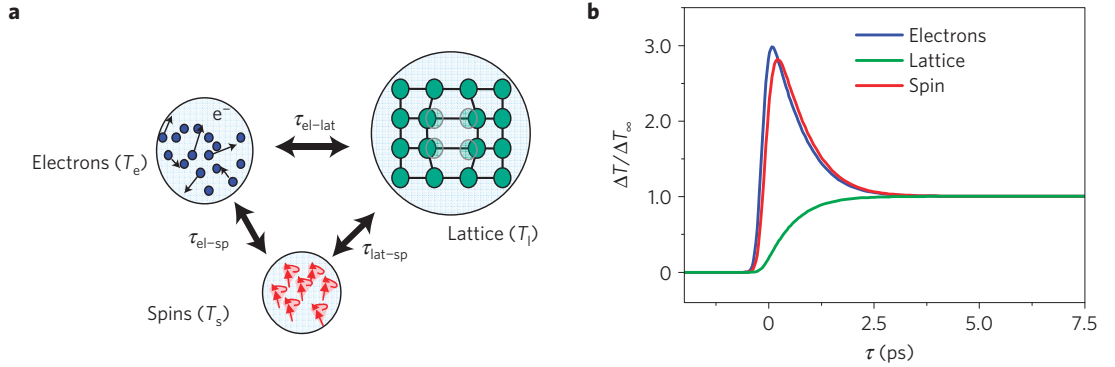


Figure 2.4: Three temperature model, in which the electrons, lattice, and spins in a system are allowed to have different temperatures. An ultrafast laser is absorbed by electrons, which couple to the lattice with a characteristic time  $\tau_{e-ph} \sim 1$  ps. The spin temperature is important in magnetic systems, and the electron-spin coupling time  $\tau_{e-sp}$  has not been measured with sufficient resolution, as discussed in Chapter 8. Figure from [18].

### 2.3 Phonons

Heat in a crystal lattice is carried and stored by vibrations of atoms about their equilibrium positions. Atoms are connected by chemical bonds to their neighboring atoms, and can be treated as masses connected by springs, as shown in the left panel of Figure 2.5. The right panel of Figure 2.5 shows a typical interatomic potential, which demonstrates the reason that this mass-spring model works so well: near equilibrium, the potential is very nearly approximated as harmonic. The allowed energies of a harmonic oscillator system are given by

$$E_n = h\nu(n + 1/2), \quad (2.5)$$

where  $n = 0, 1, 2, 3, \dots$  is an energy level counter and  $\nu$  is a fundamental frequency of vibration, describing a single phonon. In gases and other weakly-coupled systems, the harmonic energy levels are discrete, but in a solid, the levels merge together.

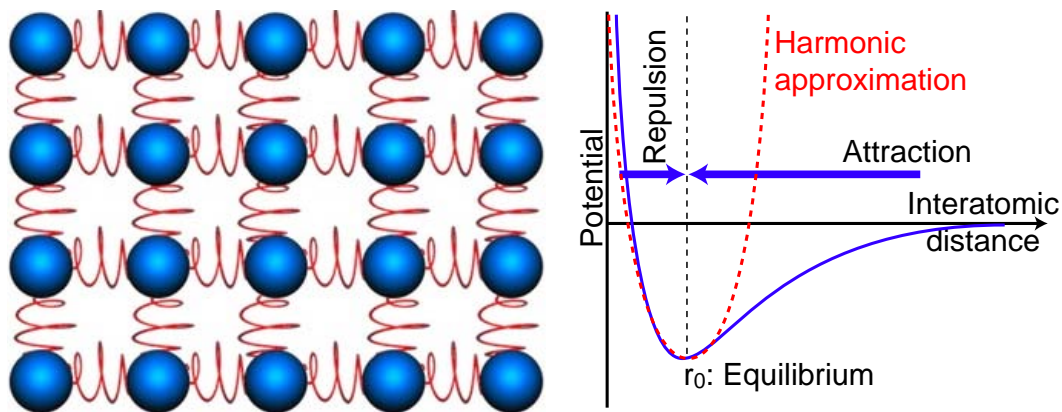


Figure 2.5: Basic model for energy transport and storage in a lattice. Left: the lattice can be treated as a collection of masses (atoms) connected by springs (interatomic potential). Right: a schematic interatomic potential.

A crystal with more than one atom per unit cell (e.g.  $\text{Al}_2\text{O}_3$  is hexagonal and Ni is cubic face-centered) will have two major phonon branches: the acoustic branch that corresponds to in-phase oscillations of all the atoms in a unit cell, and an optical branch for out-of-phase oscillations of atoms making up a unit cell, as shown in Figure 2.6. Each of these branches can be further split into three more, corresponding to longitudinal, and both transverse directions of phonon propagation.

The coherence length of room-temperature phonons is  $\sim 1$  nm [19], so in most cases, interference effects can be neglected and phonons can be treated and thought of as particles with velocity, density, and collision properties. It is these collisions that transport energy throughout the crystal, and given this phonon particle picture, it is easy to derive the Fourier law for thermal transport by phonons (or other kinetic particles) in a 1D case.

Consider a collection of phonons (particles) in a box where one side is heated and the other remains cold. We are interested in the flux along the  $x$ -direction  $q_x$ , at a

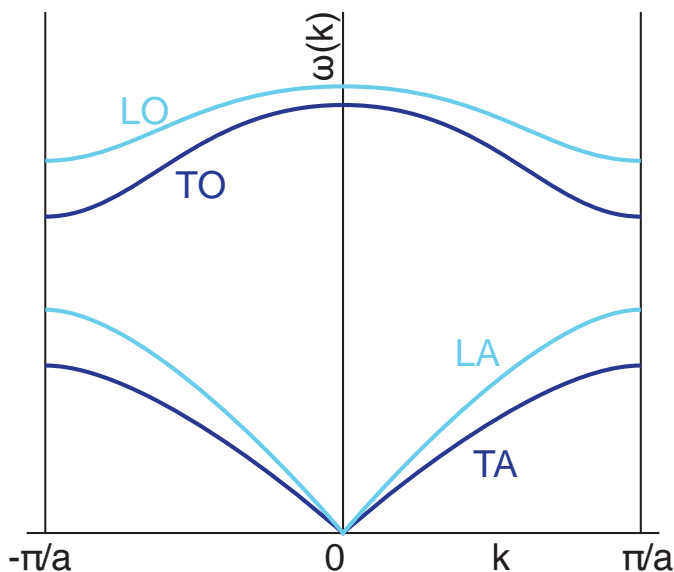


Figure 2.6: Phonon dispersion for a typical three dimensional crystal with lattice constant  $a$ . There are longitudinal (L) and transverse (T) modes for both acoustic (A) and optical (O) phonons. There are two transverse modes for each pictured because of the two transverse directions.

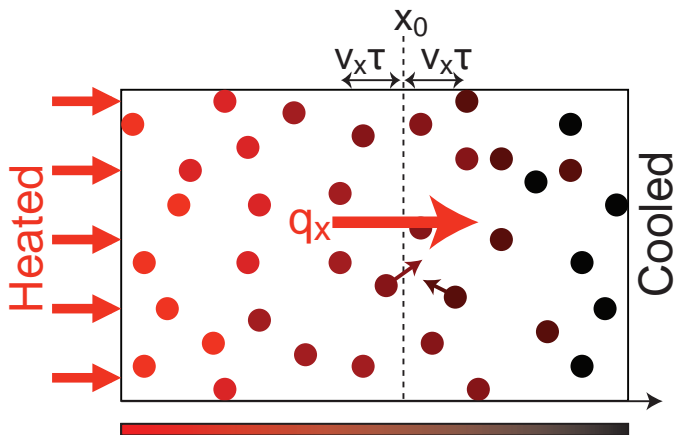


Figure 2.7: Simple calculation of the heat flux for a system of heated kinetic particles (e.g. phonons). Modified from [19].

position  $x$ , which is determined by the difference between the energy flux of the phonons flowing in the positive and negative directions. In each case, phonons within a distance  $v_x \tau$  can reach the flux surface before scattering with another carrier.  $v_x$  is the average component of the phonon velocity that is in the  $x$ -direction, and  $\tau$  is the average time

a phonon travels before being scattered, called the relaxation time. Given a phonon density per unit volume  $n$  and a particle energy  $E$ , the net flux at the surface at  $x$  is

$$q(x) = \left( \frac{1}{2} (nE(x)v_x) \right)_{x-v_x\tau} - \left( \frac{1}{2} (nE(x)v_x) \right)_{x+v_x\tau}. \quad (2.6)$$

The factors of  $1/2$  take into account the fact that only half of the phonons will be traveling in the required direction, since their motion is random. If we now apply a Taylor expansion to the two components we find

$$q_x = \frac{1}{2} \left( nE(x)v_x - v_x\tau \frac{d(nE(x)v_x)}{dx} \right) - \frac{1}{2} \left( nE(x)v_x + v_x\tau \frac{d(nE(x)v_x)}{dx} \right) = -\frac{v^2\tau}{3} \frac{dU}{dT} \frac{dT}{dx}, \quad (2.7)$$

where  $U(x) = nE(x)$  is the position-dependent energy density and  $v$  is the average velocity given by  $v_x^2 = v^2/3$ , assumed to be position-independent. Now we recognize that  $dU/dT$  is the volumetric heat capacity  $C$ , and we have obtained the Fourier law for heat conduction:

$$q_x = -\frac{Cv^2\tau}{3} \frac{dT}{dx} = -k\nabla T. \quad (2.8)$$

Here we have assumed that the thermal conductivity  $k$  can be given by

$$k = Cv^2\tau/3 = Cv\Lambda/3, \quad (2.9)$$

where  $\Lambda = v\tau$  is the average distance a phonon travels before scattering, the phonon mean free path.

This understanding of thermal transport relies on scattering occurring at a distance  $\Lambda$  determined by the material. If the scattering length is limited by the presence of interfaces or if the flux needs to be determined at shorter length scales, the Fourier law for heat diffusion will obviously fail. Chapter 7 discusses the first observation of the breakdown of Fourier description near nanostructured interfaces, as well as a discussion of how the Fourier law can be corrected to account for this error.

In addition to the phonon diffusion discussed here, it is also possible to launch and propagate coherent phonon wavepackets. In general, diffusive phonons propagation

is excited by thermal flows and coherent phonon wavepackets are excited by impulsive heating (e.g. from an ultrafast laser) causing stresses and strains that relax with the phonons.

## 2.4 Modeling thermal transport in real systems: circuit analogy

An understanding of the fundamental energy carriers and their interactions does us little good if we cannot apply that knowledge to real systems. In this section, a simple way to understand energy flow in terms of an analogy to circuit diagrams [20] is discussed, with obvious applications to practical engineering and design problems.

We will treat each transport interaction as having a resistivity to energy flow. In the literature, the terms resistance and resistivity are often used interchangeably, but we will take the term resistance ( $R$ ) to be an extensive parameter dependent on the size of the system with units K/W, while resistivity ( $r$ ) is an intensive, area-independent parameter with units  $\text{m}^2\text{K/W}$ . They are related by  $R = r \times A$ , where  $A$  is the cross-sectional area of thermal flow.

### 2.4.1 Energy transport across an interface

The concept that an interface could have a significant effect on the transport of energy was considered in the late 1930's, but not experimentally demonstrated until Kapitza's measurement of a temperature drop at a helium-solid interface when heat flowed across the boundary in 1941 [21]. The resistance to heat flow at the boundary (sometimes called Kapitza resistance or thermal boundary resistivity,  $r_{TBR}$ ) is defined as the ratio of the temperature drop at the interface to the energy flowing across the interface per unit area:

$$r_{TBR} = \frac{\Delta T_{Boundary}}{q}. \quad (2.10)$$

In practice, the boundary resistivity is so dependent on device preparation and fabrication, the presence defects and voids, and slight material disordering, that an accurate

theoretical prediction is impossible. However, it is instructive to consider the potential transport mechanisms to develop an understanding of the fundamental interactions governing interfacial energy transport.

At an interface between different materials, both phonon-phonon and electron-phonon interactions may play a role in the energy flow across the boundary. For example, an electron reflecting off of the boundary can cause the boundary to recoil and emit phonons. This possibility was considered in numerous calculations, and was determined to be negligible in the case of solid/solid interfaces. We therefore neglect the contribution from electron-phonon interactions at an interface, and consider only phonon-phonon transport.

Phonon-phonon coupling across an interface can be understood by two basic models. In the acoustic mismatch model (AMM), phonon transport at an interface is handled in much the same way as a Snell's law calculation for optical light: a phonon incident on the surface at an angle  $\theta$  can be transmitted across the boundary at a refraction angle related to the ratio of the acoustic impedances of the two sides, or reflected back at an angle  $\theta$ . This model assumes that no scattering takes place at the boundary, so the phonon spectrum emitted into the second material matches that of the phonons in the first material. Additionally, whether a given phonon is transmitted or reflected is determined by the ratio of the acoustic impedances of the materials making up the interface: a large mismatch will give a high reflectivity and vice versa. In contrast to the AMM, the diffuse mismatch model assumes that all of the phonons incident on the surface are scattered completely. Since each incident phonon is scattered, the phonon emission is determined only by the available phonon states on each side of the interface (at a typical solid-solid interface, the emission is  $\sim 50\%$  into each side [22]). Both of these models for phonon transport at an interface involve major simplifications, so their relevance to real-life situations is limited, although both are valid at temperatures below  $\sim 50$  K [22]. Other effects, such as inelastic phonon scattering [23] and disorder-induced

multiple-phonon scattering [Hopkins 18,19], may play a significant role, especially at non-cryogenic temperatures.

### 2.4.2 Energy transport in the bulk

Using the Fourier law for carrier transport derived in Equation 2.8, the flux ( $q$ ) through a bulk material of thickness  $L$  is given by

$$q = -k\nabla T = -k\frac{\Delta T}{\Delta x} = -k\frac{\Delta T}{L}. \quad (2.11)$$

Using the electrical analogy, we can recast this equation in terms of a resistivity to thermal transport, which is defined as the ratio between the material thickness and the thermal conductivity ( $r = L/k$ ),

$$q = -\frac{\Delta T}{r}. \quad (2.12)$$

As phonons and electrons carry heat simultaneously, the thermal resistivity due to these two channels must be considered in parallel. Electron transport can be described in terms of separate resistivities to electron-electron ( $e - e$ ), electron-phonon ( $e - ph$ ) and electron-dislocation/interface ( $e - d$ ) events. Similarly, phonon resistivities include phonon-phonon ( $ph - ph$ ), phonon-electron ( $ph - e$ ), and phonon-dislocation/interface ( $ph - d$ ) components. Each type of interaction creates a resistivity to heat transfer and, for one carrier, all of these resistances must be added:

$$\frac{1}{r_{Total}} = \frac{1}{r_{ph}} + \frac{1}{r_e}, \quad (2.13)$$

$$r_{ph} = r_{ph-ph} + r_{ph-e} + r_{ph-d}, \quad (2.14)$$

$$r_e = r_{e-e} + r_{e-ph} + r_{e-d}. \quad (2.15)$$

In metals, both electrons and phonons can carry heat, so they both contribute to the total resistivity (Figure 2.8, blue box). However, in semiconductors and dielectrics, the thermal transport is dominated by phonons, so we consider only phonon interactions (Figure 2.8, gray box).

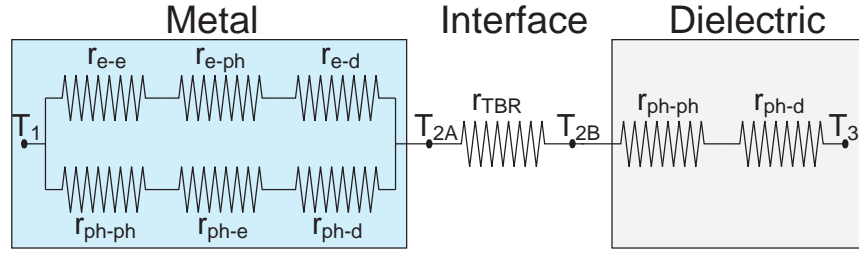


Figure 2.8: Resistivity model for determining thermal flow rates in the case of the example considered in section 2.4.3. The example layout and temperature distributions are shown in Figure 2.9.

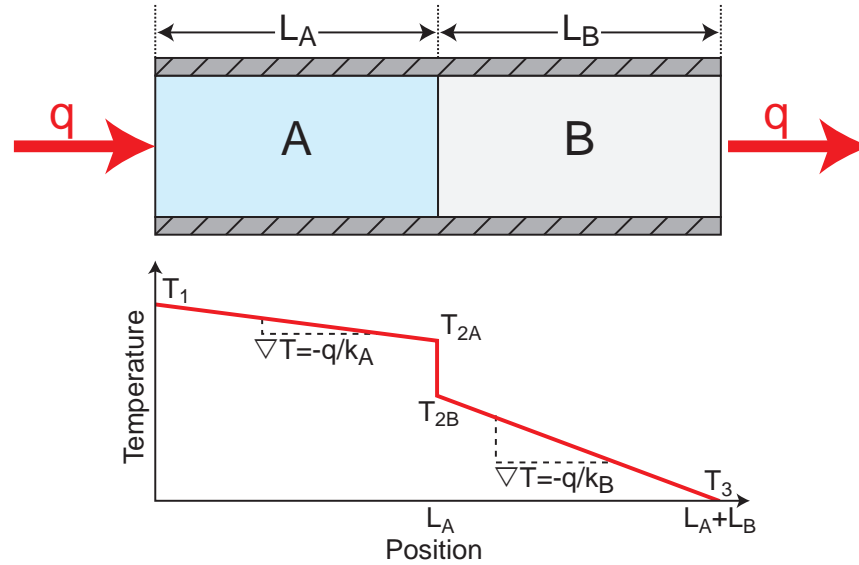


Figure 2.9: Heat flow between two solids in contact illustrating the effect of boundary resistance. Modified from [24].

### 2.4.3 Putting the pieces together

Let us consider a simple example, illustrated in Figure 2.9, of a metal (A) in contact with a dielectric (B). We know the resistivity of each of the constituent parts (A, B, and interface), and by applying energy conservation, the same flux must flow through each. The total resistivity can then be determined by summing the resistivities of each component:

$$q = \frac{\Delta T}{r_{total}} = \frac{T_1 - T_3}{L_A/k_A + r_{TBR} + L_B/k_B}, \quad (2.16)$$

where  $r_{total} = r_A + t_{TBR} + r_B$ .

This method of treating flow as channels in series or parallel is a helpful simplification that we will refer to in Chapter 7. Particularly important for our later use are the boundary resistivity and the concept that energy flow in a bulk system can be summarized by a resistivity to flow that is connected in series with the interfacial resistivity.

## 2.5 Conclusion

In conclusion, ultrafast laser pulses are a powerful tool for exciting systems through subsequent photon  $\rightarrow$  electron  $\rightarrow$  phonon excitations and subsequent equilibrations. Applications of this excitation system to study acoustic, thermal, and magnetic phenomena in nanostructures are discussed in the following chapters.

## Chapter 3

### High-order harmonic generation

#### 3.1 Introduction

The human eye will respond to photons of wavelength between about 350 to 750 nm in air (commonly referred to as "optical" light), but this represents only a miniscule portion of the entire electromagnetic spectrum. At longer wavelengths, infrared ( $\sim 10 \mu\text{m}$ ), microwave ( $\sim 10 \text{ mm}$ ), and radio ( $\sim 1 \text{ km}$ ) radiation are useful for communications and measurement. Because the energy of each photon is so small, these types of radiation can pass through many materials without being absorbed. On the other end of the scale, hard x-rays with wavelengths shorter than 0.1 nm can also pass through many materials, and by tuning the wavelength (related to the photon energy by  $E_{\text{photon}} = hc/\lambda$ , where  $h$  is Planck's constant and  $c$  is the speed of light) to a region where one material is transmissive and another absorptive, element-specific imaging can be performed. In a crude sense, this is what is taking place in a medical "x-ray", where the radiation used is of high enough energy to pass through the soft tissue like skin and clothing, but interacts strongly with bones composed of heavier elements.

#### 3.2 Advantages of EUV light

Between hard x-rays and ultraviolet light (such as the UV radiation we get from the sun) lies a vast region of the electromagnetic spectrum that was largely unexplored for many years [25]. However, the very reasons that made it challenging to explore

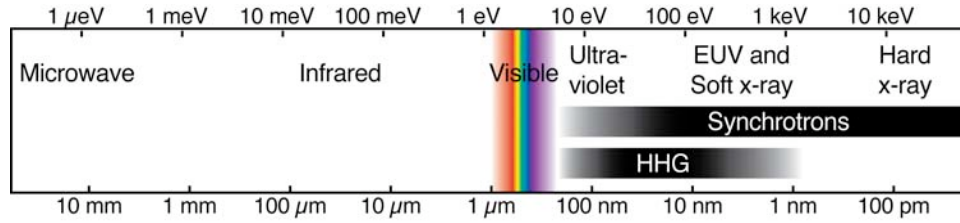


Figure 3.1: The electromagnetic spectrum

(high absorption of light due to multiple atomic resonances) make it very interesting for studying light-matter interactions.

### 3.2.1 Shorter wavelength

There are many reasons to generate and use light in the EUV region of the spectrum, and the most obvious of these is that EUV light has a much shorter wavelength than optical radiation. This allows for tighter focusing and better resolution in imaging. Similarly, short-wavelength light can also diffract from smaller structures. Consider the diffraction equation

$$m\lambda = d \sin(\theta), \quad (3.1)$$

where  $m$  is the diffraction order,  $d$  is the grating constant (center-to-center line spacing), and  $\theta$  is the angle of diffraction. If we limit ourselves to the case of first-order diffraction,  $m = 1$ , and

$$\theta = \arcsin(\lambda/d). \quad (3.2)$$

Taking the arcsin of a number greater than one is geometrically impossible, so this expression for the diffraction angle is only valid for  $\lambda < d$  and there is no diffraction for gratings with spacings smaller than the probing wavelength ("subwavelength" diffraction gratings). This diffraction signal has numerous experimental applications, including: as a spectrometer in element or photon-energy specific studies, and in the detection and imaging of nanostructures. However, Eq. 3.2 states that optical probe beams will not diffract from structures smaller than  $\sim 400$  nm. Structures down to 10 nm can be

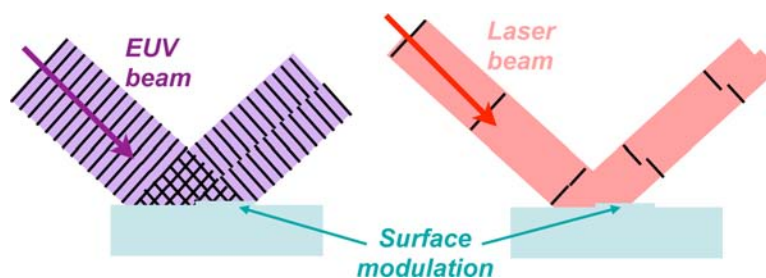


Figure 3.2: Illustration of the increased sensitivity to small phase shifts in interferometric measurements when the wavelength of light is short. This is one advantage of using EUV light to study surfaces.

manufactured with plasma beam etching, and such small structures require EUV probe light for sensitive detection, analysis, and imaging.

The shorter wavelength also provides additional contrast in interferometric measurements because a smaller absolute phase shift is required to get the same relative phase shift. This concept is illustrated in Figure 3.2, where we can see that short-wavelength light EUV light provides better phase contrast than much longer-wavelength optical light for the same phase difference. Applied to surface metrology, this means that EUV light has higher spatial resolution not only in the transverse (horizontal, perpendicular to the beam propagation) directions, but also in the vertical (displacement) direction.

### 3.2.2 Elemental selectivity

Because of the relatively high energies accessible in the EUV region of the spectrum, many core level electron resonances can be accessed. Light near resonance edges is transmitted or reflected determined by the exact wavelength. For example, the energy-dependent photon transmission for carbon and water is shown in Figure 3.3. The ability to selectively study or image the properties of a specific element in a molecule or lattice opens tremendous opportunities for fundamental chemistry and physics experiments. One particular example of the utility of this elemental selectivity is the amplified mag-

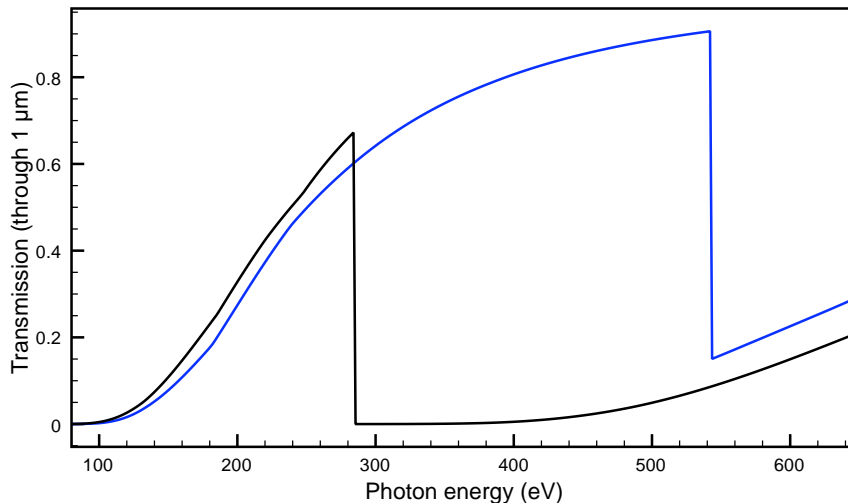


Figure 3.3: Transmission of soft x-ray light through  $1 \mu\text{m}$  of water (blue) and carbon (black). The sharp edges are useful for composition determination of materials and element-specific imaging and dynamics probing. The photon energy range between 290-540 eV is referred to as the "water window", where water is transparent and carbon is absorbing, providing contrast useful for biological imaging. Data from [26].

netic contrast near absorption edges, discussed and experimentally probed in Chapter 8.

Another advantage of working near absorption edges is that at nearby energies, the absorption can be so strong that the penetration depth is very shallow. This is the case for most materials at EUV energies below  $\sim 100$  eV, as shown in Figure 3.4. These shallow penetration depths enables high experimental sensitivity to surface properties.

### 3.3 High-order harmonic generation

The most common source of experimentally-useful soft x-ray light is a synchrotron, which is a bright (high flux) and tunable source, but requires facilities the size of a football field and is therefore expensive and has limited access. An alternative to synchrotron sources is the high-order harmonic generation light source (HHG, a comparison to synchrotrons is shown in Table 3.1), a highly-nonlinear process in which intense optical or infrared radiation can be upconverted to the EUV region of the spectrum. The non-

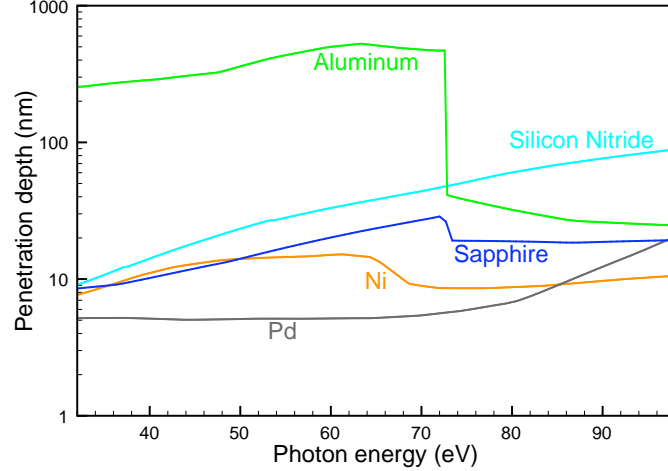


Figure 3.4: Penetration depths at  $45^\circ$  incidence for a few materials mentioned in this thesis. Penetration depth is defined as the point of  $1/e$  transmission measured along the surface normal. Data from [26].

linear nature of the HHG process requires very intense, very short laser pulses focused to a very small spot with peak intensities of  $10^{14}$  W/cm<sup>2</sup> or higher, well within the capabilities of modern ultrafast laser amplifier systems. At such intensities, the laser electric field has a strength comparable to the Coulomb field binding an electron to an atom, so the perturbative models of the light-atom interaction break down and new theory is required.

While quantum models are required to rigorously explain HHG [28] [29,30], many basic characteristics of HHG can be intuitively understood using the semi-classical model proposed by Corkum [31,32]. The semi-classical model breaks down the high harmonic

Category	Synchrotron	HHG
Photon energy	10 eV - 2 GeV	10 eV - 1 keV
Pulse duration	100 fs - 100 ps	< 10 fs
Flux (photons/second)	$10^{16}$	$10^{12}$
Spatial coherence	Poor	High
Physical size	Football field	Tabletop

Table 3.1: Synchrotron vs high harmonic generation sources of EUV light. Data from [25] and [27].

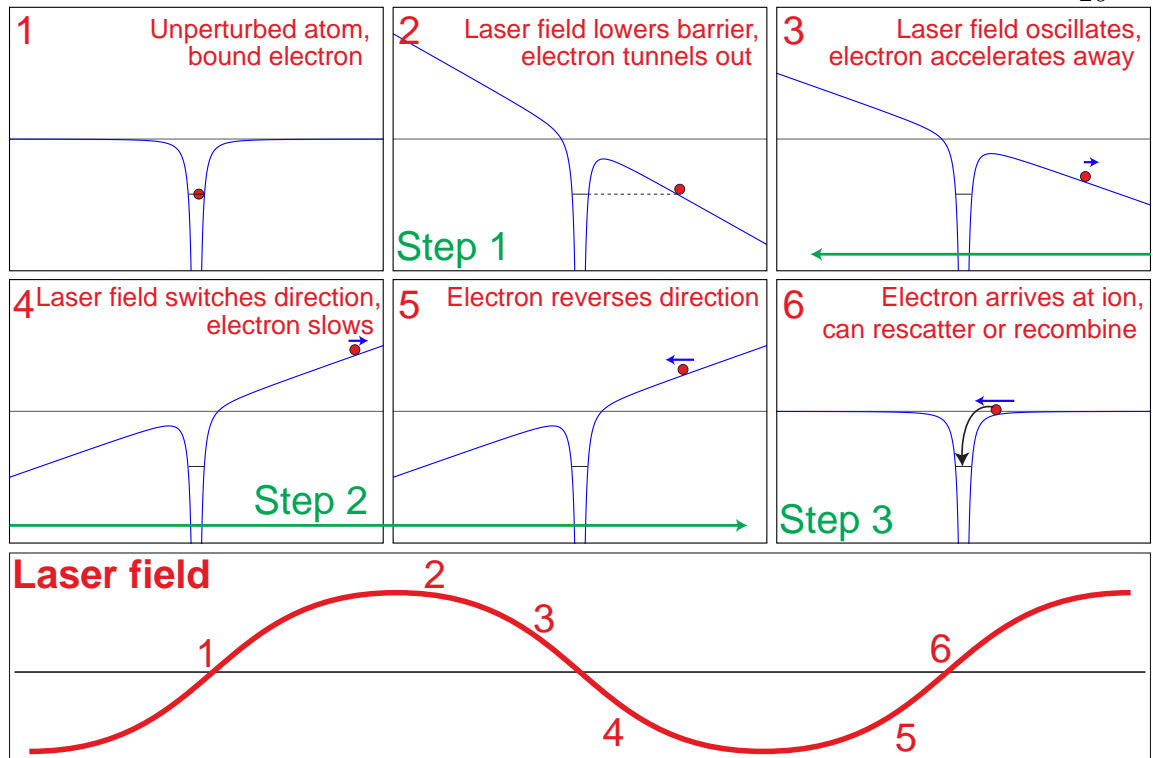


Figure 3.5: Schematic explanation of high-order harmonic generation using the semi-classical three step model. The upper panels illustrate the instantaneous potentials, while the bottom panel shows where in the laser cycle the snapshots are taken.

generation process into three steps summarized in Figure 3.5:

- (1) Tunneling ionization of an electron from a laser-modified atomic potential
- (2) Free electron propagation in the oscillating electric field of the laser
- (3) Recombination of the electron with the ion, emitting a high-energy photon.

### 3.3.1 Step 1: Tunneling ionization

The photoionization of an electron from an atom can be grouped into three regimes, depending on the strength of the exciting laser field [33]:

- Multiphoton ionization is the dominant mechanism for photoionization in the presence of a small electric field. In this case, an electron is ionized by the

absorption of enough photons to get to an energy higher than the ionization potential of the atom.

- For high intensities, ionization occurs by tunneling through a distorted Coulomb barrier. Here, the laser is strong enough to significantly modify the Coulomb potential of the parent atom, enough so that an electron can tunnel out into the continuum.
- Even higher laser fields lead to above-barrier ionization. In this case, the Coulomb potential is suppressed below the ionization potential, allowing electrons to freely leave the atom.

Tunneling photoionization rates were first calculated by Ammosov, Delone, and Krainov [34], and later, the generalized Coulomb potential of the ion was added to extend the results to more complex atom cores [35]. The result is that the ionization rate is:

$$\omega(t) = \omega_p |C_{n^*}|^2 \left(\frac{4\omega_p}{\omega_t}\right)^{2n^*-1} \exp\left(-\frac{4\omega_p}{3\omega_t}\right), \quad (3.3)$$

where

$$\begin{aligned} \omega_p &= I_p/\hbar \\ \omega_t &= (q_e E(t))/\sqrt{2m_e I_p} \\ n^* &= Z\sqrt{I_H/I_p} \\ |C_{n^*}|^2 &= 2^{2n^*}/(n^*\Gamma(n^*+1)\Gamma(n^*)). \end{aligned}$$

In these definitions,  $I_p$  is the ionization potential of the atom,  $\hbar$  is Planck's constant  $h$  divided by  $2\pi$ ,  $E(t)$  is the time-dependent laser electric field,  $m_e$  and  $q_e$  are the electron mass and charge,  $Z$  is the ion charge after ionization,  $I_H$  is the ionization potential of atomic hydrogen, and  $\Gamma(x)$  is the Gamma function.

The fraction of electrons that have escaped an atom is given by the fraction of atoms that have been ionized, determined by:

$$\eta(t) = \exp\left(-\int_{-\infty}^t \omega(t') dt'\right). \quad (3.4)$$

Figure 3.6 shows a calculation of the time dependence of the ionization of argon within an ionizing laser pulse. Also shown is the electric field of the ionizing laser pulse – the steps in the ionization fraction occur at times that match peaks in the electric field, demonstrating that the ionization is very sensitive to the time-dependent field. The ionization also depends strongly on spatial variations in the intensity, so an accurate understanding of laser profile and propagation is important for determination of the ionization process.

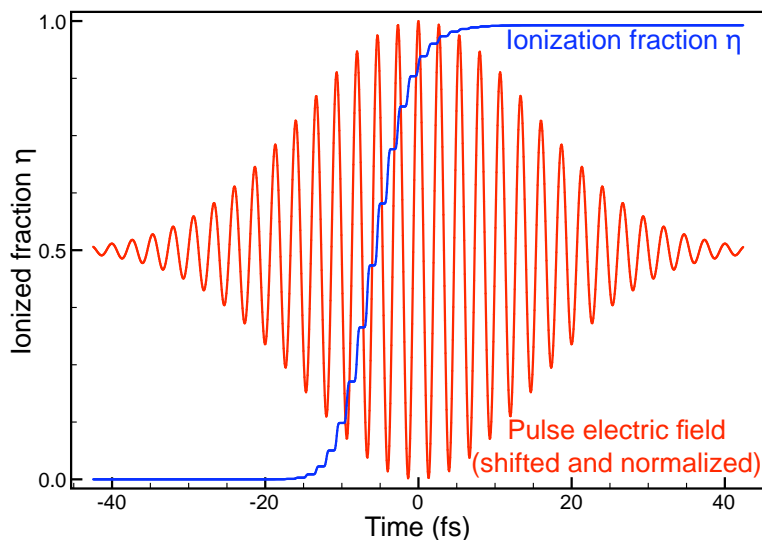


Figure 3.6: Fraction of ionization of Argon from a 25 fs,  $5 \times 10^{14}$  W/cm<sup>2</sup> peak intensity pulse.

### 3.3.2 Step 2: Free electron propagation in a laser field

After an electron is ionized, the three-step model assumes that it is accelerated in the laser field, starting with zero velocity. The basic idea is as follows: the laser field first accelerates the electron away from the ion core, but the field is oscillating, so it

soon changes direction. This accelerates the electron back toward the ion, slowing it until eventually it is heads back towards the ion it came from, where it can recombine and emit radiation.

The propagation of the now-free electron can be calculated using classical equations of motion. If we take the laser field to be  $E(t) = E_0 \cos(\omega t)$  (In the case of ultrashort laser pulses, this is an approximation because the sinusoidally-oscillating field is modulated by the pulse envelope, as shown in Figure 3.6), then the electron velocity is determined by  $F = ma$  and  $F = qE$ . The acceleration of the electron is then  $a(t) = (q_e/m_e)E(t)$ , and the velocity can be determined by integration

$$\begin{aligned} v(t, t_0) &= \frac{q_e}{m_e} \int_{t_0}^{t'} E(t') dt' \\ v(t, t_0) &= -\frac{q_e E_0}{m_e \omega} (\sin(\omega t) - \sin(\omega t_0)). \end{aligned} \quad (3.5)$$

The position can be determined by integrating further to get

$$x(t, t_0) = \frac{q_e E_0}{m_e \omega^2} (\cos(\omega t_0) - \cos(\omega t) - \sin(\omega t_0)(\omega t - \omega t_0)). \quad (3.6)$$

The resulting electron propagation is highly-dependent on the phase of ionization with respect to the laser field. One might expect the optimal results to occur when the electron is excited at the peak of the laser field, but since the electron started with an initial velocity of zero and experiences a symmetric potential, it would arrive back at the atom with zero velocity, as shown by the black curve at laser phases of  $2\pi$  and  $4\pi$ . Electron paths for various phases of ionization with respect to the laser field are shown in Figure 3.7. Zero crossings for the position represent opportunities for the electron to collide with the parent ion with a velocity (recall that kinetic energy  $KE \propto v^2$ ) given by the slope of the curve at that point. While some paths do not ever return to the ion (e.g.  $\pi/2$ ), others encounter the ion multiple times (e.g.  $\pi/32$ ). The semiclassical model only considers the first interaction event because the electron distribution spreads transversely as it propagates at a rate of  $\sim 1.5 \text{ \AA}/\text{fs}$  [31], meaning

that the electron distribution is broader at later times and therefore much less likely to recombine with the parent ion.

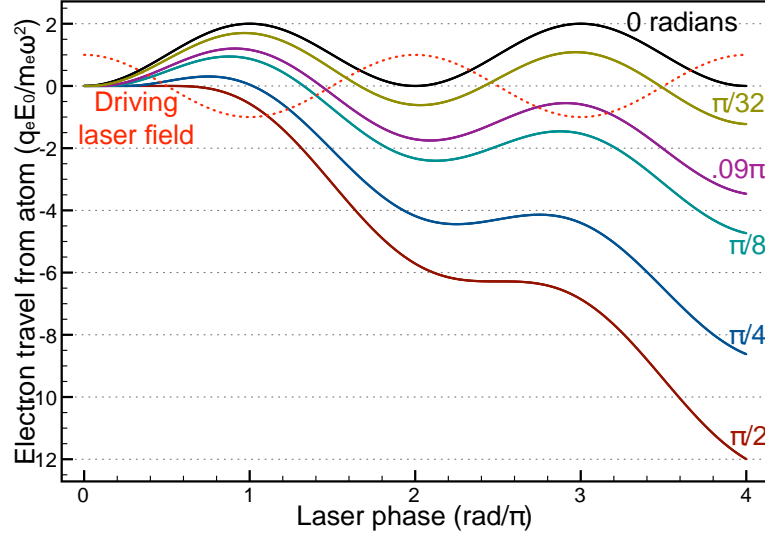


Figure 3.7: Free electron propagation in a sinusoidal laser field (red dotted line). Electron displacement from the atom is shown for electrons excited at several delays (marked at right) relative to the peak laser field. Every zero-crossing for a particular trajectory is a potential collision even with the ion core.

### 3.3.3 Step 3: Recombination and radiation

When an electron that has been ionized (Step 1) and accelerated in the laser's electric field (Step 2) returns to the atom, it can recombine with the atom, falling back into the potential energy well it originated in. The excess energy the electron had, both kinetic and potential, is given out as a radiated photon. The potential energy component is given by the ionization potential of the atom ( $I_p$ ). In order to get the highest-energy harmonics, we use Noble gases that have filled (and therefore tightly bound with a high ionization potential) valence electron shells. For example, the ionization potential of argon is 15.7 eV, and that of neon is 21.6 eV. The kinetic energy component is given by  $m_e v^2/2$ , where  $v$  is the electron velocity when it arrives back at the atom. This return velocity can be determined by finding the first zero-crossing of Equation 3.6 and

plugging that value in to Equation 3.5. Figure 3.8 shows the electron's return kinetic energy as a function of laser phase when the electron was ionized. The peak occurs for a phase of  $\sim 0.1\pi$  radians, and has a value of  $\sim 3.2 \times U_p$ , where  $U_p$  is the ponderomotive energy, which is the maximum kinetic energy gained by the electron due to acceleration in one cycle of the laser field. The maximum photon energy that can be radiated is then given by

$$E_{ph,max} = PE_e + KE_{e,max} = I_p + 3.2U_p. \quad (3.7)$$

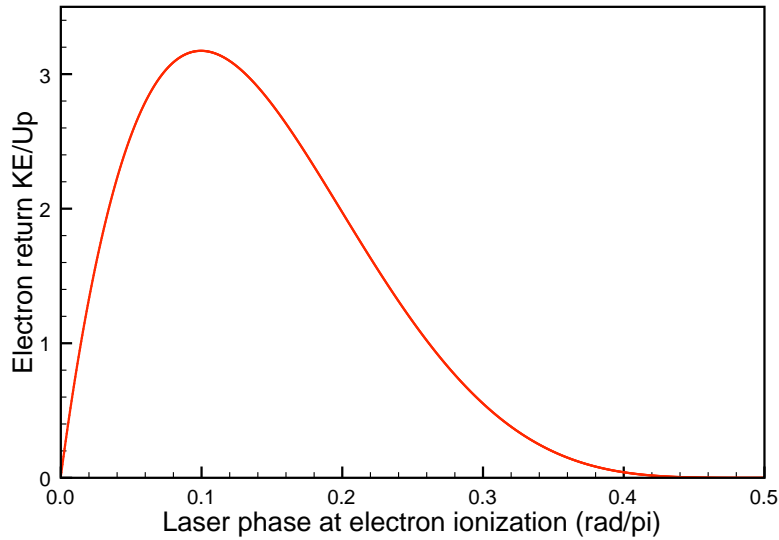


Figure 3.8: Kinetic energy of electron returning to the atom as a function of laser phase when the electron was ionized.

An understanding of the kinetic energy of the returning electron (Figure 3.8) yields additional insights into the HHG process. First, the peak return kinetic energy is proportional to the ponderomotive potential, which depends on the properties of the driving laser:  $U_p \propto I\lambda^2$ , where  $I$  and  $\lambda$  are the intensity and wavelength of the laser. So to get higher-energy harmonic light, we can increase the laser peak intensity (shorter pulses or tighter focii) or increase the wavelength (of course, using a longer wavelength will increase the time an electron spends in the driving laser field, so the distribution spread will decrease the recollision probability [31]). Also, there are two laser phases

which give the same kinetic energy, known as the short (highest initial phase value) and long(smallest phase) trajectories. These electrons each spend a different amount of time in the driving laser field, so comparing their amplitude as a function of laser intensity and wavelength gives insight into intensity-dependent induced phase [36,37]. In general, both harmonics from both short and long trajectories are generated, but by using phase matching techniques, a single trajectory can be selected, which is important for experiments in which a highly monochromatic spectrum is desired [38].

### 3.3.4 HHG in hollow waveguides

High-order harmonic generation can be performed by focusing an ultrafast laser pulse into a collection of gas atoms (gas jet), but this technique offers a very limited interaction region because of the tight pump focus and limited jet size. An alternative technique pioneered by the Kapteyn-Murnane group uses hollow glass waveguides to hold the gas, guide the laser, dramatically extend the interaction region, and provide more control over the harmonic generation process [39]. Like any parametric conversion process, efficient harmonic conversion requires that the process be phase-matched. As the driving laser beam propagates, harmonics are generated coherently and build up, adding constructively with past generation events only if the driving laser light and generated harmonic light travel with the same phase velocity in the medium. For conversion that is not phase-matched, generation is limited to a distance known as the coherence length  $L_c = \pi/\Delta k$ , the distance over which the driving and generated waves slip in phase by half a cycle, leading to constructive interference between new and past generated light. The phase mismatch  $\Delta k = qk_{laser} - k_{EUV}$ , where  $q$  is the harmonic order, and has contributions from vacuum, neutral gas dispersion, non-linear refractive index, plasma dispersion, and waveguide dispersion [39]. Fortunately, these components have different sign: the first three add positively to the dispersion, while the last two are negative. This means that by balancing the atomic and waveguide dispersion by

pressure tuning, we can obtain phase-matching ( $\Delta k = 0$ ) and see coherent buildup of the generated harmonic beam along the propagation direction, with an increase of up to two orders of magnitude more flux for a given pulse energy [40].

Unfortunately, this phase-matching technique works only at relatively low photon energies ( $E_{EUV} < 50$  eV for argon and  $E_{EUV} < 130$  eV for helium), because above these photon energies, high levels of laser-induced ionization cause the plasma dispersion term to dominate beyond what can be compensated by simple pressure tuning. Instead, quasi-phase-matching techniques must be used, which include the use of modulated waveguides [41] and counterpropagating pulses [42].

At the single-atom level, the HHG process is governed by the (usually excellent) coherence of the driving laser, but the highly-nonlinear process also gives rise to a dynamically-changing index of refraction and complex multi-mode generation that leads to only partially-coherent light being generated [43–45]. However, when the HHG process is phase-matched in a hollow waveguide, a fully spatially-coherent beam with an improved mode quality results [46]. Thus, high-order harmonic generation in a hollow waveguide gives high-flux, coherent beams of extreme ultraviolet light useful for sensitive detection of chemical and physical phenomena.

### 3.3.5 Characteristics of HHG

Regardless of whether the harmonics are generated in a gas jet or a hollow waveguide, the experimentally-observed harmonics have common features. The most obvious of these is given by the name: spectrally, a series of harmonics of the driving laser energy is observed that extend up to the cutoff energy in Equation 3.7, as shown on the right side of Figure 3.9. Experimentally, we typically observe a HHG spectrum from argon gas as shown in Figure 3.10: a comb of  $\sim 5$  harmonics strongly peaked near 42 eV (27th harmonic). There are two reasons we don't observe a plateau of even-amplitude harmonics: at the lower energies, the generated harmonics are absorbed by the Ar gas [39, 47],

and at the higher energies, we see the ionization limit to phase-matching [39]. Using neon as the harmonic medium, the spectrum is a plateau comb of harmonics from 35 eV to above 70 eV. A typical spectrum from neon is shown in Figure 8.7.

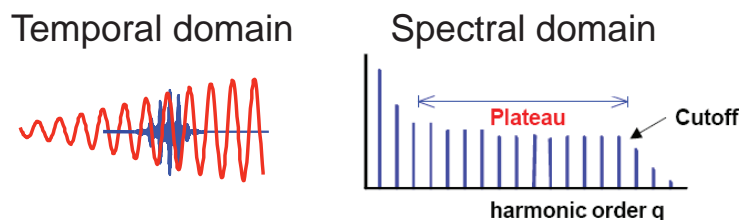


Figure 3.9: Characteristic light from HHG in the temporal (left) and spectral (right) domains.

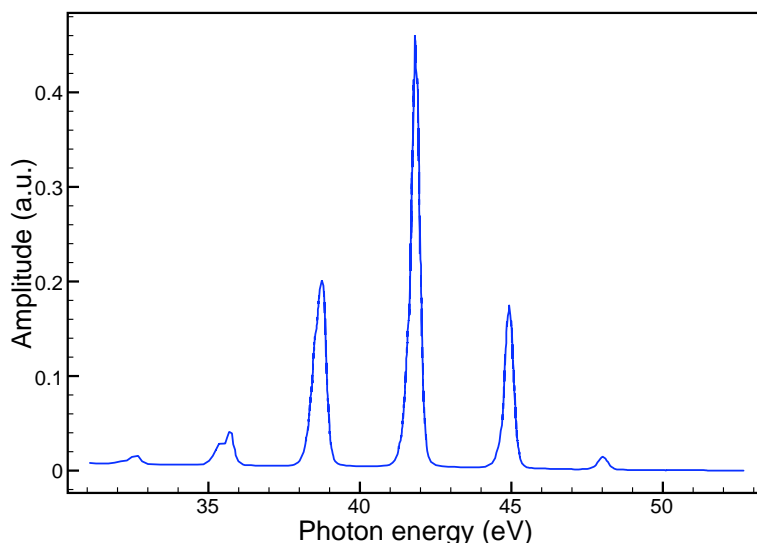


Figure 3.10: Typical harmonic spectrum from Argon.

The temporal structure of a harmonic beam is a series of attosecond bursts spaced by half an optical cycle (as shown in Figure 3.9, left) because harmonics are generated near each peak in the electric field. Because HHG is such a highly-nonlinear process, it is localized to the peak of the driving laser pulse: a driving laser with a duration of 25 fs generates a HHG pulse shorter than 10 fs [48].

### 3.4 Conclusion: Unique advantages of HHG

As the usable range of harmonic light that can be generated is pushed to higher and higher energies [49,50], access to new absorption edges and shorter wavelengths for finer-resolution in imaging enables experiments that previously could only be done at synchrotrons. However, the use of HHG has a few particular advantages over the general characteristics of EUV light mentioned in Section 3.2. The most obvious advantage of EUV light from HHG is the accessibility of having an EUV light source in the lab rather than at a large user facility. The strict time schedules and beamline sharing that is the norm for most synchrotron-based projects pose a significant experimental challenge. Additionally, many synchrotron users live and work far away from the source itself, requiring expensive trips and dangerous equipment transport. Another obvious advantage of HHG is the financial freedom of a source that costs  $\sim 4000x$  less to build and maintain.

The primary scientific advantage of EUV light from HHG is that the light is simultaneously short wavelength (high energy) and ultrafast, combining the photon energies of a synchrotron, with a temporal resolution even better than that possible using an ultrafast visible laser. The use of HHG as a probe has been recently demonstrated in observations of molecular rotation [51,52] and dissociation dynamics [53,54], observation of acoustic dynamics in damascene [55], and photoelectron spectroscopy of solid-state systems [48,56].

The short wavelength light from HHG makes it an obvious candidate for imaging. Most synchrotron imaging is currently performed using incoherent light, but these studies are limited to a resolution of  $\sim 15$  nm, defined by the optics (smallest minimum width on a zone plate) [57]. Coherent imaging is one way to circumvent this roadblock since the resolution is theoretically limited only by the wavelength of light. Pioneering work on applying the lensless imaging technique previously demonstrated at

a synchrotron [58] to use a high harmonic source was performed by Sandberg and Paul, and they observed images with 90 nm resolution using 29 nm light from HHG [59,60]. More recently, using a specialized sample with reference holes, they implemented Fourier transform holography capable of fast image reconstruction and 70 nm resolution [61], and by combining this with lensless imaging reconstruction algorithms, the resolution improved to 53 nm. This technique is continuing to mature and ongoing work is pursuing the use of shorter wavelengths for improved resolution, time-resolved imaging of biological samples, and the reflective geometry.

## Chapter 4

### Time-resolved EUV holography

Time resolved interferometric imaging techniques have attracted much attention recently because of their ability to precisely monitor dynamic changes in both space and time [62–64]. These experiments make use of a pump-probe geometry, where an optical pump distorts the sample, while a second, time-delayed, probe captures the induced dynamics. Interferometric information is obtained by placing the sample in one arm of a Mach-Zender or Michelson interferometer. In some experiments [62, 63], a dynamic interference pattern is then captured on a CCD camera, and a reconstruction algorithm is used to obtain the sample evolution. Specifically, femtosecond electron dynamics at metal and semiconductor surfaces can be studied with lateral spatial resolution approaching  $1\ \mu\text{m}$ , and with phase sensitivities of  $\lambda/1000$  at 800nm. Interferometric detection has also been employed to study surface deformation on ultrafast time scales [64], where a Sagnac interferometer can be used to obtain phase resolutions on the order of 1 pm.

The use of extreme ultraviolet (EUV) radiation for interferometric detection offers the potential for simultaneous sub-Angstrom displacement sensitivity and increased lateral spatial resolution, because of the shorter probe wavelength. However, the use of EUV light in interferometric measurements has proven difficult because of the poor reflectivity of optical components ( $\sim 1\%$ ) at these wavelengths, and because even poorer transmission makes an EUV beamsplitter impractical. Typical sample reflectivities are

around 1%, making a Michelson interferometer impractical. Nevertheless, a few experiments to date have employed interferometric detection with EUV light on relatively long timescales and large spatial dimensions. For example, the electron density profile of laser-produced plasmas can be measured using EUV interferometry [65] because the high frequency of the EUV light is above the plasma frequency of the expanding plasma. Other interferometric experiments have directly measured the complex index of refraction of sample materials at EUV wavelengths [66]. However, to date EUV interferometry or holography with simultaneously high spatial and temporal resolution has not been experimentally realized.

#### 4.1 Holography with EUV light from HHG

Among EUV sources, high-order harmonic particularly useful for dynamics experiments because the very short pulse duration ( $\sim 10$  fs) allows for excellent temporal resolution. In this experiment, we implement a dynamic, time-resolved extension of previous work in our group that used EUV light from HHG for static Gabor holography [46]. Here, we study the dynamics of optically-initiated thermoelastic processes in a thin metal film with simultaneously high time resolution and spatial resolution in the vertical dimension. A femtosecond near-infrared laser pulse is used to launch the acoustical processes. A fully-coherent EUV beam [46] generated using the process of high-order harmonic generation in a gas-filled waveguide serves as the probe of the subsequent acoustic oscillations at the surface of the thin film. We use a novel excitation geometry shown in Figure 4.1: a area is excited by a line-focused infrared-pump laser, which is then probed by a much larger EUV beam. The unperturbed sample reflects the EUV (reference) beam, while the pumped region diffracts the object beam to form a dynamic hologram. This leads to a simple, robust, single-reflection geometry for studying transient dynamics on surfaces with femtosecond time resolution. We demonstrate excellent sensitivity to surface displacements and we find that EUV probing of surface

deformation is largely free of ambiguity associated with electronic effects. This allows investigation of surface deformation immediately following impulsive heating - a regime in which the surface deformation signal is generally screened by the coherent electronic signal if probed by visible wavelengths [67].

The experimental geometry is shown in Figure 4.2. Light from a titanium-doped sapphire laser-amplifier system [10, 12] operating at a repetition rate of 2 kHz, with a 25 fs pulse duration, is split into pump and probe beams. Light in the probe arm is upconverted into the EUV using the process of high harmonic generation (HHG) in an argon-filled hollow waveguide [40]. The waveguide allows the conversion process to be well phase-matched over an extended propagation length, leading to the generation of a fully coherent EUV output beam.<sup>6</sup> The EUV pulses generated in this manner yields a spectrum of 5 (odd) harmonic orders, peaked at the 27th harmonic order with a wavelength of 29 nm, as shown in Figure 3.10. The EUV light then passes through three 200 nm thick aluminum thin film filters to eliminate the residual laser light while

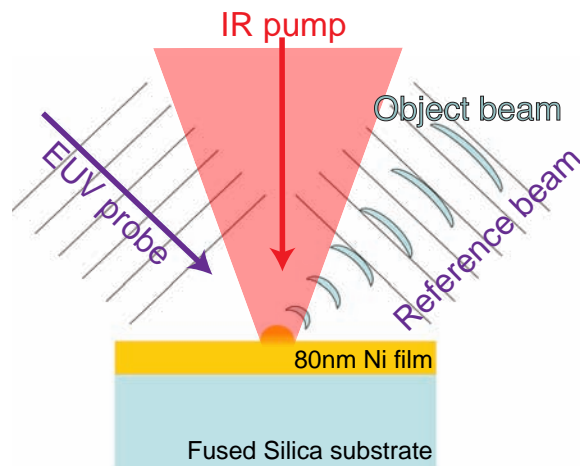


Figure 4.1: Scheme for dynamic EUV Gabor holography. The infrared laser pump is focused to a small line on the nickel thin film sample, which causes a thermal bump. The EUV probe spot is larger than the bump, so most of the EUV beam is simply reflected, forming the reference beam. The EUV that is diffracted from the thermal bump is the object beam. The interference between these beams is detected on a CCD.

transmitting approximately 3% of the EUV radiation. The pump beam is sent into a computer-controlled delay line. A single cylindrical lens is used to generate a  $1.5\text{ cm} \times 77\text{ }\mu\text{m}$  line focus on the sample. Experiments were performed on thin metal films that were thermally evaporated onto fused silica substrates. The probe spot is 1 mm in diameter and is spatially and temporally overlapped with the pump beam on the sample surface, as shown in Figure 4.1. In contrast with conventional pump-probe techniques, the excitation region of the sample resides wholly within the region being probed. This geometry allows the EUV reflection from the unperturbed region of the sample to serve as the reference beam for holographic detection. When the sample is perturbed by the line-focus pump excitation, the EUV intensity pattern on the camera corresponds to the interference of light reflected from the flat surfaces of the sample and light diffracted from a dynamically varying, line-pumped, region. We observe a dynamically changing single-slit diffraction pattern that is shown in Figure 4.3. This representative image was taken by reflecting EUV light from a  $2\text{ }\mu\text{m}$  thick aluminum film, at a time delay of 150 ps after the pump pulse.

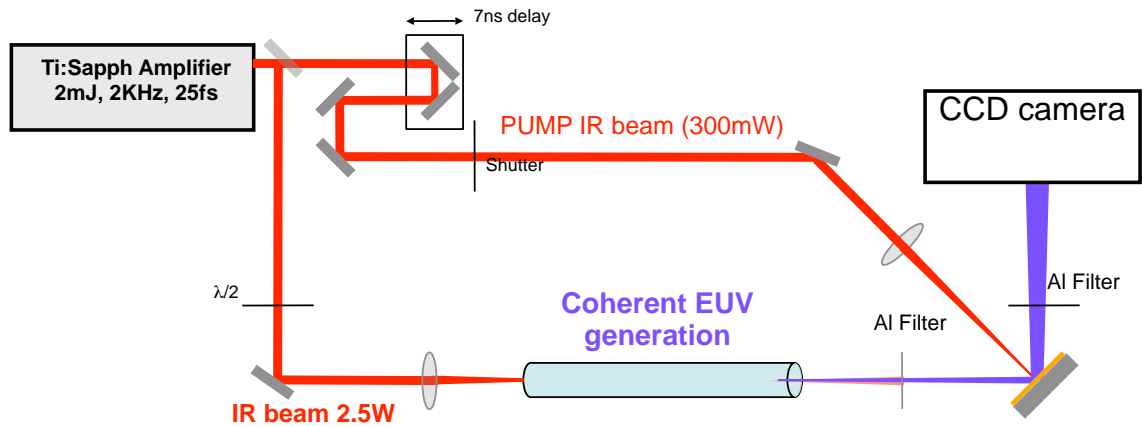


Figure 4.2: Experimental setup for time-resolved EUV Gabor holography. The infrared laser pump is absorbed by the thin nickel film, and the thermal and acoustic transients that follow are dynamically probed with EUV pulses.

The simplicity and ease of alignment of this method for holographic imaging of

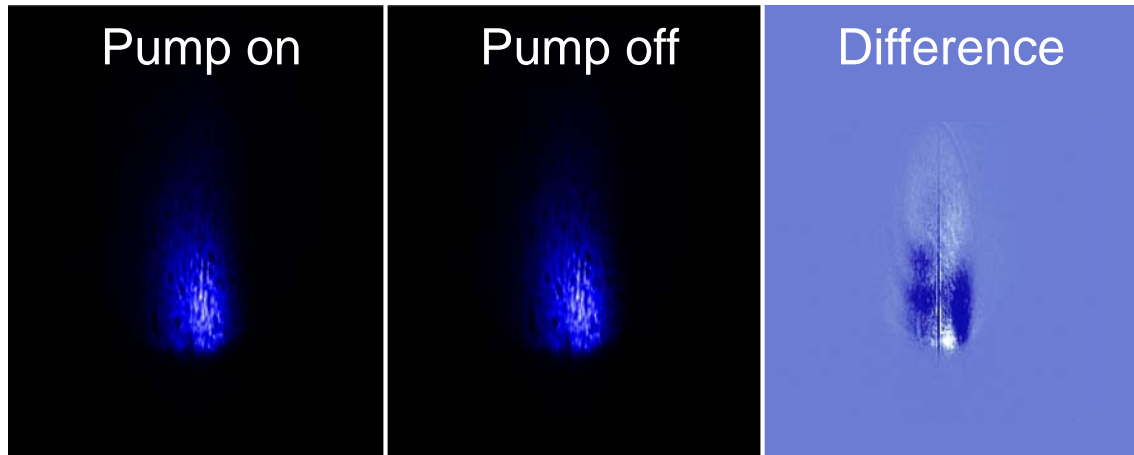


Figure 4.3: Recorded holograms with the pump on, pump off, and pump-probe difference hologram. It is impossible to see a change between the pump on and off images, but the difference image is clear. Figure 4.4 shows the image reduced to 1D by vertical binning.

surfaces is not without its drawbacks. We would like to extend this technique to a higher lateral resolution, but we are limited by the finite spread of the reference beam. Since the image and reference beams will only interfere where they overlap and the finest-detail information is located furthest from beam center, the signal we observe contains only low-resolution information. In the experiment described here, we imaged an optically-pumped spot with a width of approximately  $100\ \mu\text{m}$ , which is much larger than the limit of our optical focusing system – we were unable to see a holographic signal for smaller surface features. It may be this is a signal to noise problem: as the pump spot is made smaller and smaller, the relative strength between the object and reference beams is made weaker and weaker. This could be remedied by using a smaller probe spot, but it is desirable to have a large reference beam at the interference plane and necessary to have a pump spot much smaller than the probe spot on the sample, so these factors must be balanced.

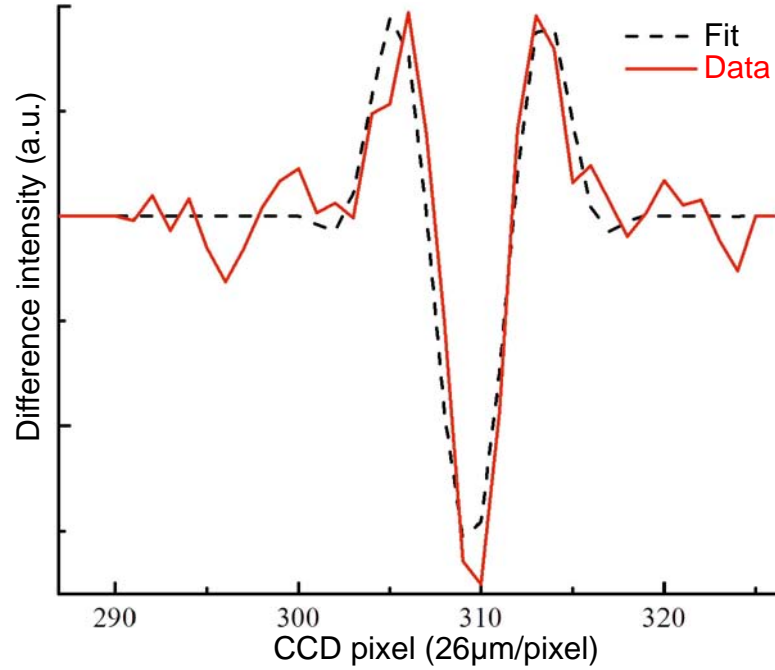


Figure 4.4: Difference in reflected EUV intensity from a  $2 \mu\text{m}$  thick aluminum film, with and without the pump pulse present, at a time delay of 150 picoseconds. The solid line shows the dynamic hologram exhibiting the characteristic far field diffraction pattern of a slit. The calculated signal is shown as a dashed line. By analyzing many such images as a function of time delay, the amplitude of the diffraction pattern oscillates as a bulk longitudinal acoustic wavepacket propagates into the bulk and undergoes multiple reflections at the film/substrate interface..

## 4.2 Fresnel propagation model

In determining how to model the optical propagation, an important parameter is the  $F$ -number  $F = D^2/(z\lambda)$ , where  $D$  is the diffraction feature size on the sample and  $z$  is the sample to CCD distance. In this experiment,  $D$  is equal to the pump beam spot on the sample,  $D \sim 100 \mu\text{m}$ .  $z$  was measured to be 25 cm so  $F = 1.4 > 1$ , and therefore the propagation is in the Fresnel regime.

Given an electric field distribution  $U(x')$  at  $z = 0$ , the field  $S(x)$  at a distance  $z$  away (as shown in Figure 4.5) can be calculated by

$$S(x) = -\frac{i}{\lambda} \int \int U(x') \frac{e^{ikr}}{r} \cos(\theta) dx', \quad (4.1)$$

where  $k = 2\pi/\lambda$ ,  $r = \sqrt{(x - x')^2 + z^2}$ , and  $\cos(\theta) = z/r$ . The Fresnel approximation

assumes that the scale of the entire image planes  $U(x')$  and  $S(x)$  is less than  $z$ , which is valid here ( $x'_{max} \sim 1$  mm,  $x_{max} \sim 2$  mm,  $z = 250$  mm). In this case, calculation of  $r$  can be simplified by the use of a Taylor series expansion and the angle  $\theta$  can be assumed to be very close to zero, so  $\cos(\theta) \sim 1$ . Under these assumptions, Equation 4.1 reduces to

$$S(x) = -\frac{i}{\lambda} \frac{e^{ikz}}{z} \int \int U(x') e^{ik(x-x')^2/2z} dx', \quad (4.2)$$

which is the Fresnel diffraction equation [68, 69].

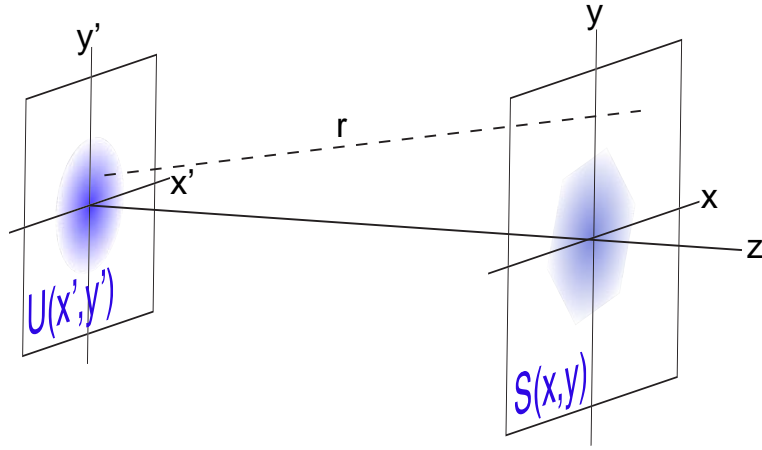


Figure 4.5: Object and image plane definitions for the discussion of the Fresnel diffraction integral. In the Fresnel approximation,  $r \sim z$  and  $S(x, y)$  can be calculated by a convolution with a transfer function [70].

One way to proceed with Fresnel propagation is to use a transfer function  $h(x)$  and its Fourier transform  $H(f_x)$  defined as [70]

$$h(x) = \frac{e^{ikz}}{z} e^{-ik\pi x^2/2z} \quad \text{and} \quad H(f_x) = \sqrt{\frac{2}{ik\pi z}} e^{ikz} e^{2\pi i f_x^2 z/k} \quad (4.3)$$

where the first term is a constant phase and is neglected. The Fresnel integral in Equation 4.2 can then be expressed in terms of a convolution between the initial field  $U(x')$  and the transfer function  $h(x)$ :

$$S(x) = U(x') * h(x). \quad (4.4)$$

We can then make use of the convolution theorem, which says that the Fourier transform of the convolution of two functions  $f$  and  $g$  is the product of their Fourier transforms:  $\mathcal{F}[f * g] = \mathcal{F}[f] \times \mathcal{F}[g]$ . Then the propagated field distribution is

$$S(x) = U(x') * h(x) = \mathcal{F}^{-1} \left[ \mathcal{F}[U(x')] \times H(f_x) \right]. \quad (4.5)$$

This propagation can be performed for both  $U_{pumped}(x)$  and  $U_0(x)$  to determine the image fields in the pumped and unpumped cases. Subtracting the intensities ( $I(x) = |S(x)|^2$ ) gives a calculation for what was experimentally measured. The full matlab code for the propagation calculation is shown in Appendix A.

The initial field distribution in the case of no laser pump is determined by a gaussian EUV input reflecting from a pristine surface with reflectivity  $r_0$ :

$$U_0(x', t) = r_0 \exp(-x'^2/w_{EUV}^2). \quad (4.6)$$

In the case of the laser-heated surface, the 29 nm EUV light (a single harmonic is used in the calculations) experiences a complex reflectivity coefficient of  $r_0 + \Delta r(x') \exp(i\phi(x'))$ , where  $\Delta r(x')$  represents the pump-induced change in reflectivity due to photo-elastic and electronic effects, and  $\phi(x')$  is the phase change as a result of the thermal surface deformation.<sup>11</sup> However, as we will show below, amplitude effects can be neglected because the EUV probe is only sensitive to surface displacements. Assuming that the profile of the surface deformation is proportional to the Gaussian profile of the pump intensity, the pump-induced phase change at the surface is given by:

$$\phi(x', t) = \frac{4\pi\Delta\ell(t)}{\lambda \cos(\theta)} \exp(-x'^2 \cos(\theta)^2/w_{IR}^2) \quad (4.7)$$

where  $\lambda$  is the probing wavelength,  $\Delta\ell(t)$  is the peak surface expansion dependent on the pump-probe delay time at a given a pumping fluence,  $\theta = 45^\circ$  is the angle between the probe and the surface normal, and  $w$  is the width of the pumped region, which in our experiment is 77  $\mu\text{m}$ . The complex field at the sample is then the product of the

gaussian EUV spot and the pump-induced complex reflectivity:

$$U_p(x', t) = (r_0 + \Delta r(x', t) \exp(i\phi(x', t))) \exp(-x'^2/w_{EUV}^2), \quad (4.8)$$

which can be used in Equation 4.5 to determine the field distribution propagated a distance  $z$  away.

The only free parameter in fitting the calculated to the experimental holograms is the peak surface expansion. Figure 4.4 shows one such fit to holographic data collected 150 ps after time zero, yielding a surface deformation of  $\Delta\ell = 0.022 \pm 0.003$  nm. In order to determine if this is a reasonable value, we determine the thermal expansion of the bump by

$$\Delta\ell(x) = \alpha \int \Delta T(x, y) dy, \quad (4.9)$$

where  $\alpha$  and  $\Delta T(x, y)$  are the coefficient of thermal expansion ( $\alpha_{Ni} = 12.4 \times 10^{-6}$ ) and the temperature distribution in the film. As will be discussed in section 7.4.2, this is a poor assumption that overestimates the thermal expansion by a factor of two to three [71], but it will serve an upper limit. The data was collected at a pump power of 300 mW and a repetition rate of 2 kHz, so with a nickel reflectivity at normal incidence of 69%, the energy absorbed per pulse is  $E_{absorbed} = 48 \mu\text{J}$ . Then the change in temperature is given by

$$\Delta T = \frac{E_{absorbed}}{C_p \rho V_{absorption}}, \quad (4.10)$$

where all the properties are for nickel:  $C_p = .44$  J/gK,  $\rho = 8.9$  g/cm<sup>3</sup>, and  $V_{absorption}$  is the absorption volume, equal to the product of the beam dimensions with the absorption depth  $\sim 15$  nm. This calculation yields a peak temperature change in the nickel film of  $\Delta T_{max} = 260$  K, so the heated nickel is still well below the melting temperature of  $\sim 1730$  K. Plugging in the value for  $\Delta T$  in Equation 4.9, we determine an upper bound on the surface deformation of 0.07 nm, indicating that our measurement of  $\Delta\ell = 0.022$  nm is reasonable. Differences between the signal and simulation in Figure 4.4 are likely due to beam pointing instabilities in the laser system. Based on our fit results and a

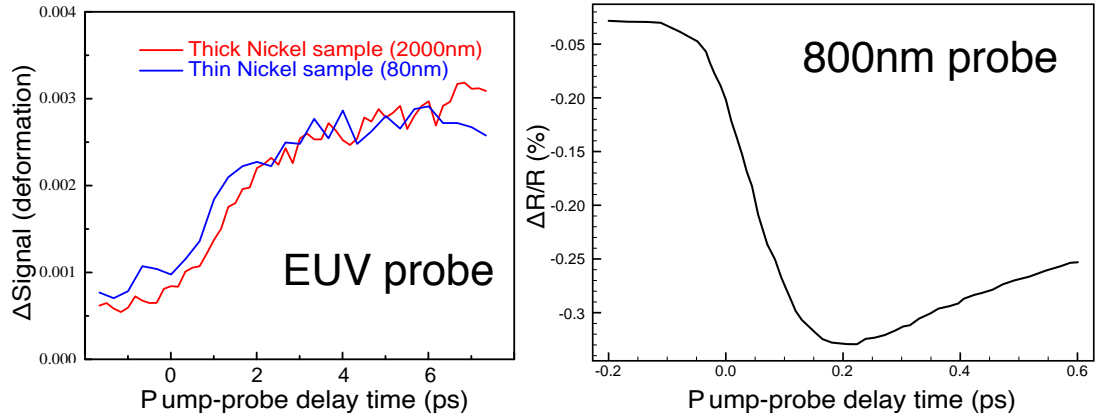


Figure 4.6: Comparison of ultrafast pump-probe data from nickel films. At left is the signal from 80 nm (blue) and 2000 nm (red) thick Ni films using an EUV probe, with a rise time  $\sim 2$  ps. At right, an 800 nm probe beam is used and a much faster rise time  $\sim .2$  ps is observed. The difference is attributed to the EUV sensitivity to the surface deformation which takes longer to occur. 800 nm data reproduced from reference [73].

peak signal-to-noise of 35 (obtained from Figure 4.7), we concluded that our sensitivity to surface deformation is 0.7 pm. This sensitivity is comparable to that obtained using the best visible interferometric techniques [72], and shows great promise for further improvements of dynamic measurement and imaging of thermal processes.

### 4.3 Longitudinal acoustic propagation measurement

By analyzing the time evolution of a diffraction pattern such as that in Figure 4.4, the transient thermo-acoustic dynamics excited by the ultrafast pump pulse can be extracted. Data are accumulated by averaging 25-75 CCD exposures, where each exposure is 20-100 ms (40-200 laser pulses) long. Scans with a good signal-to-noise ratio take about 1 hour to complete. A single data point is comprised of the integrated difference between CCD images taken with and without excitation of the sample, for example, the integrated absolute deviation from zero in Figure 4.4. Figure 4.6 shows the fast signal rise at time zero as a function of time delay between the pump and probe for an 80 nm nickel film on fused silica. The onset of transient dynamics is marked

by a sharp rise in signal level immediately after time zero, with a risetime of  $\tau_{20-80}=2$  ps. This initial rise is due to the delayed responses of electron thermalization, electron-phonon coupling and thermal expansion of the lattice surface after impulsive excitation, as discussed in Chapter 2.

The laser-induced thermal stress near the surface relaxes by launching a broadband, longitudinally-polarized strain pulse into the metal film. This acoustic wavepacket propagates through the thin film until it reaches the film-substrate interface, where a portion of the wavepacket is transmitted and the rest is reflected back towards the sample surface. The arrival of the wavepacket back at the probed surface is marked by an

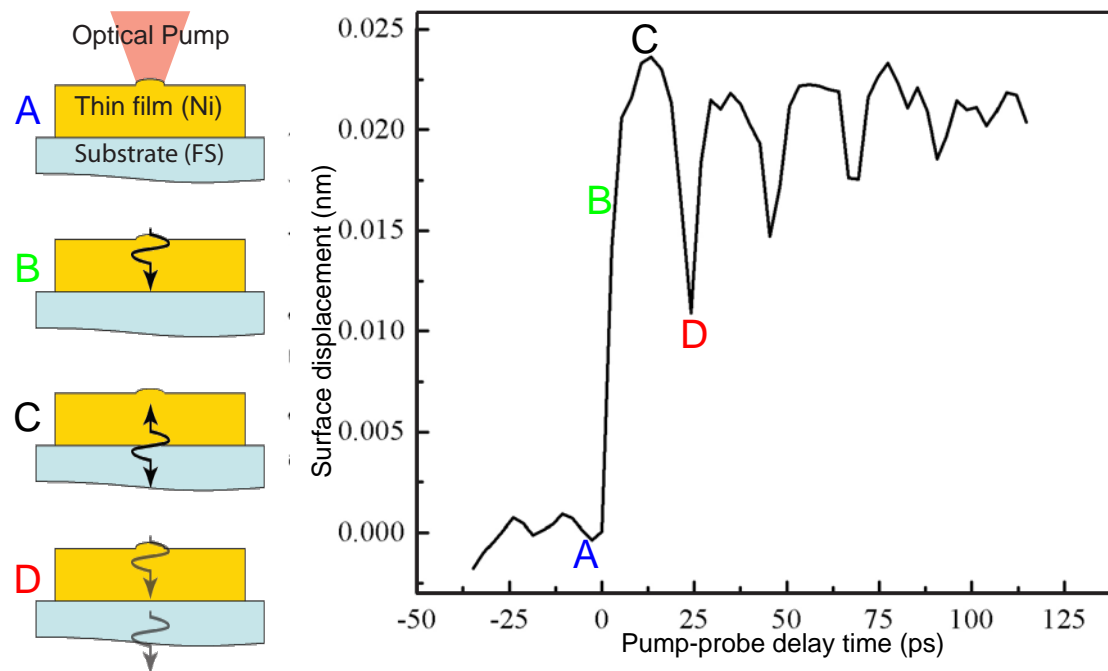


Figure 4.7: Temporal evolution of the holographic signal, measuring both the initial thermal expansion of the surface and the repeated arrival of an acoustic wavepacket at the probed surface. The acoustic dynamics are summarized in a series of steps on the left: (A) Optical absorption and thermal expansion, (B) longitudinal acoustic wavepacket is launched (C) wavepacket reaches the film-substrate interface and is partially reflected (D) the reflected portion of the acoustic pulse returns to the film surface, modulates the surface, and is reflected back into the film where steps B-D are repeated. The step locations in time are marked on the data at right. An oscillation frequency of  $\sim 46$  GHz indicates a nickel film thickness of 66 nm.

additional modulation of the surface, and detected in the experiment as a change in the holographic signal. Partial reflection of the acoustic wavepacket at the free surface leads to successive echoes as the wavepacket bounces between the two interfaces [74–76]. By Fourier transforming the temporal evolution of the diffraction patterns as shown in Figure 4.7, we extract the oscillatory surface deformation due to multiple reflection of the acoustic wavepacket with a frequency of  $45.7 \pm 1.1$  GHz. Using the accepted value for the longitudinal acoustic velocity in bulk nickel ( $v_\ell = 6040$  m/s), we retrieve a film thickness of  $66.1 \pm 1.6$  nm. This value is in qualitative agreement with the nominal film thickness of  $80 \pm 20$  nm measured by a crystal microbalance during the thin film evaporation process.

#### 4.4 Advantages of probing surface displacement with EUV light

Of particular interest in Figure 4.7 is the absence of signal arising from electron interactions at time zero, in contrast with optical probe measurements that can experience two electron effects [77]. The first is a coherent electron bleaching when the pump and probe wavelengths are the same, as shown on the left side of Figure 4.8. When electrons are excited by the pump beam to energies above the Fermi level, then probe light of the same frequency will experience a decrease in absorption and a commensurate increase in transmission and reflection [78]. This effect is very short-lived, lasting only slightly longer than the pump and probe beam overlap time since electron decoherence times are on the order of 10 fs [7]. The second electron effect is an incoherent change in reflectivity when the energy of the probe photons is near an interband transition threshold (ITT) [79]. The Fermi edge is distorted by non-equilibrium "hot" electrons that have absorbed the pump laser energy, as shown in Figure 2.3. Probe photons with energy slightly below the ITT energy see less electrons than are normally near the Fermi level, so their absorption is increased. The opposite is true for probe photons with energy above the ITT energy: there are more occupied electron states in the final probing

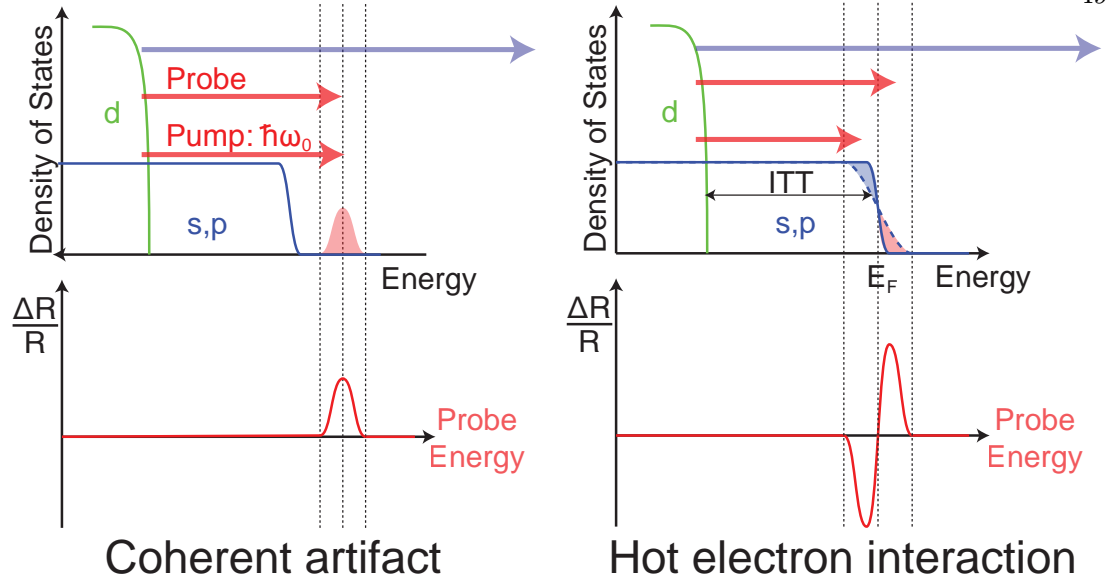


Figure 4.8: Schematic illustration of electronic effects near time zero common to optical pump-probe experiments. In the coherent artifact (left), the pump and probe energy are very similar and the probe beam interacts with electrons excited by the pump, artificially increasing the probe reflectivity. In the case of hot electrons (right), the probe light with energy near the interband transition threshold (ITT) sees a modified Fermi edge (dashed line) due to the non-thermal electrons, which changes the probe reflectivity. EUV light (shown by the light purple arrows) is insensitive to both of these effects because the photon energy is so high, it does not interact with the excited electrons.

state, so the absorption decreases. Although slightly longer than the coherent electron effect, the hot electron effect is also short-lived because the electrons thermalize with the lattice in less than a picosecond (electron-electron and electron-phonon thermalization are discussed in section 2.2). However, both the coherent and hot electron effects effectively obscure any contribution to the signal from the thermal turn-on processes in the lattice. On the other hand, the reflectivity of EUV probe light is not changed by the hot or coherent electrons, as shown in Figure 4.8 by the long purple arrows (note that the actual arrows should be much larger if on a linear energy scale). The photon energies in the EUV probe are so much higher than the optically-excited electrons, they do not interact and the EUV is sensitive only to the thermal surface displacement.

Another unique feature of using EUV light to probe surface displacement dy-

namics is that the EUV light doesn't experience the reflectivity change normally used to measure a signal. Standard transient thermorefectance (TTR) measurements use the sample reflectivity to detect thermal density change and the subsequent stresses due to the propagating wavepacket [72, 74–77, 80–82]. While these measurements give large signals, they do not give surface profile information directly, but rather a complicated convolution of dynamic density and strain information [76, 83]. A temperature increase of 260 K (as determined in section 4.2) results in a maximum density decrease of .3%, which in turn affects the index of refraction. At EUV wavelengths, the index of refraction can be written as  $n = (1-\delta)-i\beta$ , where  $\delta$  and  $\beta$  are proportional to the density [25]. For light at 42 eV incident on nickel,  $\delta_0 = 0.1467$  and  $\beta_0 = 0.1158$ , so the density-modulated values are  $\delta_\Delta = 0.1465$  and  $\beta_\Delta = 0.1156$ . The Fresnel equations can be used to relate this small change in the index of refraction to reflectivity. For reflection of *s*-polarized light incident at angle  $\theta$  (variables are defined in Figure 4.9), the field reflection coefficient is given by

$$r_s = \frac{E_r}{E_i} = \frac{n_2 \cos(\theta) - n_1 \cos(\theta')}{n_2 \cos(\theta) + n_1 \cos(\theta')}, \quad (4.11)$$

where

$$\theta' = \sin^{-1} \left( \frac{n_1}{n_2} \sin(\theta) \right), \quad (4.12)$$

and the intensity coefficient  $R_s$  is  $|r_s|^2$ . Using the values for the pumped and unpumped indices of refraction and the incident angle  $\theta = 45^\circ$ , we calculate a density-induced change in reflectivity of 0.00016. This is 20 $\times$  lower than the change in reflectivity for an optical probe, as determined from temperature-dependent absorption data in reference [84]. The modeling propagation results for holographic signal from surface displacement and reflectivity change for both 30 nm and 800 nm probe light are in Figure 4.10. According to our model, the strength of the holographic signal from this EUV reflectivity change is less than 2% of the total signal, compared to 98% for probing at 800 nm.

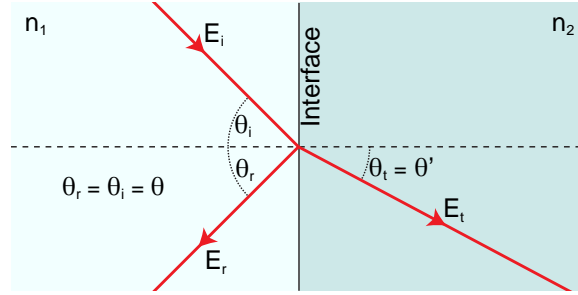


Figure 4.9: Definition of variables for the reflection of *s*-polarized light from an interface as calculated by the Fresnel equation (Equation 4.11) and the refraction angle in Equation 4.12.

The surface sensitivity is manifest in the difference in the shape of the EUV measurement of acoustic pulses (as shown in Figure 4.7) compared to the acoustic pulses normally measured using optical reflectivity measurements [82]. This is because reflectivity measurements couple to the stress in the surface, detecting the temporal profile of the acoustic wavepacket, while the EUV measurement is sensitive to the simple compression and expansion of the surface (the two are related by a derivative). The acoustic signature we measured matches the results of experiments in Wright's group [76, 77], in which they extracted a signal dominated by surface modulation of Ni. The same group later proposed an experimental method for direct measurement of surface deformation [83], but it has not been realized to date. This straightforward method for determination of surface deformation by EUV probing is largely free of ambiguities associated with electronic and photoelastic effects, a significant advantage over alternative photoacoustic measurement techniques.

## 4.5 Conclusion

We have demonstrated a simple and robust holographic geometry for dynamic phase-sensitive detection of surface deformation using coherent EUV radiation. These experiments extend the scope of previously demonstrated Gabor holography to the study of transient acoustic dynamics. With phase sensitivities of greater than  $\lambda/43000$

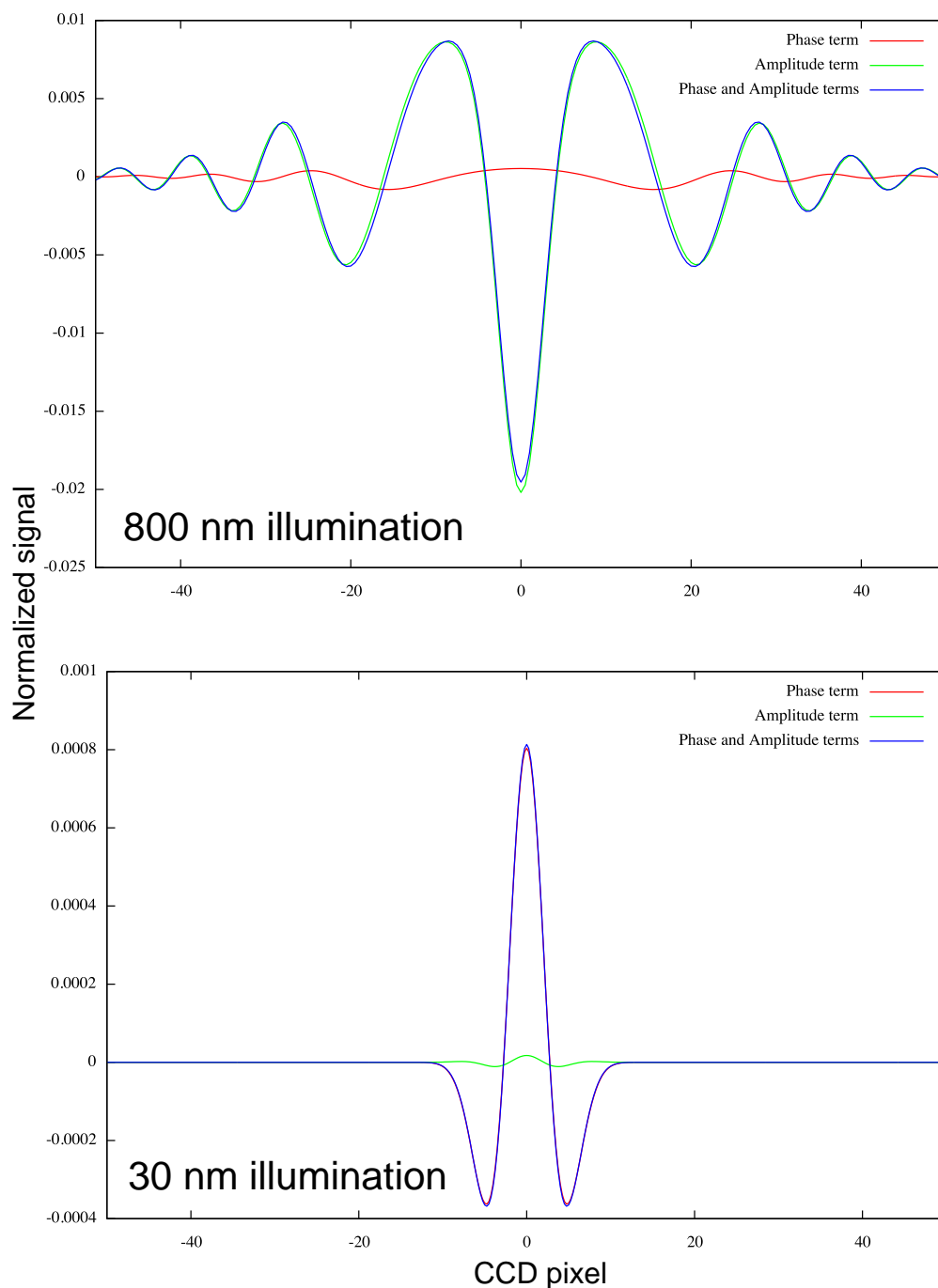


Figure 4.10: Modeled "pump on" - "pump off" image results for illumination with 800 nm near-IR light (top) and 29 nm EUV light (bottom). The total signal in each case is marked in blue while the contributions from the phase and amplitude change on the surface are in red and green, respectively. Signal from 800 nm illumination is dominated by a strong reflectivity contribution, but the signal in the case of EUV illumination is dominated by the phase bump. EUV light is therefore the logical choice for a probe of surface displacement.

at 30 nm, we detect ultrafast surface deformations and subsequent acoustic echoes in thin metal films. This surface measurement is unobscured by hot electron dynamics or stress-induced density changes in the material.

## Chapter 5

### Experimental setup for EUV probing of dynamics in nanostructures

After completing the dynamic EUV holography work discussed in the previous chapter, we decided to use EUV light to time-resolve the acoustic and thermal dynamics that occur in a nanostructure after impulsive heating by an ultrafast laser pulse. The driving motivation in pursuing these experiments was to experimentally measure the effect of a nanostructured interface on energy transport, both along and across the interface. The analysis and discussion of the interfacial effects we measured can be found in Chapters 6 and 7; here we discuss the prerequisite work in extracting small time-resolved signals from noisy backgrounds, and how the data presented in the following chapters was collected and processed.

#### 5.1 EUV detection and noise management

The HHG process is very inefficient (less than one IR photon in  $10^5$  is converted) and highly sensitive to small changes in the parameters: gas pressure, and especially the peak power and pointing of the driving laser are all critical. In order to perform an experiment, it must be carefully constructed so as to minimize noise. In his thesis three years ago [55], Ra'anan Tobey discussed a number of techniques for managing EUV noise in a system and many of his suggestions are still employed in the experiments described in this thesis. However, it is better to reduce the source noise than it is to manage it, and since Ron's noise measurements four years ago, a number of steps have

been made to improve the stability of the harmonic source.

### 5.1.1 Laser system and beam path stability

The harmonic generation process is only as stable as the laser source driving it, so perhaps the most important improvements made in the past few years are those made to the laser amplifier. The amplifier itself is now a multipass chirped-pulse amplification (CPA) "Red Dragon" system from KM labs. Along with an improvement in the multipass ring design that minimizes beam astigmatism, the most important improvement is the use of a new DM-40 pump laser from Photonics Industries. This laser reliably produces above 30 W at a repetition rate of 2 kHz with a shot-to-shot timing jitter of  $< 5$  ns and power jitter of  $< 1\%$ . These noise specifications are much better than Quantronix Falcon system used previously that also required flashlamp replacement and frequent service, and this dramatically improved the shot-to-shot power stability of the laser amplifier. Since HHG is a very high-order nonlinear process, the power fluctuation improvement has a significant effect on the EUV source stability.

Another important improvement in the stability of the driving laser involved the elimination of air currents around the beam path, both in the amplifier and on the way to the HHG setup. The amplifier housing was upgraded from a *sim*4 foot tall fiberboard box to a  $\sim 8$  inch tall metal enclosure. Even more useful was the construction of a plastic box surrounding the beam path from the laser amplifier to the HHG setup. The noise reduction after construction of such a system is shown in Figure 5.1 which compares results with a covered vs uncovered box- without a box at all, the signal is even noisier. The signal itself is a thermal excitation and decay and will be discussed more in the following sections.

A final component of the optical setup that saw significant improvement was in the design of the mounting system for the hollow-core fibers for HHG. The old system of gluing a fiber inside of a glass tube caused very slight bending in the inner fibers,

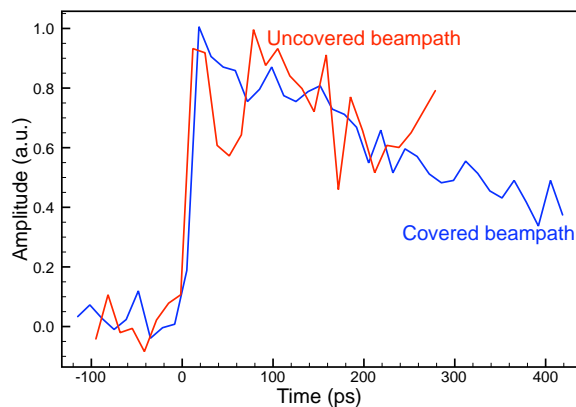


Figure 5.1: Chopped, averaged, time-resolved thermal signal for a boxed and covered beampath (blue) and a boxed but uncovered beampath (red), demonstrating the noise-reduction from enclosing the beampath before the HHG fiber.

which significantly reduced the HHG output. The new design uses a v-groove to keep the fiber supported and confined along a straight line and the resulting harmonics are brighter, more stable, and much more consistent from fiber to fiber [60].

### 5.1.2 Acquisition technique: chopping faster

In Tobey’s analysis of noise management of EUV light from HHG for measurements, he found that the noise was dominated by low frequency components. In order to filter this low frequency noise, he implemented a chopping method of toggling the pump beam on and off between consecutive exposures. The pump-induced signal could then be observed by considering the difference of the averages of the pump on and pump off exposures.

Three significant improvements were made in this technique since Tobey’s experiments, which are summarized in Figure 5.2:

- We changed the data collection scheme from computer control to be triggered off of the CCD exposure timing, eliminating the need to wait time in the computer control. In order to toggle the pump beam on and off with each CCD exposure, we designed and built the circuit shown in Figure 5.3. This circuit was an

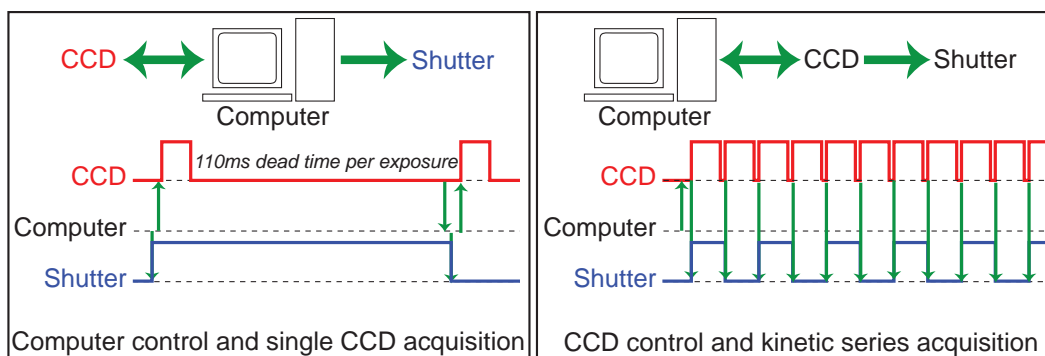


Figure 5.2: Illustration of the difference between two methods of data acquisition: computer control of a series of single CCD acquisitions (left) and CCD control with a kinetic series of acquisitions.

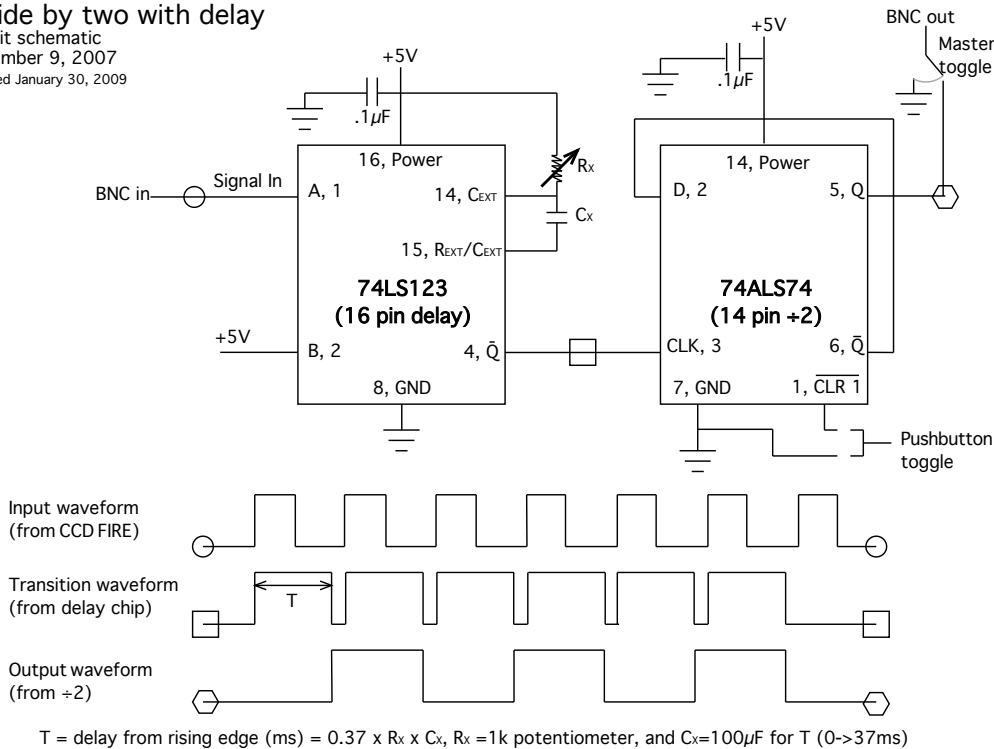
integral part of all of the data collected for the next three chapters.

- We realized that the biggest source of lag in the experiment was the CCD readout time: for each exposure, an additional 100 ms was used in downloading the data to the computer. This meant that in a 20 ms exposure, the system was collecting data only 16% of the time. This problem was solved by using a kinetic series acquisition: instead of repeated I/O commands from the computer to the CCD, a single command is sent to the CCD instructing the CCD to take the total number (say 1000) of exposures, and then download all of them to the computer when finished. This eliminated the 100 ms data transfer delay (except for one at the end of the series), and greatly improved the data acquisition speed and efficiency.
- We switched to use a faster LS 200 shutter from NM laser capable of continuous operation at 200 Hz, much faster than the 20 Hz limit of the previous shutter.

With all of these improvements, we were able to take data nearly seven times as fast as before, which not only gave better statistics faster (since signal-to-noise is proportional to  $1/\sqrt{N}$ , where  $N$  is the number of measurements), but to eliminate low-frequency noise up to frequencies  $7\times$  higher than before. This dramatically improved

### Divide by two with delay

Circuit schematic  
November 9, 2007  
Updated January 30, 2009



Note: +5V regulated by a voltage regulator and additional 1F capacitor to ground

Figure 5.3: Schematic for divide by two with delay to enable fast, synchronized excitation synchronization with the EUV CCD detection.

the signal-to-noise of our measurements, and enabled the detection of small signals with 1 photon in  $10^5$  sensitivity.

### 5.1.3 The danger of normalization

Normalization is another technique Tobey suggested to deal with EUV noise. However, normalization is dangerous because it discards information that was present in the data (total counts) for normalized data. It is also a big problem when there is pump light leakthrough because pump light hitting the CCD away from the area of detection can still influence the total signal. This caused a strong signal to show up, even before time zero, that masked the real probed signal. We found that it is better to leave the data unnormalized- in this case, the pump-only background can be subtracted

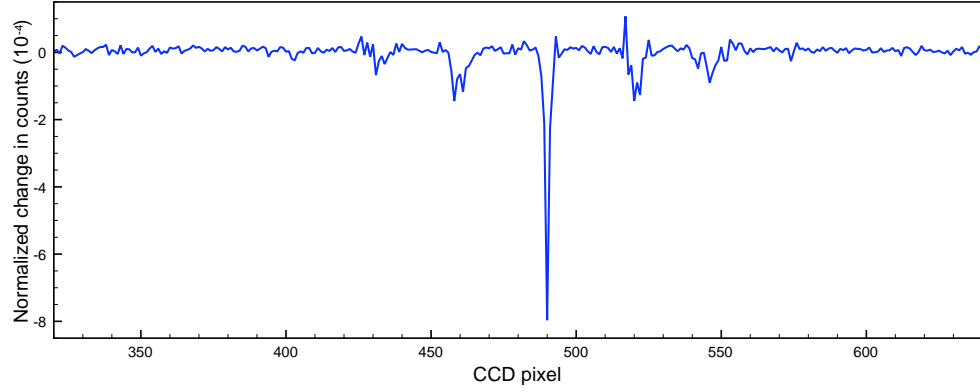


Figure 5.4: Signal before time zero caused by scattered pump light hitting the CCD and skewing the normalization. This illustrates the danger in normalizing the data. Compare with Figure 5.12 (bottom), which shows real signal before and after time zero.

as a baseline from the pumped data.

## 5.2 Sample design and fabrication

Sapphire was selected as the substrate material because it has a very high acoustic velocity (Rayleigh velocity  $v_{SAW,Sa} \sim 6300$  m/s) and is transparent to the 800 nm pump light used for exciting the nanostructure. Nickel lines were manufactured using electron beam lithography and liftoff in  $120 \mu\text{m} \times 120 \mu\text{m}$  square regions with  $240 \mu\text{m}$  between them. Within each region, the lines were  $120 \mu\text{m}$  long with a fixed width  $L$  between 65 and 2000 nm (period confirmed using a SEM, as shown in Figure 5.5). Figure 6.4 shows the two grating geometries used: one with nickel strips of height  $h = 20$  nm and period  $p = 4L$ , the other with  $h = 10$  nm and  $p = 2L$ . The periodicities were selected such that the product of the height and the duty cycle  $\eta = L/p$  was constant, useful for comparing the acoustic dispersion in the perturbative approximation discussed in section 6.3.1. To ensure uniform heating in the vertical (surface normal) direction, the height of the nanostructures was chosen to be  $< 20$  nm — between the optical penetration depth and ballistic electron transport, the nanostructure should be uniformly heated over this dimension.

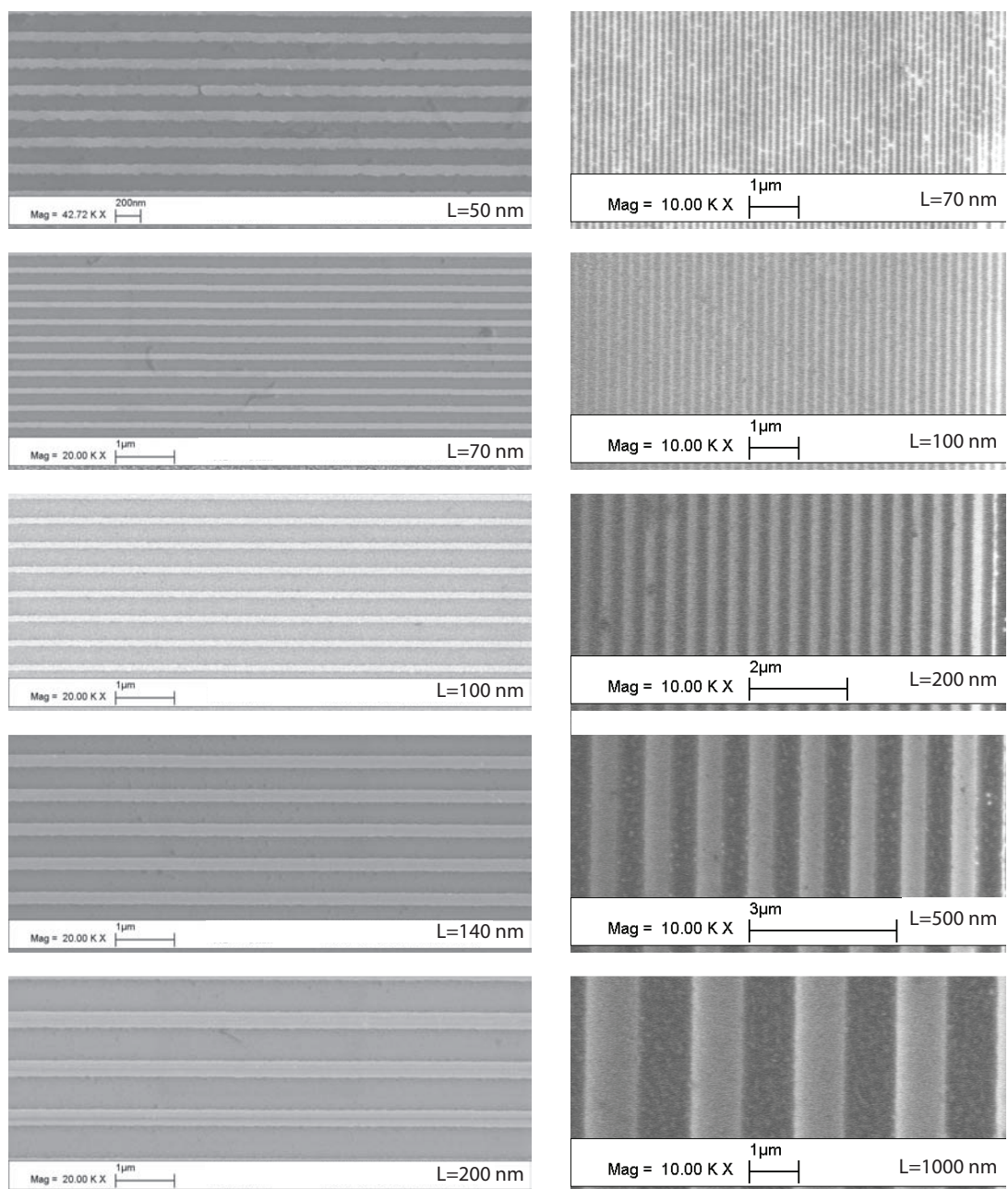


Figure 5.5: Scanning electron microscope images of typical nickel on sapphire nanograting structures.  $p = 4L$  ( $\eta = .25$ , left column) and  $p = 2L$  ( $\eta = .5$ , right column) structures are shown.

The samples were fabricated by our collaborator Erik Anderson at Lawrence Berkeley National Laboratory. The fabrication process is summarized in Figure 5.6.

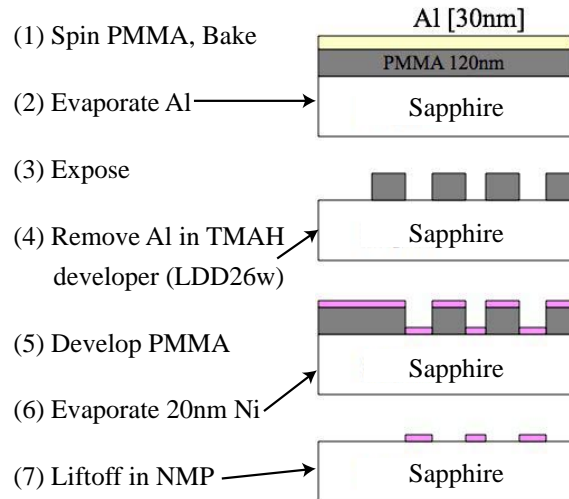


Figure 5.6: Nanograting sample fabrication process.

### 5.3 Experimental setup

As in the experiment discussed in Chapter 4, the output of an ultrafast Ti:Sapphire laser-amplifier system is split into pump and probe beams, as shown in Figure 5.7. A few notable details of the experimental setup are discussed in this section.

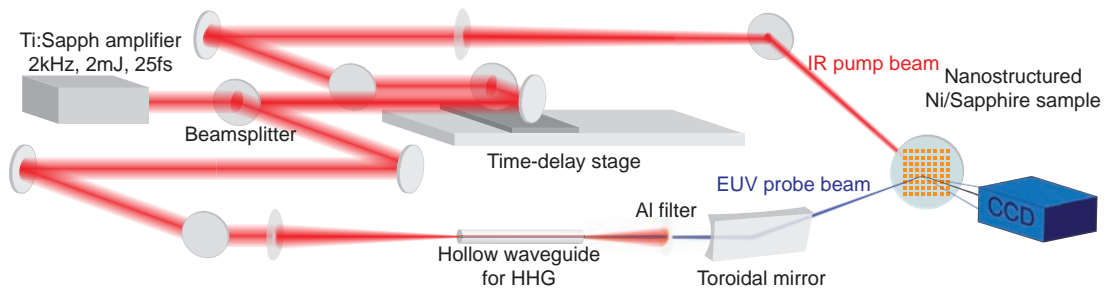


Figure 5.7: Setup for nanothermal and nanoacoustic experiments.

#### 5.3.1 Pump beam setup

The 800 nm pump beam is sent through a computer-controlled time-delay stage and is then loosely focused onto the sample. A relatively large pump spot ( $\sim 700\mu\text{m}$ ) is used so that the area probed will see a uniform laser fluence. The sapphire sub-

strate is transparent to the 800 nm pump light, so the pump pulse only heats the Ni nanostructure.

In order to determine the actual thermal excitation of the pump laser, it is important to account for the power losses of p-polarized light between the location in the beampath of the power measurement (30 mW) and the thermal excitation of the nickel:

- Beam clipping in the shutter, pellicle steering mirror reflections, and front and back reflections from a vacuum window at near-normal incidence (85% measured),
- Front and back reflections from the sapphire substrate at  $45^\circ$  incidence, as well as reflection from and transmission through the nickel (52% calculated [14, 69]).

Accounting for these losses reduces the measured power of 30 mW to 13 mW thermally exciting the sample, which is an intensity of  $1.7 \text{ mJ/cm}^2$  for a laser repetition rate at 2 kHz and a pump spot size of  $700 \mu\text{m}$ . Using this absorbed energy density in Equation 4.10 along with the density and specific heat listed immediately below that equation and a nickel thickness of 20 nm, we obtain a peak temperature rise of the nickel nanostructure of 220 K. Of course, the nonequilibrium electrons that absorb the incident pump pulses will get to much higher temperatures than this, but because our EUV detection is sensitive to the lattice response and is insensitive to electron dynamics (see section 4.4), we are not concerned with this.

In the lab, final pump alignment is performed by looking at an image of the pump beam on the sample. The pump beam covers approximately 8 gratings, so pump-probe overlap isn't critical, but the imaging setup allows for easy location of the pump beam to the grating being probed.

### 5.3.2 Glancing-incidence toroidal focusing mirror for EUV light

The probe light is converted to EUV by focusing the 800 nm light into a gas-filled hollow waveguide to generate high-order harmonics. The emitted harmonics can be treated as a gaussian beam with a  $1/e^2$  diameter of 50 nm and a wavefront curvature of 0.02 m [85]. Therefore, in order to have a small, intense EUV spot useful for probing the  $100\ \mu\text{m} \times 100\ \mu\text{m}$  sample patches, we need to focus the EUV light.

Since materials are absorptive in the EUV region of the spectrum, a transmission optic (lenses) is impossible to use. Diffractive (zone plates) enable near diffraction-limited spot sizes [25] and high-resolution imaging [57,86,87] at higher photon energies (250 eV and above), but they are very chromatic (the different harmonics will focus to different distances from the optic, giving a very smeared focus) and at for photons with energies of  $<100$  eV, they are very inefficient. Reflective (mirrors) optics can be used at any wavelength, but again the absorption is a significant challenge: for example, reflection from a gold-coated mirror is only 3.5% at normal incidence, which is where curved mirrors should be used in order to avoid astigmatism in the focused beam.

The reflectivity of normal-incidence mirrors can be improved by using multilayer coatings [25,88–90]. Like zone plates, these mirrors are also more reflective for higher-energy photons, with performance optimized at 13.3 nm: using alternating layers of Mo and Si with a periodicity of  $\lambda/2$ , a narrowband reflectivity over 70% can be obtained, but if the same materials are used in a multilayer optimized for 29 nm light, the peak reflectivity is only 25%, and even using multilayer materials optimized for this wavelength (MgC and Si) gives a peak reflectivity of 38%. These values are for narrowband reflectivity (determined by coating many  $\sim 40$  layer pairs), so all neighboring harmonic are rejected, which is useful when a single harmonic is desired for energy resolution, for example in lensless imaging or photoelectron experiments [cite Richard, Luis]. Broadband mirrors can also be manufactured (by coating fewer  $\sim 10$  layer pairs), but the

peak reflectivity is usually lower by  $\sim 50\%$  in these cases.

Another useful option when broadband reflectivity is desired is to use a glancing incidence mirror because the reflectivity at any wavelength improves dramatically as the angle of incidence increases from normal. For example, the reflectivity of 42 eV light from a gold-coated mirror is 71% at  $10^\circ$  from glancing, a dramatic improvement from 3.5% at normal incidence. As alluded to previously, the problem with this configuration is the strong astigmatism that is introduced by an off-normal reflection from a spherical mirror. For light incident at an angle  $\theta$ , as shown in Figure 5.8, the effective focal lengths in the tangential (in the plane of the angle of incidence) and sagittal (out of the plane) directions are modified as follows:

$$\begin{aligned} f_t &= R \cos(\theta)/2, \\ f_s &= R/(2 \cos(\theta)), \end{aligned} \tag{5.1}$$

where the radius and normal-incidence focal length of a curved mirror are related by  $f = R/2$ . In practice, this modification of the effective focal lengths in the two directions means (for light reflecting from a curved mirror with an incidence off-normal horizontally) that there will be two line foci: first a sharp vertical (tangential) focus, and then a blurry horizontal (sagittal) focus. This line focusing may be useful in some experiments, as in Chapter 8, but in this case we wanted a stigmatic, circular focused spot to get the EUV light efficiently on the sample.

We used a toroidal mirror to correct the astigmatism. A toroid is a donut-like surface which is a curved mirror with different radii of curvature in two perpendicular directions. The idea is to correct the two different focal lengths by using two radii of curvature, i.e. set  $f_t = f_s$  in Equations 5.1 and solve for  $R_s$  and  $R_t$ :

$$\frac{R_s}{R_t} = \cos^2(\theta). \tag{5.2}$$

If the ratio of the sagittal and tangential radii of curvature follow this equation for a given angle, then light incident on the toroid at  $\theta$  will be focused stigmatically. Note

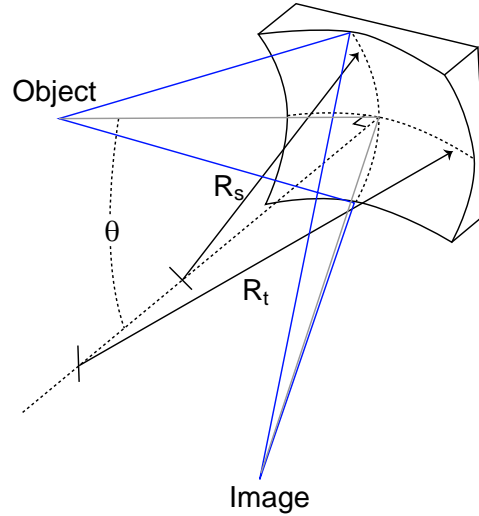


Figure 5.8: Geometry for a toroidal mirror with radii of curvature  $R_s$  and  $R_t$  in the sagittal and tangential directions, for astigmatism-corrected reflection of light incident at an angle  $\theta$  satisfying Equation 5.2. If  $R_s = R_t$ , the mirror is spherical and light incident at an angle  $\theta$  will be astigmatically reflected. Figure modified from [91].

that a toroid must be designed with a particular angle of incidence in mind, and slight deviation from that angle will introduce astigmatism.

The toroid we used was designed for use at  $\phi = 90^\circ - \theta = 10^\circ$  from glancing and a focal length of 50 cm. It was manufactured by ARW Optical, and had the following parameters: 50 mm  $\times$  25 mm Pyrex substrate,  $R_t = 3220$  mm,  $R_s = 90.5$  mm, surface roughness 0.8-1.2 nm. We gold-coated the toroid and then mounted it with spring-loaded screws to avoid thermal deformations. It was then placed in the beamline with independent fine control over the sagittal and tangential angles, as well as rotation to align the incident beam with the tangential toroid axis. With the toroid 65 cm from the end of the HHG capillary, we expected a EUV spot size of  $\sim 100 \mu\text{m}$  at the focus, where we place the nanograting sample.

### 5.3.3 Aluminum filter holder and CCD adapter

In pump-probe experiments, rejection of the pump light before it reaches the probe detector is essential to avoid signal contamination. This is a significant challenge

in optical pump, EUV probe experiments because there are so many more pump photons. For example, at  $\sim 30$  mW and 2 kHz used for the experiments discussed here, there are  $\sim 6 \times 10^{13}$  1.58 eV photons incident on the sample per pulse, which is nearly four orders of magnitude more than the number of harmonic photons generated. Since there are so many more pump photons, a very efficient filtering method is required.

Additionally, we must consider the residual laser light from the harmonic generation process: nearly 2 W of power is coupled into the waveguide, and only a small fraction of it is converted to harmonic light. This is a problem not only for detection of the harmonic photons by a CCD, but also for the integrity of the sample: the nanostructured samples sit at the focus of the beam (from the toroid), so if the laser pulses were allowed to hit the sample, the intensity of  $\sim 10^9$  W/cm<sup>2</sup> would generate a temperature  $\sim 10^{14}$  K (well above the melting point of nickel at 1728 K), and would certainly destroy any structure. So here too efficient filtering of the 800 nm light is required, while still keeping as much of the harmonic light as possible.

Although there are other methods for filtering the driving laser light from the generated EUV light (Brewster's angle reflection from silicon mirrors is one intriguing possibility [92]), transmission through thin metal foils is by far the most robust and light-tight system. The concept was developed in the 1960's in the space program [93], and the techniques for manufacturing unsupported metal films of a few hundred nanometers in thickness was developed for use in EUV spectroscopy a decade later [94, 95].

Typically in our group, we eliminate the pump and residual laser amplifier light by transmission through two aluminum films with a thickness of 200 nm. The transparency of 42 eV photons through 200 nm of pure aluminum is 62%, but aluminum oxidizes readily in atmosphere, so a few nm of more-absorptive aluminum oxide ( $\text{Al}_2\text{O}_3$ ) grows on the surface, reducing the effective transmission of each filter to  $\sim 40\%$ . Ideally, we would minimize the number of aluminum surfaces that can be oxidized by using a single, thicker filter, but unfortunately, an intrinsic property of thin film filters is the

presence of pinholes that allow a small amount of unwanted light through [96]. For this reason, at least two filters must be used, but in pump-probe experiments, we use three aluminum filters: two are needed after the sample to effectively reject the pump light, and an additional one is placed in the probe line before the sample to prevent sample damage. The total harmonic transmission through the filters is 6%, which seems low until we compare it with the the transmission of red light, which is  $10^{-34}$  smaller.

A significant challenge of using thin metal film filters is that they are extremely delicate. EUV experiments must be conducted in a vacuum because of the high atmospheric absorption, so thin film filters placed in the beamline (usually in a vacuum-tight seal to establish a light-tight seal and prevent scattered light leakthrough) must be able to withstand viscous forces applied during the evacuation and venting of the vacuum chamber. Ariel Paul developed an EUV filter wheel dealing with this problem that allows for the removal of the filters during venting and pumpdown while still giving a light-tight seal when desired [60].

Unfortunately, this filter wheel requires 6 cm of beampath, which is unreasonable in experiments looking at small structures, where the CCD must be placed very close to the sample in order to capture the diffraction. How close the CCD needs to be can be determined by calculating the diffraction angle (parameters are defined in Figure 5.9:

$$m\lambda = d(\sin(a) \pm \sin(b)), \quad (5.3)$$

where  $m = 1$  for first-order diffraction and the wavelength in these experiments  $\lambda = 29$  nm. If we consider the grating with the smallest period that we will be studying,  $d = 125$  nm, then given an angle of incidence  $a = 45^\circ$ , the diffraction angle  $a - b = 28.4^\circ$ . We can then determine the deviation of this first-order diffracted beam from the zero-order beam by

$$\tan(a - b) = A/B. \quad (5.4)$$

The CCD we used is an Andor DO-420BN, which has a sensor that is 1 inch across, so

if the reflected beam hit one edge of the sensor, the diffracted beam would have to be  $A \sim 2$  cm away. This sets an upper bound on the sample-to-CCD distance of  $B < 6.7$  cm. The sample was held in a cryostat to allow for temperature control of the substrate while under vacuum, and from the sample to the outer wall of the cryostat was  $\sim 5$  cm, so only 1.7 cm can separate the chamber and the CCD, ruling out the use of a thin film filter wheel.

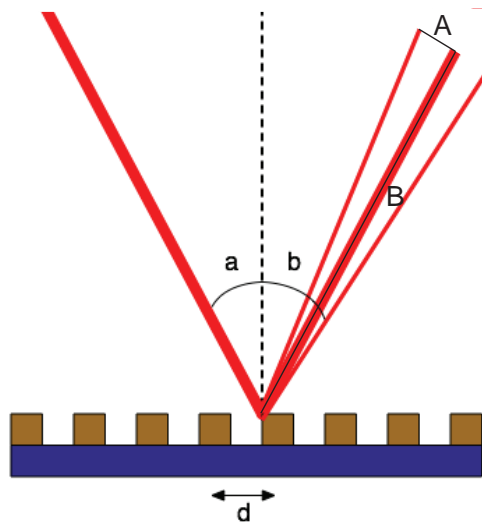


Figure 5.9: Schematic for calculation of diffraction with an angle of incidence off of normal in Equation 5.3. The deviation of the first-order diffraction from the reflected beam (A) can then be calculated as a function of distance from the grating (B).

In order to minimize the sample-to-CCD distance while still allowing for two thin film filters to be placed between the sample and the CCD, I designed and machined a thin CCD adapter with the following features:

- Vacuum is retained by o-ring seals on both sides.
- The adapter is only 1.25 cm thick so that the CCD can be placed 6 cm from the sample (the distance from the sample to the edge of the cryostat chamber is  $< 5$  cm).
- One or two Al filters can be held in the center by aluminum retaining rings.

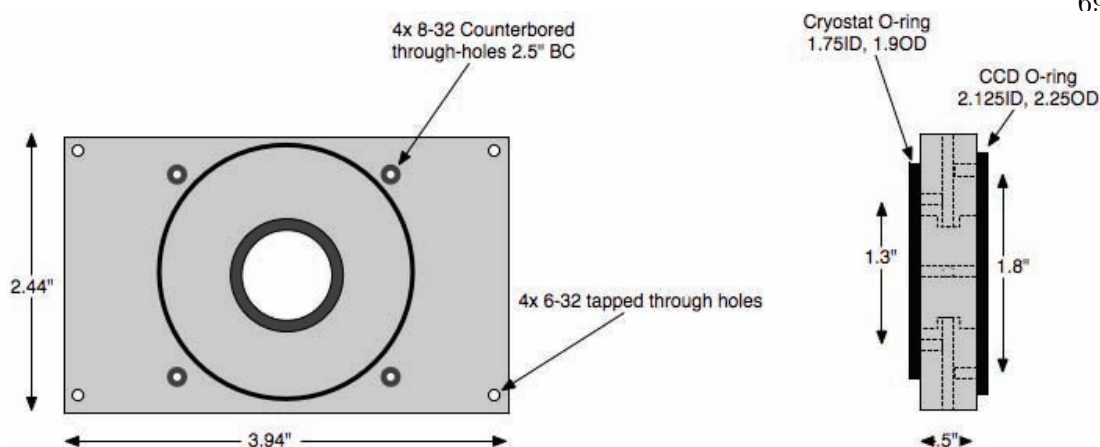


Figure 5.10: Cryostat-CCD adapter plate designed to hold two and provide vacuum bypass for two aluminum filters while minimizing the sample-to-CCD distance.

- Small holes with many right angle turns to allow air bypass around both filters but reject light scatter.

### 5.3.4 Mechanical setup

Each nanostructured grating is  $120\ \mu\text{m} \times 120\ \mu\text{m}$  in area, so they present a very small target to be hit by the  $100\ \mu\text{m}$  EUV probe beam. In order to get good probe-sample overlap, a means of fine-tuning alignment while the system is under vacuum is necessary. We considered steering the beam to the sample by turning the toroid, but this caused astigmatism in the toroid's focusing, as well as being hard to work with because of the distance between the sample and the toroid. Eventually, we settled on an alignment system that takes the opposite approach: aligning the sample to the beam. More accurately, we move the whole vacuum chamber to the beam since the sample is on a cold finger and cannot be moved inside the cryostat vacuum chamber.

The final chamber positioning system is shown in Figure 5.11. It has the following features:

- Independent control over the sample position along three axis, as shown by the red, blue, and green arrows in Figure 5.11. This allows for sample selection and

final sample-beam overlap optimization as well as sample movement along the direction of the beam to position the sample at the focus of the probe beam.

- Stable chamber support by using flange-mounted bearings to hold the chamber steady despite the vacuum pressure pulling the bellows is  $\sim 40$  pounds  $= (650 \text{ torr}) \times (.0194 \text{ psi/torr}) \times (3 \text{ in}^2)$ . Sample stability in case of a bump or small adjustment is also very good.

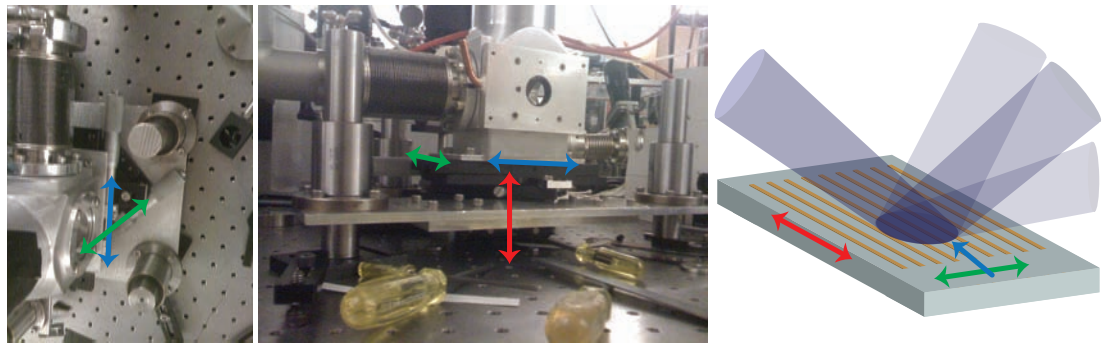


Figure 5.11: Sample positioning system that allows for vertical (red arrows) and horizontal translation of the sample along the direction of the incident beam (blue arrows) and a direction parallel to the surface of the sample (green arrows), as well as rotation, all while holding the chamber very stable.

#### 5.4 Data acquisition and analysis

There are two responses to the impulsive, localized, and periodic heating from a 800 nm pump pulse:

- (1) The heat-induced periodic stress launches SAWs that travel along the surface perpendicular to the orientation of the nickel lines, as shown in Figure 6.3. These SAWs interact with the nanostructured nickel strips as they travel, slow down (since the SAW velocity in nickel is slower than in sapphire), and displace the nanostructure surface. This displacement is periodic in time as the SAWs travel on the surface, so they introduce a sinusoidal oscillation of the signal with

a frequency given by the acoustic velocity divided by the nanostructure period.

A detailed analysis of the SAW propagation is conducted in Chapter 6.

- (2) Thermal expansion of the nanostructure as it is heated, and a slow shrinking as it cools and heat is transported across the interface into the substrate. This effect is the subject of Chapter 7, and can be seen from the same data sets considered here as the quasi-exponential thermal decay time under the SAW oscillation.

#### 5.4.1 Data acquisition and time-dependent signal extraction

Both of these effects introduce very small ( $\sim$ picometer) displacements of the nanostructure surface, which the EUV light is capable of detecting them because of the short wavelength. The displacements can be detected in changes in the diffraction efficiency of the probe EUV beam from the nanograting for a series of (pump on) - (pump off) CCD exposures, as shown in Figure 5.12. As discussed in section 5.1.2, the faster these

In order to extract a time-resolved signal, we add up the difference intensities at each time. To gain further insight into the origin of the signal, we can separately consider the contributions to the signal from the first and second-order diffraction as well as the zero-order reflection. When adding these components together, we flip the sign when appropriate (for example, the total signal in Figure 5.12 from the  $\pm 1, 0$  orders is given by inverting the diffraction components and adding them to the reflected. Repeating this process at each time delay, we obtain the dynamic signal.

#### 5.4.2 Signal linearity

In order to experimentally determine whether both the thermal and acoustic signals are linear, we can observe the dynamic signal as a function of pump power. The results of this test for 90 nm lines are shown in Figure 5.13, and clearly both the thermal

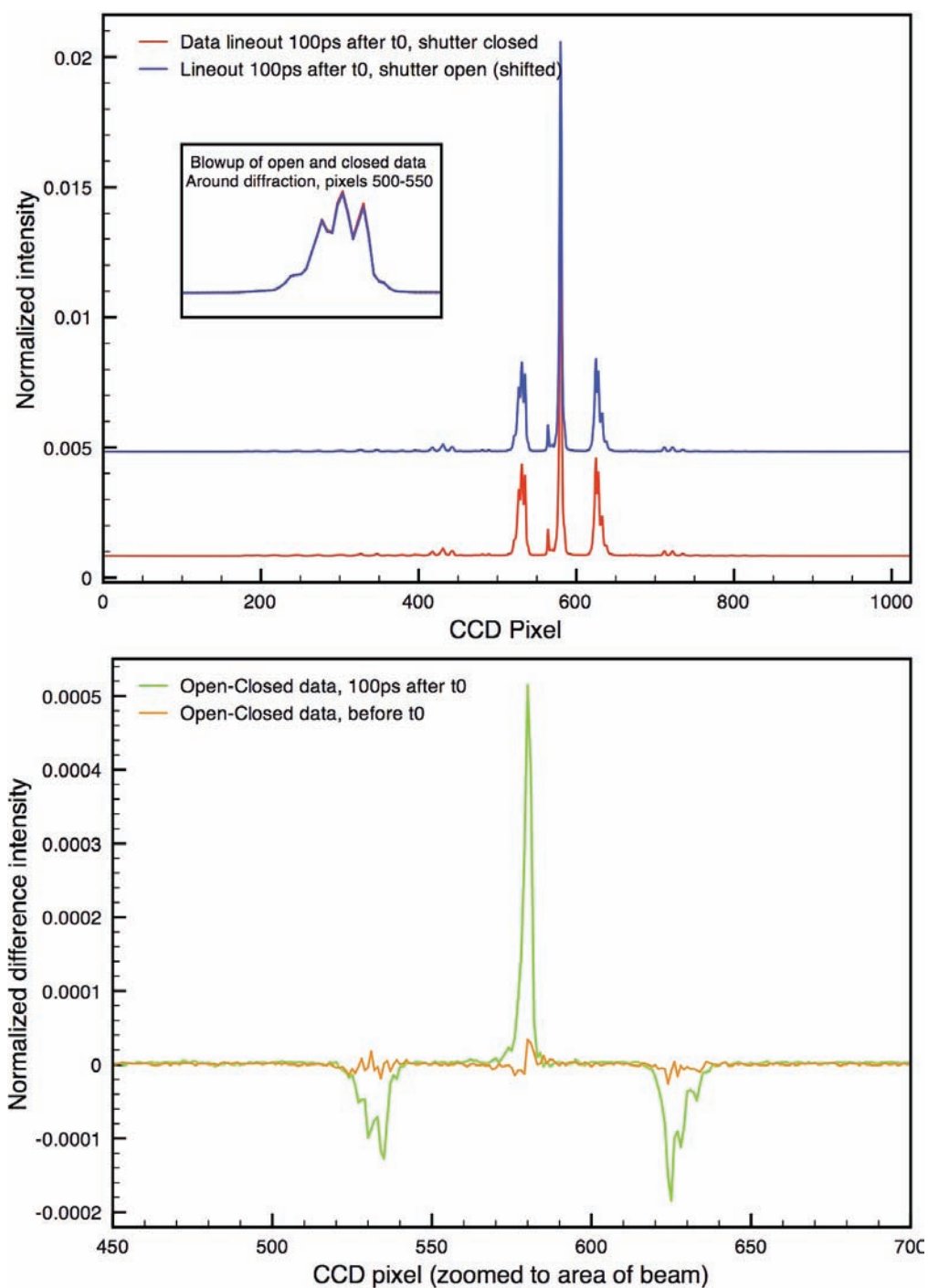


Figure 5.12: Top: raw data obtained from averaged pump-on (blue, shifted) and pump-off (red) exposures of EUV diffraction from a  $L = 1 \mu\text{m}$  nanograting. Inset shows a blow-up of the first diffracted order, demonstrating the imperceptible difference between exposures with the pump on and off. Bottom: Pump-on, pump-off difference from top figure, both before (orange, no signal) and after (green, change in diffraction efficiency signal) time zero.

decay and acoustic oscillations scale linearly with pump power in this range. Similar tests on other samples showed the same linear signal dependence. All data presented in the following chapters was taken with pump intensity at or below these values.

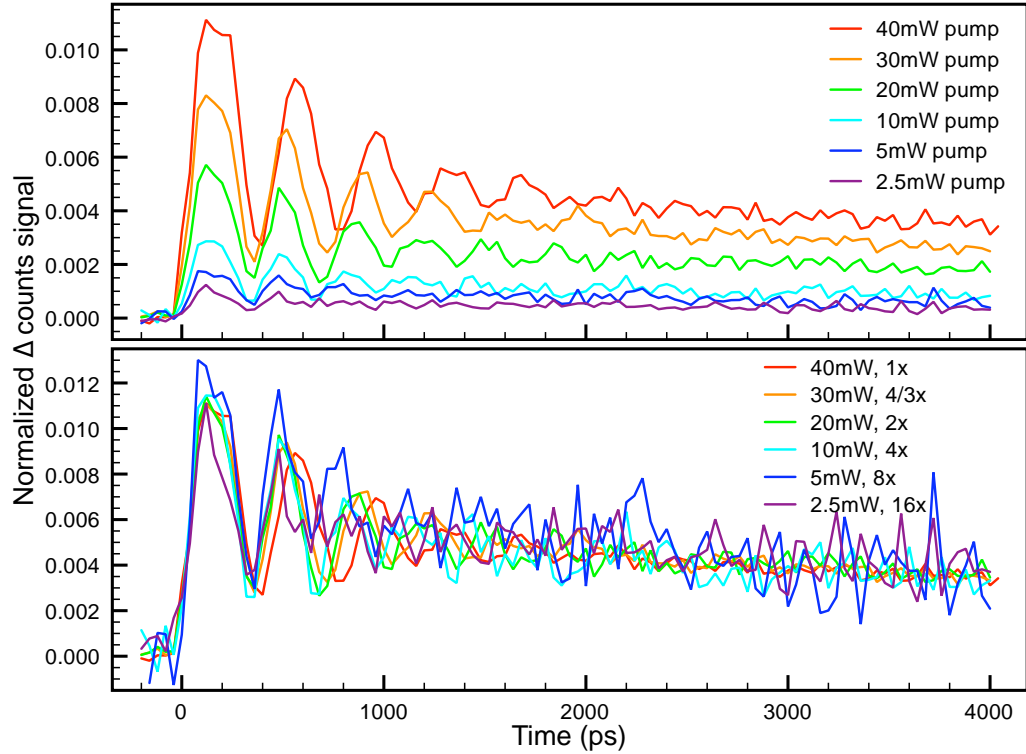


Figure 5.13: Signal from  $L = 90$  nm nanogratings as a function of pump power. The top graph shows the unscaled signals at each power, while the bottom graph scales all of the data by the appropriate power ratio in order to determine the signal linearity as a function of pump power.

Modeling of the expected signal predicts linear signal dependence on temperature as well. The thermal surface displacement is directly proportional to the change in temperature  $\Delta T$  by  $\Delta h = \alpha h \Delta T$ , where  $\alpha$  is the coefficient of thermal expansion of the heated nanostructure (for nickel,  $\alpha = 12.7 \times 10^{-6}/K$ ). In the experiments that follow, we will excite temperature changes of  $\sim 100$  K, so for a  $h = 20$  nm structure, the expected peak displacement is  $\sim 25$  pm. The calculated change in signal for a 1 pm displacement is shown in Figure 5.14, and although the signal is not linear over a few-nm scale, over a 25 pm scale, the change in the signal is very small, so the signal

can be assumed to be linear.

This brings up another point: the baseline diffraction signal in these experiments shifts with a change in the initial temperature because of thermal expansion/shrinkage of the unperturbed grating. However, whatever the initial temperature, a thermal excitation of  $\sim 100$  K can still be treated as a linear effect, as long as the baseline diffraction of the initial temperature is measured.

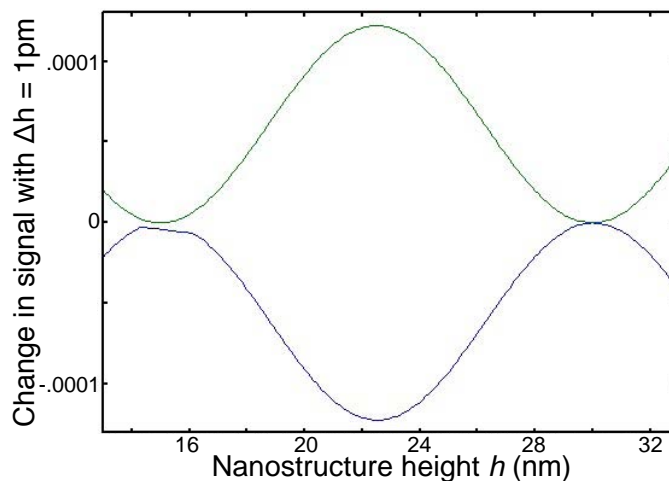


Figure 5.14: Signal from changing line height by 1pm as a function of nanostructure line height  $h$  from reflection (top, green) and diffraction (bottom, black). The total change in signal is given by to sum of the absolute value (total separation) of the two curves.

## 5.5 Time-resolved EUV acquisition outlook

There is still significant room for improvement beyond what has already been done in refining the optical, mechanical and acquisition components in the detection of EUV probes. The  $10\times$  increase in acquisition rate is a useful step, but ideally, we would do single-shot measurements. The laser amplifier runs at 2 kHz, so this would require a detector with a sub-500  $\mu\text{s}$  acquisition time,  $40\times$  faster than our current best. Such shot-to-shot measurements are possible using fast CCD cameras (Roper Scientific) using binning to run even faster or photodiode detection. Photodiodes are capable of  $> 1$  GHz acquisition rates, so they can be used with a lock-in amplifier, which would

greatly increase the signal-to-noise for a given acquisition time. However, the practical efficiency of photodiodes is much lower than CCD detectors and they provide much less spatial information than a CCD (a photodiode is a single-pixel detector), so we have used CCDs to this point. If enough flux could be obtained, it would be useful to use a hybrid CCD/photodiode system: using the CCD for alignment and the photodiode for sensitive signal detection, as shown in Figure 5.5

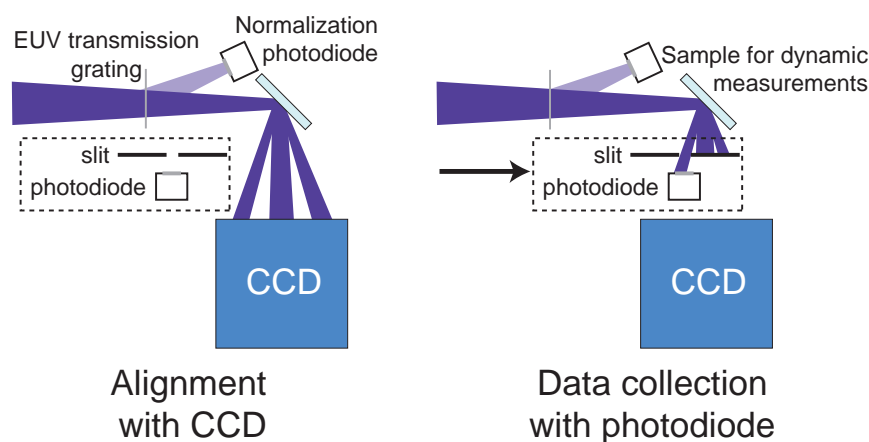


Figure 5.15: Hybrid CCD-photodiode setup. The HHG and sample alignment can be optimized by looking at the CCD (left), and then fast data collection can be conducted with a photodiode and an adjustable slit for selecting a single diffracted order (right). Also shown in this figure is a proposed technique for shot-to-shot signal normalization using a weakly diffracting grating and a photodiode to detect the HHG intensity before hitting the sample.

Despite our efforts to improve stability, the biggest source of noise in the system is the harmonic generation process. Sending a small portion of the beam to a photodiode for shot-to-shot intensity normalization would significantly reduce the noise on the signal. This is also shown in Figure 5.5. Another way to improve the signal is to improve the total HHG flux, which could be done by using a shorter hollow capillary or reducing the number of EUV filters or moving them to be before the sample (using infrared pump light would eliminate the need for filters to be between the sample and the CCD since the CCD is insensitive to infrared light).

A final source of noise that must be considered for high rep-rate CCDs with

finite exposure times is pulse-exposure offset, as illustrated in Figure 5.16. This effect gets stronger as the exposure time gets shorter, and the solution is to synchronize the exposures with the pulses by triggering the exposures at a fixed delay to the probe pulses. However, triggering a CCD exposure usually adds considerable dead time to the total acquisition, so the advantages of short exposure times must be balanced by this consideration.

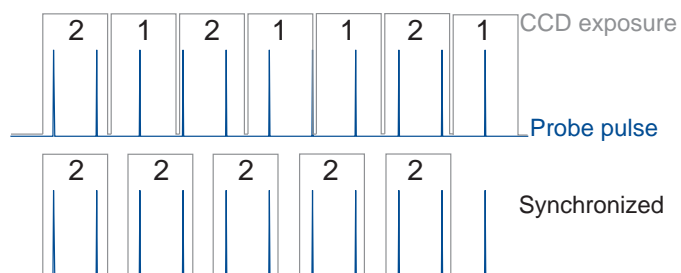


Figure 5.16: Illustration of the exposure time/probe pulse walk-off that can cause an irregular number of probe pulses to be recorded on each exposure, which becomes a bigger problem as shorter exposures are taken. The solution is to trigger the CCD exposure on the probe pulses, but this adds considerable dead time to the acquisition.

## Chapter 6

### High-Frequency Surface Acoustic Wave Propagation in Nanostructures

The previous chapter discussed the application of EUV light from HHG in probing longitudinal acoustic propagation in thin films, which can be used for measurements of thin films. Longitudinal acoustic pulses inherently propagate into a surface, and the back-reflections observed at the surface can be utilized as a diagnostic of thickness and properties of thick films. Here, "thick" means thicker than the width of the acoustic wavepacket, set by the excitation depth. In laser ultrasonics, the excitation depth is determined by the optical penetration depth  $\zeta_o$  of the pump laser and (for metals) the "hot" ballistic electron range  $\zeta_e$ . For most metals (See Table 2.2), optical penetration depths are on the order of 10 nm and ballistic electrons can carry this heat another 10-150 nm before thermalizing, so this technique is useful only for films of thickness  $h \geq 100$  nm. Thin film technology has advanced to the point that atomic-layer films can be deposited, so much better depth sensitivity is required.

Additionally, interfacial sensitivity is very low for longitudinal pulses: their propagation is dominated by the film properties because their relative interaction with interfaces is so little. A precise understanding of interface properties is of great interest to a number of engineering communities, because as thin film stacks are grown with thinner and thinner layers, the interface properties become increasingly important. Diffusion between layers is also a major concern, and the ability to perform quick, noncontact

testing of buried interfaces is important for device diagnostics and coating methodology improvements. For these reasons, an optical probe of properties of interfaces beneath very thin films is desired.

### 6.1 Surface acoustic wave propagation for thin film measurements

One technique that holds promise for studying interfaces beneath very thin films is surface acoustic wave (SAW) spectroscopy. SAW modes are confined to the surface with a very shallow surface penetration, and thus their propagation is sensitive to surface structure and layer composition. Also, because they propagate parallel to the surface, they interact strongly with buried interfaces and defects [97], so they are better-suited to detecting interfacial anomalies than longitudinal acoustic pulses. To study films of sub-micron thickness, however, it is necessary to use SAWs with comparably short wavelengths, since the penetration depth  $\zeta_{SAW}$  of the SAW is proportional to the acoustic wavelength  $\Lambda_{SAW}$  by [98]

$$\zeta_{SAW} = \frac{\Lambda_{SAW}}{2\pi}. \quad (6.1)$$

Thermally exciting the film using a transient grating geometry is a common technique for generating narrow-band surface acoustic waves [99–101]. The basic idea is illustrated in Figure 6.1 – when two pulsed laser beams are crossed at a surface, the laser intensity distribution at the surface forms an interference pattern given by

$$I(x, t) = I_0 \left( 1 + \cos(4\pi \sin(\theta)x/\lambda_{laser}) \right) \exp(-t^2/\tau^2) \exp(-x^2/a^2), \quad (6.2)$$

where  $\theta$  is half of the crossing angle and  $I_0$ ,  $a$ , and  $\tau$  denote the peak intensity, the beam radius, and the pulse duration of the laser. If the driving laser is short compared to the SAW propagation time ( $\tau \ll \Lambda_{SAW}/v_{SAW} < 1$  ps), this intensity distribution impulsively excites the surface in a spatially-periodic way, which stresses the surface and launches a narrow-band surface acoustic wave with a wavelength given by the

interference period,

$$\Lambda_{SAW} = \lambda_{laser}/(2 \sin(\theta)). \quad (6.3)$$

However, this method is limited to SAW wavelengths on the order of or higher than optical wavelengths because the generated grating can be determined by using the crossing angle of the two pump beams in Equation 3.1. As a result, the shortest acoustic wavelength generated to-date using the transient grating method is approximately 750nm [102,103]. This presents a challenge for conventional optical methods of creating and detecting SAWs, and would seem to limit this technique to film thicknesses  $h \geq 100$  nm, the same order as longitudinal methods.

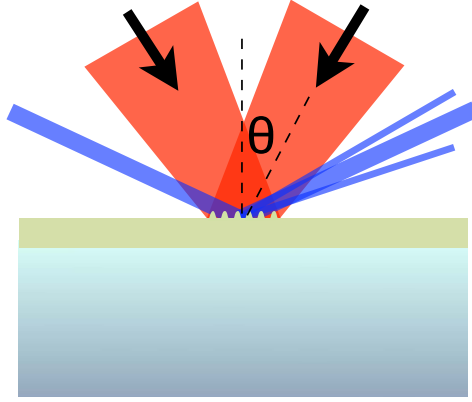


Figure 6.1: Schematic depiction of the transient grating scheme for generating surface acoustic waves. Two pulsed laser beams (red in the figure) are crossed on a surface at an angle  $\theta$ , which sets up an interference pattern and spatially-periodic heating. This generates a periodic stress that launches a SAW with wavelength set by  $\Lambda_{SAW} = \lambda_{laser}/(2 \sin(\theta))$ . The SAW dynamics can then be probed by observing the transient diffraction from the acoustic ripple of a third, probe pulse (shown in blue).

An alternative approach that overcomes this limitation is to lithographically pattern a nanostructure on the surface. This pattern can then be optically excited, locally stressing a surface and thus exciting a SAW with a wavelength limited only by the resolution of the lithographic pattern [104,105]. However, this approach raises the question of how much the presence of the nanostructure will affect the propagation of the SAW. This question is critical for analysis of the underlying sample characteristics. Past mea-

measurements employing thin Al patterned absorbers suggested that these issues can be neglected [105–108]. However, these conclusions were based on data taken at a single SAW wavelength. Very recent work has shown 2D SAW propagation in arrays of nanodisks and suggested that there may be dispersion from the nanostructure loading [109]. To date, no work has sampled the full dispersion curve of a patterned thin film in order to come to a definitive conclusion on this issue.

The Maris group at Brown University made the first to experimental attempt to generate high-frequency SAWs in a nanostructure in 1992. They used a  $\lambda = 596$  nm, 3 ps laser pulse to excite and probe  $h = 40$  nm high gold stripes on a fused silica substrate. However, they only saw vibrational modes of the wires themselves and not SAW propagation [110]. Since that time, work on similar structures has focused on whether the observed signal is dominated by SAW propagation in the substrate or normal mode resonance of individual wires [105, 107, 110].

All previous of surface acoustic wave dynamics in nanostructures used optical light to probe dynamical acoustic processes in a nanostructure, so detection is also an issue. Visible light will not diffract from a sub-wavelength structure, so current techniques measure very small ( $< 1$  part in  $10^5$  [110]) changes in surface reflectivity to observe SAW propagation [105, 107–109, 111, 112]. However, these reflectivity changes arise from a complex mix of thermal density changes and local and interfacial stresses and strains. Direct transient grating diffraction from the surface would give more reliable, easier-to-interpret, and higher signal-to-noise data — however, such an experiment requires light with a wavelength shorter than the SAW wavelength. EUV light from HHG is an ideal source to fill this need because the  $< 10$  fs pulse duration provides excellent time resolution and the short wavelength gives strong diffraction and increased sensitivity to surface displacements.

## 6.2 EUV measurements of SAW dynamics

By measuring the change in diffraction as a function of pump-probe delay time, we can observe dynamic surface acoustic wave propagation. Four scans with  $p = 3 \mu\text{m}$ ,  $1.5 \mu\text{m}$ ,  $300 \text{ nm}$ , and  $160 \text{ nm}$  are shown in Figure 6.5. The relative amplitude of the oscillatory SAW component of the signal is  $10\times$  larger than in a similar experiment using an optical probe [108]. For a given grating period  $p$ , we extract the SAW frequency  $\nu$  by performing a Fourier transform, as shown in the insets of Fig. 6.5.

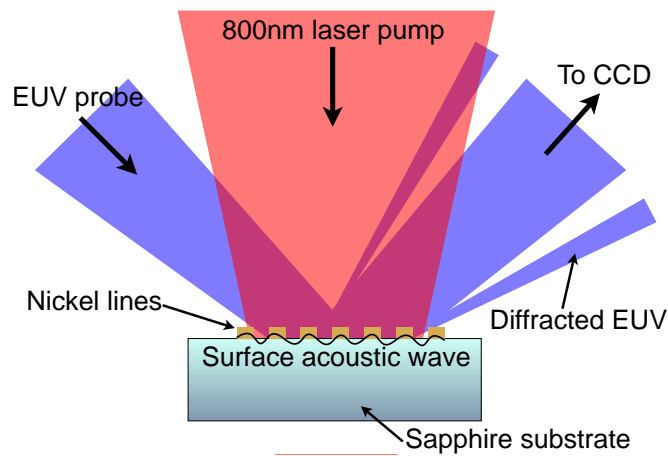


Figure 6.2: Experimental setup for ultrafast measurements of SAW propagation with EUV light. An 800nm laser pulse (red) heats the nickel nanostructure, which creates a periodic stress and excites a SAW. The propagation of this SAW is then observed by observing dynamically changing diffraction of an ultrafast EUV probe pulse (blue) from the structure.

### 6.2.1 Are we really seeing surface acoustic wave propagation?

Past work on generating and detecting acoustic waves from nanostructures was focused on whether the observed signals are due to SAW propagation or vibrations of isolated structures, so a natural question is: Are we really seeing surface acoustic wave propagation? To determine the relative contribution of these modes, we compared the results from  $p = 4L$  samples to those from  $p = 2L$  samples, as shown in Figure 6.5. A Fourier transform of the data reveals a narrow-band oscillation in all cases, and the

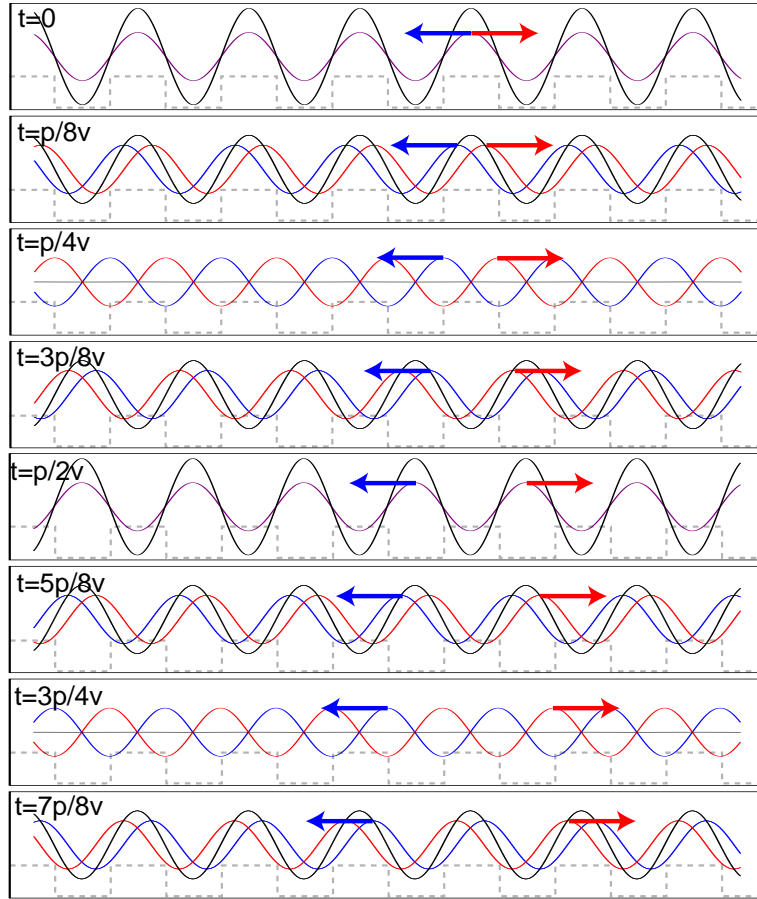


Figure 6.3: Illustration of SAW propagation: the sum of two equal-amplitude sinusoidal waves traveling in opposite directions (blue traveling left and red right, arrows mark propagation of a specific crest) is a standing wave (black). The propagation and surface displacement (black) are shown over one full cycle, with the times marked in the upper-left of each panel.

results of such an analysis are summarized in Table 6.1. In the case of the  $L = 800$  nm structures, the SAW propagation in the  $2L$  ( $p = 1.5\mu\text{m}$ ) sample has a frequency two times greater than the frequency in the  $4L$  ( $p = 3\mu\text{m}$ ) samples. The frequency of oscillation is proportional to the nickel strip period rather than the line width. If we assume that the oscillation is due to SAW propagation, both the  $4L$  and the  $2L$  data sets yield a SAW velocity  $\sim 6000$  m/s, which is the expected Rayleigh velocity for sapphire. We therefore conclude that the oscillation is due to SAW propagation in the substrate, with a SAW wavelength set by the strip period ( $\Lambda_{SAW} = p$ ).

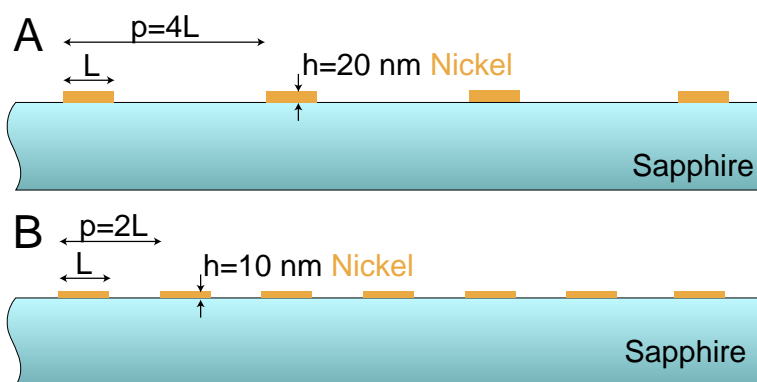


Figure 6.4: Schematic showing two sample configurations for nickel nanolines of width  $L$  on sapphire substrates: (A)  $h=20$  nm and nanostructure periodicity  $p = 4L$  (25% duty cycle), (B)  $h=10$  nm and nanostructure periodicity  $p = 2L$  (50% duty cycle).

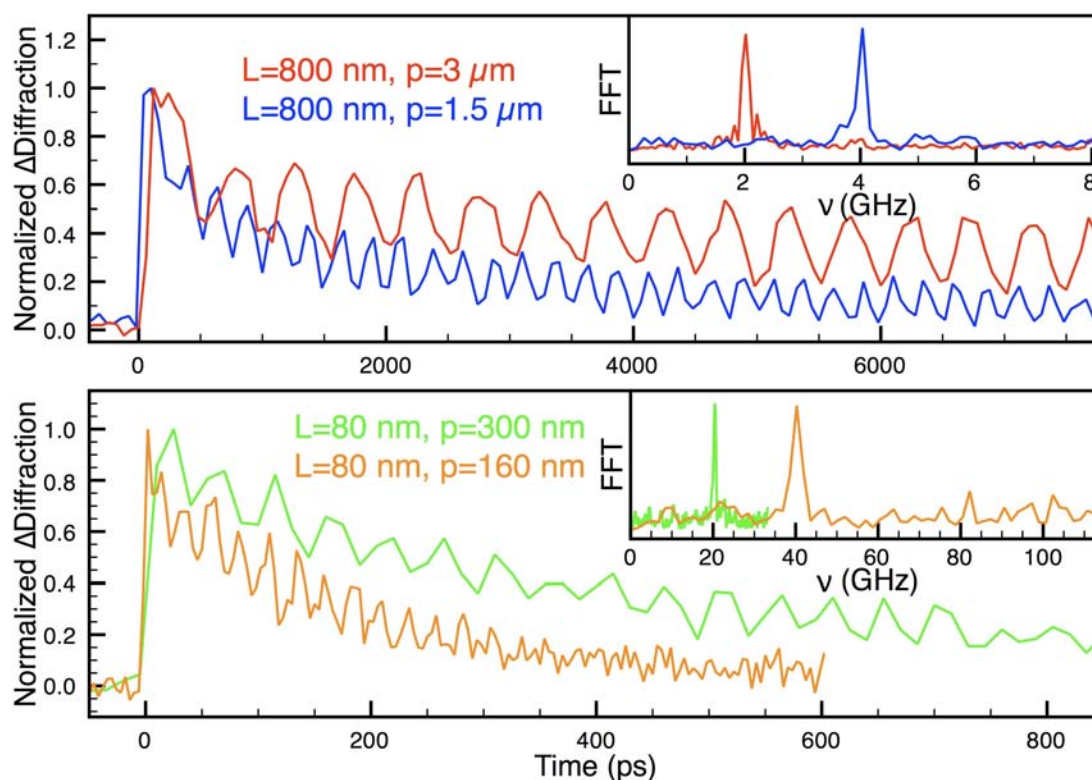


Figure 6.5: Dynamic EUV diffraction from surface acoustic waves on samples of sapphire with periodically spaced lines of nickel. Nickel line periods of  $p = 1.5$  and  $3 \mu\text{m}$  with width of  $L = 800$  nm (top) and  $p = 300$  and  $160$  nm with  $L = 80$  nm (bottom) were heated and probed. Impulsive heating and rapid thermal expansion launch surface acoustic waves whose oscillations are superimposed upon a nonoscillatory signal component that decays due to thermal diffusion. The SAW frequencies are shown in the insets.

Period $p$	Linewidth $L$	SAW frequency $\nu$	SAW velocity $v_{SAW} = p\nu$
1.56 $\mu\text{m}$	800 nm	4.01 $\pm$ .01 GHz	6280 $\pm$ 15 m/s
3.12 $\mu\text{m}$	800 nm	2.01 $\pm$ .01 GHz	6270 $\pm$ 30 m/s
145 nm	80 nm	40.5 $\pm$ .1 GHz	5880 $\pm$ 25 m/s
295 nm	80 nm	20.6 $\pm$ .1 GHz	6077 $\pm$ 30 m/s

Table 6.1: Extracted surface acoustic wave frequency  $\nu$  for samples shown in Figure 6.5. The calculated velocity is dependent on the period  $p$  rather than the linewidth  $L$ ,

### 6.2.2 Surface acoustic wave dispersion measurements

While the analysis for the large-linewidth values of  $L = 800$  nm in the previous section revealed a constant velocity, the small-linewidth velocities from  $L = 80$  nm data are different, both from the  $L = 800$  nm values and for different periods. However, the change is relatively small ( $\sim 7\%$ ), so the same mechanism of SAW propagation in the substrate is dominant, but it is being perturbed by a factor dependent on the periodicity (or acoustic wavelength  $\Lambda_{SAW}$ ). The cause of this change in measured SAW velocity is a penetration depth shift-induced dispersion: as the SAW periodicity is decreased, the penetration depth is equally decreased (recall  $\zeta = \Lambda_{SAW}/2\pi$ ), so the SAW propagation is increasingly confined in the nickel nanostructure. Therefore at small periodicities on the order of  $h\eta$ , where  $\eta$  is the nanostructure duty cycle  $\eta = L/p$ , the SAW propagation is no longer simply determined by substrate properties – the effect of the nickel must be taken into account. This effect is understood and has been clearly experimentally observed in thin films [103], but had not been observed in nanostructures.

We repeat the measurement of SAW frequency on structures with intermediate linewidths to determine the dispersion of the SAW propagation in the Ni/sapphire structure. The resulting dispersion in SAW frequency is shown in Figure 6.6 plotted against the SAW wavevector  $k = 2\pi/\Lambda_{SAW} = 2\pi/p$  up to  $k = .05$ , corresponding to a periodicity of 125 nm. This period excites a SAW wavelength of 125 nm, where we measured a SAW frequency of  $\nu = 47$  GHz, which is the shortest wavelength and highest-frequency SAW observed (and even time-resolved!) by optical means. For long acoustic

wavelengths (large  $p$ , small  $k$ ), the penetration depth is long, so the nanostructure can be ignored and the SAW velocity is equivalent to the Rayleigh velocity in the sapphire substrate, as shown in Table 6.1. Numerically, this means that measured frequency is in good agreement with  $\nu = v_{Sa}/p$ , shown as the dashed line in Figure 6.6. For shorter acoustic wavelengths (small  $p$ , large  $k$ ), the penetration depth (see top x-axis in Figure 6.6) is decreased and the SAW is increasingly localized in the nickel. The Rayleigh velocity in nickel is approximately half the velocity in sapphire, so confined SAW propagation in the nickel slows the SAW propagation, so the frequency deviates from the sapphire Rayleigh prediction.

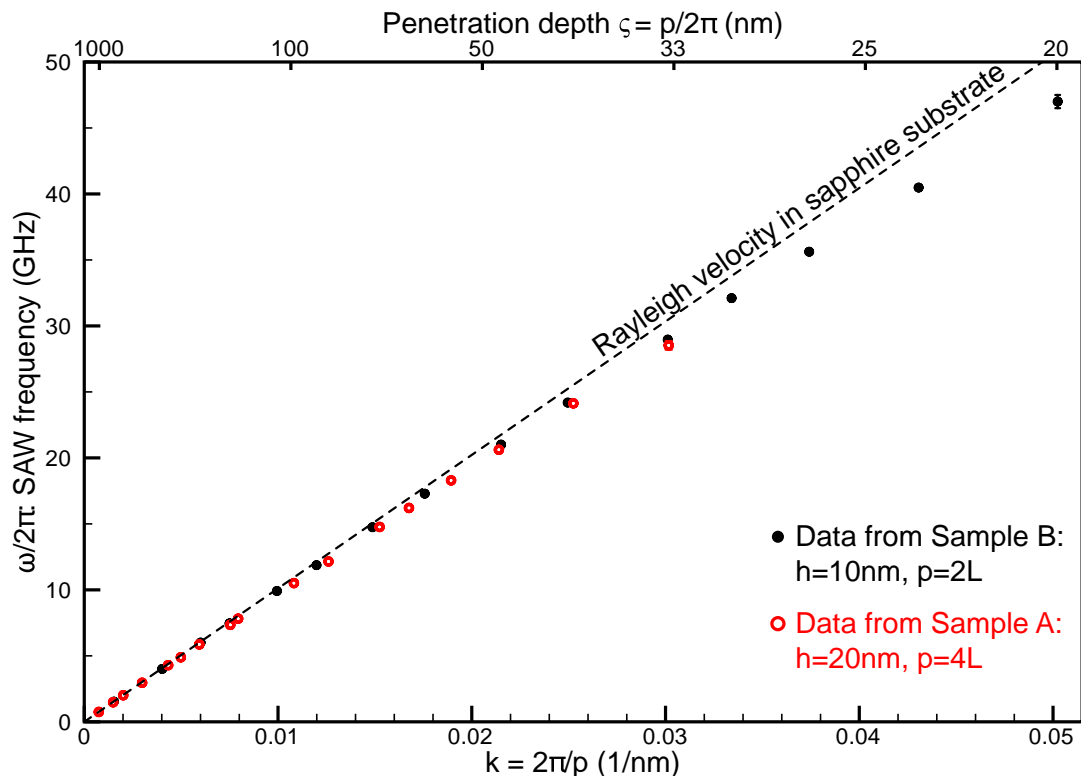


Figure 6.6: Measured surface acoustic wave frequency for propagation in two sets of samples with nanopatterned nickel on sapphire. As the periodicity  $p$  decreases with increasing wavevector ( $k = 2\pi/p$ ), the penetration depth  $\zeta$  decreases and the SAW is increasingly confined in the nickel nanostructure and deviates from substrate-dominated propagation (dashed line). Error bars are plotted for each point, but are only visible for the largest values of  $k$ .

This observation of surface acoustic wave dispersion in a nanostructure is in contrast to previous studies of Al/quartz [107] and Al/Si [108] structures at isolated acoustic wavelengths around  $\Lambda_{SAW} \sim 200$  nm, which didn't observe any deviation from substrate-dominated propagation and suggested that the SAW dispersion is minimal. Since they were dealing with only one or two data points with large error bars in properties of the nanostructure, substrate, and interfaces, it is easy to see how they came to this conclusion, but a comprehensive wavelength-dependence study such as this one is necessary to observe the SAW dispersion.

This effect is seen even more clearly when the data are converted from the measured frequency to SAW velocity by  $v_{SAW} = \nu p$ . The results of this conversion, presented in Figure 6.7, show that the velocity dispersion introduced by the nickel nanostructures is nearly linear over this range of parameters. We present the data in terms of  $hk\eta = 2\pi hL/p^2$  because in terms of this dimensionless parameter, data from the two samples should yield the same dispersive behavior. This is the case except for a small offset between the data from the two different samples, which we attribute to a slight difference in the actual duty cycles or line heights.

### 6.3 SAW dispersion calculation: Modified thin film theory

A quantitative calculation of SAW propagation is complicated by the modified Brillouin zone, stopbands, and multi-mode propagation introduced by the nanostructure [113]. However, to first approximation, an effective mass model from thin film theory can be used. We will discuss two models here: Auld's model based on a perturbative expansion of the stress at the surface [114], and Nelson's model based on the properties of the materials themselves [102, 115]. In order to connect dispersion in a thin film to dispersion in a nanostructure, the thin film theory in each case is slightly modified and compared with the measured dispersion data.

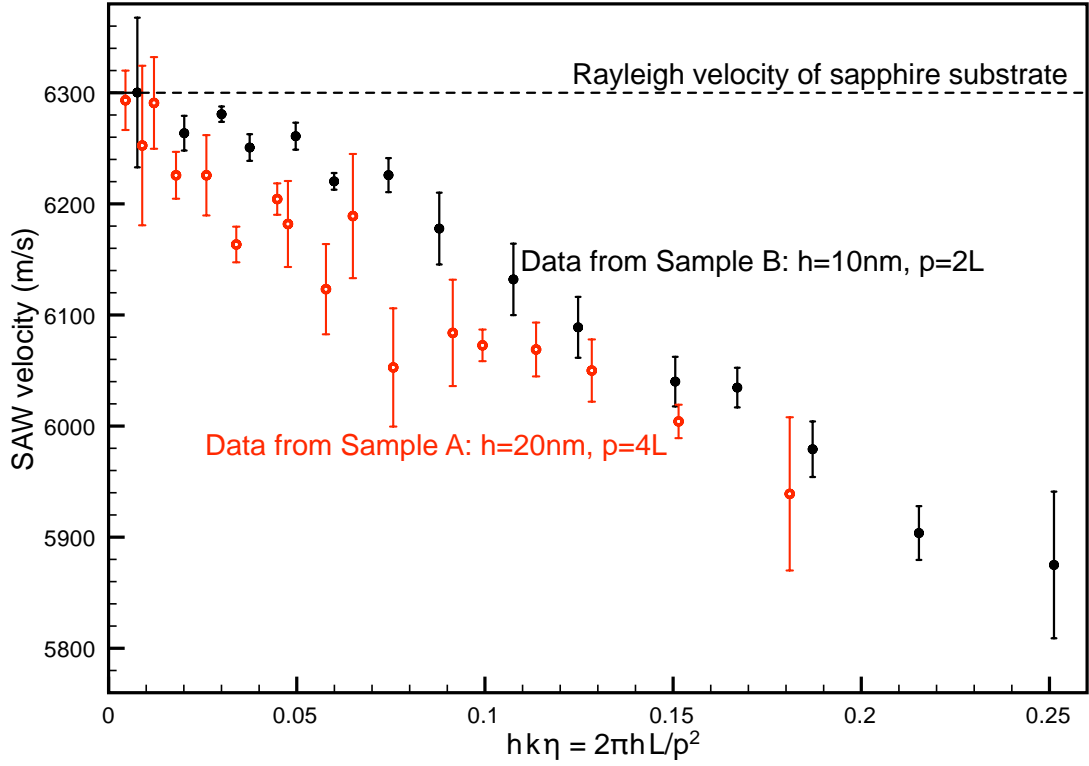


Figure 6.7: Measured surface acoustic wave velocity for propagation in two sets of samples with nanopatterned Ni on sapphire. Significant deviation from the Rayleigh velocity in sapphire is observed for the smaller grating periods, as the SAW propagation is increasingly confined in the nickel nanostructure ( $v_{Ni} \sim 3000$  m/s). The measured velocity dispersion agrees with an effective mass-loading calculation.

### 6.3.1 SAW dispersion due to a thin film: Perturbative Auld model

For very thin films or long acoustic wavelengths, the surface acoustic wave dispersion can be calculated by adding a small perturbation to the substrate value of the SAW velocity [116]. The velocity shift can be determined by calculating the first-order effect of the film on the particle velocity components at the surface. Assuming an isotropic substrate and film, the normalized particle velocity components are [114]

$$\frac{(\nu_{Ry})_{y=0}}{P_R^{1/2}} = \sqrt{\frac{f_y}{\rho_s v_s^2}} \omega \quad \text{and} \quad \frac{(\nu_{Rz})_{y=0}}{P_R^{1/2}} = \sqrt{\frac{f_z}{\rho_s v_s^2}} \omega, \quad (6.4)$$

$v_{R,Sa}$	$v_{t,Sa}$	$v_{\ell,Sa}$	$v_{t,Ni}$	$v_{\ell,Ni}$	$\rho_{Sa}$	$\rho_{Ni}$	$\mu_{Ni}$	$\lambda_{Ni}$
6312	6639	11250	3150	6040	3900	8900	76	130

Table 6.2: Parameter values used in model calculations of the acoustic dispersion from the nickel nanostructures. Units for velocity  $v$  are m/s, densities  $\rho$  are given in kg/m<sup>3</sup>, and shear modulus  $\mu$  and elastic modulus  $\lambda$  are in GPa.

where

$P_R$  = Power flow per unit width along x

$$f_y = \left( \frac{v_s}{v_R} \right)^2 \frac{4\chi^2(1 - (v_R/v_s)^2)^{3/2}}{3\chi - 2\chi(v_R/v_s)^2 - 1}$$

$$f_z = \frac{1}{\chi} f_y$$

$$\chi^2 = \frac{1 - (v_R/v_s)^2(v_s/v_\ell)^2}{1 - (v_R/v_s)^2}.$$

These parameters can then be used in an expression for the frequency-dependent SAW dispersion:

$$\frac{\Delta v_R}{v_R} = -\frac{\Delta \beta_R}{\beta_R} = -\frac{v_R h}{4} \left( \rho_f \left( \frac{|\nu_{Ry}|^2}{P_R} \right) + \left( \rho_f - \frac{4\mu_f}{v_R^2} \frac{\lambda_f + \mu_f}{\lambda_f + 2\mu_f} \right) \left( \frac{|\nu_{Rz}|^2}{P_R} \right) \right)_{y=0}. \quad (6.5)$$

Substituting  $\omega = v_R k = 2\pi v_R / \Lambda_{SAW}$  and inserting values for material properties recorded in Table 6.2, this reduces to a simple expression for the SAW dispersion in a thin film.

One final step is necessary because the case of a nanostructure is quite different from a thin film from even a simple mass loading point of view. Datta and Hunsinger extended thin film theory to nanostructures by introducing a duty cycle factor  $\eta$  ( $\eta = L/p$ )

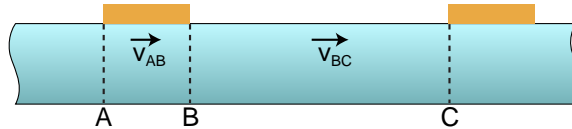


Figure 6.8: Geometry for a simple net velocity calculation. The total velocity from A to C is not given by a weighted sum of the velocities, but must be determined using Equation 6.6

by which the dispersion effect is multiplied [117]. This has been used in all work using a modified thin film theory for dispersion in a nanostructure [105, 107–109, 111, 112], and it is a very intuitive approach since we expect the dispersion to be dependent on the amount of a whole film the nanostructure covers. However, this approach fails to properly explain velocity dispersion: by saying that the nanostructure-induced dispersion is proportional to the area of coverage, the model is saying that velocities in series can be added. We can think of each period of the nanostructure as having two regions with different velocities: a perturbed velocity under the nanostructure, and pure substrate velocity in the gaps, as shown in Figure 6.8. The net surface acoustic velocity  $v_{AC}$  is determined by dividing the total distance travelled from  $A$  to  $C$  by the time it takes to go from  $A$  to  $B$  and  $B$  to  $C$ :

$$v_{AC} = \frac{d_{AB} + d_{BC}}{t_{AB} + t_{BC}} = \frac{d_{AC}}{d_{AB}/v_{AB} + d_{BC}/v_{BC}} \neq \frac{d_{AB} v_{AB} + d_{BC} v_{BC}}{d_{AC}}. \quad (6.6)$$

The expression on the right in Equation 6.6 is the result predicted by Datta and Hunsinger, and it is wrong for all values of  $\eta$  except for zero (nothing on the surface at all) and one (complete film). The dispersion curves using the correct determination of net velocity in the nanostructure from Equation 6.6 are shown in Figure 6.9 along with the linear dispersion predicted by the simple Datta and Hunsinger correction. The correct velocity expressions predict a much stronger dispersion effect that increases with decreasing duty cycle  $\eta$ , as the error of the simple velocity prediction increases. However, this is the opposite effect from the actual, nonlinear dispersion we expect to see — as we will see from the calculation in the next section that goes beyond the perturbation method. The flawed logic of the Datta and Hunsinger method that underpredicts the dispersion is compensated by the overprediction of the perturbation method. Both effects are only seen at values of  $hk\eta > .25$ , putting them outside the reach of current experiments.

In making comparisons to our measured data, we use the (admittedly flawed)

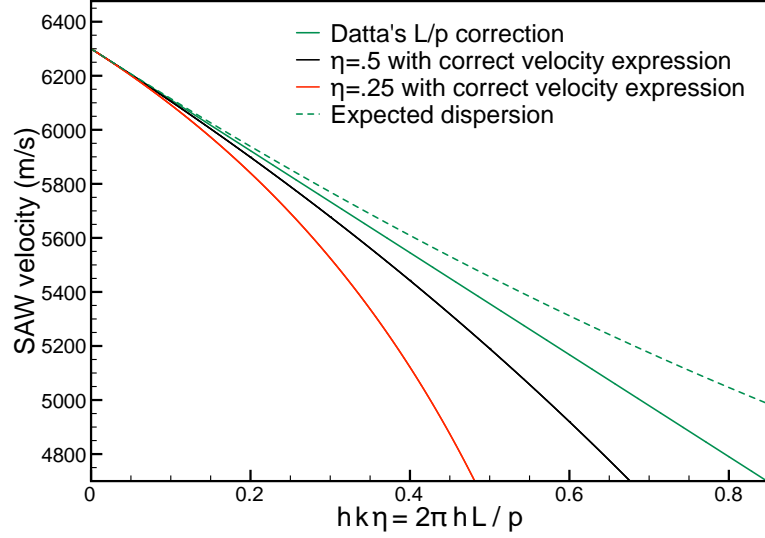


Figure 6.9: Surface acoustic wave velocity dispersion calculated using Auld’s perturbation method and (green) a simple duty-cycle scaling and (red and black) geometrically-honest velocity mapping for conversion from a thin film to a nanostructured case. The expected dispersion is shown as the dashed green line; even though the simple method is incorrect, it is closer to the expected results at large values of  $hk\eta$ , and is used here.

Datta and Hunsinger method for converting a thin film dispersion to the case of a nanostructure by a simple duty cycle factor  $\eta$ . Significantly for this experiment, the linear dependence on  $h\eta$  means that it predicts identical dispersion for our two samples since the ratio  $hk\eta$  is constant between  $(10 \text{ nm} \times .5k)$  and  $(20 \text{ nm} \times .25k)$ . In these nondimensional units, the dispersive change in velocity is given by  $\Delta v_R = -1887(hk\eta)$ , so the total velocity is

$$v_R = v_{R,Sa} - 1887(hk\eta), \quad (6.7)$$

and this linear dispersion is shown as the solid green line in Figures 6.9 and 6.11.

### 6.3.2 SAW dispersion due to a thin film: Nelson model

In reference [115], Duggal et. al laid out the framework for a rigorous calculation of the acoustic mode dispersion introduced by a thin film overlay on a substrate. They were concerned with the transient grating excitation geometry, which they referred to

as "ISTS" (Impulsive stimulated thermal scattering). While their detailed calculations of displacements and stresses were geometry-specific, the mode dispersion analysis was general: true regardless of the excitation scheme. This allows us to apply their conclusions to our nanostructure excitation geometry. In his thesis, Tobey goes through a similar analysis without assuming a particular excitation geometry and arrives at the same equations [55].

$$C = \begin{bmatrix} (1+s^2)e^{-nkh} & (1+s^2)e^{nkh} & 2ise^{-skh} & -2ise^{skh} & 0 & 0 \\ 2ine^{-nkh} & -2ine^{nkh} & -(1+s^2)e^{-skh} & -(1+s^2)e^{skh} & 0 & 0 \\ 1+s^2 & 1+s^2 & 2is & -2is & -(1+r^2)g & 2irg \\ 2in & -2in & -(1+s^2) & -(1+s^2) & 2img & (1+r^2)g \\ -1 & -1 & -is & is & 1 & -ir \\ in & -in & -1 & -1 & im & 1 \end{bmatrix}$$

with the following definitions:

$$\begin{aligned} n &= \sqrt{1 - (v^2/v_{Lf}^2)}, \\ s &= \sqrt{1 - (v^2/v_{Tf}^2)}, \\ m &= \sqrt{1 - (v^2/v_{Ls}^2)}, \\ r &= \sqrt{1 - (v^2/v_{Ts}^2)}, \\ g &= \rho_s v_{Ts}^2 / \rho_f v_{Tf}^2, \end{aligned}$$

where  $v_{Ls}$  and  $v_{Lf}$  are the longitudinal acoustic velocities in the substrate and film, and  $v_{Ts}$  and  $v_{Tf}$  are the transverse acoustic velocities in the substrate and film (values used for a nickel film and a sapphire substrate are given in Table 6.2). The dispersed mode velocity  $v$  for given wavenumber  $k$  can be determined by setting the determinant of the matrix  $C$  to zero:

$$\det(C) = 0. \tag{6.8}$$

The complete dispersion curve can be calculated by repeatedly solving Eqn. 6.8 over the desired range of  $k$  values. For a given value of  $k$ , there can be many solutions, and each corresponds to a SAW mode. Numerical solutions are dangerous because they may fall into false solutions or switch between nodes without notifying the user. A safer method that shows all of the modes is to graphically solve the determinant: plot the value of  $\det(C)$  as a function of  $v$  and look for zeros. This method is demonstrated in Figure 6.10 for a 10 nm nickel film on sapphire with  $k=0.025/\text{nm}$ , so  $\Lambda_{SAW} = 250$  nm. The zero-crossings give the solutions to Equation 6.8, and so are viable SAW modes: the mode at  $\sim 5680$  m/s is the Rayleigh mode altered by the presence of the nickel film, while the faster mode  $\sim 6030$  m/s is a higher-order (Sezawa) mode [115].

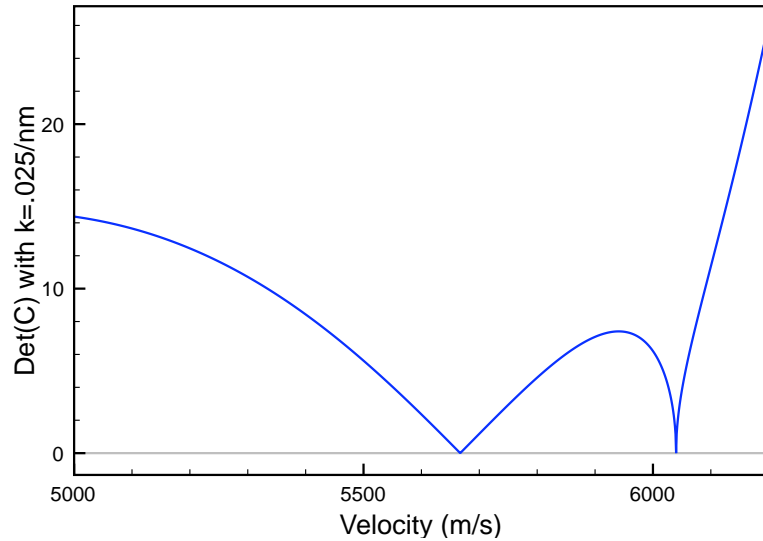


Figure 6.10: Plot of  $\det(C)$  for determining SAW modes: locations where the curve touches zero are valid SAW modes by Equation 6.8. Parameters used are  $k=0.025/\text{nm}$  ( $\Lambda_{SAW} = 250$  nm),  $h=10$  nm thick nickel film on sapphire.

Modifying the results of this calculation to account for the nanostructure is not as simple as in the previous model because this model gives the predicted velocity rather than the change in the velocity. This can be dealt with by subtracting the Rayleigh velocity for sapphire ( $v_{SAW}$  for  $k = 0$ ), then applying the correction factor  $\eta$ , and finally adding back the subtracted baseline velocity. Numerically, this means

that  $v_{SAW, film}(k)$  obtained from the model for thin film dispersion can be converted to  $v_{SAW, nanostructure}(k)$  for the velocity dispersion due to the nanostructure by

$$v_{SAW, nanostructure}(k) = (v_{SAW, film}(k) - v_{SAW}(k = 0))\eta + v_{SAW}(k = 0). \quad (6.9)$$

### 6.3.3 Comparing models to the data

The results of each model are plotted in Figure 6.11 along with the measured velocity dispersion data, and the match to the data seems to be quite good overall. The rms error values for the Auld perturbative model and the Nelson model for  $h = 20$  nm are very similar, indicating that in this range of  $hk\eta$ , either model can be used. However, at larger values of  $hk\eta$  (further along the x-axis, as shown in the inset to Figure 6.11), the models strongly diverge:

- The Nelson model predicts a dispersion limit determined by the velocities of the substrate and the nanostructure and the duty cycle  $\eta$ , which is reasonable because the dispersion of the nickel is only in effect where there is nickel, and not in the gaps:

$$v_{dispersive\ limit} = \frac{v_{Ni} v_{Sa}}{\eta v_{Sa} + (1 - \eta)v_{Ni}}, \quad (6.10)$$

where each velocity is the surface acoustic wave velocity. This leads to dramatically different dispersive limits for the  $\eta = 25\%$  and  $\eta = 50\%$  samples.

- The linear dependence on  $hk\eta$  in the Auld calculation is insensitive to velocity limits, even predicting a SAW velocity lower than  $v_{SAW, Ni}$  when  $hk\eta > 1.65$ . The model works well for values of  $hk\eta$  up to 0.25 studied here, but for larger values or smaller duty cycles (where the minimum velocity limit is higher), the model gives nonphysical predictions.

## 6.4 Conclusion

We used ultrafast, coherent, EUV beams to measure high frequency surface acoustic wave propagation in nanostructures at frequencies up to  $\sim 50$  GHz, the highest observed using optical detection. Such a high frequency corresponds to SAWs with a penetration depth  $\sim 20$  nm,  $6 \times$  lower than is possible using the state-of-the-art in optical transient grating methods. The shorter penetration depth realized in our technique allows new high-selectivity studies of the properties of interfaces beneath thin films with 10-100 nm thickness.

By repeating the measurements on nanostructures with different periods, we measured the SAW dispersion in the nanostructured system and confirmed the validity of two models modified from their original use in thin film theory. These dispersion measurements are a critical step in the advancement of this technique: by understanding the influence of the nanostructure on the SAW propagation, we can isolate it in and remove it from future measurements in order to precisely measure the properties of layers and interfaces below the nanostructure. This technique of visible laser excitation and EUV probing can easily be extended to even shorter wavelengths (higher frequencies), limited only by nanopatterning capabilities. Thus, it holds promise for studying materials and interface properties of extremely thin films.

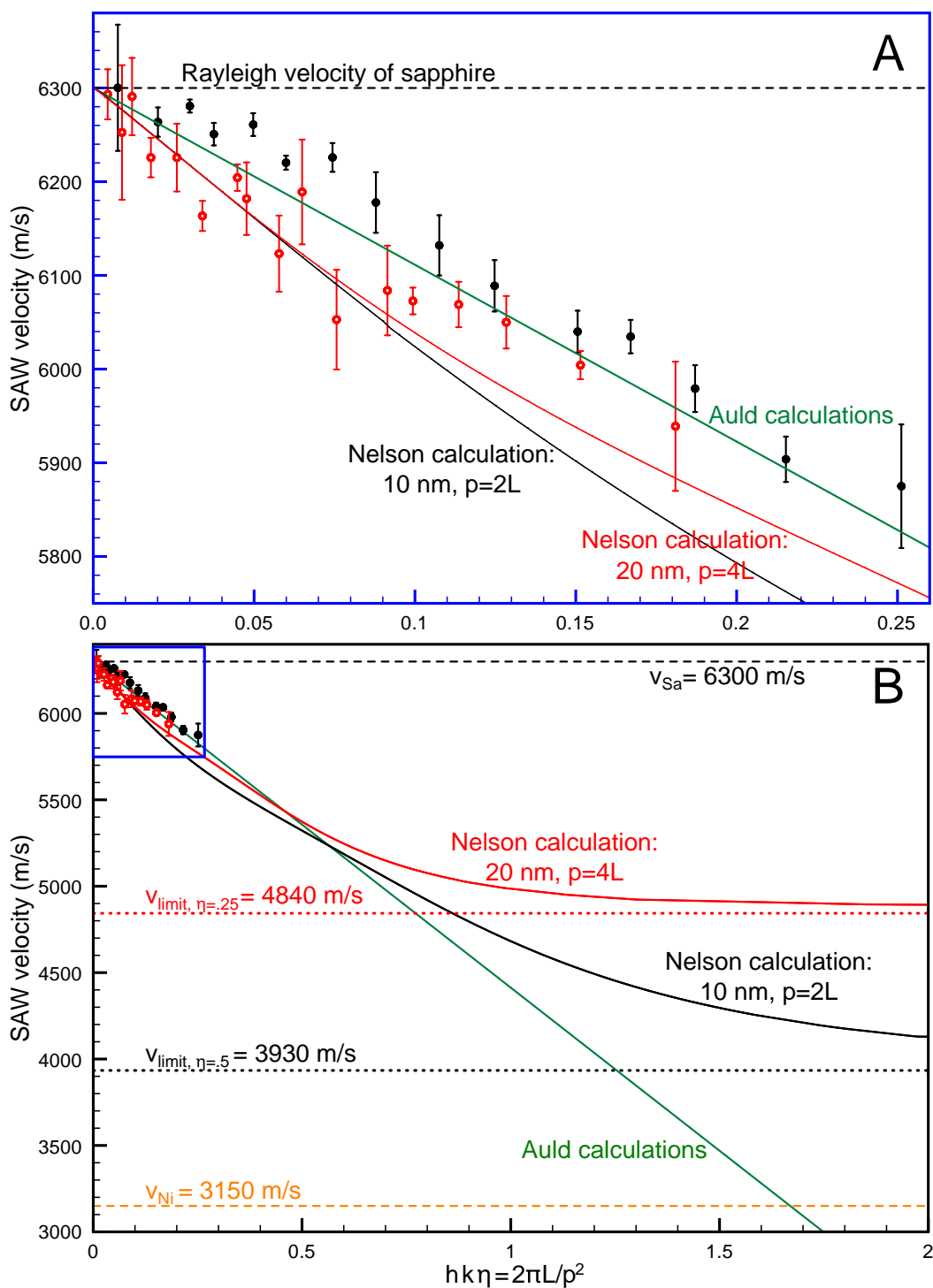


Figure 6.11: Measured velocity dispersion along with predictions from two models of SAW dispersion: a perturbation model discussed in section 6.3.1 that was proposed by Auld [114], and a detailed stress/strain model discussed in section 6.3.2 proposed by Nelson [115]. (A) shows that Auld's perturbation method fits the data better over the range of  $hk\eta$  measured in this experiment. (B) shows the calculated dispersion over a larger range of  $hk\eta$  and demonstrates the expected breakdown of the perturbative (Auld) model for  $hk\eta > .5$ . The blue box indicates the range in viewed in part (A).

## Chapter 7

### Quasi-ballistic heat transport from nanoscale interfaces

As nanofabrication techniques continue to improve and smaller structures can be manufactured for finer control of electronic, optical, mechanical and thermal properties, there is an ever-greater need to understand the fundamentals of heat transfer in such nanostructures. Of particular importance is the rapid progress in the microelectronics industry, where transistors with 45 nm gate widths are now in production and 32 nm gates are right around the corner [118]. A fundamental and quantitatively-accurate understanding of how heat flows away from a nanoscale heat source – the nanoscale “heat sink” problem – is critical for future advances in nanotechnology because the thermal energy generated in the operation of these devices must be dissipated.

For time scales shorter than the energy relaxation time and length scales smaller

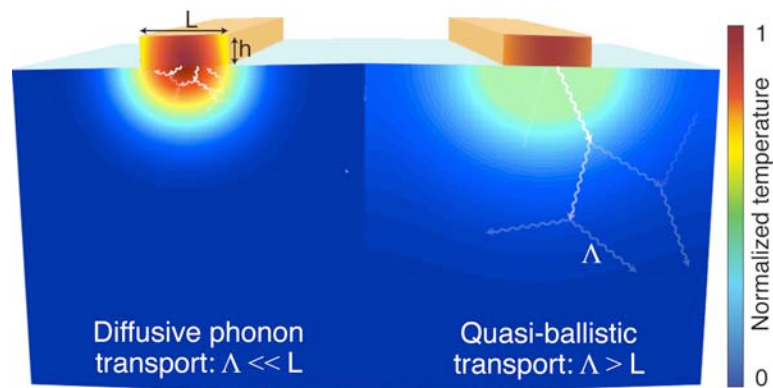


Figure 7.1: Schematic thermal images illustrating the difference between diffusive and quasi-ballistic transport for heat dissipation from a nanostructure into a substrate.

than the mean free path of energy carriers (for example, the phonon mean free path  $\Lambda$  is  $\sim 250$  nm in silicon), heat flow can deviate significantly from the Fourier conduction law  $q = -k\nabla T$ , the governing equation of diffusive thermal transport that predicts smooth temperature gradients [19, 119]. When the device size is much larger than the phonon mean free path  $\Lambda$ , heat flow is diffusive and at length scales significantly smaller than  $\Lambda$ , the transport away from the interface is ballistic (Figure 7.1). When the length scale of a device is on the same order as  $\Lambda$ , we will describe the heat transfer as quasi-ballistic.

In this chapter, we discuss the theoretical and experimental background of this transition from diffusive to ballistic thermal transport within nanostructures. Then we consider the important case of transport away from a confined heat source defined by a nanostructure coupled to a bulk substrate. This includes background, basic theory, and the first experimental observation and quantitative, time-resolved measurement of quasi-ballistic thermal transport away from a nanostructure [120].

## 7.1 Ballistic thermal transfer in and through a nanostructure

Before discussing the distinctives of heat transport away from a heated nanostructure hot spot, we will first consider the better-understood case of heat transport in or through a nanostructure. The different transport regimes in a nanostructure are illustrated in Figure 7.2, which schematically depicts temperature distributions in a

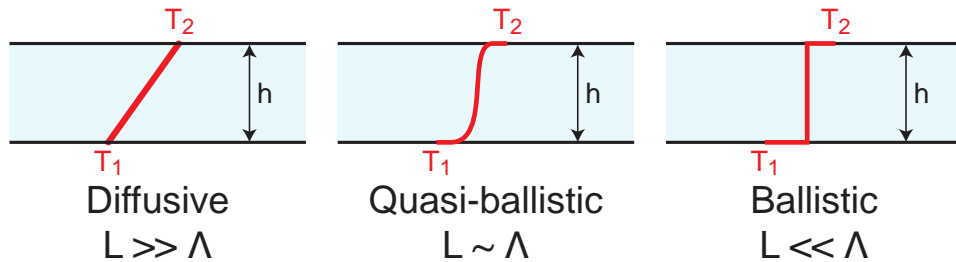


Figure 7.2: Schematic illustration of steady-state temperature distributions in the diffusive, quasi-ballistic, and ballistic transport regimes in a 1-dimensional slab of thickness  $h$ . Modified from [121].

1-dimensional slab in the diffusive, quasi-ballistic, and ballistic cases. The thermal conductivity will be affected by the nanostructure, as has been demonstrated by both basic and advanced theory, numerical simulation, and experiment.

### 7.1.1 The Boltzmann transport equation for transport in a nanostructure

When the length scale of a system is much larger than the mean free path of the energy carriers, the transport can be well-described by the Fourier law derived in section 2.3 and the transport is diffusive, i.e. dominated by multiple scattering events between energy carriers and characterized by local thermal equilibria existing throughout the system. In the opposite limit, when the length scale is much smaller than the mean free path, the energy flux can be described by the Stefan-Boltzmann law  $q = \sigma T^4$  where  $\sigma$  is the Stefan-Boltzmann constant defined in Equation 7.11, and the transport is radiative, i.e. dominated by the interfaces since carriers travel directly from interface to interface without scattering. In the transition region where the length scale of the system is on the order of the mean free path, a determination of the flux requires the solution of the time-dependent Boltzmann transport equation (BTE):

$$\frac{\partial f}{\partial t} + \vec{v} \cdot \vec{\nabla}_r f + \vec{F} \cdot \vec{\nabla}_p f = \left. \frac{\partial f}{\partial t} \right|_{collision} + s, \quad (7.1)$$

where  $f$  is the time and space-dependent carrier distribution,  $\vec{p}$  is the momentum coordinate,  $\vec{r}$  is the position coordinate,  $\vec{F}$  is an applied force, and  $s$  is a source term. The collision term is given by the matrix element

$$\langle f(\vec{p}') | S(\vec{p}', \vec{p}) | f(\vec{p}) \rangle, \quad (7.2)$$

where  $S(\vec{p}', \vec{p})$  is the scattering probability. The collision term can be converted to a set of integrals over each momentum dimension. So all together, the BTE is a seven-dimensional integro-differential equation. Approximations can be applied to reduce the complexity of the BTE, but a full analytical solution is impractical for physical systems.

Numerous numerical methods of determining energy transport in nanostructured systems have been developed [122], including Monte Carlo [123] and molecular dynamics simulations [124], and a numerical solution of the BTE using a discretize lattice [125–127]. Chen proposed a simplification in which the BTE is split into ballistic and diffusive terms (called “ballistic diffusive equations”, or BDE) describing the thermal transport [128, 129]. An alternative simplification (called the “equation of phonon radiative transfer”, or EPRT) was proposed by Majumdar [121, 130], which yields slightly different results than the BDE [131].

### 7.1.2 Basic theory of quasi-ballistic thermal transfer in a nanostructure

By considering a basic model for thermal conductivity based on the Fourier heat conduction law (Equation 2.8) derived in Chapter 2, we can gain insight into a few basic questions regarding ballistic phonon transport effects in nanostructures:

- Why do we expect to see ballistic thermal transport in a nanostructure?
- At what length scale do we expect to see ballistic effects?
- How will ballistic transport affect the thermal conductivity?

In the Fourier law for diffusive transport, the constant of proportionality connecting the temperature gradient to the flux is the conductivity  $k = Cv\Lambda/3$  (Equation 2.9). This expression uses the Debye approximation, which assumes that all of the phonons can be lumped together with a single velocity (given by the  $k \rightarrow 0$  limit of the acoustic velocity) and specific heat. The thermal conductivity of a bulk material can then be determined if the average phonon mean free path is known, or, as is more commonly the case, a mean free path can be determined from a known thermal conductivity. This was the standard method for determining the phonon mean free path until the recent observation that the phonon dispersion can have a significant effect on the results [132]. The

example of sapphire at room temperature will demonstrate just how bad this approximation is for real materials. Using textbook parameters  $C_{Sa} = .7788 \text{ J/gK}$ ,  $\rho_{Sa} = 4 \text{ g/cm}^3$ ,  $v_{l,Sa} = 11250 \text{ m/s}$ , and  $k_{Sa} = 46 \text{ W/mK}$ , the mean free path from  $k = Cv\Lambda/3$  is  $\Lambda_{Sa} = 3.9 \text{ nm}$ . Because this model assumes that *all* phonons have the acoustic velocity, which is the highest phonon velocity in the material, the mean free path of the phonons that actually carry heat is significantly under-estimated. Numerical calculations taking the phonon dispersion into account predict  $\Lambda_{Sa} \sim 100 - 150 \text{ nm}$  for heat-carrying (acoustic) phonons.

In a crystalline material, the phonon mean free path is dominated by different effects depending on the temperature, with a typical temperature dependence shown in Figure 7.3. For temperatures within an order of magnitude of the Debye temperature ( $T_{Debye,Sa} \sim 900 \text{ K}$ ), the phonon mean free path is dominated by phonon-phonon scattering outside of the Brillouin zone. This is known as Umklapp scattering and gives rise to a phonon with opposite momentum [5]. Umklapp scattering increases as the phonon temperature increases (nearer  $T_{Debye}$ ) because higher-energy phonons are thermally excited, making outside-the-Brillouin-zone scattering more likely, so the mean free path decreases in this temperature region ( $\Lambda \propto 1/T$ ). As the temperature is decreased, phonons travel much further between scattering events and begin to scatter off of defects and impurities in the sample. If the temperature is further decreased and approaches absolute zero, the phonon mean free path is determined by the dimensions of the material: phonons travel ballistically from interface to interface without scattering in-between. The mean free path is limited by the interface scattering, so this sample dimension sets an absolute limit:  $\Lambda < L$ , where  $L$  is the structure size.

Combining this information about the phonon mean free path with the fact that the thermal conductivity is directly proportional to  $\Lambda$ , it is then easy to see how the thermal conductivity is determined by the nanostructure size. As the nanostructure dimension is decreased below the phonon mean free path, the thermal conductivity

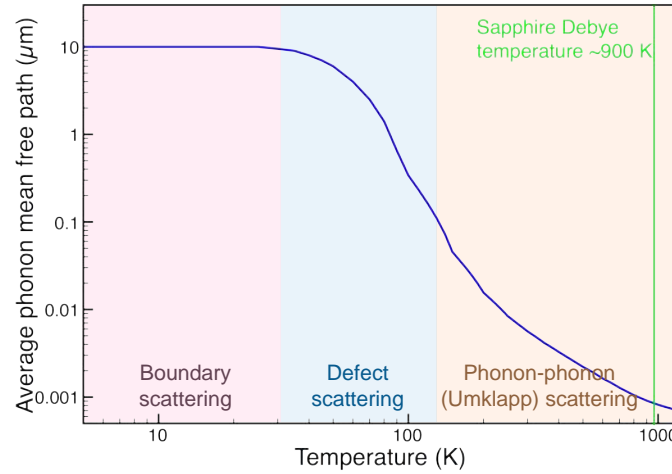


Figure 7.3: Temperature dependence of the phonon mean free path  $\Lambda$  for sapphire (from  $k$  and  $C$  and the Debye model).  $\Lambda$  is determined by Umklapp phonon-phonon scattering at high temperature (orange), defect and impurity scattering at somewhat lower temperature (blue), and sample size near zero temperature (pink). The mean free path is shown here for a 10  $\mu\text{m}$ -thick slab of sapphire.

should decrease in direct proportion to the dimension of the structure. This is illustrated in Figure 7.4, where the low-temperature thermal conductivity is decreased by two orders of magnitude when the sample size is decreased from 10  $\mu\text{m}$  to 100 nm. The phonon mean free path is constant at low temperature, so the thermal conductivity is directly proportional to the specific heat  $C$  in the ballistic case. Also, the temperature at which the thermal conductivity peaks is shifted higher for a smaller structure – compare dark and light green curves on Figure 7.4).

### 7.1.3 Experimental observations of ballistic transport in nanostructures

The transition from diffusive to ballistic transport regimes has been studied aggressively for the past ten years, with numerous experimental observations of non-Fourier heat transport across and through nanostructures in different geometries. Early experiments observed ballistic thermal transport in a thin film (see Figure 7.5) and a series of thin films (superlattice) [19, 119, 133–135]. Recent experiments have demonstrated reduced thermal conductivity of nanowires [136, 137], nanocomposites [138, 139],

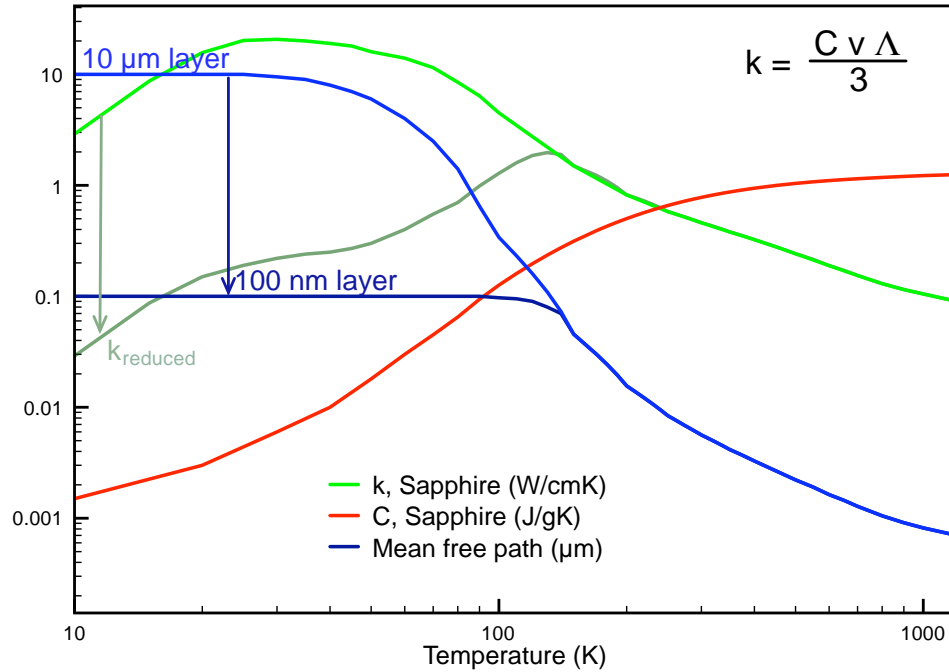


Figure 7.4: Thermal conductivity  $k$ , specific heat  $C$ , and phonon mean free path  $\Lambda$  of sapphire, related by  $k = Cv\Lambda/3$ . As the sapphire thickness is reduced,  $\Lambda$  is also decreased, which causes a reduction in the thermal conductivity.

molecular chains [140] and multi-walled carbon nanotubes [?, 141]. Theoretical work has also predicted quantized thermal transport in single-walled carbon nanotubes [142].

Current experiments are driven in large part by potential application to thermoelectric energy conversion (TEC) [145–147]. For TEC devices to function efficiently, a temperature difference must be maintained while a current is generated, so a material with high electrical conductivity and low thermal conductivity is required. Introducing multiple interfaces to reduce the thermal conductivity is one route that shows promise, although interfaces inhibiting thermal flow also affect electrical transport, so engineered geometries and surfaces are required [139]. Silicon nanowires are particularly interesting because they can be made so narrow as to force the phonon transport beyond ballistic into a quantum regime (restricted not by phonon mean free path, but by phonon wavelength), while retaining a relatively high electrical conductivity [136, 137, 148].

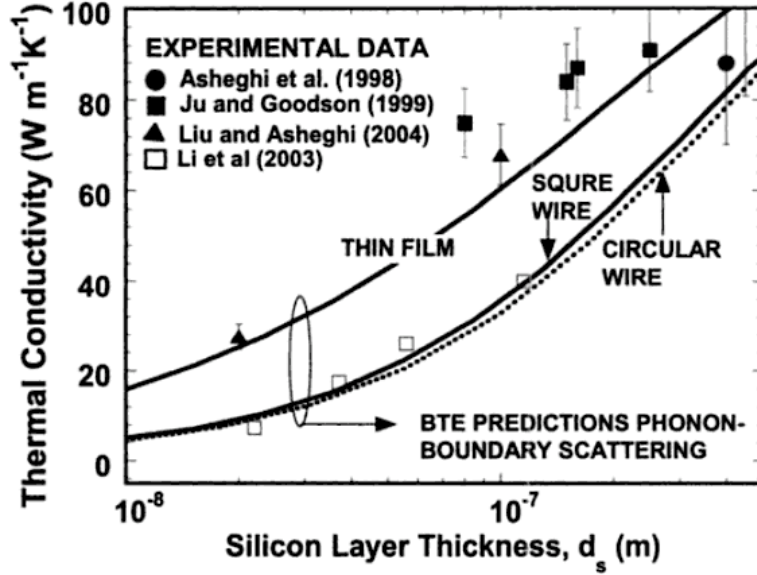


Figure 7.5: Thermal conductivity of silicon as a function of film thickness or wire diameter. Figure from [19], and data in the figure are from [134, 136, 143, 144].

## 7.2 Quasi-ballistic thermal transport at an interface

As described in the previous section, a number of past experiments have studied non-diffusive thermal transport in nanostructured systems. However, despite its direct relevance to the practical issue of thermal management in nanoelectronics [149], nano-enabled energy systems [10, 11], nanomanufacturing [150], and nanomedicine [13], the nanoscale heat sink problem (i.e. heat transfer from a nanoscale heat source into its bulk surroundings) has received much less attention. Here, we are concerned not with energy flow *within* a nanostructure, but the efficient coupling of thermal energy *out* of the structure and into the substrate. When heat flows from a hotspot with a dimension  $L$  that is smaller than the mean free path of phonons in the heat sink  $\Lambda$ , energy-carrying phonons travel ballistically away from the source for a significant distance before experiencing collisions. In the Fourier picture, heat flow is assumed to be diffusive, with the thermal flux  $q$  determined by the temperature gradient ( $q = -k\nabla T$ , where  $k$  is thermal conductivity). When there is a significant energy density change over a distance

less than the phonon mean free path, as is the case for heat flow away from a small source, there is no local phonon equilibrium near the source and therefore temperature cannot be defined, as illustrated in Figure 7.1. Under these circumstances, the Fourier law, which assumes sufficient scattering events to obtain local thermal equilibrium, overestimates the thermal transport [151–153].

Numerical simulations using the BDE [154], EPRT [155], and discrete BTE methods [156] have demonstrated the error in the Fourier law for dissipation of thermal energy from a heat source smaller than the phonon mean free path in the heat-sinking material. However, there is no agreement as to the strength or exact dependence of this effect on temperature and structure size.

### 7.2.1 Thermal boundary resistance across a bulk-constricted interface

In practice, there often exists an interface between a small heated region and the heat-sink substrate, and this interface thermal resistance must also be taken into account. Measurements of the interface thermal resistance can be performed for structures at bulk length scales and in thin films using time-resolved optical pump-probe methods such as transient thermoreflectance (TTR) measurements [133, 157]. The interface resistance between two materials in contact is called thermal boundary resistance (TBR).

There is some confusion in the literature regarding how to describe ballistic thermal transport away from an interface. It is important to distinguish this ballistic interface effect from the thermal boundary resistance and spreading resistance that are used to characterize interfaces in the bulk approximation, valid when the interface contact size is much larger than the phonon mean free path of the heat sink. In that bulk/Fourier case, the total effective resistance is given by a sum of these two and the Fourier resistance of the substrate slab:

$$R_{Interface} = R_{TBR} + R_{Spreading} + R_{Fourier}. \quad (7.3)$$

As described in section 2.4.1,  $R_{TBR}$  describes the interfacial phonon resistance [22]. It has been (misleadingly) called the ballistic component of the boundary resistance. However, it has no dependence on the phonon mean free path and instead scales with the Biot number [158] (see Equation 7.16), which measures the prevalence of surface vs bulk resistance.

Spreading resistance is also a bulk concept, which accounts for thermal resistance due to heat diffusion into the substrate (along with  $R_{Fourier}$  from section 2.4.2 that accounts for diffusion in a slab). It is a means to express the geometrical thermal spreading in the substrate in terms of a single resistance that can be applied in series with other resistivities to heat flow, as discussed in section 2.4.3. It is commonly used in thermal engineering as a way to estimate the resistance to thermal flows after passing through a constriction, e.g. heat flow from a transistor, through a film, and into a substrate. It has been analytically calculated for a number of different geometries [159], and for the infinite strip we are concerned with here, it is related to the ratio  $\epsilon$  of the contact size  $L$  to the structure repeat distance by [160]

$$R_{spreading} = \frac{1}{\pi^3 \epsilon^2 k_s} \sum_{n=1}^{\infty} \frac{\sin^2(n\pi\epsilon)}{n^3}. \quad (7.4)$$

In the case of our samples with nickel nanostructures of width  $L$  and fixed periodicity  $4L$  on sapphire,  $\epsilon = .25$  and  $R_{spreading} = .00202$  Km/W, which is in units of resistance per length since it assumes an infinite contact in one dimension. Spreading resistance will be neglected in our final analysis because we calculate the thermal diffusion in the substrate directly from the heat equation. However, it is important to distinguish between diffusive spreading effects and ballistic effects, and the concept of spreading resistance does motivate the assumption we will make later: the ballistic effect due to transport surrounding a nanoscale heat source can be accounted for by including an additional resistance to energy flow at the boundary between the heat source and its surroundings (heat sink).

Some models claim to show that the boundary resistance goes up as the structure size is decreased, but in these models [158], the effect is due only to geometric scaling of the system (for example, from Equation 7.4,  $\lim_{\epsilon \rightarrow 0} R_{spreading} = \infty$ ) — similar to the electrical resistance of a wire increasing with decreasing diameter. This is obviously not a truly ballistic effect because it has no dependence on the phonon mean free path and further, it can be predicted by the Fourier law! In order to avoid this confusion, we discuss non-diffusive heat transport in terms of the intensive parameter resistivity  $r$ , which is independent of linewidth in the bulk approximation for a single line (the case of  $\epsilon \rightarrow 0$ ). In the case studied here where  $\epsilon$  is constant for all nanostructured samples,  $R_{spreading}$  is a constant and so  $r_{spreading}$  is proportional to  $L$ , as is  $r_{Fourier}$ . The ballistic effect would then be manifest as an additional component  $r_{BC}$  in the boundary resistivity, so the total resistivity lumped into an interface effect is given by

$$r_{Interface} = r_{TBR} + r_{Spreading} + r_{Fourier} + r_{BC}. \quad (7.5)$$

### 7.2.2 Simple analytical prediction: ballistic-diffusive model

Gang Chen made the first prediction of this ballistic effect near a nanoscale heat source in 1996 [161]. He considered the heat transfer between concentric spheres (with the outer sphere having an infinite radius) in the limits of purely radiative/ballistic and purely diffusive/bulk transport. He assumed that the component predicting a lower heat flux would constrain the transport to that value. Chen found that when the heated inner sphere was larger than the phonon mean free path of the material between the spheres, many scattering events occurred and thermal diffusion was the dominant transport mechanism. However, when the inner sphere was small compared with  $\Lambda$ , scattering events were greatly reduced and the heat transport could be considered to be radiative, so the ballistic component dominated.

The net heat flux is easier thought of in terms of resistivity (as discussed above, where  $r = \Delta T/q$ ), where the total resistivity is simply the sum of the Fourier and

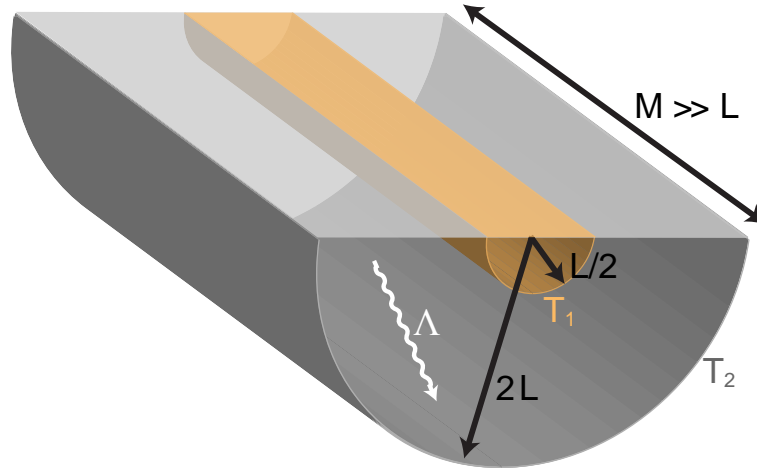


Figure 7.6: Geometry for simple analytic model to demonstrate the transition from diffusive to ballistic thermal transport away from a nanoscale heated strip of width  $L$ . For simplicity in cylindrical coordinates, the nickel strip is modeled as a cylinder of diameter  $L/2$ , and the outer bounding cylinder has a diameter of  $2L$ ,  $4\times$  greater than the inner diameter as in the experiment. The transport is determined in both the ballistic and diffusive regimes.

ballistic components, which will automatically provide the correct limits to the heat flux. In this case, the Fourier law under-predicts the resistivity at length scales shorter than the mean free path, and ballistic transport over-predicts the resistivity in the bulk.

Of course, our system of nanoscale lines on a substrate is not obviously connected to the worked example of concentric spheres. Our system does have something close to cylindrical geometry, so we modified the calculation to get results directly related to our situation. The simplified geometry used in this calculation is summarized in Figure 7.6, where the line contact of width  $L$  is treated as an embedded half-cylinder of diameter  $L$ . This is the heated surface, which is analogous to the inner sphere in Chen's calculation. The outer surface is a half-cylinder in the substrate with a diameter of  $4L$ , which is determined by the line separation. The entire sample can be considered by lining up a series of these half-cylinder shells edge-to-edge, and we will assume that they are non-interacting so that the heat transport of the entire sample can be understood by considering a single unit half-cylinder. Of course, neighboring half-cylinder units

do interact, but periodic boundary conditions are equivalent to insulating boundary conditions.

We will first consider the diffusive transport between the half-cylinders. In the Fourier equation, the heat flux is determined by the temperature gradient:  $\vec{q} = -k\vec{\nabla}T$ . In this cylindrical geometry, the gradient operator is

$$\vec{\nabla} = \frac{\partial}{\partial r}\hat{r} + \frac{1}{r}\frac{\partial}{\partial\theta}\hat{\theta} + \frac{\partial}{\partial z}\hat{z}, \quad (7.6)$$

where  $\theta$  is the angle about the axis of the cylinder and  $z$  is along the direction of  $M$ , the length of the nano-lines. We assume that the heat will diffuse radially from the inner cylinder and the length of these lines is much greater than the diameter ( $M \gg L$ ), so we can neglect the  $\hat{\theta}$  and  $\hat{z}$  components of the derivative. The Fourier expression then reduces to  $\vec{q} = -kdT/dr\hat{r}$ . The heat flux  $q$  is given by the total heat  $Q$  divided by the area over which the heat flows, which is  $A = \pi rM$  for a half-cylinder. Plugging this in to the radial Fourier law and regrouping terms, we obtain

$$Q\frac{dr}{r} = -\pi MkdT. \quad (7.7)$$

Integrating both sides from  $r_1 = L/2$  to  $r_2 = 2L$ , we get an expression for the total heat flow between the half-cylinders

$$Q = \frac{2\pi Mk(T_1 - T_2)}{\log(r_2/r_1)}. \quad (7.8)$$

Now we can plug in the high-temperature Debye law approximation,  $k = Cv\Lambda/3$  and divide the area back out to get the flux between the half-cylinders

$$q_{Fourier} = \frac{2Cv\Lambda(T_1 - T_2)}{3\log(4)L/2}. \quad (7.9)$$

Finally, we convert to resistivity

$$r_{Fourier} = \frac{\Delta T}{q_{Fourier}} = \frac{3\log(4)L}{4Cv\Lambda}. \quad (7.10)$$

In calculating the ballistic thermal transport, we start with the Stefan-Boltzmann law  $q = \sigma T^4$ .  $\sigma$  is the Stefan-Boltzmann constant, derived from other fundamental constants including the Boltzmann constant  $k_B$ :

$$\sigma = \frac{2\pi^5 k_B^4}{15c^2 h^3} = 5.67 \times 10^{-8} \text{ J s}^{-1} \text{ m}^{-2} \text{ K}^{-4}. \quad (7.11)$$

The radiation flux between concentric cylinders is given by [162, 163]

$$q = \frac{\sigma(T_1^4 - T_2^4)}{1/\epsilon_1 + (1/\epsilon_2 - 1)A_1/A_2}, \quad (7.12)$$

where  $\epsilon_{1,2}$  are the spectral emissivities of the inside and outside cylinder, respectively. If we assume that both surfaces are blackbody radiators,  $\epsilon_{1,2} = 1$ , then the denominator of Equation 7.12 is 1. The numerator can be simplified by applying  $\sigma T^4 = CvT$ . Finally, the temperature rise at the interface is also changed because we assume that there are no reflections at the interface, therefore the inner surface temperature  $T_1$  is the average of the emitted phonon temperature from  $A_1$  and the phonons arriving from the outer surface  $A_2$ :  $T_1 \rightarrow (T_1 + T_2)/2$  [151]. This results in an extra factor of two, giving us an expression for flux in the ballistic case, which can be simply converted to resistivity,

$$r_{Ballistic} = \frac{\Delta T}{q_{Ballistic}} = \frac{1}{2Cv}. \quad (7.13)$$

The ballistic resistivity is independent of  $L$ , so we normalize both the ballistic and the Fourier resistivities to the ballistic value, and plot the results in Figure 7.7. When the linewidth  $L$  is much larger than the phonon mean free path  $\Lambda$ , the resistivity is dominated by the Fourier component (blue), but for  $L < \Lambda$ , the ballistic resistivity (red) is more significant. The total linewidth-dependent resistivity is given by the sum of the Fourier and ballistic parts, and the ballistic correction resistivity  $r_{BC}$  that accounts for the error of using the Fourier law alone is determined by

$$r_{BC} \propto \frac{r_{Ballistic}}{r_{Fourier}} = \frac{2\Lambda}{3 \log(4)L} \propto \frac{\Lambda}{L}. \quad (7.14)$$

Chen determined the same  $\Lambda/L$  proportionality in the spherical case, so this is characteristic of the ratio between diffusive and ballistic transport away from a nanoscale hot

spot. Therefore, we will be looking for a deviation from the Fourier law proportional to  $\Lambda/L$  in our experimental data.

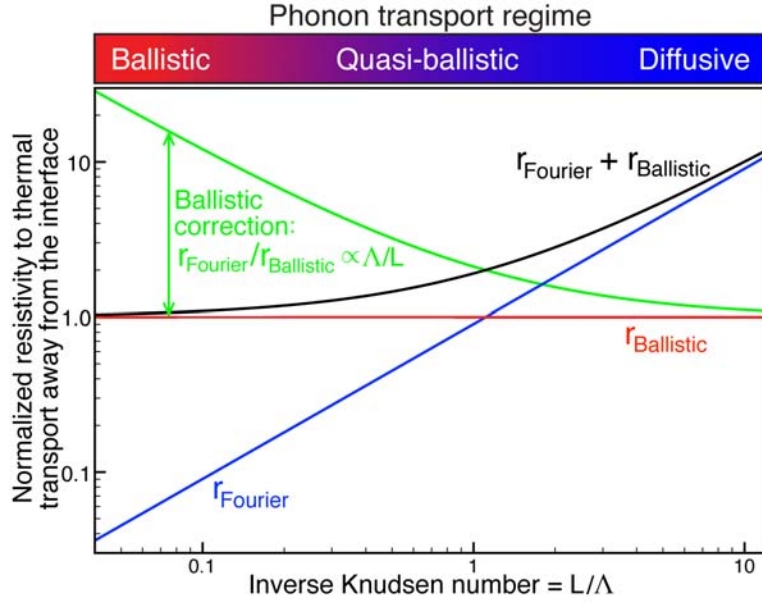


Figure 7.7: Analytical prediction of the Fourier (blue) and ballistic (red) components of the resistivity for thermal transport away from a half-cylinder of diameter  $L$  as shown in Figure 7.6, based on the spherical case discussed in [161]. We measure the correction term (green) that can be used to modify the Fourier law.

### 7.2.3 Propagating vs reservoir phonons

Phonon dispersion is another factor that becomes increasingly important in the case of non-local transport where there are not enough scattering events to establish phonon equilibrium near the a hot spot. In Fourier transport, phonons are assumed to be in local equilibrium, so for a given phonon temperature, the phonon distribution can be computed directly from the density of states and the Bose-Einstein occupation function at that temperature (as shown in Figure 7.8). Therefore the energy and velocity of the phonons can be determined if the dispersion is known – see Figure 7.9 for the phonon density of states and dispersion in sapphire. Even in a bulk system, the dispersion must be taken into account because phonons of different energy have different velocity, as seen

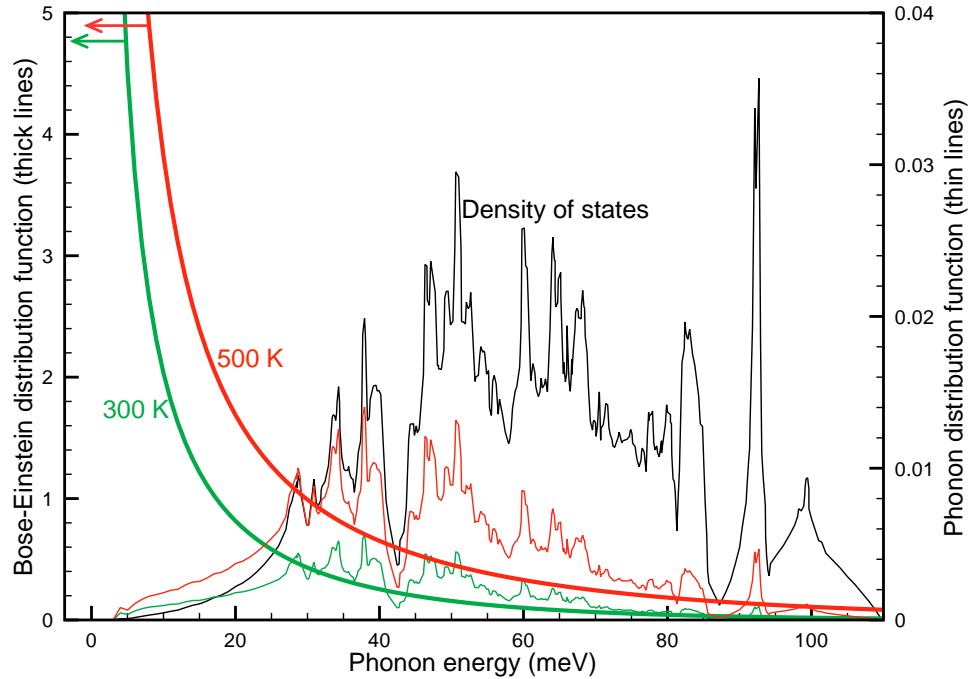


Figure 7.8: Phonon distribution in sapphire at 300 K (green) and 500 K (red). The total distribution is given by the product of the phonon density of states (black, from [165]) and the Bose-Einstein occupation function at that temperature (thick curves, left axis). This method of determining the phonon modes at a given location is valid only if there is local phonon equilibrium and a temperature can be defined.

by the slope of the dispersion in the right panel of Figure 7.9. The dashed purple line shows an approximate division between fast phonons (efficient energy carriers because they move quickly) at lower energy and slow phonons at higher energies. We will refer to these two sets of phonons as propagating (fast) and reservoir (slow) [164].

In the case of many scattering events, equilibrium between fast and slow phonons is maintained and the thermal energy in the slow phonons can be efficiently transported by first transferring the energy to the fast phonons by scattering. However, as the number of scattering events is reduced at short length scales, the slow phonons no longer have opportunities to “offload” their energy onto more efficient carriers, but are trapped as “reservoir” phonons. Meanwhile, the faster “propagating” phonons travel quickly and freely out of the heated area. This issue has been examined before in the

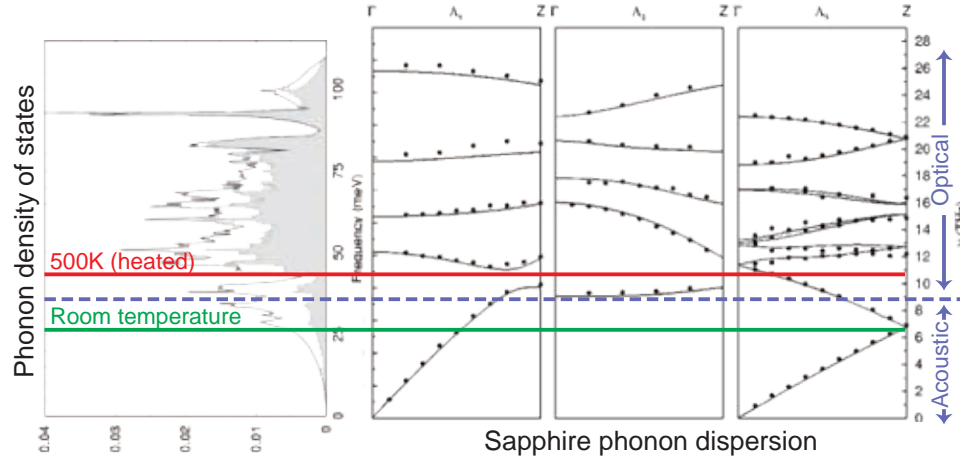


Figure 7.9: Phonon density of states (left) and dispersion (right) in sapphire. The green and red lines represent the energy in meV of  $k_B T$  at room temperature and 500 K, respectively. The dashed purple line is an approximate delimiter between "slow" optical (higher energy) and "fast" acoustic (lower energy) phonons. Both parts of this figure are taken from [165].

case of thermal transport away from a nanoscale source, and was determined to cause a significant reduction in flux from that predicted by the Fourier law with a change in resistance of  $R_{Reservoir}/R_{Fourier} = \Lambda^2/L^2$  [166, 167]. A ratio of resistances is the same as a ratio of resistivities because the width dependence is present in both numerator and denominator. However, this experiment considered heat generated by direct electron excitations, and since electrons readily excite optical phonons, they assumed that only reservoir phonons were excited.

Since we are assuming that the electrons and phonons in the heated nickel nanostructures are in equilibrium ( $> 1$  ps after initial laser heating) and the energy transport across the nickel-sapphire interface is driven by phonon-phonon processes (see section 2.4.1), we expect to excite acoustic phonons. However, the question remains: how much of an effect will we see from the inefficient transport of reservoir phonons? The answer depends on exactly what is happening as phonon energy is transported across the interface. We will consider results as determined by the two models for phonon-phonon transport at an interface discussed briefly in section 2.4.1: The acoustic mismatch model

(AMM) and the diffusive mismatch model (DMM).

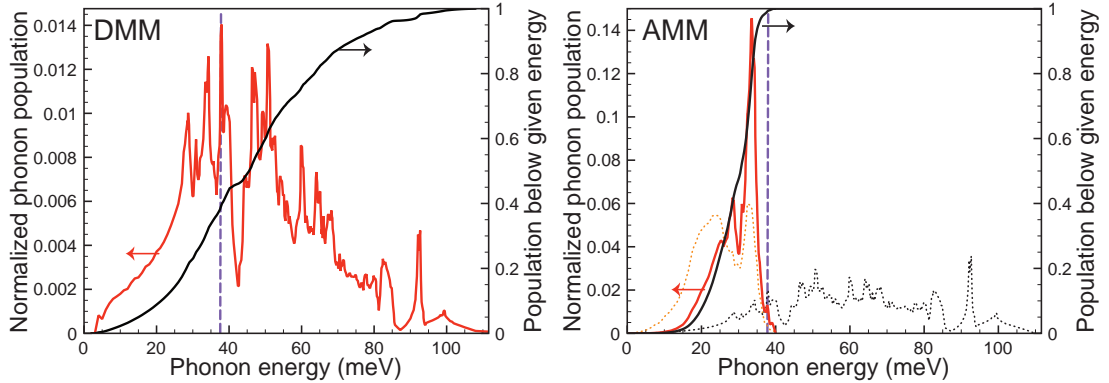


Figure 7.10: Excited phonon population (red) as a function of energy for thermal flow between nickel and sapphire. The left figure uses the diffuse mismatch model (DMM), in which the excited phonons match the available density of states in the sapphire. The figure at right is derived from the acoustic mismatch model (AMM), in which phonon states are excited directly by same-energy phonons in nickel (orange dotted line, from [168]). In each figure, the dashed purple line represents an approximate boundary between optical (higher energy) and acoustic (lower energy) phonons, as shown in Figure 7.9.

In the DMM, the excited phonon spectrum (shown in the left panel of Figure 7.10) is determined solely by the available density of states. In this case,  $\sim 50\%$  of the excited phonons are the slower, reservoir phonons. In the other limiting case, the excited phonons are determined by both the available density of states and the exciting phonon energies, determined by the phonon density of states in nickel. This results in the excitation of much lower-energy phonons (see the right panel of Figure 7.10), with nearly all of them being the highly-efficient propagating phonons. As discussed in section 2.4.1, These models for phonon interactions at a boundary break down at high temperatures such as room temperature, so the real excited phonon spectrum is probably somewhere in between the predictions of the diffuse and acoustic models. However, since  $> 50\%$  of the excited phonons are in propagating modes, we do not expect this to be a dominant effect, as it was in the case of electrical excitation [166, 167]. The strength of this effect at real surfaces and high temperatures is another open experimental question. We will

keep this effect in mind if we see  $\Lambda^2/L^2$  deviation from the Fourier law in our data.

#### 7.2.4 Previous experiment and open questions

Although there have been many models predicting a non-diffusive effect at the boundary of a nanoscale heat source, only one experiment has claimed to observe it. In that experiment, Sverdrup et al. used electrical resistance thermometry to observe steady-state temperature distributions in a thin 5  $\mu\text{m}$  silicon membrane near a 300 nm-wide doped resistor and saw slight deviation from the Fourier prediction below 200 K, but no size-dependent effect at room temperature [167]. However, this experiment did not allow for any systematic and quantitative comparison between experiment and theory due to the limitations posed by the sample geometry and steady-state measurement, leaving several open experimental questions:

- How does the ballistic effect show up at an interface?
- Can it be measured at room temperature?
- Is the effect of ballistic transport time-dependent?
- Will it still be present in a bulk substrate, or is a thin membrane required?
- How does the strength of the ballistic transport vary with linewidth?
- What is the quantified effect of ballistic transport- can heatsink calculations that use Fourier transport be easily corrected?

### 7.3 Measurement of ballistic heat transport at a nanoscale interface

Here, we use a beam of ultrafast coherent soft x-rays, at a wavelength of  $\sim 29$  nm, to directly observe cooling of a nanoscale heat source into its bulk surroundings. By interferometrically monitoring displacement in a heated nanostructure using diffraction of short wavelength light, we can detect dynamic temperature changes more sensitively

than would be possible using optical probing. This short-wavelength transient diffraction methodology, illustrated in Figure 7.11 and described in detail in Chapter 5, represents a newly-developed experimental technique that allows us to map out nanoscale thermal transport over a range of nanostructure sizes. In this experiment, an infrared laser pulse heats nanoscale nickel lines deposited on a transparent substrate (sapphire or fused silica), making it possible to heat a confined area, as illustrated schematically in Figure 7.1. The response (i.e. thermal expansion and acoustic response) is observed by monitoring the diffraction of the coherent soft x-rays from the nanostructure. This allows us to observe heat propagation through the interface and into the substrate.

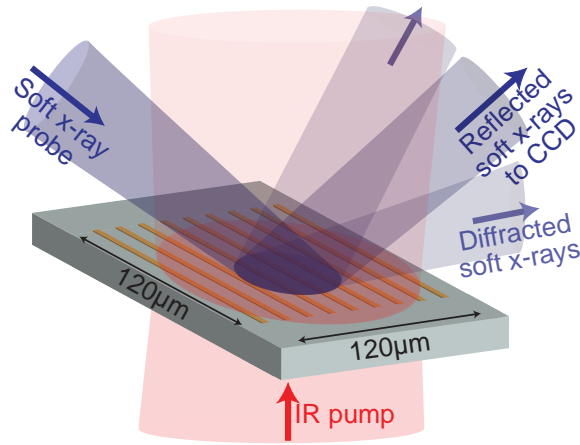


Figure 7.11: Geometry of the sample showing infrared laser illumination and EUV detection scheme.

In this experiment, we used a sapphire substrate for two reasons: it is transparent to the 800 nm laser used for heating the nanostructure, and the average mean free path of heat-carrying phonons in sapphire is long (phonon mean free path in sapphire is  $\sim 100 - 150$  nm at room temperature). An identical sample of nanostructured nickel lines was prepared on a fused silica substrate (phonon mean free path is  $\sim 2$  nm at room temperature) in order to compare the thermal transport between substrates with very different values of  $\Lambda$ . The pump-probe setup, and data optimization, collection, and processing are described in detail in Chapter 5. Results from four characteristic

scans at varying nanostructure linewidth  $L$  are shown in Figure 7.12, along with two fitting results at each linewidth. The red curve is the best fit using the thermal model that will be discussed in the following section, and the blue curve results from using the bulk value of  $r_{Interface}$  in the model. As the linewidth is decreased, the bulk resistivity increasingly under-estimates the best fit resistivity. This error is due to size-dependent ballistic effects that cannot be accounted for in a Fourier model.

We approach the analysis in a way similar to standard TTR measurements of thermal boundary resistance at thin film interfaces [23, 133, 157, 169–171]. In these experiments, the Fourier model is used to interpret experimentally measured data; we attribute deviation of our experiments from the Fourier model to a size-dependent ballistic correction resistivity  $r_{BC} \propto r_{Ballistic}/r_{Fourier}$ , given by Equation 7.14. Recall that the effective total resistivity including ballistic effects (lumped into the total resistivity which will be applied at the interface) is then given by

$$r_{Interface} = r_{TBR} + r_{BC}. \quad (7.15)$$

By fitting our data to a multiphysics model described in the next section, we will retrieve the linewidth-dependent effective interface resistivity  $r_{Interface}$ , and by subtracting  $r_{TBR}$ , determine the ballistic correction resistivity.

## 7.4 Multiphysics model for data analysis

Data analysis is complicated by thermal expansion of the substrate as heat is dissipated from the nickel lines. In order to extract the cooling dynamics of the nickel lines, we used the parameters in Table 7.1 in a multiphysics model.

### 7.4.1 Thermal transport across the interface and diffusion

In order to understand how the heat flowing from the nanostructure into the substrate affects the signal, we must be able to accurately calculate the thermal transport

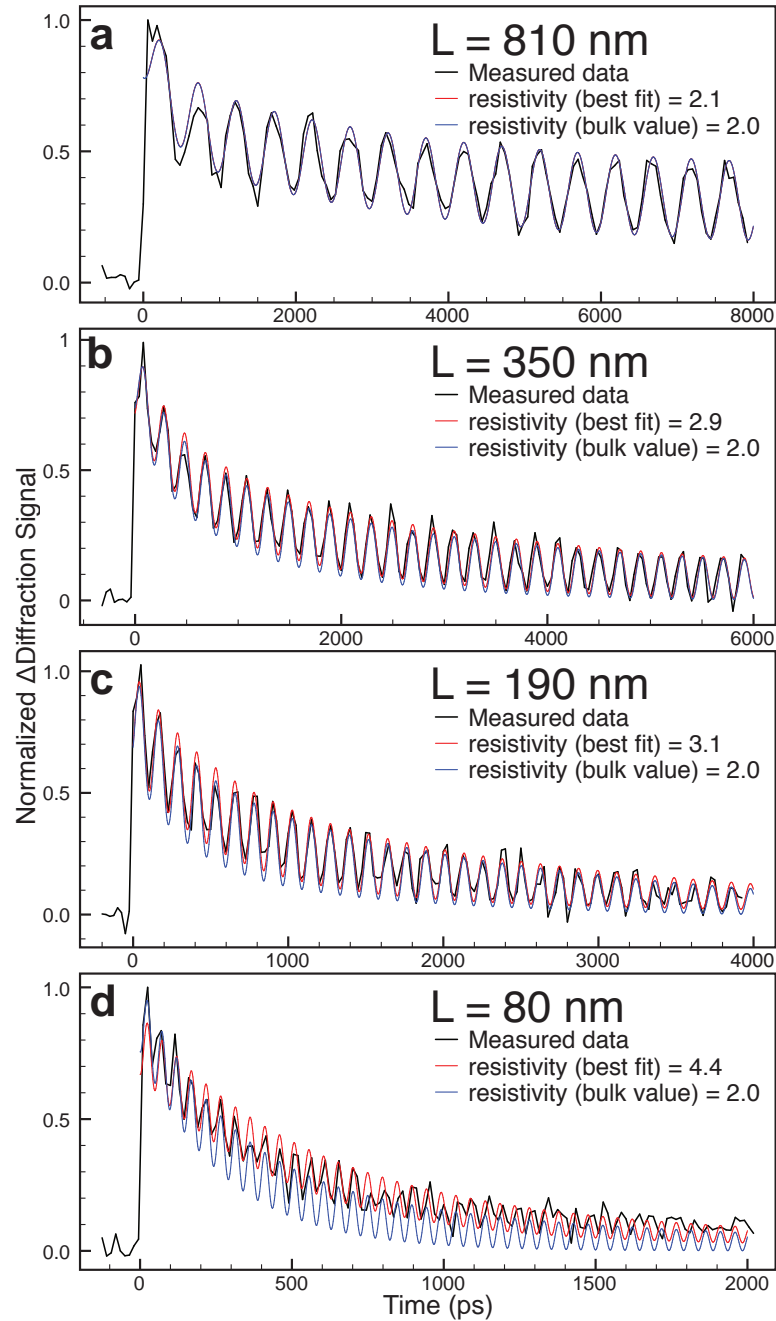


Figure 7.12: Normalized dynamic diffraction signal demonstrating the observed deviation from bulk theory for thermal transport from small nanostructures. Experimental data (black) from Ni linewidths of a. 810 nm, b. 350 nm, c. 190 nm, and d. 80 nm are shown. The signal in each case consists of a sharp rise due to impulsive laser heating, a thermal decay due to interfacial thermal transport, and an oscillation from surface acoustic wave propagation. The best fit for  $r_{Interface}$  for each linewidth is shown as the red line, while the blue line shows the result of plugging in the bulk value of  $r_{Interface} = r_{TBR}$ .

Parameter	Physical meaning	Value in Model (Ni, Sa, FS)
$h$	Nanostructure thickness	20 nm
$C_{Ni}, C_s$	Volumetric specific heat	Ni: 4.07, Sa: 2.63, FS: 2.2 [ $10^6$ W/m <sup>3</sup> K]
$r_{Interface}$	Boundary conductivity	Determined from data, [W/m <sup>2</sup> K]
$\alpha_s$	Thermal diffusivity= $k/C$	Sa: 15.64, FS: .54 [ $10^{-6}$ m <sup>2</sup> /s]
$\sigma_s$	Substrate Poisson ratio	Sa: .25, FS: .17
$\alpha_{Ni}, \alpha$	Linear coef of thermal expansion	Ni: 12.77, Sa: 5.31, FS: .54 [ $10^{-6}$ /K]
$\rho$	Density	Ni: 8.91, Sa: 4.00, FS: 2.65 [g/cm <sup>3</sup> ]

Table 7.1: Parameters used in the multiphysics model described in this section.

across the boundary, the diffusion into the substrate, and the effect of the boundary conditions. The fixed periodicity of the nanostructure means that the entire system can be studied by simply looking at one cycle of the repeated structure: one nickel line and the substrate beneath it, as shown in Figure 7.13. In the case of the 25% duty cycle samples studied here, that means a nickel line of width  $L$  and a substrate beneath it of width  $4L$ .

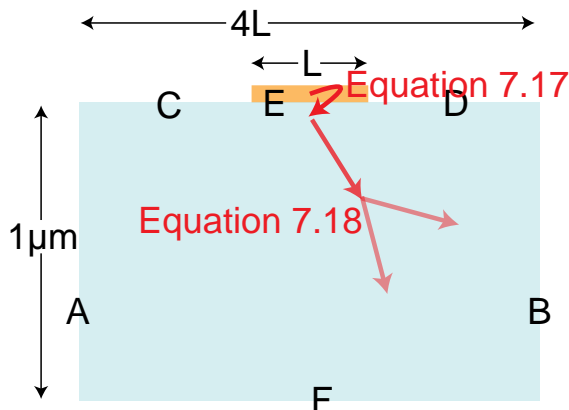


Figure 7.13: Setup for model “cell” for thermal transport from a nanoscale contact of width  $L$  and periodicity  $4L$  into a bulk heat sink. The two equations governing transport across the interface and within the substrate are indicated, as well as the interfaces for identification of boundary conditions.

We assume that the nickel nanoline can be treated as a “lumped capacitance”, which means that it is thin enough that we can neglect transport inside the nickel. This assumption can be checked by calculation of the Biot number  $Bi$  for the interface, which

is a measure of the relative importance of bulk and boundary effects:

$$Bi = \frac{h}{r_{TBR}k_{Ni}}, \quad (7.16)$$

where  $k_{Ni}$  is the thermal conductivity of the nanostructure. If  $Bi < 1$ , it is valid to use the lumped capacitance model to ignore diffusion in the nickel. The room-temperature thermal conductivity of nickel is  $k_{Ni} = 90.62$  W/mK and later measurements will show that  $r_{TBR} \sim 2 \times 10^{-9}$  m<sup>2</sup>K/W. So for a  $h = 20$  nm nanostructure,  $Bi = .1 < 1$  — the lumped capacitance model is valid. This means that the nanostructure can be modeled as having no temperature dependence in the vertical direction. Temperature dependence across the surface is still considered, however, as the edges of the nanostructure cool more rapidly than the center due to thermal spreading.

Since we can neglect diffusion inside the nanostructure, the thermal model is composed of only two parts:

- (1) Coupling of the nanostructure and substrate boundary temperatures, accomplished by conservation of energy across the interface. This is determined by

$$\rho_{Ni}hC_{Ni}\frac{dT_{Ni}(x,t)}{dt} = -\frac{(T_{Ni}(x,t) - T_s(x,y=0,t))}{r_{Interface}}, \quad (7.17)$$

where  $T_{Ni}$  and  $T_s$  are the time and position-dependent nickel nanostructure and substrate temperatures, and  $x$  and  $y$  are the coordinates along the surface and depth directions, as shown in Figure 7.16. Equation 7.17 essentially says that the amount of energy lost by the nanostructure (left side) in a differential amount of time is equal to the energy flowing across the interface, into the substrate (right side).

- (2) Diffusion of heat in the substrate beneath each nickel line, which is modeled by numerically solving the heat equation

$$\frac{\partial T_s(x,y,t)}{\partial t} = \alpha_s \nabla^2 T_s(x,y,t). \quad (7.18)$$

This equation is solved numerically in two spatial dimensions with time-stepping using the Crank-Nicolson and Alternating-Direction Implicit (ADI) methods. The following boundary conditions are used (see Figure 7.13 for boundary labels):

A,B: vertical sides of modeling cell have periodic boundary conditions, which is equivalent to saying that there is no flux across the boundaries –

$$\frac{\partial T_s(x = 0 \text{ or } 4L, y, t)}{\partial x} = 0 \quad (7.19)$$

C,D: twin regions on top of the substrate flanking the nanostructure have vacuum on the other side of the interface and therefore cannot have heat flow across them (other than radiation, which is neglected), so they also have no flux boundary conditions –

$$\frac{\partial T_s(x, y = 0, t)}{\partial y} = 0. \quad (7.20)$$

E: specified flux boundary condition –

$$\frac{\partial T_s(x, y = 0, t)}{\partial y} = -\frac{T_f(x, t) - T_s(x, 0, t)}{r_{Interface}k_s}. \quad (7.21)$$

Numerical implementation of this boundary condition is challenging because of the finite grid size. The usual numerical derivative at an interface

$$\frac{\partial f(y_0)}{\partial y} \simeq \frac{f(y_0 + dy) - f(y_0)}{dy} + O(dy) \quad (7.22)$$

is valid only when the grid spacing  $dy$  is much smaller than the distance over which the derivative acts. In the case of thermal propagation, this distance is the thermal diffusion length  $\ell = \sqrt{\alpha_s t}$ . For sapphire,  $\alpha_s = 1.5748 \times 10^{-5} \text{ m}^2/\text{s}$ , so for a time one picosecond after excitation,  $\ell \sim 4 \text{ nm}$ . Computing the thermal propagation on such a fine grid is unreasonable for

the larger nanostructures, so instead we chose to implement a multi-point numerical derivative, still centered at  $y_0$  (with  $y_1 = y_0 + dy\dots$ ) [172]:

$$\frac{\partial f(y_0)}{\partial y} \simeq \frac{-3f(y_4) + 16f(y_3) - 36f(y_2) + 48f(y_1) - 25f(y_0)}{12dy} + O(dy^4), \quad (7.23)$$

which greatly increases the accuracy of the derivative calculation.

F: back of the substrate has a no flux boundary condition assuming that the semi-infinite approximation is valid –

$$\frac{\partial T_s(x, y = 1\mu\text{m}, t)}{\partial x} = 0. \quad (7.24)$$

The semi-infinite approximation requires that the substrate is thick enough that no heat will be able to diffuse to the back surface in the given amount of time  $t$ . Our pump pulse delay stage is limited to  $\sim 8$  ns, and the maximum extent of thermal diffusion in sapphire at this timescale is  $\ell = \sqrt{\alpha_s t} \sim .35 \mu\text{m}$ . This means that the semi-infinite approximation is valid both in the modeling, where we used a  $1 \mu\text{m}$  depth, and the experiment, where the substrate was 3 mm thick.

The initial conditions describe uniform laser-induced heating in the nickel and an unheated sapphire substrate. Final modeling was run using a nickel heated temperature of 500 K (determined from deposited laser energy and nickel properties), but actual-temperature results deviate from normalized temperature (heated nickel temperature initially set to 1 K, sapphire set to 0 K) by less than 2% (error due to temperature-dependent changes in the materials properties, shown in Figure 7.15), so we present normalized results here. The initial conditions, then are:

$$T_{Ni}(x, t = 0) = 1, \quad T_s(x, y, t = 0) = 0. \quad (7.25)$$

Figure 7.14 presents modeling results for  $L = 1 \mu\text{m}$  (top) and  $L = 50 \text{ nm}$  (bottom) at selected times after the excitation of the nickel nanostructure. The half-width of the modeling region in the first case is  $2 \mu\text{m}$ , much farther than heat diffusion travels in 8 ns (longest time available for measurement). This leads to a thermal distribution that is primarily confined beneath the heated  $L = 1 \mu\text{m}$ , even at 8 ns. This result is in contrast to the modeling results using a nanostructure linewidth of  $L = 50 \text{ nm}$ . In this case, the modeling region half-width is only 100 nm, and there is nearly-uniform thermal distribution across the surface only 1 ns after excitation. Therefore, thermal expansion of the substrate, is expected to be localized beneath the nanostructure for  $L = 1 \mu\text{m}$  and evenly-distributed across the surface for  $L = 50 \text{ nm}$ . These results represent extreme but indicative examples of the sample sizes we used in experiments.

#### 7.4.2 Thermal expansion

Linear thermal expansion is described by a linear coefficient of thermal expansion  $\alpha$  in the equation

$$\Delta h_x = \alpha \int \Delta T(x) dx, \quad (7.26)$$

where  $\Delta T(x)$  is the temperature difference from equilibrium. We will refer to this as the “vertical integration technique”, and it has implicit assumptions:

- The temperature change is low; the coefficient of thermal expansion is actually temperature-dependent (see Figure 7.15), so very large changes in temperature can cause errors. This can be corrected by including a temperature-dependent coefficient of thermal expansion and integrating over the change in temperature.
- The object is free to expand; otherwise, pressure and stress will build up without causing displacement.

This expression is valid for the vertical displacement of the nickel lines because they are bound on the bottom only and are free to expand away from the substrate.

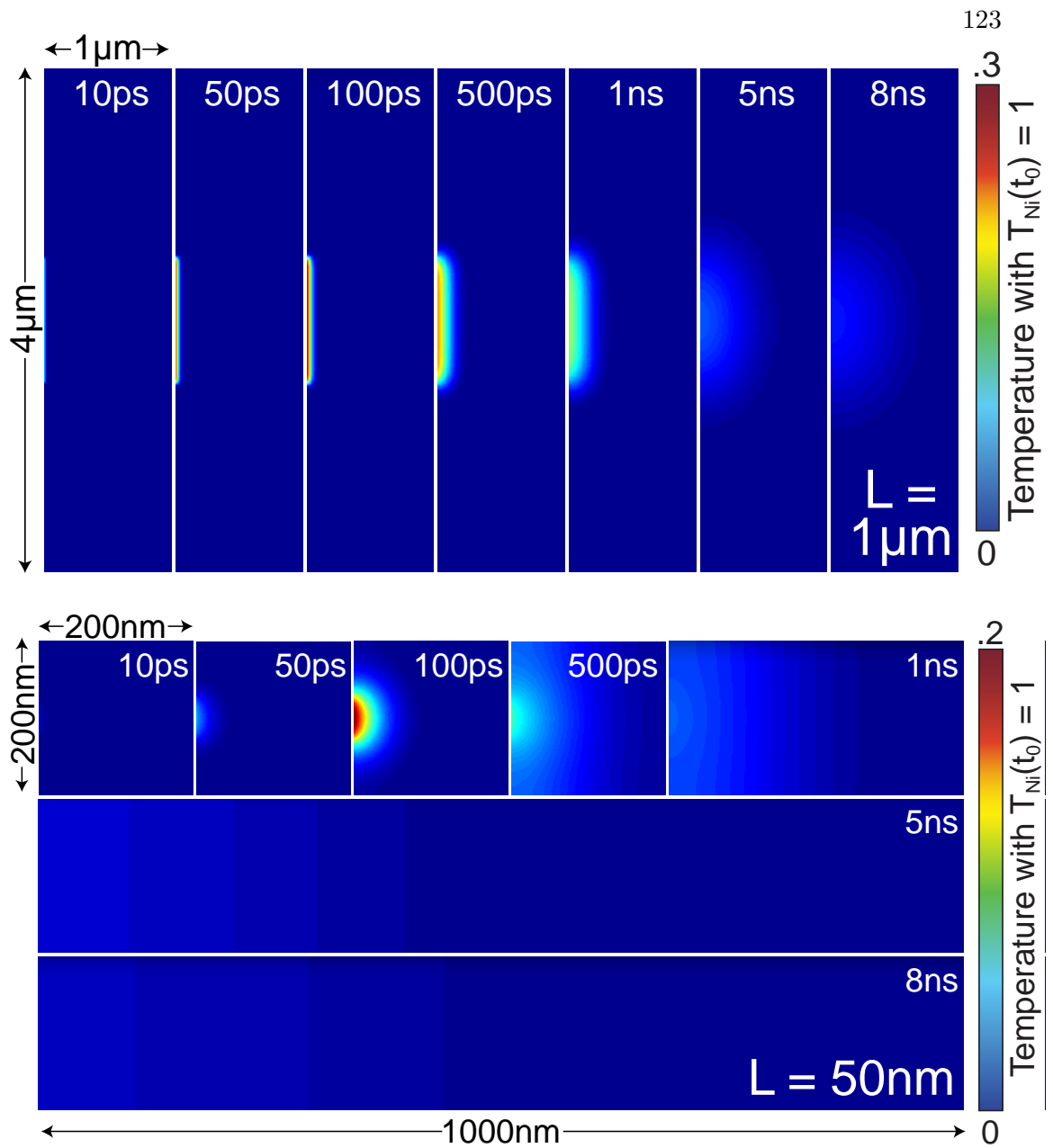


Figure 7.14: Time snapshots of thermal diffusion modeling for a single sapphire cell from 10 ps to 8 ns. Results are shown with a 4 μm wide region with a 1 μm nickel heater (top) and 200 nm wide region with a 50 nm nickel heater (bottom). The different temperature scales are the result of different peak temperatures at these times- the nanostructured nickel heaters started at the same temperature. These thermal images are rotated 90° counter-clockwise from the modeling setup shown in Figure 7.13 for ease of presentation.

Their horizontal displacement is neglected in the model because it will be much smaller since the nickel is rigidly bound to the substrate in that direction. Also, in the EUV

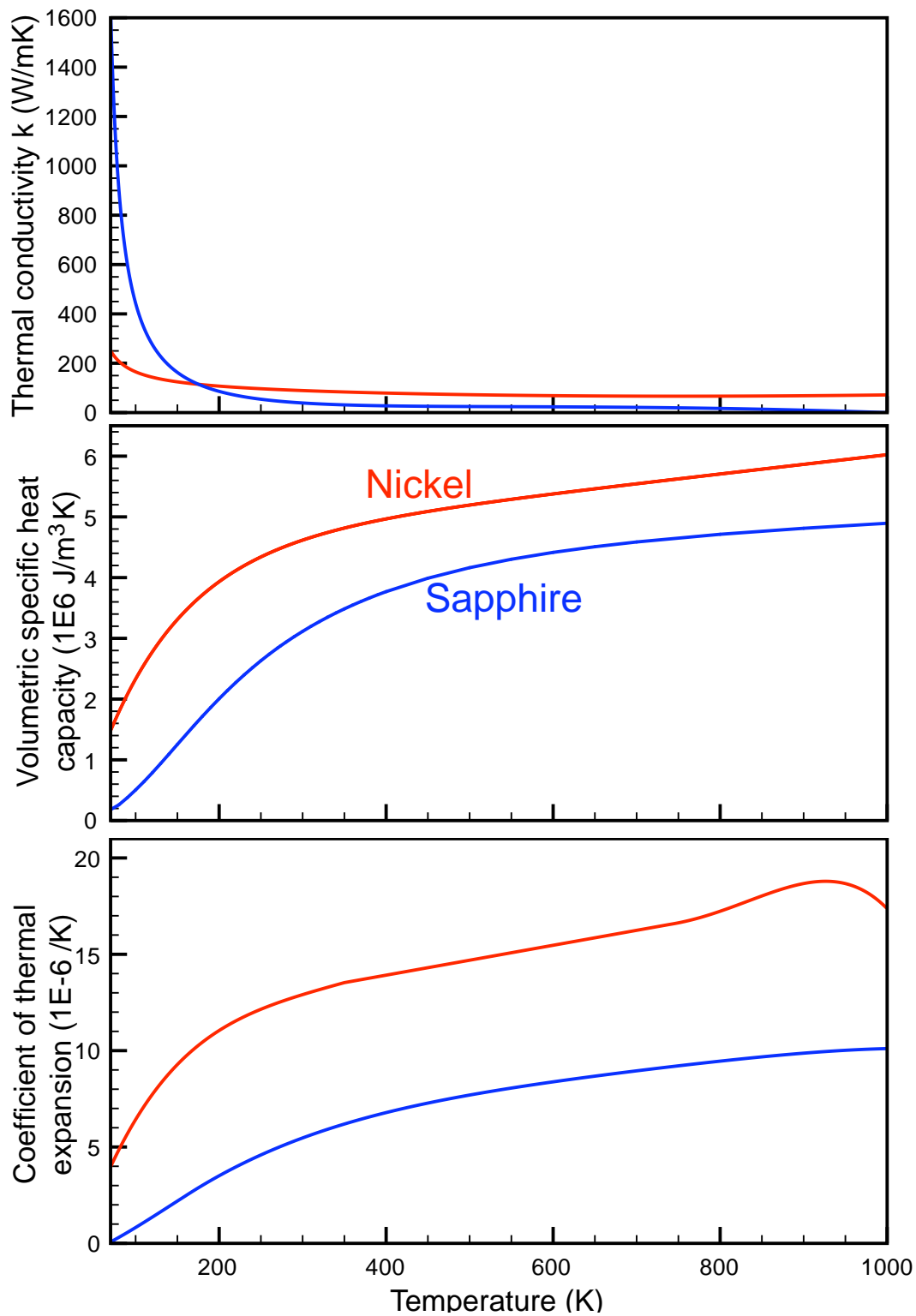


Figure 7.15: Temperature-dependence of thermal conductivity  $k$ , specific heat  $C$ , and coefficient of thermal expansion for nickel [173] and sapphire [174–177].

diffraction detection method used, horizontal displacement has a much smaller effect than a vertical one. Because there is no depth dependence of the nickel lines in the thermal model, the position-dependent displacement is directly-proportional to the change in temperature:

$$\Delta h_{Ni,y}(x) = \alpha_{Ni} h_{Ni} \Delta T(x). \quad (7.27)$$

In contrast to the simple treatment for thermal expansion of the nickel lines, the thermal expansion of the surface of the substrate can *not* be determined by integrating the thermal profile vertically and multiplying by the coefficient of thermal expansion (see Figure 7.17). A simple integration of the thermal profile implies that a hotspot deep within the substrate has the same effect as the same hotspot on the surface, which can't be true because there are forces binding each lattice point to its neighbors. The thermal expansion should actually be calculated starting from the time-dependent Navier-Stokes equation [178]

$$\mu \nabla^2 \vec{u} + (\nu + \mu) \vec{\nabla}(\vec{\nabla} \cdot \vec{u}) + \vec{F} - \alpha \vec{\nabla} T = \rho \frac{\partial^2 \vec{u}}{\partial t^2}, \quad (7.28)$$

where  $\mu$  is the shear modulus,  $\nu$  is Poisson's ratio,  $\vec{F}$  is an external force term, and  $\vec{u}$  is the displacement at a particular location. If we assume that there are no external forces acting on the system, then  $\vec{F} = 0$ . It is also assumed that the material is isotropic, which is true for fused silica and is  $> 97\%$  true for sapphire (based on ratio of thermal conductivities along and orthogonal to the axis).

Further simplification can be made under the quasi-static assumption  $\partial^2 \vec{u} / \partial t^2 = 0$ , which implies that the acceleration of the surface can be neglected. This will give us a stationary, time-independent partial differential equation that assumes that the surface displacement at a given time is coupled to the temperature distribution at that time only. That this is valid is not obvious for the picosecond time scale we are dealing with here, but we can make a rough estimate of the time scale of these surface acceleration effects. Assuming that the maximum surface velocity is given by

the longitudinal acoustic velocity, and the maximum surface expansion is 1 nm, then we can neglect surface acceleration effects for time step sizes  $> 100$  fs (this is much longer than the typical time step  $\sim 10$  ps used in these experiments). Implementing these three assumptions, Equation 7.28 simplifies to the thermoelastic equation [179]

$$\frac{3(1-\nu)}{1+\nu}\vec{\nabla}(\vec{\nabla}\cdot\vec{u})-\frac{3(1-2\nu)}{2(1+\nu)}\vec{\nabla}\times\vec{\nabla}\times\vec{u}=\alpha\vec{\nabla}T. \quad (7.29)$$

In order to obtain a useful solution to the thermoelastic equation, we make a final assumption that the surface is stress-free. This is true at the unbound (free) surface of a thin film or substrate, but not technically true at the surface of our substrate, where the center is coupled to a nickel strip. However, the stress-induced change to the deformation is a second order effect and therefore much smaller than the thermal displacement itself [180]. The thermoelastic equation can then be solved using Green's functions to determine the vertical displacement at the surface as a function of position [71]

$$\Delta h_y(x,z)=\frac{(1+\nu)\alpha}{3\pi}\int dx_0\int dy_0\int dz_0\frac{z_0}{((x-x_0)^2+(z-z_0)^2+y_0^2)^{3/2}}, \quad (7.30)$$

which involves a weighted integration over the three-dimensional temperature distribution at each point on a two-dimensional surface (see Figure 7.16, 2D).

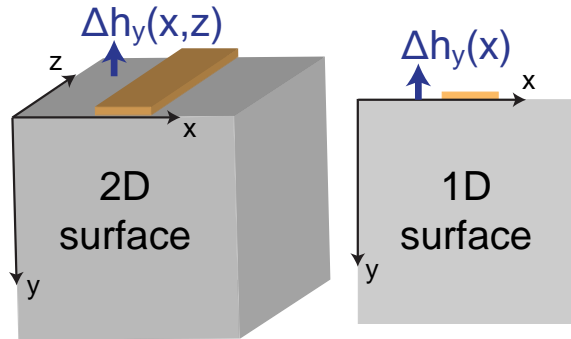


Figure 7.16: Coordinate systems for surface displacement calculation for a two-dimensional (left, Equation 7.30) and one-dimensional (right, Equation 7.31) surface.

We convert this to a two-dimensional distribution by integrating over the  $z$ -axis from  $-\infty \rightarrow \infty$ . Finally, the remaining integrals are converted to discrete sums and

nearest neighbor temperature profiles are included in the calculation (since the neighboring cells can have a significant effect near the edges – neighbor properties determined by wrapping original cell), leading to the final expression for the thermal surface displacement of the substrate:

$$\Delta h_y(x) = 2 \frac{(1 + \nu_s) \alpha_s dx}{3\pi} \sum_{N=-1}^1 \sum_{i_x=1}^{i_{x,max}} \sum_{j_y=1}^{j_{y,max}} T(i_x, j_y) \frac{j_y}{(x/dx + N \times i_{x,max} - i_x)^2 + (j_y)^2}. \quad (7.31)$$

Here,  $i_x$  and  $j_y$  are the summing steps in  $x$  and  $y$  respectively,  $dx$  is the step size in  $x$ , and  $N$  is an index accounting for nearest neighbors. The results of the calculation are shown as the red curve in Figure 7.17A for a typical temperature distribution shown in 7.17B. There is significant deviation in both amplitude and shape from the vertical integration technique.

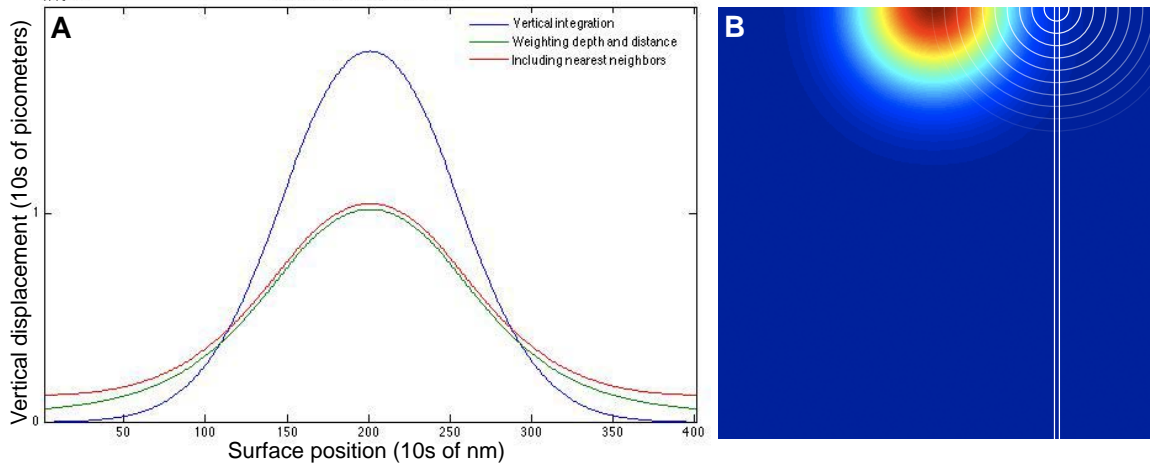


Figure 7.17: (A) Calculated surface displacement using three different techniques: vertical integration (blue), and depth and distance weighting and integration with (red, as in Equation 7.31) and without (green) including contributions from neighboring lines. The most realistic results are given by the weighted calculation including neighbors (red), and are used in this model. (B) Illustration of the difference between the vertical integration method (long white rectangle) and weighted integration method (concentric diminishing circles) for determination of the vertical displacement of a point on the surface.

### 7.4.3 Fresnel optical propagation

To complete the connection of the thermal model to the measured data, we need to calculate how the thermally-induced surface profile affects the diffraction of the EUV probe, which we measure experimentally. We use the same Fresnel optical propagation model discussed in section 4.2 and Appendix A to calculate the diffraction from the thermal surface deformation, which can then be subtracted from the diffraction of the undeformed structure to yield the expected signal. A summary of the steps in the calculation is shown in Figure 7.18, with the final change in diffraction shown in the bottom panel. This calculated change in diffraction compares well with our raw experimental data, as seen by the green curve in Figure 5.12. Integrating the absolute value of the change in diffraction gives the total signal, which can be compared directly to the experimentally measured values when both are normalized to the peak signal.

### 7.4.4 Discussion of model results

In order to provide insight into the significance of the contributions to the measured signal, the Fresnel propagation portion of the calculation is performed three times to determine the signal from: the nickel lines alone, the sapphire substrate alone, and the combined effect of the Ni and Sa together. These results are summarized in the top panel of Figure 7.19 for the  $L = 1000$  nm nanostructures. The signal from the nickel lines is close to a double-exponential decay, as expected for thermal transport across a surface and into a substrate. Because of the quasi-static approximations discussed in section 7.4.2, the decay of the Ni and the rise time of the sapphire signal are directly related to the rate of thermal energy flow between them, and by conservation of energy, are equal.

The signal from the substrate logically starts at zero since it is initially unheated, gradually increases as heat flows from the Ni lines into the substrate, and eventually

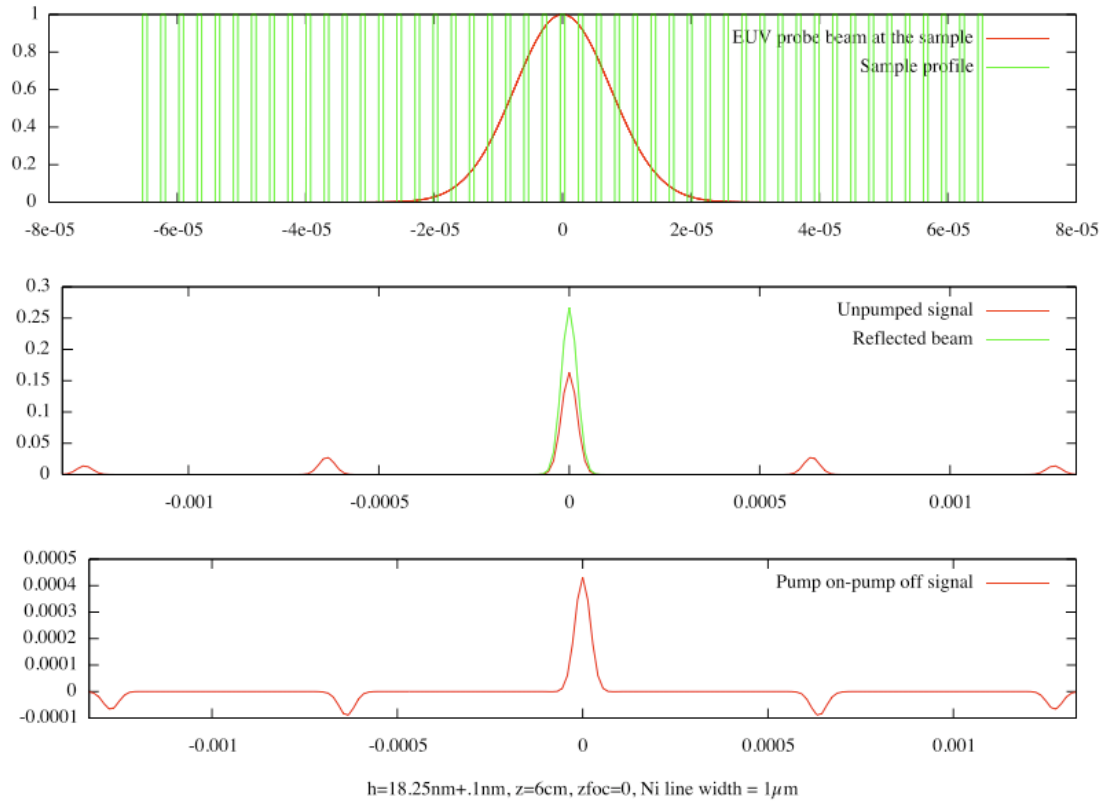


Figure 7.18: Results of Fresnel propagation calculation of diffraction signal change. Top: sample profile and EUV beam on sample. Middle: Reflected beam (as if there were no grating present) and diffracted beam. Bottom: pump-on, pump-off difference signal, showing a change in diffraction efficiency.

decreases. The EUV probe makes an interferometric measurement, so it is the *relative* displacement between the substrate and the nickel lines that matters. This fall time of the signal from the sapphire substrate is determined by the diffusion time for heat to flow in the substrate from the edge of a nickel line to the center between two lines. The fixed duty cycle of the nanostructured samples means that this diffusion distance is proportional to  $L$  itself, so the time for heat to diffuse to the edge of the modeling cell is strongly linewidth-dependent, as shown in Figure 7.14. In fact, this diffusion time is quadratic in  $L$  [19]–

$$\tau \sim L^2/\alpha_s. \quad (7.32)$$

This dramatic decrease of the decay time as the linewidth is reduced means that for

very small structures (which are very close together), the contribution to the total signal from the sapphire substrate is much smaller than their large- $L$  counterparts which are much further apart, as alluded to at the end of section 7.4.1. This is borne out in the calculations of the contributions to the signal from the nickel and sapphire for different linewidths, as shown in the bottom panel of Figure 7.19.

The total signal measured in the experiment is equal to the sum of the contributions from thermal expansion in the nanostructure and the substrate, and therefore cannot be fit by an exponential, as we tried to do in our original data analysis. In this erroneous analysis, we observed decay times dominated by  $L^2$  at large linewidths for the sapphire, and no linewidth dependence for the data on fused silica substrates. This  $L^2$  dependence is due to the diffusion time for the heat to flow to between the lines (Equation 7.32), and can be corrected by thorough numerical modeling, as described above. The effect of the substrate in the case of the fused silica substrate is much smaller because of the smaller coefficient of thermal expansion.

#### 7.4.5 Fitting the model to our experimental data

In order to fit the modeling results to the data, we ran the model several times for a given nickel linewidth, varying the input interface resistivity between runs. Results from a typical series of modeling runs for  $L = 1 \mu\text{m}$  linewidths are shown in Figure 7.20, where each curve corresponds to modeling results using a different resistivity (values of conductivity  $h$  are shown,  $h = 1/r$ ). Each curve is fit to a quasi-exponential function, with terms optimized for best fitting. For example, for small linewidths, the modeled total signal is very close to an exponential, but for large linewidths, additional terms are required to get good fits. The fitting parameters are then fit to a quadratic function, with the result being a parameterization of the modeled time-dependent “signal” as a function of interface resistivity. This result for the thermal component is then added to a decaying sinusoid to account for the surface acoustic wave component discussed

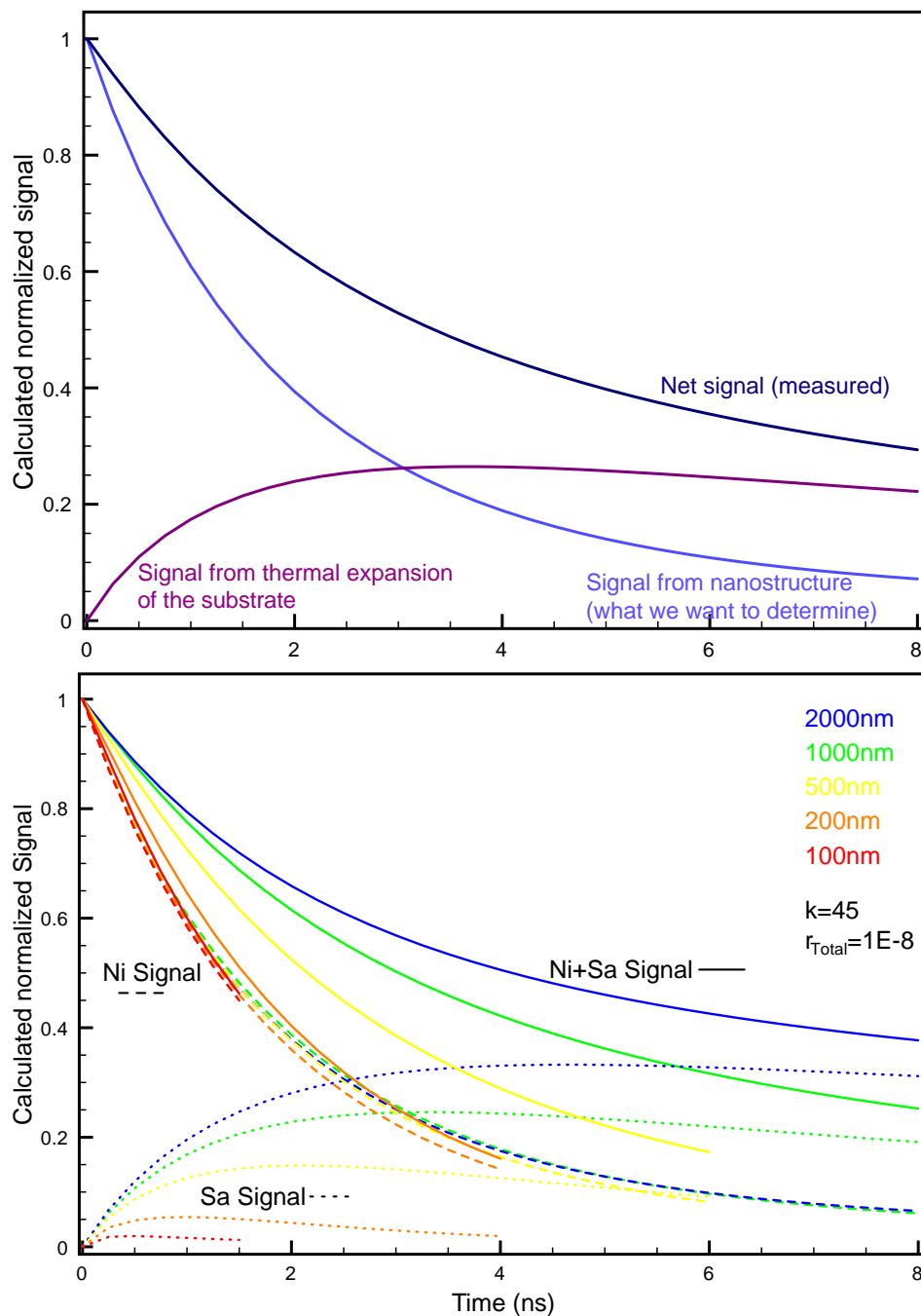


Figure 7.19: Calculated change in diffraction signal from thermal expansion. The top panel shows the signal from  $L = 1000$  nm lines from the Ni nanostructure itself (light blue), the sapphire substrate (purple), and total (dark blue). The bottom panel shows the linewidth dependence of these signals: as the linewidth is decreased, the signal from the sapphire substrate becomes smaller.  $r_{\text{Interface}} = 10^{-8} \text{ m}^2\text{K/W}$  in these calculations.

in Chapter 6 and finally fit to the data by minimizing the RMS error between the experimental data and the fitting function.

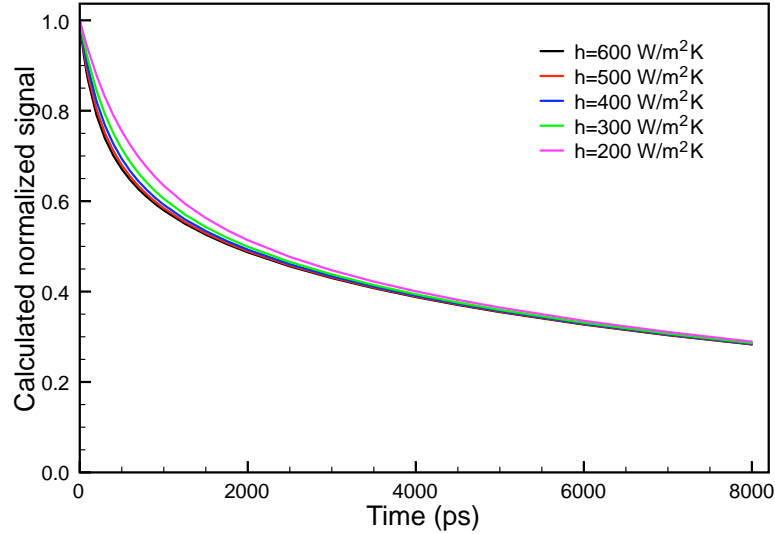


Figure 7.20: Normalized dynamic total signal from full thermal diffusion-thermal expansion-optical propagation model for  $L = 1 \mu\text{m}$  linewidth as a function of conductivity (conductivity  $h = 1/r$ , and units of given conductivities are in  $10^6$ ).

For each data set at a given linewidth, we retrieve the total boundary resistivity  $r_{Interface}$ , which includes both conventional thermal boundary resistivity and ballistic effects in the substrate, and fit to the time-resolved thermal decay data. The best fits to the data shown in Figure 7.22 (red lines) demonstrate that the measured interface resistivity increases as the heated interface gets smaller. The measured values of  $r_{Interface}$ ,  $r_{TBR}$ , and  $r_{BC}$  for both sapphire and fused silica substrates are shown in Figure 7.22. The Fourier resistivity,  $r_{Fourier}$  (including spreading resistance discussed in section 7.2.1), is automatically accounted for in our numerical model for heat propagation in the substrate (Equation 7.18). By definition, large linewidth measurements on samples with both samples (sapphire and fused silica substrates) yield the bulk values of thermal boundary resistivity  $r_{TBR}$  (equivalent to TTR measurements of thermal boundary resistance on thin lms), as shown by the horizontal dotted lines in Figure 7.22. We measured a very small (zero within error bars) deviation from  $r_{TBR}$  for the fused silica

substrate, because the phonon mean free path in fused silica ( $\Lambda_{FS} \sim 2$  nm) is much shorter than the smallest nickel linewidths. However, in the case of samples on sapphire substrates, the extracted resistivity at the smallest linewidths is more than three times higher than the bulk value. The blue dotted and red dashed lines in Figure 7.22 show the predicted resistivity values  $r_{Interface}$  (with  $r_{BC} = r_{Interface} - r_{TBR}$  proportional to  $\Lambda/L$ ) determined from the analytical ballistic-diffusive model (Figure 7.6 and Equation 7.14) for phonon mean free paths of  $\Lambda_{FS} = 2$  nm and  $\Lambda_{Sa} = 120$  nm.

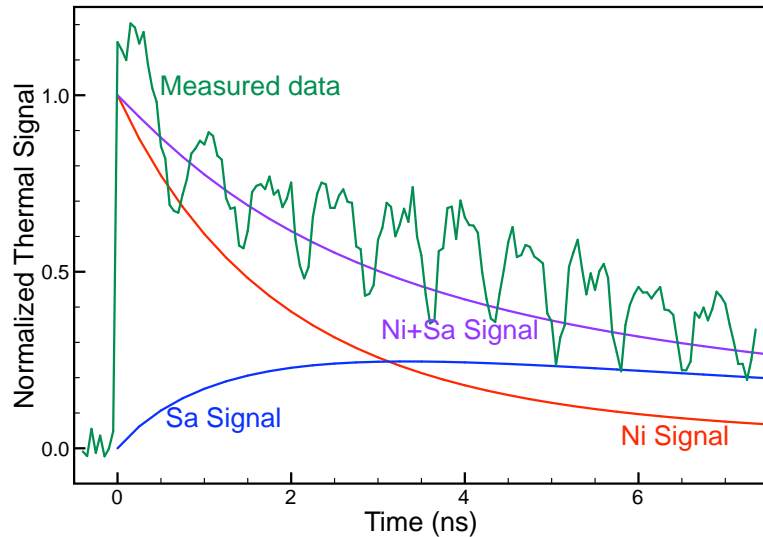


Figure 7.21: Results of the multiphysics model for  $L = 1000$  nm linewidth structures with the best fit value of  $r_{Interface} = 2.2 \times 10^{-9}$  m<sup>2</sup>K/W (purple). Also included is a sample measurement (green). At this linewidth, the sapphire substrate makes a significant contribution to the total signal.

## 7.5 Implications of the measurement

One way that we can understand these results is by considering what we will call a “minimum heated region” model, in which the thermal conductivity surrounding a nanoscale heat source is reduced in an area including one phonon mean free path length [161]. We can see the effect of this idea by considering a simplified calculation, starting with the Fourier law for heat flow:  $q = -k\nabla T$ . If we consider only a single

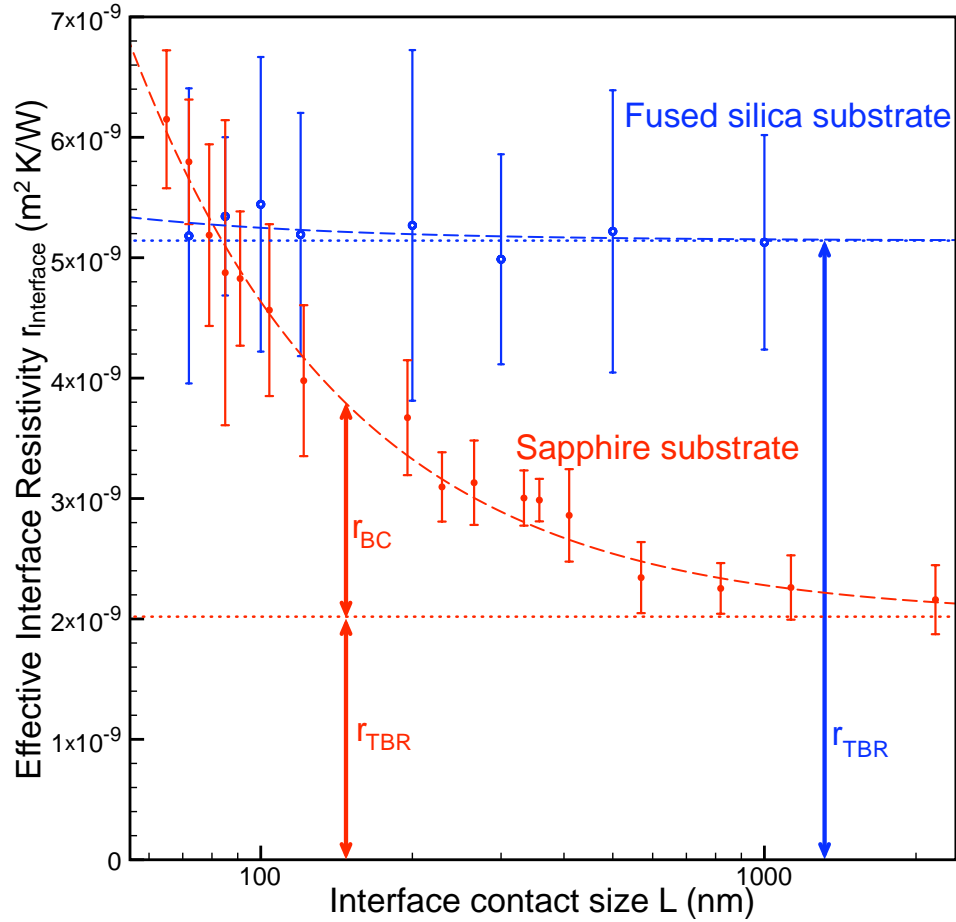


Figure 7.22: Measured effective interface resistivity for nickel nanostructures of width  $L$  on fused silica (blue hollow dots) and sapphire (red solid dots) substrates. The measured resistivity for the samples with fused silica substrates ( $\Lambda_{FS} \sim 2$  nm) is nearly independent of linewidth, while the boundary resistivity for the sapphire substrates ( $\Lambda_{Sa} \sim 120$  nm) increases rapidly as the linewidth is decreased due to the ballistic correction of the over-prediction of the flux by the Fourier law.

dimension,  $\nabla T$  is  $\partial T/\partial x \sim \Delta T/\Delta x$ . The normal dimension of the system is  $\Delta x \sim L$ , but in this case, we use the phonon mean free path  $\Lambda$  as a minimum to the length scale:  $\Delta x \sim L + \Lambda$ . So for  $L \gg \Lambda$ ,  $\Delta x \sim L$ , and for  $L \ll \Lambda$ ,  $\Delta x \sim \Lambda$ . The modified Fourier law for the minimum heated region model is then

$$q_{\text{Minimum heated region model}} = -\frac{k\Delta T}{L + \Lambda}, \quad (7.33)$$

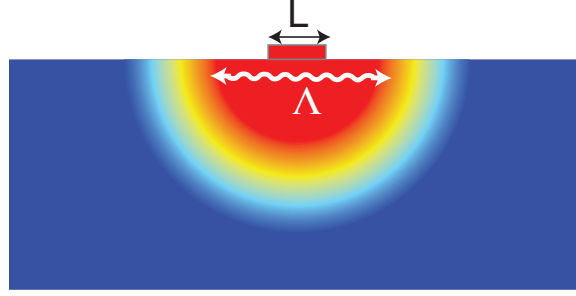


Figure 7.23: Minimum heated region model: If the size of a heated area is smaller than the phonon mean free path  $\Lambda$ , heat flows as if coming from a spot of size  $\Lambda$ .

and if we consider the ratio of this modified flux to the traditional Fourier flux, we find

$$\frac{q_{\text{Minimum heated region model}}}{q_{\text{Fourier}}} = \frac{L}{L + \Lambda}. \quad (7.34)$$

In terms of resistivity ( $r = \Delta T/q$ ),

$$\frac{r_{\text{Minimum heated region model}}}{r_{\text{Fourier}}} = 1 + \frac{\Lambda}{L}. \quad (7.35)$$

This is the same result as the calculation in section 7.2.2, and agrees with our experimental results. The model effectively says that the system can only respond to a heated spot larger than a phonon mean free path; if the heated area is smaller than  $\Lambda$ , the heat flows as if it were coming from a spot of size  $\Lambda$ .

It is important then to distinguish the case of heat transfer away from a nanoscale heat source and transport inside a nanostructure.

- For heat transfer inside a nanostructure, illustrated in Figure 7.2, ballistic transport means that the phonon mean free path is limited by the size of the structure (for  $L \ll \Lambda$ ,  $\Lambda \rightarrow L$ ).
- In the case considered in this experiment of heat transfer away from a nanoscale heat source, illustrated in Figure 7.23, ballistic transport means that the effective source size is limited by the phonon mean free path (for  $L \ll \Lambda$ ,  $L \rightarrow \Lambda$ ).

Therefore, our measurement of ballistic thermal transport away from a nanoscale heat source is fundamentally different from previous experiments which observed ballistic transport in or through a nanostructure.

## 7.6 Discussion of the time-resolved measurement

One important aspect of this experiment that we haven't yet emphasized is the dynamic time-resolved nature of the measurement. This is in contrast to most experimental techniques for studying thermal transport in a nanostructure, which use steady-state [141] or oscillatory (alternating current) [181] measurements. Without emphasizing its importance, we have already seen the importance of the time-resolved nature of the experiment in Figure 7.12d. In this figure, the difference between the bulk and ballistic-sensitive fits is only seen at short times ( $< 1$  ns). The importance of a dynamic measurement is also illustrated in Figure 7.24, which shows normalized modeling results for the temperature decay in the nickel lines for  $L = 1000$  nm (red) and 65 nm (blue lines). The dark blue line shows the thermal decay in the nanostructure using the best-fit value of  $r_{Interface}$ , and the light blue curve shows the thermal decay when the bulk interface resistivity is used. The difference between the two curves, which depict a change in  $r_{Interface} > 3\times$ , is very interesting: the bulk-resistivity curve predicts much faster thermal decay in the first 500 ps, but by 3 ns, the predicted temperature profiles are the same. This long-time convergence is due to the thermal conductivity in the bulk portion of the substrate, which is independent of the interface resistivity. Therefore, a dynamic measurement is necessary to observe ballistic effects from an impulsive excitation.

This result, determined from the modeling fit to our time-resolved experimental data, gives insight into the time-dependent temperature in the nanostructure that isn't possible using static probes. This short-time information is also quite useful: the green line at 500 ps corresponds to a frequency of 2 GHz, which is the operating frequency of

the processor in my computer.

## 7.7 EUV probing of nanoscale thermal transport outlook

The ballistic effect seen near a nanostructured interface should be even larger for materials with longer phonon mean free paths. The obvious example is silicon, which has a phonon mean free path  $\Lambda \sim 250$  nm at room temperature, and is commonly used in the IC industry as a substrate. We have already obtained a sample with a silicon substrate, and are now in the process of modifying the experimental setup to accommodate the sample. One problem is that Si is not transparent to the 800 nm pump light, so we cannot pump from the backside. The absorption of Si also presents a problem in that we will no longer be able to assume that the substrate not directly heated by the laser pump pulse. However, the penetration depth for 800 nm light in silicon is rather long (7.5  $\mu\text{m}$  [14]), so this may not change the calculation critically.

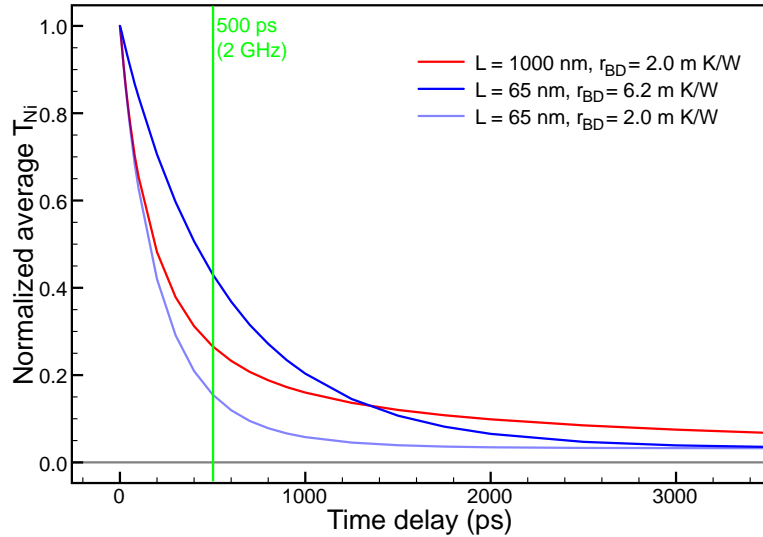


Figure 7.24: Modeling results for best fits to data showing the extracted average temperature of the heated nickel line as a function of time. The red curve shows the best fit to the data from the  $L = 1000$  nm linewidth samples, which gives the bulk value of boundary resistivity. The light blue and dark blue curves are the results for a 65 nm linewidth, using the bulk and best fit values of resistivity respectively. Resistivity values should be  $\times 10^{-9}$ .

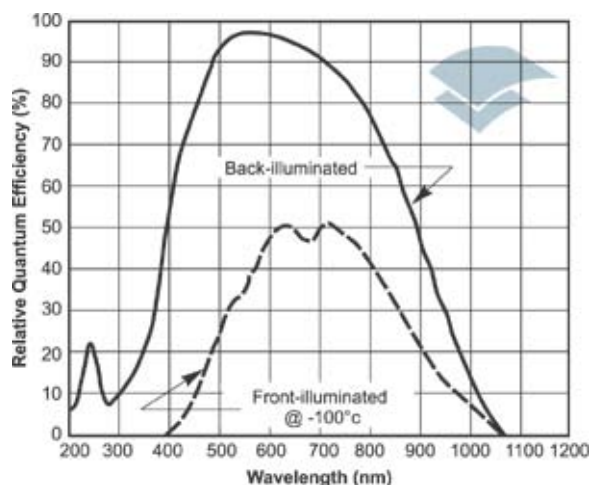


Figure 7.25: Quantum efficiency of Andor CCD as a function of wavelength. Note the zero efficiency above 1100 nm. Figure from [183].

On the other hand, the thermal expansion of silicon is about half as large as that in sapphire, so the signal from the substrate will be smaller.

The concerns about the transparency of the silicon substrate bring up an interesting consideration: using laser light with a longer wavelength to pump the sample (such infrared light can be obtained by downconversion of the 800 nm light from the laser amplifier to a wavelength of 1100-3000 nm using an optical parametric amplifier [182]), would allow for the same backside pumping we used before, and because of the reduced efficiency of silicon-based CCDs in the infrared (see Figure 7.25), may allow for the removal of one or both of the aluminum filters between the sample and the CCD. This would allow for  $3\times$  higher flux on the CCD, could enable faster vacuum pumpdown and venting, and would reduce or eliminate beam deformities caused by transmission through the filters after the sample. In this setup, silicon windows would be used on the cryostat containing the sample to allow the infrared pump light to enter while effectively blocking the optical light in the room.

Another advantage of using a silicon substrate is that as a semiconductor, silicon has a much lower electrical resistivity than sapphire and fused silica. This higher elec-

tron mobility will hopefully allow experiments at low temperature, where the sapphire substrates became quickly contaminated because of space-charge buildup.

## 7.8 Conclusion

In summary, we have observed the transition from diffusive to quasi-ballistic heat transport at nanoscale interfaces smaller than the phonon mean free path. We saw the breakdown of the Fourier law at such short length scales, and demonstrated that heat transfer calculations can be corrected by adding a ballistic correction resistivity proportional to the Knudsen number  $\Lambda/L$ . We also demonstrated that at a basic level, the heat flow from a nanoscale source smaller than the phonon mean free path can be thought of as emanating from a spot the size of the mean free path, which sets a fundamental limit on the ability of the system to handle small hot spots. These experiments advance understanding of heat transport fundamentals, and are important for thermal management and design for integrated circuits.

## Chapter 8

### Magneto-optics with EUV light

Ultrafast magnetism at nanometer scale lengths is a topic directly relevant to industry, since individual bits stored on a hard disk are already of sub-micron dimension. Advances in storage capacity depend on further increases in magnetic storage density. A thorough understanding of switching dynamics is also critical for improving writing speeds commensurate with capacity. Continued technological progress depends on developing an understanding of the dynamics of magnetic systems at a fundamental level, which ultimately requires studies that combine nanometer spatial resolution with femtosecond time resolution. This is a challenging proposition, but one that can be addressed using newly-developed experimental tools. Magneto-optical measurements [184–186] for magnetic properties currently use either x-rays from large-scale synchrotron x-ray facilities or visible-wavelength light from ultrafast lasers. X-rays gives high spatial resolution and high contrast at the elemental absorption edges of the ferromagnetic materials; for example, magnetic soft x-ray microscopy takes advantage of circular dichroism (XMCD - a difference in the absorption of left and right-circularly polarized light near a core-level absorption edge) as a contrast mechanism for the microscope. Using soft x-ray photons 700 eV and zone plate imaging, domain structures with elemental selectivity have been imaged with a resolution of 15 nm [86, 187]. However, with photons from synchrotron radiation, the time resolution is too low to see the fastest dynamics involved in domain switching. Visible ultrafast lasers, on the other hand, give

short pulses ( $\sim 30$  fs), enabling studies in the ultrafast regime using the magneto-optical Kerr effect (MOKE). But magneto-optical signals are usually very small and the long wavelengths used limit these studies to low spatial resolution.

### 8.1 Historical development of the magneto-optic Kerr effect (MOKE)

The field of magneto-optics (MO) has a long history, dating back to 1845, when Michael Faraday observed polarization rotation of light passed through lead-boroilicate glass in a magnetic field [188]. This first observation of the interaction of light with magnetism was followed in 1876 by John Kerr's discovery of a similar effect in reflection [189]. Kerr observed a that linearly polarized light reflecting off of the surface of a magnet experienced an induced polarization ellipticity. He observed a change both when the magnetic field was oriented orthogonal (polar geometry, P-MOKE) and parallel to the surface and the plane of incidence [190] (longitudinal geometry, L-MOKE). The final possible geometry for the Kerr effect (transverse, T-MOKE, where the magnetization of the sample is parallel to the surface but perpendicular to the plane of incidence) was first demonstrated by Zeeman in 1896 [191]. These observations encouraged thinking that light and magnetism were coupled, and played a significant role in the development of the theory of electromagnetism.

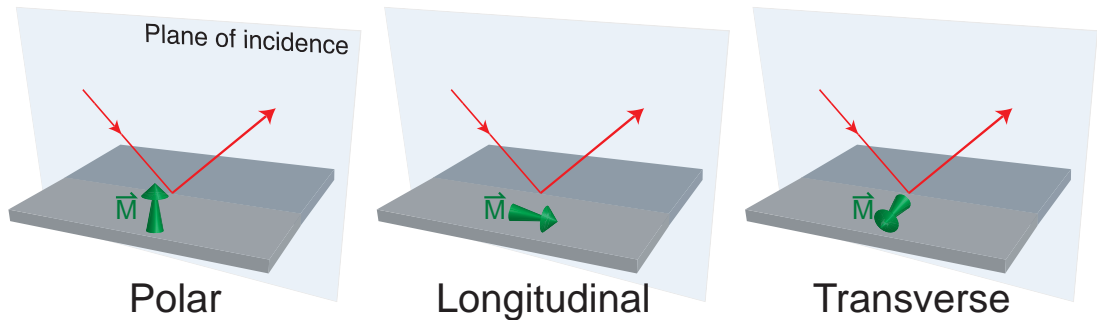


Figure 8.1: The polar, longitudinal, and transverse geometries of the magneto-optic Kerr effect.

More than 100 years later, the Kerr MOKE is still used to make optical measure-

ments of the magnetic properties of materials. At optical wavelengths, the P-MOKE and L-MOKE geometries are commonly used with laser probes with very precise polarization properties, enabling very sensitive measurements of MO polarization rotation. The T-MOKE geometry is less-commonly used however, because although it does not require polarization analysis, T-MOKE signals from 3p transition metals (e.g. Fe, Co, Ni) are small ( $\ll 1\%$  upon full magnetization rotation [192]) when using visible laser probing. However, the strength of the T-MOKE signal is increased at soft x-ray wavelengths where the energy of the incident light is just above or just below absorption edges. Most experiments use the stronger T-MOKE effect at the L edge (700-800 eV), but recent studies have found a change in reflectivity greater than 50% [192] at the M edge (50-70 eV) [192–194]. All past work was performed using a synchrotron source. In this chapter, we describe the first observation of the T-MOKE at the M-edge using a tabletop source of soft x-ray light.

## 8.2 Derivation of the transverse magneto-optic Kerr effect

In the case of EUV probing discussed here, polarization analysis is challenging because of the low transmission of most materials. It can be done using multiple reflections [186, 195, 196], but since each reflection is  $< 1\%$  efficient, the reduction in flux is significant and makes hard experiments even more challenging. For this reason, the fact that T-MOKE can be measured without polarizers greatly simplifies the experiment, and of the magneto-optic effects, we will focus our attention on the specifics of the T-MOKE geometry.

### 8.2.1 Macroscopic (phenomenological) description

The response of isotropic materials to light at a given wavelength can be described by the dielectric constant  $\epsilon$ . This constant connects the electric field  $\vec{E}$  to the displacement  $\vec{D}$  by  $\vec{D} = \epsilon\vec{E}$ . However, the high-symmetry conditions are broken when

a magnetization  $\vec{M}$  is present, and in this case,  $\epsilon$  must now be expressed as a tensor  $\overleftrightarrow{\epsilon}$ , given by

$$\overleftrightarrow{\epsilon} = \epsilon_0 + iQ\vec{M} \times \vec{E}/|\vec{E}|, \quad (8.1)$$

where  $Q$  is a complex material parameter that is roughly proportional to the saturation magnetization of the sample and that describes the strength of the Kerr effect [197].

In the case of a cubic ferromagnet, the dielectric tensor can be expressed in Cartesian coordinates as

$$\overleftrightarrow{\epsilon} = \begin{bmatrix} \epsilon_{xx} & \epsilon_{xy} & \epsilon_{xz} \\ -\epsilon_{xy} & \epsilon_{xx} & \epsilon_{yz} \\ -\epsilon_{xz} & -\epsilon_{yz} & \epsilon_{xx} \end{bmatrix}.$$

The off-diagonal components of the dielectric tensor arise from the occurrence of magnetism, and indicate magneto-optical anisotropy. The Onsager relations  $\epsilon_{mn} = -\epsilon_{nm}$  use symmetry to simplify the off-diagonal components further [198].

In the transverse geometry with the coordinates as defined in Figure 8.2, the magnetic field is in the  $\pm\hat{x}$  direction, so the dielectric tensor reduces to [199]

$$\overleftrightarrow{\epsilon} = \begin{bmatrix} \epsilon_1 & 0 & 0 \\ 0 & \epsilon_1 & \epsilon_2 \\ 0 & -\epsilon_2 & \epsilon_1 \end{bmatrix},$$

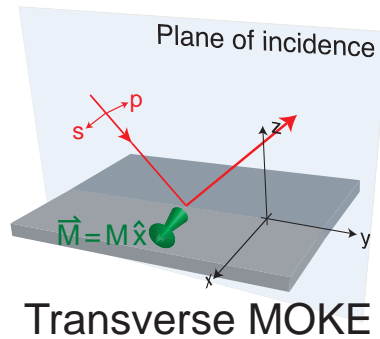


Figure 8.2: Detailed geometry for the transverse magneto-optic Kerr effect. The magnetization is in the  $x$ -direction and the incident light can be  $s$ -polarized ( $x$ -direction, no magnetic signal) or  $p$ -polarized ( $y + z$ -direction, maximum signal).

where  $\epsilon_1$  and  $\epsilon_2$  are the on and off-diagonal elements respectively.

Now that we have an expression for the dielectric permeability, we must step back and consider the fundamental connection between magnetism and the optical response: Maxwell's equations.

$$\vec{\nabla} \cdot \vec{D} = 4\pi\rho \quad (8.2)$$

$$\vec{\nabla} \cdot \vec{B} = 0 \quad (8.3)$$

$$\nabla \times \vec{E} = -\mu_0 \frac{\partial \vec{H}}{\partial t}, \quad (8.4)$$

$$\nabla \times \vec{H} = \epsilon_0 \overleftrightarrow{\epsilon} \cdot \frac{\partial \vec{E}}{\partial t}. \quad (8.5)$$

A laser incident on the surface can be described by a plane electromagnetic wave with  $\vec{E}$  and  $\vec{H}$  given by

$$\begin{aligned} \vec{E} &= \vec{E}_0 \exp(-i(\omega t - \vec{k} \cdot \vec{r})) \\ \vec{H} &= \vec{H}_0 \exp(-i(\omega t - \vec{k} \cdot \vec{r})) \end{aligned} \quad (8.6)$$

where  $\omega$  is the frequency and  $k$  is the wavevector of the incoming laser light. By taking the curl of Equations 8.6, we see that  $\nabla \times \vec{E} = i\vec{k} \times \vec{E}$  and  $\nabla \times \vec{H} = i\vec{k} \times \vec{H}$ . Time derivation of the same equations yields  $\partial \vec{E} / \partial t = -i\omega \vec{E}$  and  $\partial \vec{H} / \partial t = -i\omega \vec{H}$ . These expression can be used in Equations and 8.5 to get  $\vec{k} \times \vec{E} = \omega \mu_0 \vec{H}$  and  $\vec{k} \times \vec{H} = -\omega \epsilon_0 \overleftrightarrow{\epsilon} \cdot \vec{E}$ . We can eliminate  $\vec{H}$  from these equations and use the vector relationship  $\vec{A} \times (\vec{A} \times \vec{B}) = \vec{A}(\vec{A} \cdot \vec{B}) - A^2 \vec{B}$  to arrive at

$$\vec{k}(\vec{k} \cdot \vec{E}) - k^2 \vec{E} + \epsilon_0 \mu_0 \omega^2 \overleftrightarrow{\epsilon} \cdot \vec{E} = 0. \quad (8.7)$$

If we now use the relation for the speed of light  $c = 1/\sqrt{\mu_0 \epsilon_0}$  and define  $\vec{n} \equiv c\vec{k}/\omega$ , then the Fresnel equation results [200]

$$(n^2 \vec{1} - \overleftrightarrow{\epsilon} - \vec{n} : \vec{n}) \cdot \vec{E} = 0, \quad (8.8)$$

with  $\vec{1}$  the identity matrix and  $\vec{n} \cdot \vec{n} = n_i n_j$  the dyadic product. Because the dielectric

tensor is a given, fixed quantity, the normal modes follow from the solutions of

$$\det [n^2 \vec{1} - \overleftarrow{\epsilon} - \vec{n} : \vec{n}]. \quad (8.9)$$

One interesting feature of this expression is that it gives at most two independent vector solutions for  $\vec{n}$  [197]. The eigenmodes for the electric field are also required, and these also follow directly from the solution of Equation 8.9.

In the transverse geometry, the solutions of Equation 8.9 are

$$n_s^2 = \epsilon_1, \quad n_p^2 = \epsilon_1 + \frac{\epsilon_2^2}{\epsilon_1}, \quad (8.10)$$

and we immediately see that there is no magnetic coupling for  $s$ -polarized light because it depends only on  $\epsilon_1$ . The electric field  $k$ -vectors corresponding to these modes are as shown in Figure 8.2:

- $s$ -polarized,  $E_z = E_y = 0$ , so  $\vec{E}_s = E_0 \hat{x}$ ,
- $p$ -polarized,  $E_z = E_y$ ,  $E_x = 0$ , so  $\vec{E}_p = E_0(\hat{y} + \hat{z})/\sqrt{2}$ .

Unique to the transverse geometry, the normal modes of the system are the two directions of linearly-polarized light, unlike the P-MOKE and L-MOKE geometries where circular polarizations comprise the normal modes. This is significant because in the transverse geometry, linearly-polarized light reflected from a magnetic material will experience a magnetism-dependent change in intensity, rather than a polarization rotation. Remarkably, the index of refraction is directly proportional to the off-diagonal component (which is in turn proportional to the magnetization in Equation 8.1), so the change in reflectivity is *directly proportional to the magnetization* in the T-MOKE geometry [201].

### 8.2.2 Microscopic (fundamental) description

To this point, we have considered magneto-optic effects in terms of macroscopic explanations and symmetry arguments. The fundamental origins of the magneto-optical

effect are electron transition selection rules and spin-orbit coupling. In the case of linear,  $p$ -polarized light with components in the  $y$  and  $z$  directions, the selection rules are  $\Delta l = \pm 1$  and  $\Delta m_l = 0, \pm 1$ . Spin-orbit coupling links the orbital momentum  $\vec{L}$  to the spin momentum  $\vec{S}$ , allowing optical probing of the spin state as shown below.

The fundamental quantity of the magneto-optic interaction is not the dielectric tensor, but the conductivity, which is related to the dielectric tensor by

$$\overleftrightarrow{\epsilon} = \overleftrightarrow{1} + 4\pi i \overleftrightarrow{\sigma}. \quad (8.11)$$

Making use of Equation 8.1, which says that the off-diagonal components of the dielectric tensor are proportional to the magnetization  $\vec{M}$ , we see that the conductivity is directly proportional to the magnetization, and by Equation 8.10, directly proportional to the index of refraction (and therefore the detected signal) for  $p$ -polarized light.

The conductivity (and the related off-diagonal components of the dielectric tensor) can be calculated by [197]

$$\sigma_{\alpha\beta} = \frac{\epsilon_1}{4\pi i} = \frac{iq_e^2}{m_e^2 \hbar V} \sum_{nn'} \frac{f(\epsilon_n) - f(\epsilon_{n'})}{\omega_{nn'}} \frac{\Pi_{n'n}^\alpha \Pi_{nn'}^\beta}{\omega^+ - \omega_{nn'}}, \quad (8.12)$$

where  $q_e$  and  $m_e$  are the electron charge and mass,  $E_n$  is the energy of state  $n$ ,  $\hbar\omega_{nn'} = E_n - E_{n'}$ ,  $f(E)$  is the Fermi-Dirac function,  $\Pi_{nn'}^\alpha = \langle n | p_\alpha | n' \rangle$  the matrix element of the momentum operator, and  $\tau$ , the lifetime broadening of the transition [78].

The matrix elements  $\Pi_{nn'}^\alpha$  determine the transition strengths and are proportional to the density of available electron states. In an unmagnetized medium, the  $\uparrow$  and  $\downarrow$  spin states have the same valence levels, but in a magnetized system, the valence levels of the  $\uparrow$  and  $\downarrow$  spin states shift according to  $-\mu \cdot \vec{B}$ , where the magnetic field  $\vec{B}$  is proportional to the magnetization  $\vec{M}$ . This shift of the valence levels, illustrated in the left panel of Figure 8.3, causes an energy shift in the density of electron states dependent on the magnetic spin, illustrated in the top-right of Figure 8.3. The full-contrast magnetic signal( probed by excitation of an inner-shell electron), given by the difference between

the conductivity of the  $\uparrow$  and  $\downarrow$  spin states has an up-down shape centered at the Fermi level, as shown in the bottom right panel of Figure 8.3 [202,203]. If optical probe light is used, the situation is much less clear because the matrix elements are a convoluted mess of smeared contributions from initial and final electron energies that may be anywhere in the continuum, rather than starting with a defined, bound energy. This removes the direct proportionality between magnetization and total signal strength, and gives much smaller and more complex signals [202].

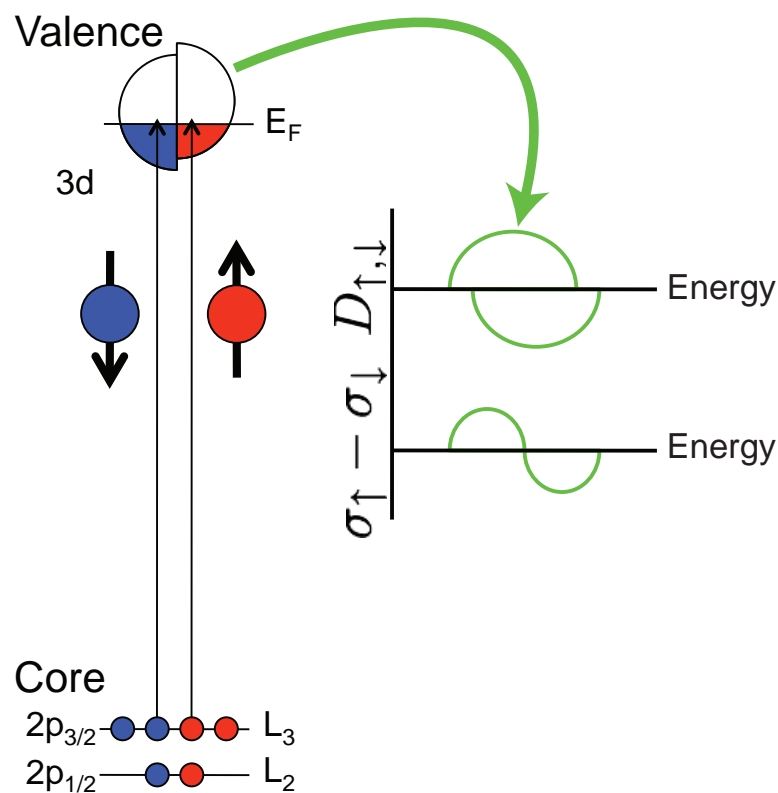


Figure 8.3: Microscopic origin of the magneto-optic Kerr effect at an absorption edge. The applied magnetic field shifts the valence levels for up and down spins relative to each other, which affects the relative density of states. The difference between the available spin-up and spin-down density of states goes into Equation 8.12 for the conductivity, which is proportional to the magneto-optic signal.

### 8.3 Experimental Magneto-Optic Kerr effect using EUV from HHG

Previous experimental studies of magneto-optics in the EUV region of the spectrum have been limited to synchrotron sources. Particularly relevant work is summarized in Figure 8.4, which shows the measured Faraday rotation signal as a function of energy for a permalloy ( $\text{Ni}_{80}\text{Fe}_{20}$ ) sample [194] and the T-MOKE signal near 55 eV from an iron sample [192]. There is great interest in using HHG light for these same sorts of measurements since the source is more accessible and also offers much better temporal resolution.

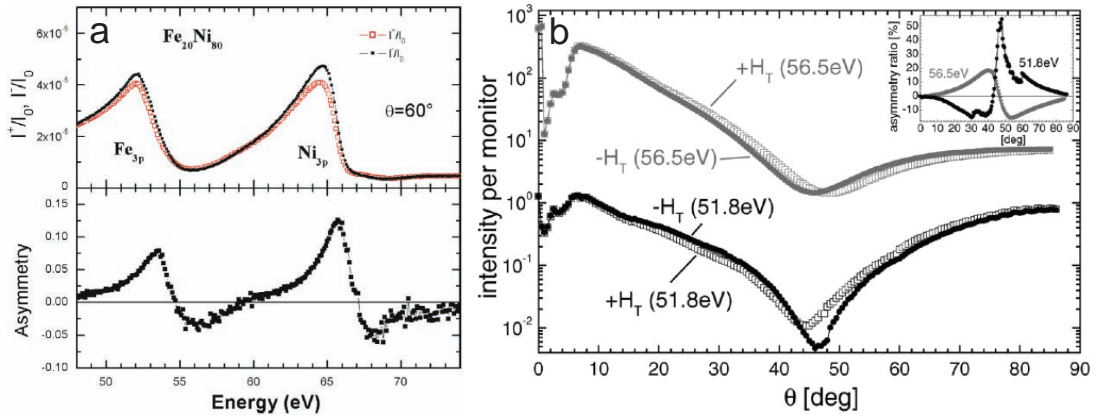


Figure 8.4: Results of previous magneto-optic experiments at the M-edge, demonstrating the expected signal. a) shows results of the Faraday effect on Permalloy, and b) shows angle-resolved measurements on iron.

#### 8.3.1 Experimental setup

In the experiment, we use light from a Ti:sapphire laser amplifier system operated at 3 kHz with an average power of 4.3 W, which we couple into a hollow fused-silica capillary (Figure 8.5a). The capillary is filled with neon gas to phase-match a broad range of harmonics from 42 eV to 72 eV covering both Fe and Ni M-edges, as shown in Figure 8.7. The comb of harmonics emerging from the capillary is separated from the residual driving laser light by transmission through two 200 nm thick aluminum filters.

The harmonics are then focused by a near-glancing reflection from a 2 m focal length gold-coated curved mirror. Finally, they are spectrally resolved by diffraction from a  $1\ \mu\text{m}$  line ( $2\ \mu\text{m}$  period) ferromagnetic permalloy grating, Figure 8.8), and the resulting diffraction is recorded on an x-ray CCD. The Permalloy grating was fabricated by a lift-off process whereby photolithography was used to define the grating pattern over a  $1\ \text{cm} \times 1\ \text{cm}$  area on a thermally oxidized Si wafer. Ion beam deposition was used to deposit a 3 nm Ti seed layer and a 10 nm Permalloy layer which was lifted-off in an ultrasonic acetone bath.

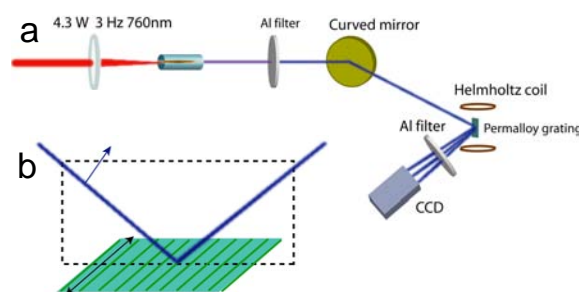


Figure 8.5: Typical CCD image, showing reflected beam containing all harmonics (on left) and diffracted monochromatic stripes (first-order in middle, second-order on right).

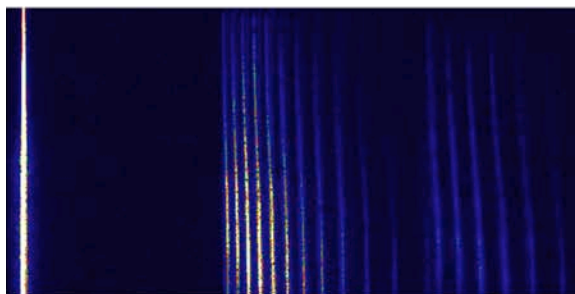


Figure 8.6: Typical CCD image, showing reflected beam containing all harmonics (on left) and diffracted monochromatic stripes (first-order in middle, second-order on right).

A typical energy-calibrated harmonic spectrum is displayed in Figure 8.7, which shows the discrete harmonics diffracting from the permalloy grating. Due to the spherical symmetry of the non-linear medium (noble gas), each harmonic is separated by 3.16

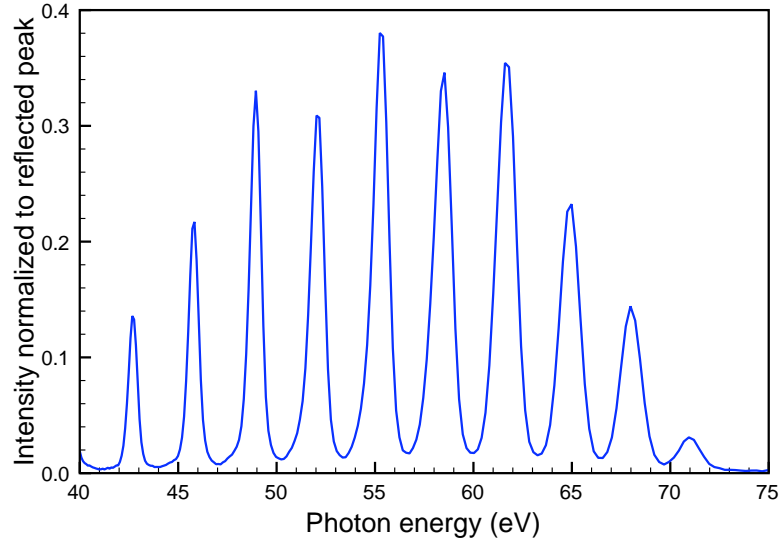


Figure 8.7: Typical harmonic spectrum in neon.

eV, which is twice the photon energy of the fundamental laser light of 1.58 eV. The sudden edge above which no harmonic light is seen corresponds to the strong absorption edge of the aluminum filters at 72 eV. It is then straightforward to calibrate the harmonic spectrum: we identify the photon energy immediately below the Al edge ( $72.5 \text{ eV}/1.58 \text{ eV} = 45.8$  harmonic order at cutoff, so last harmonic before absorption edge is given by  $1.58 \text{ eV} \times 45 = 71.1 \text{ eV}$ ) and determine the energies of the lower harmonics accordingly. The angle of incidence and the position of higher diffraction orders can also be related to this information by an oblique incidence diffraction formula for a grating.

The system is set up in a transverse geometry (T-MOKE), i.e. the magnetic field is applied perpendicular to the plane of incidence, as shown in Figure 8.5a. Since only p-polarized light contributes to the T-MOKE signal, we rotate the polarization of the fundamental laser light, which minimizes the reflected intensity of harmonics from the sample. The sample magnetization is oriented by a Helmholtz coil capable of producing magnetic fields as large as  $\pm 60$  Gauss, well above the coercivity field (field required to reverse the magnetization) of the permalloy of  $\sim 10$  Gauss. The coil must be water-cooled since it is inside a vacuum chamber with a pressure of  $10^{-5}$  torr.

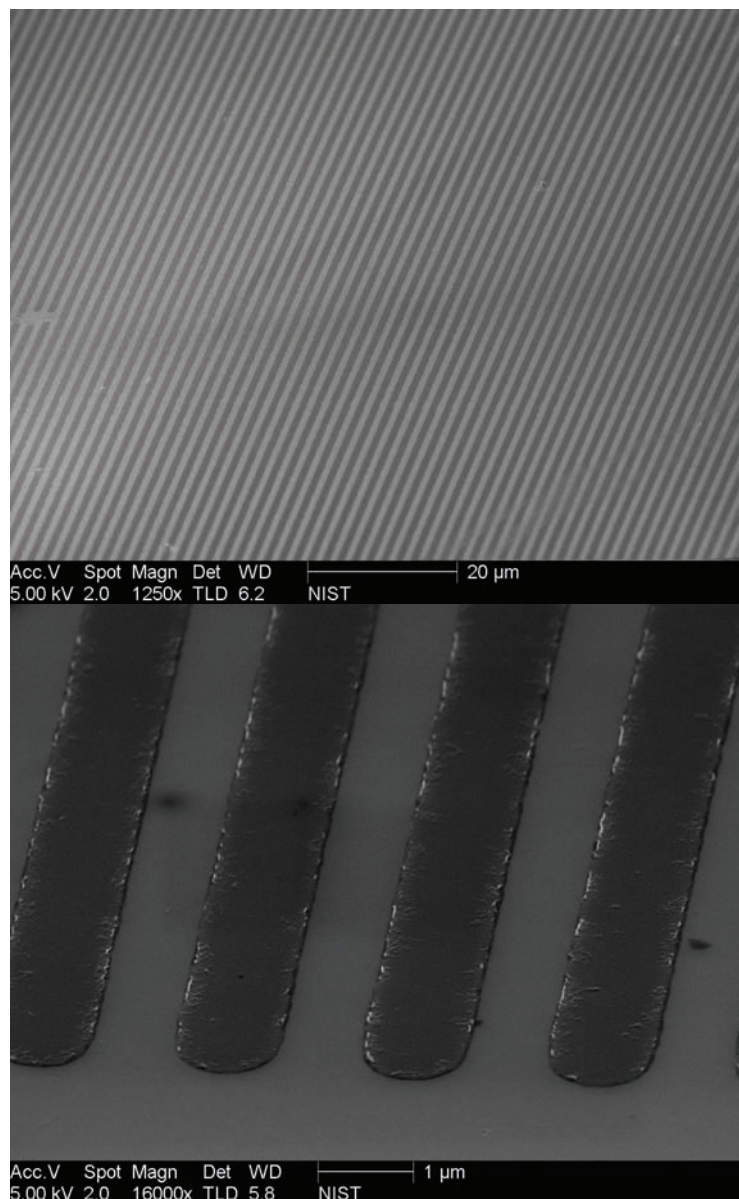


Figure 8.8: Scanning electron microscope images of a permalloy grating fabricated by Justin Shaw at NIST Boulder, shown at  $1250\times$  (top) and  $16000\times$  (bottom) magnification. The ferromagnetic permalloy ( $\text{Ni}_{80}\text{Fe}_{20}$ ) stripes are  $1\ \mu\text{m}$  wide and separated by  $2\ \mu\text{m}$  (center-to-center), with a height of 10 nm.

The diffracted harmonic intensities are measured at magnetic fields of  $\pm 60$  Gauss and expressed in terms of asymmetry, defined in Equation 8.13. In order to improve the signal-to-noise level of the measurement, we alternate the field between  $+60$  and  $-60$  Gauss (to flip the magnetization completely, as shown in Figure 8.5b) between each

exposure of the harmonic spectrum, and average these two sets of exposures before calculating the asymmetry. This removes low frequency noise due to slow drifts in the harmonic intensity and pointing.

### 8.3.2 Magnetic contrast measured with EUV light from HHG

This geometry enables straightforward detection of the magnetic state with soft x-ray light. The strength of the T-MOKE is traditionally reported in terms of asymmetry between two magnetization states, defined as

$$A = \frac{I_{\uparrow} - I_{\downarrow}}{I_{\uparrow} + I_{\downarrow}} \quad (8.13)$$

where  $I_{\uparrow}$  and  $I_{\downarrow}$  denote the reflected intensities recorded for the two magnetizations. The shape of the resulting asymmetry for different incidence angles of the probe light is shown in Figure 8.10 as the colored lines. Large changes in sign and magnitude of asymmetry are found at M absorption edges of Ni (67 eV) and Fe (55 eV). Because the T-MOKE signal is so strong at the absorption edges, the signal is clearly visible after only a second of acquisition, and a signal-to-noise ratio of more than 30 is evident in 100 seconds. The shape of the asymmetry, shown along with raw spectral data from the CCD in Figure 8.9, is in agreement with both theoretical arguments based on spin-orbit coupling in the valence band discussed in section 8.2.2, and with the measurement of Faraday rotation in a permalloy film using synchrotron radiation [194]. We also show the dependence of the T-MOKE signal on polarization by repeating the measurement with s-polarized light, where we see no asymmetry, as shown in Figure 8.10. We measure asymmetries up to 6% near the Ni M-edge, when the angle of incidence of the probe light is nearest 45 degrees [185], and observe a decrease as the angle of incidence is increased.

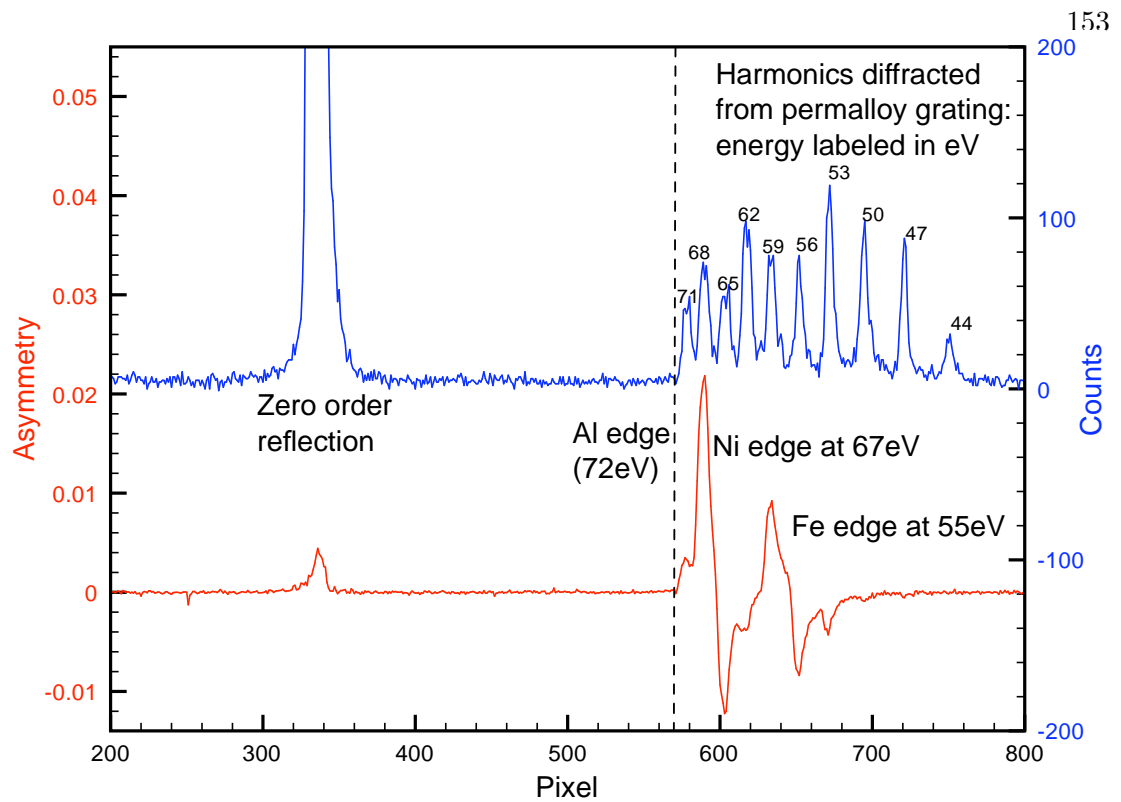


Figure 8.9: Spectral data from CCD. The blue curve (right axis) shows the total counts measured in a single 100 ms exposure (data collected by full vertical binning an image, as shown in Figure 8.6). The red curve (left axis) shows the asymmetry after a series of exposures with the magnetization alternating between up and down.

### 8.3.3 Hysteresis measurement

In order to demonstrate the use of the HHG source as a useful analytical probe of magnetization, we measured the hysteresis of the asymmetry, which is proportional to magnetization. Figure 8.11 shows three hysteresis loops: the first one (a) monitoring the harmonic close to the Ni edge, the second (b) close to the Fe edge, and the third (c) is data from an element-insensitive optical measurement of the T-MOKE signal [204]. As expected, both edges yield identical hysteresis loops, with a coercivity field of around 10 Gauss.

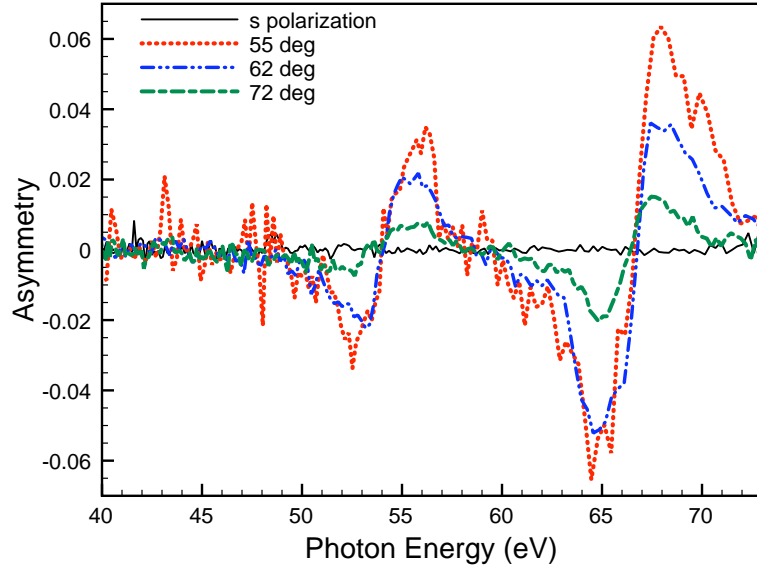


Figure 8.10: Magnetic asymmetry from the permalloy grating sample at various angles of incidence from normal (p-polarized light). The asymmetry increases as the angle of incidence approaches  $45^\circ$ , since  $\vec{M} \times \vec{E}$  is maximized there (see Equation 8.1). Also shown is data from s-polarized light, which shows no asymmetry, as expected from Equation 8.10.

### 8.3.4 Surface sensitivity measurement

As with soft x-ray light from other sources, light from HHG interacts strongly with most materials, and the short penetration depth can be utilized to examine surface-sensitive processes. Furthermore, light just below an absorption edge has a penetration depth  $\sim 4\times$  longer than light above the edge [26], so depth-dependent properties of magnetic materials can be measured with elemental specificity.

In order to demonstrate the surface sensitivity of this technique, we measure the asymmetry of permalloy gratings with nonmagnetic palladium films of different thickness coated on top, as shown in Figure 8.12. Here a series of identical Permalloy gratings had varying thickness (2 - 15 nm) of sputtered Pd deposited on top. Pd was used since it doesn't oxidize or have an M-edge signature near that of Ni or Fe. This allows us to systematically bury the Permalloy and measure how quickly the signal decays for Fe and Ni strictly from adsorption by the Pd. We perform the measurements at an angle of

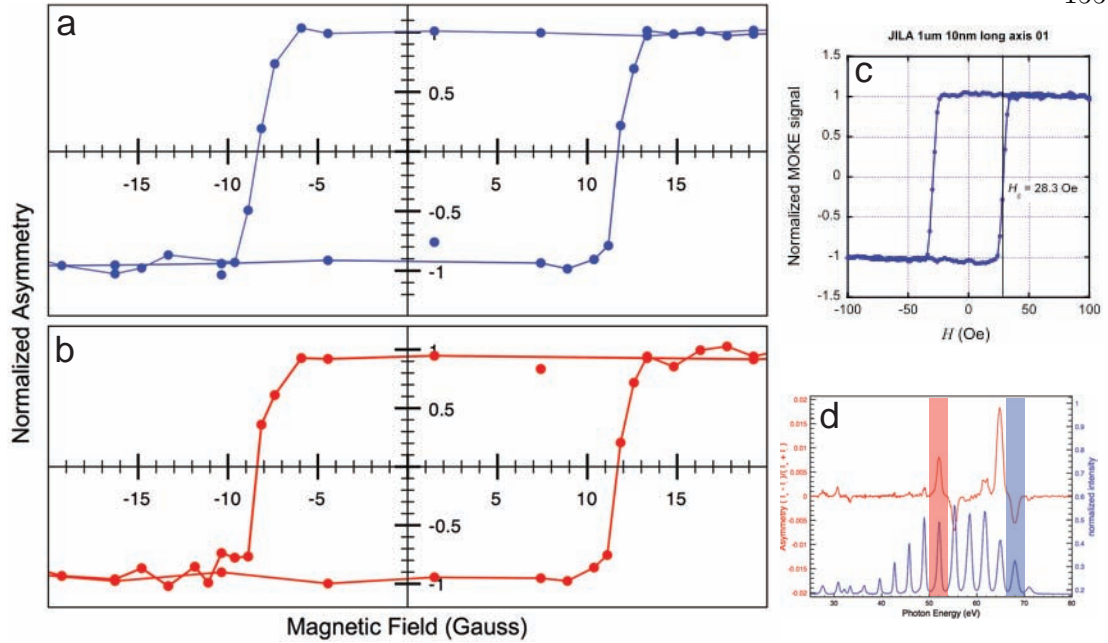


Figure 8.11: EUV measurement of element-specific asymmetry as a function of magnetic field (hysteresis) near the nickel (a) and iron (b) edges, with the selected regions for (a) and (b) highlighted in (d). Part (c) shows an optical hysteresis measurement performed in the Silva lab at NIST, Boulder [204].

incidence of 63 degrees, where we had observed good reflectivity of p-polarized light as well as a high asymmetry value (see Figure 8.10). The measured asymmetries near the Ni and Fe absorption edges are plotted in Figure 8.13 as a function of permalloy capping layer thickness. The measurements show an exponential decay of the asymmetry as a function of the capping layer thickness. Exponential fits give decay constants of 3.01 nm (Ni edge) and 2.67 nm (Fe edge). This shallow penetration depth shows the potential for using this technique as a surface-sensitive probe for characterization of magnetic structure, and also for surface magnetization imaging.

#### 8.4 Outlook: EUV measurement of demagnetization dynamics

As discussed in Chapter 3, HHG offers significant advantages over other sources of EUV light because the sub-10 fs pulse duration [48] provides excellent temporal resolution for dynamics measurements. This makes HHG an ideal light source for studying

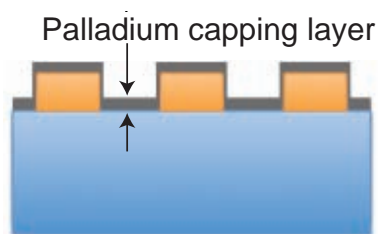


Figure 8.12: Schematic demonstrating the presence of the palladium capping layer, present over the whole surface (not just the nanostructure).

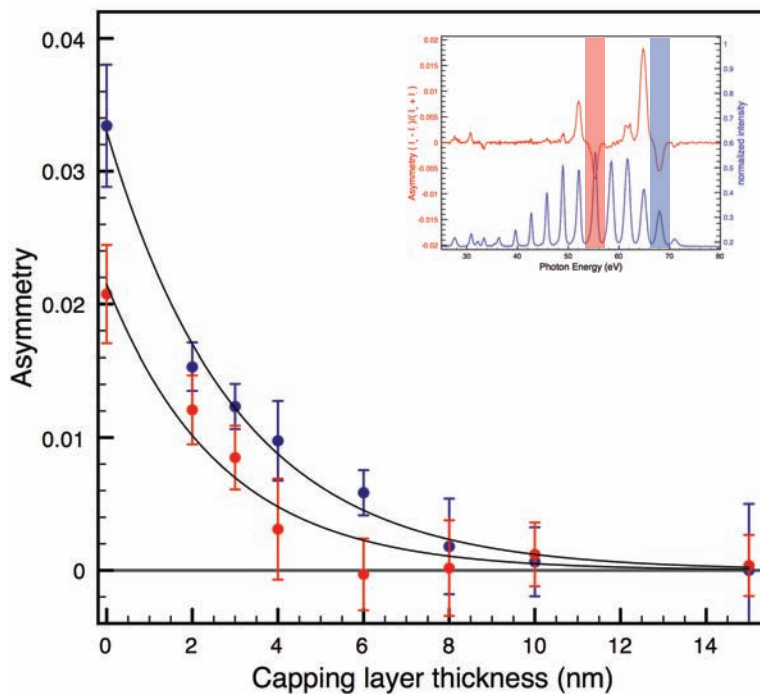


Figure 8.13: Measurement of element-specific asymmetry as a function of capping layer thickness. The red and blue data correspond to data taken at the harmonics labelled in the inset. In each case, the penetration depth was measured to be 3 nm, demonstrating the highly surface-sensitive nature of the measurement.

demagnetization dynamics following thermal excitation by an ultrashort intense laser pulse [205–207]. The pulse duration advances the currently available soft x-ray source resolution of the fs slicing of synchrotron radiation by more than an order of magnitude [208].

Because the soft x-ray light from HHG is fully spatially coherent [46], coherent

diffractive imaging techniques can be applied to magnetic systems in order to determine the domain sizes and patterning which can scale from a few  $\mu\text{m}$  down to few nm. The lensless imaging techniques demonstrated by Sandberg et. al [61] could be adapted to magnetic systems as a new microscope for observing magnetic domain patterns similar to the Fresnel-zone plate technique [86] or a scanning Kerr microscope [209]. This technique could be applied to image magnetic orientation in nanostructures, where exotic effects are predicted [210, 211].

## 8.5 Conclusion

We measure the T-MOKE effect on permalloy at the M-edges of Fe and Ni with soft x-ray light from a HHG source. By using photon energies near absorption edges of the elements of interest, the T-MOKE signal is much higher than at optical wavelengths and the information about a magnetic material can be measured with elemental specificity, high signal-to-noise, and short acquisition time. We find high asymmetries at 55 eV (4%) and 65 eV (6%), corresponding to the absorption edges of Fe and Ni, respectively. We further demonstrate that light from HHG is a useful source for studying magnetic materials by the measurement of hysteresis and the surface sensitivity of the asymmetry. This work enables many further possibilities for a tabletop ultrafast light source to study magnetic systems.

## Chapter 9

### Conclusion

One exciting aspect about applying EUV light to surface science is the broad range of available phenomena that EUV light lends itself to studying. In this thesis, I have focused on the application of Extreme Ultraviolet/soft x-ray light from high-order harmonic generation to study acoustic, thermal, and magnetic processes in nanostructures. In the previous chapters, we:

- Performed dynamic EUV holography and surface displacement measurement with sub-picometer sensitivity [212]. In this experiment, we demonstrated the fact that in the EUV region of the electromagnetic spectrum, small density changes do not change the index of refraction, so our surface displacement measurement was unpolluted by changes in reflectivity that dominate optical measurements.
- Made a dynamic measurement of surface acoustic wave propagation, observing the highest-frequency narrowband SAWs ever detected optically and the dispersive effect of acoustic propagation in a nanostructure [213]. Here, we took advantage of the full spatial coherence of phase-matched harmonic generation [46].
- Observed quasi-ballistic thermal transport away from a nanostructured heat source, and quantified the size-dependent error in the Fourier law [120]. This experiment utilized the short wavelength of the EUV light to not only diffract from sub-100 nm structures that would be undetectable to optical light, but also

provide a sensitive, interferometric measurement of displacement that could be connected to temperature.

- Probed the magnetic orientation using the T-MOKE for the first time using EUV light from HHG [214]. Here, we took advantage of the elemental selectivity of the EUV light: by looking at photon energies near an atomic absorption edge, we saw a significant increase in magnetic signal and were able to measure the magnetic orientation of an alloy with elemental specificity.

Each of the last three chapters detailing experimental observation of surface acoustic wave (Chapter 6), thermal (Chapter 7) and magnetic (Chapter 8) effects in nanostructures included a brief description of the immediate future of that experiment. Indeed, the future is bright for application of EUV light from high-order harmonic generation to study surface science. Of course, the real power of these experiments lies in the short wavelength of the EUV probe light. We are currently taking advantage of surface sensitivity (and elemental selectivity in the magnetic studies), but the potential for small spot sizes and diffraction from very small objects has not yet been explored in the context of thermally-sensitive measurements. Probing of a small spot on an isolated nanostructure would enable other experimental possibilities studying a broad range of phenomena, such as:

- In acoustics experiments, high-resolution surface profile imaging would give insight into the acoustic mode shaping as a surface acoustic wave passes through a nanostructure.
- Time-resolved thermal microscopy of the surface near a sub-100 nm line would give direct insight into the dynamic evolution of the non-local temperature distribution shown schematically in Figure 7.1.
- Dynamic microscopy of magnetic systems offers the potential to time-resolve

the magnetic orientation of sub-100 nm domains, something no other tabletop source can do.

The simultaneously short pulse duration and short photon wavelength of EUV light from HHG makes it a uniquely useful tool in studying fundamental length and time scales of processes. This thesis has discussed some of the first applications of this source to study acoustic, thermal, and magnetic effects in nanostructures, and the future prospects for dynamic imaging these and other effects with sub-10 fs time resolution and sub-100 nm spatial resolution is very exciting.

## Bibliography

- [1] C. A. Paddock and G. L. Eesley, "Transient thermorefectance from thin metal films," Journal of Applied Physics, vol. 60, no. 1, pp. 285–290, Jul 1986.
- [2] M. Berglund, L. Rymell, M. Peuker, T. Wilhein, and H. Hertz, "Compact water-window transmission X-ray microscopy," Journal of Microscopy- Oxford, vol. 197, no. Part 3, pp. 268–273, Mar 2000.
- [3] J. M. Schins, P. Breger, P. Agostini, R. C. Constantinescu, H. G. Muller, G. Grillon, A. Antonetti, and A. Mysyrowicz, "Observation of laser-assisted auger decay in argon," Phys. Rev. Lett., vol. 73, no. 16, pp. 2180–2183, Oct 1994.
- [4] D. E. Sayers, E. A. Stern, and F. W. Lytle, "New technique for investigating noncrystalline structures: Fourier analysis of the extended x-ray absorption fine structure," Physical Review Letters, vol. 27, p. 1204, 1971.
- [5] N. W. Ashcroft and N. D. Mermin, Solid State Physics. Holt, Rinehart, and Winston, 1976.
- [6] M. Born and E. Wolf, Principles of Optics. Pergamon Press, Oxford, 1980.
- [7] D. vonderLinde, K. Sokolowski-Tinten, and J. Bialkowski, "Laser-solid interaction in the femtosecond time regime," Applied Surface Science, vol. 110, pp. 1–10, Feb 1997.
- [8] R. W. Schoenlein, W. Z. Lin, J. G. Fujimoto, and G. L. Eesley, "Femtosecond studies of nonequilibrium electronic processes in metals," Phys. Rev. Lett., vol. 58, no. 16, pp. 1680–1683, Apr 1987.
- [9] D. E. Spence, P. N. Kean, and W. Sibbett, "60-fsec pulse generation from a self-mode-locked ti:sapphire laser," Opt. Lett., vol. 16, no. 1, pp. 42–44, 1991. [Online]. Available: <http://ol.osa.org/abstract.cfm?URI=ol-16-1-42>
- [10] M. T. Asaki, C.-P. Huang, D. Garvey, J. Zhou, H. C. Kapteyn, and M. M. Murnane, "Generation of 11-fs pulses from a self-mode-locked ti:sapphire laser," Opt. Lett., vol. 18, no. 12, pp. 977–979, 1993. [Online]. Available: <http://ol.osa.org/abstract.cfm?URI=ol-18-12-977>
- [11] W. R. Rapoport and C. P. Khattak, "Titanium sapphire laser characteristics," Appl. Opt., vol. 27, no. 13, pp. 2677–2684, 1988. [Online]. Available: <http://ao.osa.org/abstract.cfm?URI=ao-27-13-2677>

- [12] S. Backus, R. Bartels, S. Thompson, R. Dollinger, H. C. Kapteyn, and M. M. Murnane, "High-efficiency, single-stage 7-khz high-average-power ultrafast laser system," Opt. Lett., vol. 26, no. 7, pp. 465–467, 2001.
- [13] J. Hohlfeld, S. S. Wellershoff, J. Gudde, U. Conrad, V. Jahnke, and E. Matthias, "Electron and lattice dynamics following optical excitation of metals," Chemical Physics, vol. 251, no. 1-3, pp. 237–258, Jan 2000.
- [14] Luxpop online collection of optical properties of materials. [Online]. Available: [www.luxpop.com](http://www.luxpop.com)
- [15] S. I. Anisimov, "Effect of very short laser pulses on absorbing substances," Soviet Physics JETP, vol. 31, no. 1, July 1970.
- [16] S. Anisimov, B. Kapeliovich, and T. Perel'man, "Electron emission from metal surfaces exposed to ultrashort laser pulses," Soviet Physics JETP, vol. 39, no. 2, August 1974.
- [17] Z. B. Lin and L. V. Zhigilei, "Temperature dependences of the electron-phonon coupling, electron heat capacity and thermal conductivity in ni under femtosecond laser irradiation," Applied Surface Science, vol. 253, no. 15, pp. 6295–6300, May 2007.
- [18] G. M. Mueller, J. Walowski, M. Djordjevic, G.-X. Miao, A. Gupta, A. V. Ramos, K. Gehrke, V. Moshnyaga, K. Samwer, J. Schmalhorst, A. Thomas, A. Huetten, G. Reiss, J. S. Moodera, and M. Muenzenberg, "Spin polarization in half-metals probed by femtosecond spin excitation," Nature Materials, vol. 8, no. 1, pp. 56–61, Jan 2009.
- [19] G. Chen, Nanoscale Energy Transport and Conversion. Oxford University Press, 2005.
- [20] P. Chantrenne, M. Raynaud, D. Baillis, and J. L. Barrat, "Study of phonon heat transfer in metallic solids from molecular dynamic simulations," Microscale Thermophysical Engineering, vol. 7, no. 2, pp. 117–136, Apr-Jun 2003.
- [21] P. Kapitza, "The study of heat transfer in helium ii," J. Phys. (USSR), vol. 4, p. 181, 1941.
- [22] E. T. Swartz and R. O. Pohl, "Thermal-boundary resistance," Reviews of Modern Physics, vol. 61, no. 3, pp. 605–668, Jul 1989.
- [23] P. E. Hopkins, P. M. Norris, and R. J. Stevens, "Influence of inelastic scattering at metal-dielectric interfaces," Journal of Heat Transfer, vol. 130, no. 2, p. 022401, 2008.
- [24] Wikipedia, "Thermal contact conductance." [Online]. Available: [http : //en.wikipedia.org/wiki/Thermal\\_contact\\_conductance](http://en.wikipedia.org/wiki/Thermal_contact_conductance)
- [25] D. Attwood, Soft X-Rays and Extreme Ultraviolet Radiation. Cambridge University Press, 1999.

- [26] E. Gullikson, “X-ray interactions with matter, center for x-ray optics,” 2009. [Online]. Available: [http://henke.lbl.gov/optical\\_constants/](http://henke.lbl.gov/optical_constants/)
- [27] H. Kapteyn, M. Murnane, and I. Christov, “Extreme Nonlinear Optics: Coherent X Rays from Lasers,” *Physics Today*, vol. 58, no. 3, pp. 030 000–44, Mar. 2005.
- [28] J. Krause, K. Schafer, and K. Kulander, “High-order Harmonic Generation from Atoms and Ions in the High-Intensity Regime,” *Physical Review Letters*, vol. 68, no. 24, pp. 3535–3538, Jun 15 1992.
- [29] T. Auguste, B. Carre, and P. Salieres, “Quasi-phase-matching of high-order harmonics using a modulated atomic density,” *Physical Review A*, vol. 76, no. 1, JUL 2007.
- [30] T. Pfeifer and M. C. Downer, “Direct experimental observation of periodic intensity modulation along a straight hollow-core optical waveguide,” *Journal of the Optical Society of America B-Optical Physics*, vol. 24, no. 5, pp. 1025–1029, May 2007.
- [31] P. Corkum, “Plasma perspective on Strong-field Multiphoton Ionization,” *Physical Review Letters*, vol. 71, no. 13, pp. 1994–1997, SEP 27 1993.
- [32] M. Lewenstein, P. Balcou, M. Ivanov, A. LHuillier, and P. Corkum, “Theory of High-Harmonic-Generation by Low-Frequency Laser Fields,” *Physical Review A*, vol. 49, no. 3, pp. 2117–2132, Mar 1994.
- [33] L. Keldysh, “Ionization in field of a strong electromagnetic wave,” *Soviet Physics JETP-USSR*, vol. 20, no. 5, p. 1307, 1965.
- [34] M. Ammosov, N. Delone, and V. Krainov, “Tunnel ionization of complex atoms and of atomic ions in an alternating electromagnetic field,” *Soviet Physics JETP-USSR*, vol. 64, no. 6, p. 1191, 1986.
- [35] A. Scrinzi, M. Geissler, and T. Brabec, “Ionization above the coulomb barrier,” *Physical Review Letters*, vol. 83, no. 4, p. 706, 1999.
- [36] P. Balcou, P. Salieres, A. LHuillier, and M. Lewenstein, “Generalized phase-matching conditions for high harmonics: The role of field-gradient forces,” *Physical Review A*, vol. 55, no. 4, pp. 3204–3210, Apr 1997.
- [37] M. Lewenstein, P. Salieres, and A. LHuillier, “Phase of the Atomic Polarization in High-order-Harmonic Generation,” *Physical Review A*, vol. 52, no. 6, pp. 4747–4754, Dec 1995.
- [38] X. Zhang, A. L. Lytle, O. Cohen, M. M. Murnane, and H. C. Kapteyn, “Quantum-path control in high-order harmonic generation at high photon energies,” *New Journal of Physics*, vol. 10, Feb 29 2008.
- [39] C. G. Durfee, A. R. Rundquist, S. Backus, C. Herne, M. M. Murnane, and H. C. Kapteyn, “Phase matching of high-order harmonics in hollow waveguides,” *Phys. Rev. Lett.*, vol. 83, no. 11, pp. 2187–2190, Sep 1999.

- [40] A. Rundquist, C. Durfee, Z. Chang, C. Herne, S. Backus, M. Murnane, and H. Kapteyn, "Phase-matched generation of coherent soft X-rays," *Science*, vol. 280, no. 5368, pp. 1412–1415, May 29 1998.
- [41] A. Paul, R. A. Bartels, R. Tobey, H. Green, S. Weiman, I. P. Christov, M. M. Murnane, H. C. Kapteyn, and S. Backus, "Quasi-phase-matched generation of coherent extreme-ultraviolet light," *Nature*, vol. 421, no. 6918, pp. 51–54, 01 2003/01/02/print. [Online]. Available: <http://dx.doi.org/10.1038/nature01222>
- [42] X. Zhang, A. L. Lytle, T. Popmintchev, X. Zhou, H. C. Kapteyn, M. M. Murnane, and O. Cohen, "Quasi-phase-matching and quantum-path control of high-harmonic generation using counterpropagating light," *Nat Phys*, vol. 3, no. 4, pp. 270–275, 04 2007/04//print. [Online]. Available: <http://dx.doi.org/10.1038/nphys541>
- [43] P. Salieres, A. L'Huillier, and M. Lewenstein, "Coherence control of high-order harmonics," *Physical Review Letters*, vol. 74, no. 19, pp. 3776–3779, May 1995.
- [44] T. Ditmire, E. T. Gumbrell, R. A. Smith, J. W. G. Tisch, D. D. Meyerhofer, and M. H. R. Hutchinson, "Spatial coherence measurement of soft x-ray radiation produced by high order harmonic generation," *Phys. Rev. Lett.*, vol. 77, no. 23, pp. 4756–4759, Dec 1996.
- [45] P. Salieres, T. Ditmire, M. Perry, A. L'Huillier, and M. Lewenstein, "Angular distributions of high-order harmonics generated by a femtosecond laser," *Journal of Physics B-Atomic Molecular and Optical Physics*, vol. 29, no. 20, pp. 4771–4786, Oct 28 1996.
- [46] R. A. Bartels, A. Paul, H. Green, H. C. Kapteyn, M. M. Murnane, S. Backus, I. P. Christov, Y. W. Liu, D. Attwood, and C. Jacobsen, "Generation of spatially coherent light at extreme ultraviolet wavelengths," *Science*, vol. 297, no. 5580, pp. 376–378, Jul 2002.
- [47] E. Constant, D. Garzella, P. Breger, E. Mével, C. Dorrer, C. Le Blanc, F. Salin, and P. Agostini, "Optimizing high harmonic generation in absorbing gases: Model and experiment," *Physical Review Letters*, vol. 82, no. 8, pp. 1668–1671, Feb 1999.
- [48] L. Miaja-Avila, C. Lei, M. Aeschlimann, J. L. Gland, M. M. Murnane, H. C. Kapteyn, and G. Saathoff, "Laser-assisted photoelectric effect from surfaces," *Physical Review Letters*, vol. 97, no. 11, p. 113604, Sep 15 2006.
- [49] A. L. Lytle, X. Zhang, P. Arpin, O. Cohen, M. M. Murnane, and H. C. Kapteyn, "Quasi-phase matching of high-order harmonic generation at high photon energies using counterpropagating pulses," *Opt. Lett.*, vol. 33, no. 2, pp. 174–176, 2008. [Online]. Available: <http://ol.osa.org/abstract.cfm?URI=ol-33-2-174>
- [50] T. Popmintchev, M.-C. Chen, O. Cohen, M. E. Grisham, J. J. Rocca, M. M. Murnane, and H. C. Kapteyn, "Extended phase matching of high harmonics driven by mid-infrared light," *Opt. Lett.*, vol. 33, no. 18, pp. 2128–2130, 2008. [Online]. Available: <http://ol.osa.org/abstract.cfm?URI=ol-33-18-2128>

- [51] X. Zhou, R. Lock, W. Li, N. Wagner, M. M. Murnane, and H. C. Kapteyn, "Molecular recollision interferometry in high harmonic generation," *Physical Review Letters*, vol. 100, no. 7, Feb 22 2008.
- [52] W. Li, X. Zhou, R. Lock, S. Patchkovskii, A. Stolow, H. C. Kapteyn, and M. M. Murnane, "Time-Resolved Dynamics in N<sub>2</sub>O<sub>4</sub> Probed Using High Harmonic Generation," *Science*, vol. 322, no. 5905, pp. 1207–1211, Nov 21 2008.
- [53] E. Gagnon, P. Ranitovic, X.-M. Tong, C. L. Cocke, M. M. Murnane, H. C. Kapteyn, and A. S. Sandhu, "Soft X-ray-driven femtosecond molecular dynamics," *Science*, vol. 317, no. 5843, pp. 1374–1378, SEP 7 2007.
- [54] A. S. Sandhu, E. Gagnon, R. Santra, V. Sharma, W. Li, P. Ho, P. Ranitovic, C. L. Cocke, M. M. Murnane, and H. C. Kapteyn, "Observing the Creation of Electronic Feshbach Resonances in Soft X-ray-Induced O-2 Dissociation," *Science*, vol. 322, no. 5904, pp. 1081–1085, Nov 14 2008.
- [55] R. I. Tobey, "Linear and nonlinear photo-acoustic spectroscopy with extreme ultraviolet radiation," Ph.D. dissertation, University of Colorado, 2006.
- [56] L. Miaja-Avila, G. Saathoff, S. Mathias, J. Yin, C. La-o vorakiat, M. Bauer, M. Aeschlimann, M. M. Murnane, and H. C. Kapteyn, "Direct measurement of core-level relaxation dynamics on a surface-adsorbate system," *Physical Review Letters*, vol. 101, no. 4, p. 046101, Jul 25 2008.
- [57] W. Chao, B. Harteneck, J. Liddle, E. Anderson, and D. Attwood, "Soft X-ray microscopy at a spatial resolution better than 15nm," *Nature*, vol. 435, no. 7046, pp. 1210–1213, Jun 30 2005.
- [58] J. Miao, P. Charalambous, J. Kirz, and D. Sayre, "Extending the methodology of x-ray crystallography to allow imaging of micrometre-sized non-crystalline specimens," *Nature*, vol. 400, no. 6742, pp. 342–344, 07 1999. [Online]. Available: <http://dx.doi.org/10.1038/22498>
- [59] R. L. Sandberg, A. Paul, D. A. Raymondson, S. Haedrich, D. M. Gaudiosi, J. Holtsnider, R. I. Tobey, O. Cohen, M. M. Murnane, and H. C. Kapteyn, "Lensless diffractive imaging using tabletop coherent high-harmonic soft-x-ray beams," *Physical Review Letters*, vol. 99, no. 9, p. 098103, Aug 31 2007.
- [60] A. J. Paul, "Coherent euv light from high-order harmonic generation: Enhancement and applications to coherent euv light from high-order harmonic generation: Enhancement and applicaitons to lensless diffractive imaging," Ph.D. dissertation, University of Colorado, 2007.
- [61] R. Sandberg, D. Raymondson, W. Slaughter, M. Murnane, and H. Kapteyn, "Closing the gap to the diffraction limit: Tabletop soft x-ray fourier transform holography," *Optics Letters*, 2009 (In press).
- [62] D. J. Funk, D. S. Moore, S. D. McGrane, J. H. Reho, and R. L. Rabie, "Ultrafast spatial interferometry: a tool for characterizing material phase and hydrodynamic motion in laser-excited metals," *Applied Physics A-Materials Science & Processing*, vol. 81, no. 2, pp. 295–302, Jul 2005.

- [63] V. Temnov, K. Sokolowski-Tinten, P. Zhou, and D. von der Linde, “Femtosecond time-resolved interferometric microscopy,” Applied Physics A-Materials Science & Processing, vol. 78, no. 4, pp. 483–489, Mar 2004.
- [64] D. H. Hurley and O. B. Wright, “Detection of ultrafast phenomena by use of a modified sagnac interferometer,” Opt. Lett., vol. 24, no. 18, pp. 1305–1307, 1999. [Online]. Available: <http://ol.osa.org/abstract.cfm?URI=ol-24-18-1305>
- [65] J. Filevich, J. J. Rocca, M. C. Marconi, R. F. Smith, J. Dunn, R. Keenan, J. R. Hunter, S. J. Moon, J. Nilsen, A. Ng, and V. N. Shlyaptsev, “Picosecond-resolution soft-x-ray laser plasma interferometry,” Appl. Opt., vol. 43, no. 19, pp. 3938–3946, 2004. [Online]. Available: <http://ao.osa.org/abstract.cfm?URI=ao-43-19-3938>
- [66] C. Chang, E. Anderson, P. Naulleau, E. Gullikson, K. Goldberg, and D. Attwood, “Direct measurement of index of refraction in the extreme-ultraviolet wavelength region with a novel interferometer,” Opt. Lett., vol. 27, no. 12, pp. 1028–1030, 2002. [Online]. Available: <http://ol.osa.org/abstract.cfm?URI=ol-27-12-1028>
- [67] G. L. Eesley, “Generation of nonequilibrium electron and lattice temperatures in copper by picosecond laser-pulses,” Physical Review B, vol. 33, no. 4, pp. 2144–2151, Feb 1986.
- [68] E. Hecht, Optics, 3rd ed. Addison Wesley Publishing Company, 1997.
- [69] M. Born and E. Wolf, Principles of Optics: Electromagnetic Theory of Propagation, Interference and Diffraction of Light, 7th ed. Cambridge University Press, 1999.
- [70] J. W. Goodman, Introduction to Fourier Optics. McGraw-Hill, Boston, 1996.
- [71] M. Vicanek, A. Rosch, F. Piron, and G. Simon, “Thermal deformation of a solid-surface under laser irradiation,” Applied Physics A-Materials Science & Processing, vol. 59, no. 4, pp. 407–412, Oct 1994.
- [72] C. J. K. Richardson, M. J. Ehrlich, and J. W. Wagner, “Interferometric detection of ultrafast thermoelastic transients in thin films: theory with supporting experiment,” Journal of the Optical Society of America B-Optical Physics, vol. 16, no. 6, pp. 1007–1015, Jun 1999.
- [73] M. van Kampen, J. Kohlhepp, W. de Jonge, B. Koopmans, and R. Coehoorn, “Sub-picosecond electron and phonon dynamics in nickel,” Journal of Physics-Condensed Matter, vol. 17, no. 43, pp. 6823–6834, Nov 2 2005.
- [74] N. W. Pu and T. C. Li, “Pulse-echo measurement of longitudinal sound velocity in nanometer thin films,” Applied Physics B-Lasers and Optics, vol. 82, no. 3, pp. 449–453, Mar 2006.

- [75] C. Thomsen, J. Strait, Z. Vardeny, H. J. Maris, J. Tauc, and J. J. Hauser, “Coherent phonon generation and detection by picosecond light pulses,” Physical Review Letters, vol. 53, no. 10, pp. 989–992, 1984.
- [76] O. B. Wright and K. Kawashima, “Coherent phonon detection from ultrafast surface vibrations,” Phys. Rev. Lett., vol. 69, no. 11, pp. 1668–1671, Sep 1992.
- [77] T. Saito, O. Matsuda, and O. B. Wright, “Picosecond acoustic phonon pulse generation in nickel and chromium,” Physical Review B, vol. 67, no. 20, p. 205421, May 2003.
- [78] M. van Kampen, “Ultrafast spin dynamics in ferromagnetic metals,” Ph.D. dissertation, Eindhoven University of Technology, 2003.
- [79] J. G. M. S. S. W. J. Hohlfield, U. Conrad and E. Matthias, “Femtosecond time-resolved linear and second-order reflectivity of metals,” in Nonlinear Optics in Metals, ser. Oxford Science Publications, K. H. Bennemann, Ed. Clarendon Press, 1998, ch. 4, pp. 219–267.
- [80] X. Wang and X. Xu, “Thermoelastic wave induced by pulsed laser heating,” Applied Physics A-Materials Science & Processing, vol. 73, no. 1, pp. 107–114, Jul 2001.
- [81] O. Matsuda and O. B. Wright, “Reflection and transmission of light in multilayers perturbed by picosecond strain pulse propagation,” Journal of the Optical Society of America B-Optical Physics, vol. 19, no. 12, pp. 3028–3041, Dec 2002.
- [82] C. Thomsen, H. T. Grahn, H. J. Maris, and J. Tauc, “Surface generation and detection of phonons by picosecond light pulses,” Physical Review B, vol. 34, no. 6, pp. 4129–4138, Sep 1986.
- [83] O. Matsuda, K. Aoki, T. Tachizaki, and O. B. Wright, “Direct measurement of ultrafast surface displacement in laser picosecond acoustics,” Journal de Physique IV, vol. 125, pp. 361–363, Jun 2005.
- [84] M. Shiga and G. P. Pells, “The optical properties of nickel above and below the curie temperature,” Journal of Physics C (Solid State Physics), vol. 2, no. 2, pp. 1847–1856, 1969.
- [85] A. Paul and R. Sandberg, personal communication regarding gaussian parameters used to model the coherent HHG mode emerging from the capillary.
- [86] P. Fischer, T. Eimuller, G. Schutz, G. Denbeaux, A. Pearson, L. Johnson, D. Attwood, S. Tsunashima, M. Kumazawa, N. Takagi, M. Kohler, and G. Bayreuther, “Element-specific imaging of magnetic domains at 25 nm spatial resolution using soft x-ray microscopy,” Review of Scientific Instruments, vol. 72, no. 5, pp. 2322–2324, May 2001.
- [87] P. Fenter, C. Park, Z. Zhang, and S. Wang, “Observation of subnanometre-high surface topography with x-ray reflection phase-contrast microscopy,” Nature Physics, vol. 2, no. 10, pp. 700–704, Oct 2006.

- [88] T. Barbee and D. Keith, "Synthesis of metastable materials by sputter deposition techniques," in Synthesis and Properties of Metastable Phases, E. Machlin and T. Rowland, Eds. Metallurgical Society, Amer. Inst. Mech. Eng., 1980, p. 93.
- [89] J. Underwood and T. Barbee, "Soft-x-ray imaging with a normal incidence mirror," Nature, vol. 294, no. 5840, pp. 429–431, 1981.
- [90] R. Haelbich and C. Kunz, "Multilayer interference mirrors for the xuv range around 100 ev photon energy," Optics Communications, vol. 17, no. 3, pp. 287–292, 1976.
- [91] Optometrics llc optical components catalog. [Online]. Available: [www.optometrics.com](http://www.optometrics.com)
- [92] E. Takahashi, H. Hasegawa, Y. Nabekawa, and K. Midorikawa, "High-throughput, high-damage-threshold broadband beam splitter for high-order harmonics in the extreme-ultraviolet region," Optics Letters, vol. 29, no. 5, pp. 507–509, Mar 1 2004.
- [93] W. R. Hunter, "Thin films and their uses for the extreme ultraviolet," Applied Optics, vol. 4, p. 891898, 1965.
- [94] G. N. Steele, "Development and fabrication of large-area extreme ultraviolet filters for the applo telescope month," Space Optics Proceedings, Ninth International Congress of the International Commission for Optics, 1974.
- [95] W. R. Hunter, "The preparation and use of unbacked metal films as filters in the extreme ultraviolet," Phys. Thin Films, vol. 7, pp. 43–114, 1973.
- [96] W. R. Hunter, J. D. Purcell, and G. N. Steele, "Evaluation of pinholes in unbacked metal film filters to be used in rocket- and satellite-borne spectrographs," Applied Optics, vol. 12, no. 8, p. 1874, 1973.
- [97] C. Glorieux, K. Van de Rostyne, J. Beers, W. Gao, S. Petillion, N. Van Riet, K. Nelson, J. Allard, V. Gusev, W. Lauriks, and J. Thoen, "Acoustic waves at interfaces studied by laser ultrasonics (invited)," Review of Scientific Instruments, vol. 74, no. 1, Part 2, pp. 465–469, Jan 2003.
- [98] A. Every, "Measurement of the near-surface elastic properties of solids and thin supported films," Measurement Science & Technology, vol. 13, no. 5, pp. R21–R39, May 2002.
- [99] A. A. Maznev, A. Mazurenko, L. Zhuoyun, and M. Gostein, "Laser-based surface acoustic wave spectrometer for industrial applications," vol. 74, no. 1. AIP, 2003, pp. 667–669. [Online]. Available: <http://link.aip.org/link/?RSI/74/667/1>
- [100] A. P. M. A. Lomonosov and P. Hess, "Laser-based surface acoustic waves in materials science," in Modern acoustical techniques for the measurement of mechanical properties, ser. Experimental Methods in the Physical Sciences, H. E. B. M. Levy and R. Stern, Eds. Academic Press, 2001, vol. 39, ch. 3, pp. 65–134.

- [101] J. A. Rogers, M. Fuchs, M. J. Banet, J. B. Hanselman, R. Logan, and K. A. Nelson, "Optical system for rapid materials characterization with the transient grating technique: Application to nondestructive evaluation of thin films used in microelectronics," Applied Physics Letters, vol. 71, no. 2, pp. 225–227, 1997. [Online]. Available: <http://link.aip.org/link/?APL/71/225/1>
- [102] J. A. Rogers, L. Dhar, and K. A. Nelson, "Noncontact determination of transverse isotropic elastic moduli in polyimide thin films using a laser based ultrasonic method," Applied Physics Letters, vol. 65, no. 3, pp. 312–314, 1994.
- [103] R. I. Tobey, M. E. Siemens, M. M. Murnane, H. C. Kapteyn, D. H. Torchinsky, and K. A. Nelson, "Transient grating measurement of surface acoustic waves in thin metal films with extreme ultraviolet radiation," Applied Physics Letters, vol. 89, no. 9, p. 091108, Aug 2006.
- [104] R. I. Tobey, E. H. Gershgoren, M. E. Siemens, M. M. Murnane, H. C. Kapteyn, T. Feurer, and K. A. Nelson, "Nanoscale photothermal and photoacoustic transients probed with extreme ultraviolet radiation," Applied Physics Letters, vol. 85, no. 4, pp. 564–566, Jul 2004.
- [105] G. A. Antonelli, P. Zannitto, and H. J. Maris, "New method for the generation of surface acoustic waves of high frequency," Physica B: Condensed Matter, vol. 316, pp. 377–379, May 2002.
- [106] G. A. Antonelli, H. J. Maris, S. G. Malhotra, and J. M. E. Harper, "Picosecond ultrasonics study of the vibrational modes of a nanostructure," Journal of Applied Physics, vol. 91, no. 5, pp. 3261–3267, 2002. [Online]. Available: <http://link.aip.org/link/?JAP/91/3261/1>
- [107] B. Bonello, A. Ajinou, V. Richard, P. Djemia, and S. M. Cherif, "Surface acoustic waves in the ghz range generated by periodically patterned metallic stripes illuminated by an ultrashort laser pulse," The Journal of the Acoustical Society of America, vol. 110, no. 4, pp. 1943–1949, 2001.
- [108] D. Hurley and K. Telschow, "Picosecond surface acoustic waves using a suboptical wavelength absorption grating," Physical Review B, vol. 66, no. 15, Oct 15 2002.
- [109] C. Giannetti, B. Revaz, F. Banfi, M. Montagnese, G. Ferrini, F. Cilento, S. Maccalli, P. Vavassori, G. Oliviero, E. Bontempi, L. E. Depero, V. Metlushko, and F. Parmigiani, "Thermomechanical behavior of surface acoustic waves in ordered arrays of nanodisks studied by near-infrared pump-probe diffraction experiments," Physical Review B (Condensed Matter and Materials Physics), vol. 76, no. 12, p. 125413, 2007.
- [110] H.-N. Lin, H. J. Maris, L. B. Freund, K. Y. Lee, H. Luhn, and D. P. Kern, "Study of vibrational modes of gold nanostructures by picosecond ultrasonics," Journal of Applied Physics, vol. 73, no. 1, pp. 37–45, 1993.
- [111] D. H. Hurley, R. Lewis, O. B. Wright, and O. Matsuda, "Coherent control of gigahertz surface acoustic and bulk phonons using ultrafast optical pulses,"

- Applied Physics Letters, vol. 93, no. 11, p. 113101, 2008. [Online]. Available: <http://link.aip.org/link/?APL/93/113101/1>
- [112] D. H. Hurley, “Optical generation and spatially distinct interferometric detection of ultrahigh frequency surface acoustic waves,” Applied Physics Letters, vol. 88, no. 19, p. 191106, 2006.
- [113] A. A. Maznev, “Band gaps and brekhovskikh attenuation of laser-generated surface acoustic waves in a patterned thin film structure on silicon,” Physical Review B (Condensed Matter and Materials Physics), vol. 78, no. 15, p. 155323, 2008. [Online]. Available: <http://link.aps.org/abstract/PRB/v78/e155323>
- [114] B. A. Auld, Acoustic Fields and Waves in Solids. Robert E. Krieger Publishing Company, 1990, vol. II.
- [115] A. R. Duggal, J. A. Rogers, and K. A. Nelson, “Real-time optical characterization of surface acoustic modes of polyimide thin-film coatings,” Journal of Applied Physics, vol. 72, no. 7, pp. 2823–2839, 1992.
- [116] H. Robinson, Y. Hahn, and J. N. Gau, “A comprehensive analysis of surface acoustic wave reflections,” Journal of Applied Physics, vol. 65, no. 12, pp. 4573–4586, 1989. [Online]. Available: <http://link.aip.org/link/?JAP/65/4573/1>
- [117] S. Datta and B. J. Hunsinger, “First-order reflection coefficient of surface acoustic waves from thin-strip overlays,” Journal of Applied Physics, vol. 50, no. 9, pp. 5661–5665, 1979.
- [118] International technology roadmap for semiconductors. [Online]. Available: <http://www.itrs.net>
- [119] D. G. Cahill, W. K. Ford, K. E. Goodson, G. D. Mahan, A. Majumdar, H. J. Maris, R. Merlin, and S. R. Phillpot, “Nanoscale thermal transport,” Journal of Applied Physics, vol. 93, no. 2, pp. 793–818, Jan 2003.
- [120] M. Siemens, Q. Li, R. Yang, K. Nelson, E. Anderson, M. Murnane, and H. Kapteyn, “Quasi-ballistic thermal transport from nanoscale hotspots observed using ultrafast coherent soft x-ray beams,” Nature (submitted), 2009.
- [121] A. A. Joshi and A. Majumdar, A., “Transient ballistic and diffusive phonon heat-transport in thin-films,” Journal of Applied Physics, vol. 74, no. 1, pp. 31–39, Jul 1993.
- [122] S. Sinha and K. Goodson, “Review: Multiscale thermal modeling in nanoelectronics,” International Journal for Multiscale Computational Engineering, vol. 3, no. 1, pp. 107–133, 2005.
- [123] D. Lacroix, K. Joulain, D. Terris, and D. Lemonnier, “Monte carlo simulation of phonon confinement in silicon nanostructures: Application to the determination of the thermal conductivity of silicon nanowires,” Applied Physics Letters, vol. 89, no. 10, p. 103104, 2006. [Online]. Available: <http://link.aip.org/link/?APL/89/103104/1>

- [124] S. K. Saha and L. Shi, "Molecular dynamics simulation of thermal transport at a nanometer scale constriction in silicon," Journal of Applied Physics, vol. 101, no. 7, p. 074304, Apr 2007.
- [125] R. A. Escobar, S. S. Ghai, M. S. Jhon, and C. H. Amon, "Multi-length and time scale thermal transport using the lattice boltzmann method with application to electronics cooling," International Journal of Heat and Mass Transfer, vol. 49, no. 1-2, pp. 97 – 107, 2006. [Online]. Available: <http://www.sciencedirect.com/science/article/B6V3H-4HVDNBP-1/2/263fbe183aac5224ee972f7a63e2c799>
- [126] S. V. J. Narumanchi, J. Y. Murthy, and C. H. Amon, "Boltzmann transport equation-based thermal modeling approaches for hotspots in microelectronics," Heat and Mass Transfer, vol. 42, no. 6, pp. 478–491, Apr 2006.
- [127] R. Yang and G. Chen, "Thermal conductivity modeling of periodic two-dimensional nanocomposites," Physical Review B, vol. 69, no. 19, p. 195316, May 2004.
- [128] G. Chen, "Ballistic-diffusive heat-conduction equations," Physical Review Letters, vol. 86, no. 11, pp. 2297–2300, Mar 12 2001.
- [129] —, "Ballistic-diffusive equations for transient heat conduction from nano to macroscales," Journal of Heat Transfer, vol. 124, no. 2, pp. 320–328, Apr 2002.
- [130] A. Majumdar, "Microscale heat-conduction in dielectric thin-films," Journal of Heat Transfer, vol. 115, no. 1, pp. 7–16, Feb 1993.
- [131] F. X. Alvarez and D. Jou, "Memory and nonlocal effects in heat transport: From diffusive to ballistic regimes," Applied Physics Letters, vol. 90, no. 8, p. 083109, Feb 2007.
- [132] G. Chen, "Thermal conductivity and ballistic-phonon transport in the cross-plane direction of superlattices," Physical Reivew B, vol. 57, no. 23, pp. 14 958–14 973, Jun 1998.
- [133] W. S. Capinski, H. J. Maris, T. Ruf, M. Cardona, K. Ploog, and D. S. Katzer, "Thermal-conductivity measurements of gaas/alas superlattices using a picosecond optical pump-and-probe technique," Physical Reivew B, vol. 59, no. 12, pp. 8105–8113, Mar 1999.
- [134] Y. S. Ju and K. E. Goodson, "Phonon scattering in silicon films with thickness of order 100 nm," Applied Physics Letters, vol. 74, no. 20, pp. 3005–3007, 1999.
- [135] R. Costescu, D. Cahill, F. Fabreguette, Z. Sechrist, and S. George, "Ultra-low thermal conductivity in W/Al<sub>2</sub>O<sub>3</sub> nanolaminates," Science, vol. 303, no. 5660, pp. 989–990, Feb 13 2004.
- [136] D. Li, Y. Wu, P. Kim, L. Shi, P. Yang, and A. Majumdar, "Thermal conductivity of individual silicon nanowires," Applied Physics Letters, vol. 83, no. 14, pp. 2934–2936, 2003.

- [137] R. Chen, A. I. Hochbaum, P. Murphy, J. Moore, P. Yang, and A. Majumdar, "Thermal conductance of thin silicon nanowires," Physical Review Letters, vol. 101, no. 10, p. 105501, Jan 2008.
- [138] C. Chiritescu, D. G. Cahill, N. Nguyen, D. Johnson, A. Bodapati, P. Keblinski, and P. Zschack, "Ultralow thermal conductivity in disordered, layered WSe<sub>2</sub> crystals," Science, vol. 315, no. 5810, pp. 351–353, Jan 19 2007.
- [139] B. Poudel, Q. Hao, Y. Ma, Y. Lan, A. Minnich, B. Yu, X. Yan, D. Wang, A. Muto, D. Vashaee, X. Chen, J. Liu, M. S. Dresselhaus, G. Chen, and Z. Ren, "High-thermoelectric performance of nanostructured bismuth antimony telluride bulk alloys," Science, vol. 320, no. 5876, pp. 634–638, Jan 2008.
- [140] Z. Wang, J. A. Carter, A. Lagutchev, Y. K. Koh, N.-H. Seong, D. G. Cahill, and D. D. Dlott, "Ultrafast flash thermal conductance of molecular chains," Science, vol. 317, no. 5839, pp. 787–790, Aug 10 2007.
- [141] P. Kim, L. Shi, A. Majumdar, and P. L. McEuen, "Thermal transport measurements of individual multiwalled nanotubes," Phys. Rev. Lett., vol. 87, no. 21, p. 215502, Oct 2001.
- [142] S. Berber, Y.-K. Kwon, and D. Tománek, "Unusually high thermal conductivity of carbon nanotubes," Phys. Rev. Lett., vol. 84, no. 20, pp. 4613–4616, May 2000.
- [143] M. Asheghi, M. Touzelbaev, K. Goodson, Y. Leung, and S. Wong, "Temperature-dependent thermal conductivity of single-crystal silicon layers in SOI substrates," Journal of Heat Transfer- Transactions of the ASME, vol. 120, no. 1, pp. 30–36, Feb 1998.
- [144] W. Liu and M. Asheghi, "Phonon-boundary scattering in ultrathin single-crystal silicon layers," Applied Physics Letters, vol. 84, no. 19, pp. 3819–3821, 2004. [Online]. Available: <http://link.aip.org/link/?APL/84/3819/1>
- [145] G. Chen, "Nanoscale heat transfer and nanostructured thermoelectrics," IEEE Transactions on Components and Packaging Technologies, vol. 29, no. 2, pp. 238–246, Jun 2006.
- [146] F. DiSalvo, "Thermoelectric cooling and power generation," pp. 703–706, Jan 1999.
- [147] C. Wood, "High-temperature thermoelectric energy conversion. 2. materials survey," Energy Conversion Management, vol. 24, no. 4, pp. 331–343, Jan 1984.
- [148] A. I. Hochbaum, R. Chen, R. D. Delgado, W. Liang, E. C. Garnett, M. Najarian, A. Majumdar, and P. Yang, "Enhanced thermoelectric performance of rough silicon nanowires," Nature, vol. 451, no. 7175, pp. 163–U5, Jan 2008.
- [149] E. Pop, S. Sinha, and K. E. Goodson, "Heat generation and transport in nanometer-scale transistors," Proceedings of the IEEE, vol. 94, no. 8, pp. 1587–1601, Aug 2006.

- [150] J. Lee, T. Beechem, T. L. Wright, B. A. Nelson, S. Graham, and W. P. King, "Electrical, thermal, and mechanical characterization of silicon microcantilever heaters," Journal of Microelectromechanical Systems, vol. 15, no. 6, pp. 1644–1655, Dec 2006.
- [151] G. Chen, D. Borsa-Tasciuc, and R. Yang, "Nanoscale heat transfer," in Encyclopedia of Nanoscience and Nanotechnology, H. Nalwa, Ed. American Scientific Publishers, 2004, vol. 7, pp. 429–459.
- [152] F. Claro and G. D. Mahan, "Transient heat transport in solids," Journal of Applied Physics, vol. 66, no. 9, pp. 4213–4217, Nov 1989.
- [153] G. D. Mahan and F. Claro, "Nonlocal theory of thermal conductivity," Physical Review B, vol. 38, no. 3, pp. 1963–1969, Jul 1988.
- [154] R. G. Yang, G. Chen, M. Laroche, and Y. Taur, "Simulation of nanoscale multi-dimensional transient heat conduction problems using ballistic-diffusive equations and phonon boltzmann equation," Journal of Heat Transfer, vol. 127, no. 3, pp. 298–306, Mar 2005.
- [155] S. V. J. Narumanchi, J. Y. Murthy, and C. H. Amon, "Simulation of unsteady small heat source effects in sub-micron heat conduction," Journal of Heat Transfer, vol. 125, no. 5, pp. 896–903, 2003. [Online]. Available: <http://link.aip.org/link/?JHR/125/896/1>
- [156] P. Heino, "Multiscale Lattice-Boltzmann finite difference model for thermal conduction from nanoscale hot spots," International Journal for Multiscale Computational Engineering, vol. 6, no. 2, pp. 169–178, 2008.
- [157] D. G. Cahill, "Analysis of heat flow in layered structures for time-domain thermoreflectance," Review of Scientific Instruments, vol. 75, no. 12, pp. 5119–5122, 2004.
- [158] R. Prasher, "Predicting the thermal resistance of nanosized constrictions," Nano Letters, vol. 5, no. 11, pp. 2155–2159, 2005.
- [159] M. Yovanovich, Y. Muzychka, and J. Culham, "Spreading resistance of isoflux rectangles and strips on compound flux channels," Journal of Thermophysics and Heat Transfer, vol. 13, pp. 495–500, 1999.
- [160] Mikic and Rohsenow, "Thermal contact resistance," Rohsenow Heat and Mass Transfer Laboratory Technical Reports, vol. 4542, 1966.
- [161] G. Chen, "Nonlocal and nonequilibrium heat conduction in the vicinity of nanoparticles," Journal of Heat Transfer, vol. 118, no. 3, pp. 539–545, Aug 1996.
- [162] R. Siegel and J. Howell, Thermal Radiation Heat Transfer, 4th ed. Taylor and Francis, 2001.
- [163] C. H. Christiansen, "Absolute bestimmung des emissions-und absorptionsvermögens für warmes," Ann. Phys. Wied., vol. 19, p. 267, 1883.

- [164] B. H. Armstrong, "Two-fluid theory of thermal conductivity of dielectric crystals," Physical Review B, vol. 23, no. 2, pp. 883–899, Jan 1981.
- [165] R. Heid, D. Strauch, and K. P. Bohnen, "Ab initio lattice dynamics of sapphire," Physical Reivew B, vol. 61, no. 13, pp. 8625–8627, Apr 2000.
- [166] P. G. Sverdrup, "Simulation and thermometry of sub-continuum heat transport in semiconductors," Ph.D. dissertation, Stanford University, Dec 2000.
- [167] P. G. Sverdrup, S. Sinha, M. Asheghi, S. Uma, and K. E. Goodson, "Measurement of ballistic phonon conduction near hotspots in silicon," Applied Physics Letters, vol. 78, no. 21, pp. 3331–3333, May 2001.
- [168] M. Kresch, O. Delaire, R. Stevens, J. Y. Y. Lin, and B. Fultz, "Neutron scattering measurements of phonons in nickel at elevated temperatures," Physical Review B (Condensed Matter and Materials Physics), vol. 75, no. 10, p. 104301, 2007. [Online]. Available: <http://link.aps.org/abstract/PRB/v75/e104301>
- [169] R. J. Stoner and H. J. Maris, "Kapitza conductance and heat flow between solids at temperatures from 50 to 300 k," Physical Reivew B, vol. 48, no. 22, pp. 16 373–16 387, Dec 1993.
- [170] K. E. Goodson, O. W. Kading, M. Rosler, and R. Zachai, "Experimental investigation of thermal conduction normal to diamond-silicon boundaries," Journal of Applied Physics, vol. 77, no. 4, pp. 1385–1392, 1995.
- [171] A. P. Caffrey, P. E. Hopkins, J. M. Klopff, and P. M. Norris, "Thin film non-noble transition metal thermophysical properties," Microscale Thermophysical Engineering, vol. 9, no. 4, pp. 365–377, Oct-Dec 2005.
- [172] sitmo, "Resources for financial engineers, equations archive." [Online]. Available: <http://www.sitmo.com/eq/262>
- [173] T. G. Kollie, "Measurement of the thermal-expansion coefficient of nickel from 300 to 1000 k and determination of the power-law constants near the curie temperature," Physical Reivew B, vol. 16, no. 11, pp. 4872–4881, Dec 1977.
- [174] Tabulated data for sapphire. [Online]. Available: [http://global.kyocera.com/prdct/fc/product/pdf/s\\_c\\_sapphire.pdf](http://global.kyocera.com/prdct/fc/product/pdf/s_c_sapphire.pdf)
- [175] S. Burghartz and B. Schulz, "Thermophysical properties of sapphire, aln and mgal2o4 down to 70 k," Journal of Nuclear Materials, vol. 215, pp. 1065–1068, Sep 1994.
- [176] Y. S. Touloukian, Ed., Thermophysical Properties of High Temperature Solid Materials. The Macmillan Company, 1967, vol. 4. [Online]. Available: TA418.26.P8
- [177] Y. S. Touloukian, R. W. Powell, C. Y. Ho, and P. G. Klemens, Eds., Thermal conductivity: Nonmetallic Solids, Thermophysical Properties of Matter. IFO/Plenum, NY, 1970, vol. 4. [Online]. Available: QC171.P83

- [178] W. Nowacki, Thermoelasticity. Addison-Wesley Publishing Company, Inc., 1962.
- [179] Landau and Lifshitz, Theory of Elasticity. Pergamon Press, 1986.
- [180] Albagli, D and Dark, M and Vonrosenberg, C and Perelman, L and Itzhan, I and Feld, MS, “Laser-induced Thermoelastic Deformation - a 3-dimensional Solution and its Application to the Ablation of Biological Tissue,” Medical Physics, vol. 21, no. 8, pp. 1323–1331, Aug 1994.
- [181] D. G. Cahill, “Thermal conductivity measurement from 30 to 750 k: the 3 omega method,” Review of Scientific Instruments, vol. 61, no. 2, pp. 802–808, 1990. [Online]. Available: <http://link.aip.org/link/?RSI/61/802/1>
- [182] G. Cerullo and S. De Silvestri, “Ultrafast optical parametric amplifiers,” Review of Scientific Instruments, vol. 74, no. 1, pp. 1–18, Jan 2003.
- [183] A. Technology, “Ccd spectral response (quantum efficiency).” [Online]. Available: [http://www.andor.com/learn/digital\\_cameras/?docID=315](http://www.andor.com/learn/digital_cameras/?docID=315)
- [184] P. Pershan, “Magneto-optical effects,” Journal of Applied Physics, vol. 38, no. 3, pp. 1482–&, 1967.
- [185] M. Freiser, “A survey of magneto-optic effects,” IEEE Transactions on Magnetics, vol. MAG4, no. 2, pp. 152–&, 1968.
- [186] H. Mertins, S. Valencia, A. Gaupp, W. Gudat, P. Oppeneer, and C. Schneider, “Magneto-optical polarization spectroscopy with soft X-rays,” Applied Physics A-Materials Science & Processing, vol. 80, no. 5, pp. 1011–1020, Feb 2005.
- [187] D. Kim, P. Fischer, W. Chao, E. Anderson, M. Im, S. Shin, and S. Choe, “Magnetic soft x-ray microscopy at 15 nm resolution probing nanoscale local magnetic hysteresis (invited),” Journal of Applied Physics, vol. 99, no. 8, APR 15 2006.
- [188] M. Faraday, Philosophical Transactions of the Royal Society, vol. 136, p. 1, 1846.
- [189] J. Kerr, Report of the British Association for the Advancement of Science, p. 40, 1876.
- [190] —, Philosophical Magazine, vol. 5, p. 161, 1878.
- [191] P. Zeeman, Leiden Communications, vol. 29, 1896.
- [192] M. Hecker, P. Oppeneer, S. Valencia, H. Mertins, and C. Schneider, “Soft X-ray magnetic reflection spectroscopy at the 3p absorption edges of thin Fe films,” Journal of Electron Spectroscopy and Related Phenomena, vol. 144, no. Sp. Iss. SI, pp. 881–884, Jun 2005.
- [193] M. Pretorius, J. Friedrich, A. Ranck, M. Schroeder, J. Voss, V. Wedemeier, D. Spanke, D. Knabben, I. Rozhko, H. Ohldag, F. U. Hillebrecht, and E. Kisker, “Transverse magneto-optical kerr effect of fe at the fe 3p threshold,” Physical Review B, vol. 55, no. 21, pp. 14 133–14 135, Jun 1997.

- [194] S. Valencia, A. Gaupp, W. Gudat, H.-C. Mertins, P. M. Oppeneer, D. Abramssohn, and C. M. Schneider, “Faraday rotation spectra at shallow core levels: 3p edges of Fe, Co, and Ni,” New Journal of Physics, vol. 8, Oct 25 2006.
- [195] P. Antoine, B. Carre, A. LHuillier, and M. Lewenstein, “Polarization of high-order harmonics,” Physical Review A, vol. 55, no. 2, pp. 1314–1324, Feb 1997.
- [196] X. Zhou, R. Lock, N. Wagner, W. Li, H. C. Kapteyn, and M. M. Murnane, “Elliptically polarized high-order harmonic emission from molecules in linearly polarized laser fields,” Physical Review Letters, vol. 102, no. 7, p. 073902, 2009. [Online]. Available: <http://link.aps.org/abstract/PRL/v102/e073902>
- [197] P. M. Oppeneer, “Magneto-optical kerr spectra,” in Handbook of Magnetic Materials, K. H. J. Buschow, Ed. Elsevier, 2001, vol. 13, ch. 3, pp. 229–422.
- [198] I. Boswarva, R. Howard, and A. Lidiard, “Faraday effect in semiconductors,” Proceedings of the Physical Society of London Series A- Mathematical and Physical Sciences, vol. 269, no. 1336, pp. 125–&, 1962.
- [199] Birss, Symmetry and Magnetism. North-Holland Publishing Company, Amsterdam, 1964.
- [200] K. Shinagawa, “Faraday and kerr effects in ferromagnets,” in Magneto-Optics, ser. Solid State Sciences, S. Sugano and H. Kojima, Eds. Springer, 2000, vol. 128, pp. 137–178.
- [201] Z. J. Yang and M. R. Scheinfein, “Combined three-axis surface magneto-optical kerr effects in the study of surface and ultrathin-film magnetism,” Journal of Applied Physics, vol. 74, no. 11, pp. 6810–6823, 1993. [Online]. Available: <http://link.aip.org/link/?JAP/74/6810/1>
- [202] J. L. Erskine and E. A. Stern, “Magneto-optic kerr effects in gadolinium,” Phys. Rev. B, vol. 8, no. 3, pp. 1239–1255, Aug 1973.
- [203] J. Erskine and E. Stern, “Calculation of the m23 magneto-optical absorption spectrum of ferromagnetic nickel,” Phys. Rev. B, vol. 12, no. 11, pp. 5016–5024, Dec 1975.
- [204] T. Silva, J. Shaw, and H. Nembach, “Optical measurement of t-moke signal,” measurement performed at National Institute of Standards and Technology, Electromagnetics Division.
- [205] A. Laraoui, V. Halte, M. Vomir, J. Venuat, M. Albrecht, E. Beaurepaire, and J.-Y. Bigot, “Ultrafast spin dynamics of an individual CoPt3 ferromagnetic dot,” European Physical Journal D, vol. 43, no. 1-3, pp. 251–253, Jul 2007.
- [206] G. Malinowski, F. D. Longa, J. H. H. Rietjens, P. V. Paluskar, R. Huijink, H. J. M. Swagten, and B. Koopmans, “Control of speed and efficiency of ultrafast demagnetization by direct transfer of spin angular momentum,” Nature Physics, vol. 4, no. 11, pp. 855–858, Nov 2008.

- [207] M. Cinchetti, M. S. Albaneda, D. Hoffmann, T. Roth, J.-P. Wustenberg, M. Krauss, O. Andreyev, H. C. Schneider, M. Bauer, and M. Aeschlimann, “Spin-flip processes and ultrafast magnetization dynamics in co: Unifying the microscopic and macroscopic view of femtosecond magnetism,” Physical Review Letters, vol. 97, no. 17, p. 177201, 2006. [Online]. Available: <http://link.aps.org/abstract/PRL/v97/e177201>
- [208] H. A. Duerr, C. Stamm, T. Kachel, N. Pontius, R. Mitzner, T. Quast, K. Holldack, S. Khan, C. Lupulescu, E. F. Aziz, M. Wietstruk, and W. Eberhardt, “Ultrafast electron and spin dynamics in nickel probed with femtosecond X-ray pulses,” IEEE Transactions on Magnetics, vol. 44, no. 7, Part 2, pp. 1957–1961, JUL 2008.
- [209] A. Hubert and R. Scäfer, Magnetic Domains- The Analysis of Magnetic Microstructure. Springer, 1998.
- [210] R. D. McMichael and M. D. Stiles, “Magnetic normal modes of nanoelements,” vol. 97, no. 10. AIP, 2005, p. 10J901. [Online]. Available: <http://link.aip.org/link/?JAP/97/10J901/1>
- [211] J. M. Shaw, T. J. Silva, M. L. Schneider, and R. D. McMichael, “Spin dynamics and mode structure in nanomagnet arrays: Effects of size and thickness on linewidth and damping,” Physical Reivew B (in press), 2009.
- [212] R. I. Tobey, M. E. Siemens, O. Cohen, M. M. Murnane, H. C. Kapteyn, and K. A. Nelson, “Ultrafast extreme ultraviolet holography: dynamic monitoring of surface deformation,” Optics Letters, vol. 32, no. 3, pp. 286–288, Feb 2007.
- [213] M. E. Siemens, Q. Li, M. M. Murnane, H. C. Kapteyn, R. Yang, E. H. Anderson, and K. A. Nelson, “High-frequency surface acoustic wave propagation in nanostructures characterized by coherent extreme ultraviolet beams,” Applied Physics Letters, vol. 94, no. 9, p. 093103, 2009. [Online]. Available: <http://link.aip.org/link/?APL/94/093103/1>
- [214] C. La-O-Vorakiat, M. Siemens, J. Shaw, H. Nembach, S. Matthias, R. Adam, C. M. Schneider, M. A. T. Silva, M. Murnane, and H. Kapteyn, “Magneto-optical kerr effect probed using ultrafast high-order harmonic euv light,” Physical Review Letters, in preparation, 2009.

## Appendix A

### Fresnel propagation code

```
% fresnel.m Use the fresnel approximation to calculate the interference of gaussian pump-
% induced height and reflectivity changes. All distances and constants are given in meters

lambda = 30E-9;
z = 25E-2;
w = 50E-6;
spot = 2E-3;
h = .13E-9;
dx0 = 6.5E-6;
r0 = sqrt(.0535);
dr = sqrt(.0533)-sqrt(.0535);
N = 1024;
k = 2*pi/lambda;
I=sqrt(-1);

zcrit = N * dx0^2/lambda;
x = -N/2: 1 :N/2-1; % Initialize x-array
x0 = dx0 * x; % Set x-array to pixel size of camera

bump = h * exp(-x0.^2 / w^2); % Phase term of reflectivity amplitude coefficient
refl = r0 + dr * exp(-x0.^2 / w^2); % Amplitude term of reflectivity amplitude coefficient
gauss = exp(-x0.^2 / spot^2); % Probe spot of reflectivity amplitude coefficient
iB = spot^-2*z/k;
Bfactor = (1+i*iB)^-1
spotz = sqrt(real(Bfactor))^-1 * spot
```

```

f1 = gauss .* exp(I*4*pi/lambda * bump) * r0; % Probe spot modulated by phase term
fa = gauss .* refl; % Probe spot modulated by amplitude reflectivity term
ff = gauss .* exp(I*4*pi/lambda * bump) .* refl;% Probe spot modulated by amplitude and phase terms

du = 1./(N*dx0);
u = [0:N/2-1 -N/2:-1]*du; % Note order of points- for convolution
H = exp(-i*2*pi^2*u.^2*z/k); % Fourier transform of kernel
f2 = ifft( fft(f1) .* H ); % Convolution with phase term
fb = ifft( fft(fa) .* H ); % Convolution with amplitude term
fF = ifft( fft(ff) .* H ); % Convolution with both terms
f0 = ifft( fft(gauss*r0) .* H ); % Convolution with no modulation
dx1 = lambda*z*du/26E-6; % dx0 / 26E-6
x1 = [-N/2:N/2-1]*dx1; % Baseline for output in pixels

pti = abs(f2).^2 - abs(f1).^2; % Phase term intensity
ati = abs(fb).^2 - abs(fa).^2; % Amplitude term intensity
bti = abs(fF).^2 - abs(ff).^2; % Both terms intensity

plot(x1, pti, x1, ati, x1, bti)
axis([-10,10]);
title('Holographic signal including amplitude effects for a 30nm probe');
xlabel('CCD pixel') % label the x-axis
ylabel('signal level'); % label the y-axis

bump_max = max(pti);
refl_max = max(ati);
both_max = max(bti);
gauss_max = max(abs(gauss).^2);
ratio_separate = refl_max / bump_max;
ratio_amp = refl_max / both_max;
ratio_both = (both_max-bump_max) / both_max
signaltoprobe = both_max/gauss_max

```

## Appendix B

### Multiphysics thermal and optical model

```
% New in version 8: take T-dependence of k, C, CTE (with heating) into
% account

clear;

dt=1*10^-12; tf=8*10^-9; dt2=dt;

Tsave=[0:.1d-10:1d-10 2d-10:1d-10:1d-9 1.25d-9:.25d-9:2d-9 2.5d-9:.5d-9:5d-9 6d-9:1d-9:tf 10d-9];
TempVary=[310 300];
Lvary=[1000]*1d-3;
hBDvary=[150 200 350 500 700]*1d6;
Tf0=500;

for xVary=Lvary
% Define grid parameters
width=xVary; xscale=2; dx=width/xscale*10^-8; xs=width*4*10^-6; ys=xs; xf=width*10^-6;
Nt=round(tf/dt)+1; Nxs=round(xs/dx); Nys=round(ys/dx); Nxf=round(xf/dx);
Nx1=round(3*Nxs/8); Nx2=round(5*Nxs/8);

df=2*10^-8; % film thickness in m

%----- Set up diffraction model -----%
I = sqrt(-1);

% lambda = Wavelength of the probe light
lambda = 29E-9;
```

```

kk = 2*pi/lambda;

% dx0 = Original mesh resolution, N = # of points in mesh
dx0 = dx*xscale;
N = 1024*1024;
x = -N/2: 1 :N/2-1; % Initialize x-array
x0 = dx0 * x; % Set x-array

% z = Distance from the sample to the camera
z = 6E-2;

% w = Full linewidth of the Ni line on the sample, dw = pump-induced change, off = pump offset from center
w = xf;
dw = 0E-12;
off = 0*dx0;

% spot = EUV 1/2, 1/e width at the focus from the toroid
spot = 50E-6;

% h = height of the Ni line on the sample, dw = pump-induced change
% h = 18.25E-9;
h = df;
% dh = 18.7E-12;

% r0 = reflectivity of the sapphire substrate (45), dr = reflectivity
% difference between sapphire and Ni
r0 = sqrt(.0535);
dr = sqrt(.0529)-sqrt(.0535);

% zfoc = distance from EUV focus to the sample, prop = propagator for that distance
zfoc = 0E-3;
prop = (1+I*2*zfoc/(kk*spot^2))^-1;

% wsample/wcamera = unperturbed probe size at sample and camera, respectively
wsample = sqrt(real(prop/spot^2))^-1;
wcamera = sqrt(real(1/spot^2*(1+I*2*(z+zfoc)/(spot^2*kk))^-1))^-1;

```

```

zcrit = N * dx0^2/lambda;

% Normalization of probe counts: say 1E4 photons in EUV beam at sample (including
% toroid reflectivity (71%), quantum efficiency of the CCD (20%), and the 3 Al
% filters). This is distributed over the entire gaussian, integrated to sqrt(pi/a),
% where a=1/spot^2. This leads us to a normalization constant 'C' for the amplitude
% gaussian: C = sqrt(1E4/(spot*sqrt(pi/2)));
C=1;

nmax = floor(120/(xs*2d6));
dutyicycle = 1;
bump = grating((x0)/w, nmax, dutyicycle); % Profile of Ni line on sample

amp = r0 + dr*grating((x0-off)/w, nmax, dutyicycle); % Reflectivity on sample
amp2 = r0 + dr*grating((x0-off)/(w+dw), nmax, dutyicycle);

gauss0 = C*exp(-x0.^2/spot^2); % Probe spot at focus
gauss = C*prop * exp(-x0.^2/spot^2*prop);

f = amp.* gauss.* exp(I*4*pi/lambda * h*bump);
f2 = FProp(f,x0,dx0,N,z);

xmax2=Nxs; ymax2=Nys;
xmax1=Nxf; ymax1=1; dy=dx; dy0=dx0;

% Initialize CN calculation matrices
a=zeros(Nxs,1); b=a; c=a; d=a; % Substrate matrix coefficients for x-implicit
b(1)=-1; c(1)=1; % Top boundary
a(Nxs)=1; b(Nxs)=-1; % bottom boundary

a2=zeros(Nys,1); b2=a2; c2=a2; d2=a2; % Substrate matrix coefficients for y-implicit
b2(1)=-1; c2(1)=1; % Top boundary
a2(Nys)=1; b2(Nys)=-1; % bottom boundary

fa=zeros(Nys,1); fb=fa; fc=fa; fd=fa; % substrate matrix coefficients beneath film
fa(Nys)=1; fb(Nys)=-1; % bottom boundary

```

```

for Temp=TempVary
Tsh=Temp-69;

    % Define thermal parameters of the film (nickel) and substrate (sapphire)
load kKCTENiSaT5.txt;
ksT= kKCTENiSaT5(:,4); kfT= kKCTENiSaT5(:,2);           % W/m K
asT= kKCTENiSaT5(:,5); afT= kKCTENiSaT5(:,3);          % J/m^3 K
axsT=kKCTENiSaT5(:,6)*1d-6; axfT=kKCTENiSaT5(:,7)*1d-6;
    CfT=kKCTENiSaT5(:,8)*8.9d6;
sig=.25;           % Poisson ratio for sapphire

% Cf = 2.44*10^6; kf = 237;           % Aluminum film
% ks = 1.38; Cs = .740*2.2E6; axs=.54d-6; sig=.17; % FS substrate
asxT=asT;

    for hBD=hBDvary
        C2=1; C1=100;

        %Define initial conditions in the film and substrate
        Ts1=zeros(Nxs,Nys); Ts2=Ts1; Tft=Tf0*ones(Nxf,1); Tft2=Tft;

        FileName2 = sprintf('SigNi%02d T%03d h%02d.txt',[xf*1d9 Temp round(hBD/1e6)]);
        FileName3 = sprintf('SigNiSa%02d T%03d h%02d.txt',[xf*1d9 Temp round(hBD/1e6)]);
        %   FileName4 = sprintf('TNiMid%02d T%03d k%02d h%02d.txt',[xf*1d9 Temp round(ks) round(hBD/1e6)]);
        %   FileName5 = sprintf('TNiEdge%02d T%03d k%02d h%02d.txt',[xf*1d9 Temp round(ks) round(hBD/1e6)]);
        %   FileName6 = sprintf('TSaMid%02d T%03d k%02d h%02d.txt',[xf*1d9 Temp round(ks) round(hBD/1e6)]);
        %   FileName7 = sprintf('TSaEdge%02d T%03d k%02d h%02d.txt',[xf*1d9 Temp round(ks) round(hBD/1e6)]);
        %   FileName8 = sprintf('TSaCorner%02d T%03d k%02d h%02d.txt',[xf*1d9 Temp round(ks) round(hBD/1e6)]);

        for t=2:Nt,           % Time stepping

            if(t.*dt>=Tsave(C2));
                for k=1:Nxs/xscale
                    hSa(k)=0;
                end
            end
        end
    end
end

```

```

% Determine thermal deformation at the surface of the substrate
for Neighbors=-1:1 % Sum over nearest neighbors
    for Ci=(1:xscale:Nxs)+floor(xscale/2) % Sum over x (across surface)
        for Cj=(1:xscale:Nys)+floor(xscale/2) % Sum over z (into substrate)
            for Ck=1:round(Nxs/xscale) % Sum over new index (across surface)
                hSa(Ck)=hSa(Ck)+2*(1+sig)*axsT(round(Ts1(Ci,Cj))+Tsh)*dx0*dy0/(3*pi)*...
                    (Ts1(Ci,Cj))*Cj*dy/((Ck*xscale+Neighbors*Nxs-Ci)^2*dx^2+Cj^2*dy^2);
            end
        end
    end
end

% Determine thermal expansion of the Ni lines
for Ci=1:xmax1/xscale
    hNi(Ci)=sum(axfT(round(Tft(Ci*xscale-floor(xscale/2),:))+Temp-69)*...
        Tft(Ci*xscale-floor(xscale/2),:))*h/ymax1;
end

pump = transpose(bumpNi2(hNi,x0,nmax)); % Profile of pumped Ni line on sample
hump = transpose(gauss3(hSa,x0,nmax)); % Profile of pumped Ni with Sa deformation

p = amp.* gauss.* exp(I*4*pi/lambda * (h*bump + pump));
q = amp.* gauss.* exp(I*4*pi/lambda * (h*bump + pump + hump));

p2 = FProp(p,x0,dx0,N,z);
q2 = FProp(q,x0,dx0,N,z);

sigbump=sum(abs((abs(p2).^2-abs(f2).^2)));
sighump=sum(abs((abs(q2).^2-abs(f2).^2)));
if C2==1, SigNorm=sighump; end;

SigNi(C2,1:2)=[round(Tsave(C2)*1e12),sigbump];
SigSa(C2,1:2)=[round(Tsave(C2)*1e12),sighump/SigNorm];
% TNiMid(C2,1:2)=[round(Tsave(C2)*1e12),Tft(100)];
% TNiEdge(C2,1:2)=[round(Tsave(C2)*1e12),Tft(1)];
% TsaMid(C2,1:2)=[round(Tsave(C2)*1e12),Ts1(400,1)];
% TsaEdge(C2,1:2)=[round(Tsave(C2)*1e12),Ts1(300,1)];

```

```

%           TSaCorner(C2,1:2)=[round(Tsave(C2)*1e12),Ts1(1,1)];
%           PercentRealSignal(C2+1)=sigbump/sighump;
%           PercentRealSignal(C2+1)

%           FileName = sprintf('PercentRealSignal%04d.dat',xf*1d9);
%           dlmwrite(FileName,PercentRealSignal(:), ' ');
%           dlmwrite(FileName2,SigNi(:,:), ' ');
%           dlmwrite(FileName3,SigSa(:,:), ' ');
%           dlmwrite(FileName4,TNiMid(:,:), ' ');
%           dlmwrite(FileName5,TNiEdge(:,:), ' ');
%           dlmwrite(FileName6,TSaMid(:,:), ' ');
%           dlmwrite(FileName7,TSaEdge(:,:), ' ');
%           dlmwrite(FileName8,TSaCorner(:,:), ' ');
%           fprintf(1,'%03d ', t);fprintf(1,'%s ','/');fprintf(1,'%03d \n',Nt);

%           C2=C2+1;
end;

%           Tf0 = dt*hBD/(df*Cf)*(0-Tf0)+Tf0;

%           implicit in y direction

for i=1:Nxf           % In and under the film
    k=i+Nx1;
%           d(1)=-dx*hBD/ks*(Tft(i)-Ts1(k,1));           % Set u_y at film-substrate interface
    DeltaTf=dt*hBD/(df*CfT(round(Tft(i))+Tsh))*(Ts1(k,1)-Tft(i));

    fb(1)=-25; fc(1)=48;           % Left boundary
    for j = 2:Nys-1
        as=asT(round(Ts1(k,j))+Tsh);
        fa(j) = -2*as*dt; fb(j) = 4*dx^2+4*as*dt; fc(j) = -2*as*dt;
        fd(j) = 2*as*dt*Ts1(k,j+1)+(4*dx^2-4*dt*as)*Ts1(k,j)+2*dt*as*Ts1(k,j-1);
    end
    Z=16+3*fb(4)/fc(4); Y=36-3*fa(4)/fc(4)+Z*fb(3)/fc(3);
    fb(1)=fb(1)+Y*fa(2)/fc(2); fc(1)=fc(1)-Z*fa(3)/fc(3)+Y*fb(2)/fc(2);
    fd(1)=-12*dx*hBD/ksT(round(Ts1(k,1))+Tsh)*(Tft(i)-Ts1(k,1))+...

```

```

3*fd(4)/fc(4)-Z*fd(3)/fc(3)+Y*fd(2)/fc(2);
Tft(i) = DeltaTf+Tft(i);

[Ts2(k,:)] = TDMA solver(fa,fb,fc,fd);           % Solve the system

%      DeltaEfi=DeltaTf*Cf*df*dx;
%      DeltaEsi=(sum(Ts2(k,:))-sum(Ts1(k,:)))*Cs*dx^2;
%      Ts2(k,:)=Ts1(k,:)+abs(DeltaEfi/DeltaEsi)*(Ts2(k,:)-Ts1(k,:));
%      uy0=(Ts2(k,1)-Ts2(k,2))/dx;
%      fprintf(1,'uy0 = %03d, d(1) = %03d \n', uy0/abs(DeltaEfi/DeltaEsi), d(1)/dx);
%      if i==1, fd(i)=0;           % Pure implicit in x- 1D in the
%      film
%      elseif i==Nxf, fd(i)=0;
%      else fd(i) = 2*af*dt*Tft(i+1)+(4*dx^2-4*dt*af)*Tft(i)+2*dt*af*Tft(i-1); end
end
%      [Tft(:)] = TDMA solver(fa,fb,fc,fd);           % Solve the system- film temperature in 1D

for i=1:Nx1           % Flanking film
    d2(1)=0; d2(Nys)=0;   % u_x = 0 at both edges
    m=i+Nx2;           % index for on the other side of the film
    for j = 2:Nys-1
        as=asT(round(Ts1(i,j))+Tsh);
        a2(j) = -2*as*dt2;  b2(j) = 4*dx^2+4*as*dt2;  c2(j) = -2*as*dt2;
        d2(j) = 2*as*dt*Ts1(i,j+1)+(4*dx^2-4*dt*as)*Ts1(i,j)+2*dt*as*Ts1(i,j-1);
    end

    [Ts2(i,:)] = TDMA solver(a2,b2,c2,d2);           % Solve the system

    for j = 2:Nys-1
        as=asT(round(Ts1(m,j))+Tsh);
        a2(j) = -2*as*dt2;  b2(j) = 4*dx^2+4*as*dt2;  c2(j) = -2*as*dt2;
        d2(j) = 2*as*dt*Ts1(m,j+1)+(4*dx^2-4*dt*as)*Ts1(m,j)+2*dt*as*Ts1(m,j-1);
    end

    [Ts2(m,:)] = TDMA solver(a2,b2,c2,d2);           % Solve the system

```

```

end

% implicit in x direction
for(j=1:Nys)          % In the substrate
    for(i=2:Nxs-1)
        asx=asxT(round(Ts2(i,j))+Tsh);
        a(i) = -2*asx*dt2;  b(i) = 4*dx^2+4*asx*dt2;  c(i) = -2*asx*dt2;
        d(i) = 2*asx*dt*Ts2(i+1,j)+(4*dx^2-4*dt*asx)*Ts2(i,j)+2*dt*asx*Ts2(i-1,j);
    end
    [Ts1(:,j)]=TDMAsolver(a,b,c,d);          % Solve the system
end

%          DeltaEs=(sum(sum(Ts2(:,:)))-sum(sum(Ts1(:,:))))*Cs*dx^2;  % Calculate DeltaEnergy substrate
%          EnergyConservation=-DeltaEf/DeltaEs;
%          Ts1(:,:)=Ts1(:,:)+EnergyConservation*(Ts2(:,:)-Ts1(:,:));
%          C1=C1+1;
%          if C1>=100 fprintf(1,'Energy Conservation = %03d \n', -DeltaEfi/DeltaEsi); C1=0; end
end
end
end
end
end

```